Academic Studies in
ENGINEERING SCIENCES

Editor

Assoc. Prof. Dr. Halil İbrahim Kurt

Engineering

🌐 **livredelyon.com**

🐦 **livredelyon**

📷 **livredelyon**

in **livredelyon**

LIVRE DE LYON

Lyon 2020

ACADEMIC STUDIES

IN

ENGINEERING SCIENCES

Editor
Assoc. Prof. Dr. Halil İbrahim Kurt

LIVRE DE LYON

Lyon 2020

The chapters in this book have been checked for plagiarism by 🦁 intihal.net

LIVRE DE LYON

PREFACE

Experimental researches have contributed to the development of education and training definitions in various periods. Although the importance given to science and data-based academic studies is mentioned today, it is observed that the studies conducted are far from the scientific method. Disciplinary and/or interdisciplinary studies allow for synthesis of ideas and the synthesis of characteristics from many disciplines. At the same time it addresses scientists, engineers and students' individual differences and helps to develop important, transferable skills. These skills, like critical thinking, communication, analysis, interpretation and discussion are important and continually developing at all stages of life.

One of the major objectives of this 'Academic Studies in Engineering' was to present evidence and gather together the results of research and development carried out on the engineering applications during recent years. The book brought together scientists and engineers involved in assessing the various engineering areas, with particular emphasis on academic studies, applications and opinions.

The editor and editorial board hope that this book will be useful to engineers and to scientists working towards an understanding of and the resolution of the applications in the various fields of engineering that we have to face in near future.

<div align="right">Assoc. Prof. Dr. Halil İbrahim Kurt</div>

CONTENTS

REFEREES

Prof. Dr. Duygu Kavak, Eskişehir Osmangazi University, Turkey

Assoc. Prof. Dr. Ali Hakan Işık Burdur Mehmet Akif Ersoy University, Turkey

Assoc. Prof. Dr. Cengiz Polat Uzunoğlu, İstanbul University, Turkey

Assoc. Prof. Dr. İbrahim Aydoğdu Akdeniz University, Turkey

Assoc. Prof. Dr. Mehmet Fırat Baran, Siirt University, Turkey

Assoc. Prof. Dr. Sezgin Ersoy, Marmara University, Turkey

Asst. Prof. Dr. Alper Polat Munzur University, Turkey

THE EFFECTS OF COUNTER GRAVITY CASTING PROCESS PARAMETERS ON SOLIDIFICATION BEHAVIOUR OF Al-Si ALLOY PRODUCED BY REAL CASTING CONDITIONS

Hasan Hasirci[1]

[1](Assoc. Prof. Dr.), Gazi University, e-mail: hasirci@gazi.edu.tr,
ORCID *0000-0001-5520-4383*

1. INTRODUCTION

In each casting process, inherent limitations are exhibited in either performance or manufacturing cost. These processes include well-documented technologies, such as low pressure, vacuum-assisted casting, combinations of low pressure and vacuum, and squeeze casting (Campbell, 1999; Rasmussen, 2000; Dash and Malkhlouf 2001:1). In most cases, performance is hindered by non-uniform metal flow, entrainment of gases during the mould filling process, or segregation of impurities during solidification (Dash and Malkhlouf 2001:1; Lee, Chang and Yeh 1990:187; Loper and Prucha 1999:165). The development of the Counter Gravity Casting (CGC) process eliminates these deficiencies by controlling mould fill to insure true metal flow uniformity, preventing the entrance of gases during filling and providing both directional and uniform solidification (Rasmussen, 2000; Dash, 2001:1; Loper, 1999). This results in outstanding strength and ductility for components produced by the CGC process (Campbell, 1999; Dash and Malkhlouf 2001:1; Kuo, Hsu and Hwang 2001:2). CGC process is shown in Fig. 1 (Hasirci, 2006). A mould is prepared from a wet sand mixture with air (gas) permeability to be used in casting process. The bottom part of the mould has a cavity in order to be filled up with liquid metal and the mould is immersed under vacuum into the liquid metal. Vacuum is maintained until solidification of the liquid metal has been completed. In the subsequent stage, the mould is removed from the liquid metal. Finally, the mould is broken to get the castings.

The process has many advantages in terms of quality and process control as well. These advantages include the ability to control the rate of metal flow; formation of surface slag and re-oxidation macro inclusions formed by the turbulence of pouring; and uniform fill out of all sections, including superior flow into sections as thin as 1 mm (Campbell, 1999; Dash and Malkhlouf 2001:1; Lee, Chang and Yeh 1990:187).
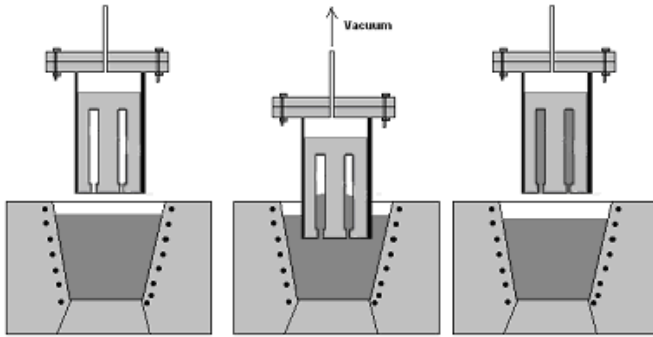
Fig. 1. Schematic illustration of the CGC method (Hasirci, 2006)

The increased use of cast alloys in automotive applications such as engine blocks and cylinder heads creates the need for a deeper understanding of fatigue performance and the influences of processing parameters. In designing of cast automotive parts, it is important to have an intimate knowledge of how alloy solidifies at different cross sections of the cast part and how this influences mechanical properties (Dobrzañski, Maniara and Sokolowski 2000:28). This knowledge enables the designer to ensure that the casting will achieve the desired properties for its intended application. The casting structure developed during solidification depends not only on the nucleation potential of the melt, but also on the thermal gradient imposed during solidification. Therefore, the features of casting structure (grain size, secondary dendrite arm spacing and silicon modification level) can be evaluated by examining the cooling curve parameters (Hasirci, 2006; Dobrzañski, Maniara and Sokolowski 2000:28).

Mentioned above factors are of great importance in determining material properties. While there are many studies in the literature about the effects of various casting methods on solidification characteristics, the effects of CGC method have not been investigated. The aim of this study was to determine the effects of CGC process at real casting conditions on cooling rate, grain size and other solidification characteristics of Al–9.42 wt.% Si alloy. At the same time, the grain size, solidification starting temperature, time and range at different cooling rates (conventional casting and CGC processes) were examined.

2. EXPERIMENTAL WORKS

The experimental alloy used in this investigation was melted in electric resistance furnace at 670 ºC. The melt material was poured in insulated mould (Fig. 2). Molten AlSi alloy was poured under 0 (Gravity casting), 0.133 and 0.666 bar vacuum levels. The chemical composition of this alloy is given in Table 1.
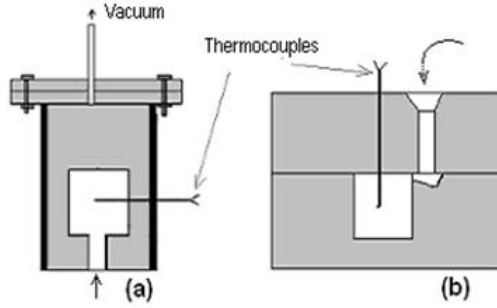
Fig. 2. Schematic illustration of experimental set-ups; (a) the CGC, and (b) conventional casting process

Table 1. Chemical compositions of Al-Si commercial alloy

Si	Fe	Cu	Mn	Mg
9,42	0,38	0,05	0,431	0,36

Cr	Ni	Zn	Ti	Pb
0,015	0,04	0,06	0,10	0011
Al (Bal.)				

The test specimens with $\varnothing 50x70$ mm dimension were produced at real casting conditions. The moulds had insulating coatings to allow for low heat transfer only. Thermal analysis of cooling curve was performed on all samples using high sensitivity thermocouples of K type (Fig. 2). Data were acquired by a high speed data acquisition system linked to a personal computer. Each poured sample was sectioned horizontally where the tip of the thermocouple was located and it was prepared by standard grinding and polishing procedures. Light microscopy was used to characterize the macrostructures. Macrostructure measurements were carried out using an Image-J analyzer program. Metallographic specimens were etched using Tucker etching solution (15 ml HF, 45 ml HCl, 15 ml HNO_3 and 25 ml H_2O).

3. RESULTS AND DISCUSSION

Research on the effects of the CGC processes on solidification macro structures, cooling properties, solidification time and temperature is very limited. In addition, a study on the cooling rate, grain size, solidification temperature and duration of this method is not available. Therefore, the results of this study were compared to the former study results on pressure die and squeeze casting. In some studies (Kuo, Hsu and Hwang 2001:2; Lee, Kim, Won and Cantor 2002:338; Niu, Hu, Pinwill and Li 2000:105), it was mentioned that increased heat flow led to accelerated solid activity. In earlier work (Lee, Kim, Won and Cantor 2002:338), it

was pointed out that the increasing applied pressure shortens solidification time in squeeze casting. The solidification time of a casting by Chvorinov's rule is the ratio of volume to surface area of casting. Therefore, by increasing surface area of casting solidification time decreased (Hasirci, 2006). The solidification time also depends on heat transfer constant of casting alloy and mould material. The effect of pressure on the solidification time was not taken into consideration in Chvorinov's rule. The vacuums on solidification processes have two type effects. The first effect is suction pressure and other is increased cooling rate due to heat absorption. Solidification under pressure occurs more quickly and reduce feeding requirement due to the influence of pressure (Hasirci, 2006; Lee, Kim, Won and Cantor 2002:338). In this study, the experimental results showed that the increase in applied pressure leads to an increase in solidification rate and even a very low pressure generates a significant effect.

CGC process is a kind of low pressure casting method. In this process, negative pressure (suction by vacuum) was used instead of positive pressure (push). However, both of them have similar effects on solidification. On the other hand, in some studies (Shabestari and Malekan 2005:44; Dobzaski, Kasprzak, Sokowski, Maniara and Krupiski 2005; MacKay, Djurdjevic and Sokolowski 2000; Boileau, Zindel and Allison 1997:106; Bäckerud, Chai and Tamminnen 1992:2), it was found that processing parameters (i.e. pressure, modification, grain refinement) have shown a decreasing effect on grain size, solidification temperature and time. The results of this experimental study revealed that vacuum has a similar effect.

The casting structure developed during solidification depends not only on the nucleation potential of the melt, but also on the thermal gradient imposed during solidification. Therefore, the features of the casting structure (grain size, silicon modification level) can be evaluated by examining the cooling curve parameters. The cooling curves recorded for Al-Si alloy at various vacuum levels are shown in Fig. 3. The cooling curves indicate that higher vacuum levels lead to shorter solidification times. The solidification time of 491 sec recorded in conventional casting process was found to have decreased down to 126 and 97 sec, resulted from vacuum applications of 0.133 and 0.666 bar, respectively. These figures clearly reveal the significant effect of vacuum on the solidification time. Due to the increased solidification rate, the grain size of the cast material has become smaller as shown in Fig. 3. On the other hand, the cooling rate curves produced on the basis of the shortened solidification time and their effects on the Al-Si equilibrium diagram are given in Fig. 4. Fig. 4a illustrates the variations on the Al-Si equilibrium diagram associated with the variations in the cooling rates. It can be seen that cooling rate and

solidification starting temperatures vary with increasing vacuum level. The cooling rate increases with increasing vacuum level. The variation in cooling rates affects the characteristic parameters of thermal analysis particularly in the liquid region. The cooling rate is proportional to the heat extraction from the sample during solidification. Therefore, at a low cooling rate (0.24 °C s^{-1}), the rate of heat extraction from the sample is slow and the slope of the cooling curve is small. So, it creates a wide cooling curve Fig. 3 and 4b. But, at a high cooling rate (1.24 °C s^{-1}) the rate of heat extraction from the sample is fast, the slope of the cooling curve is steep and it makes a narrow cooling curve (Fig. 4c and d). Fig. 3 and Fig. 4c and d show the variation of the aluminum nucleation (solidification starting) temperature as a function of cooling rate and the increase of vacuum level. It is evident from the plot that the Al nucleation temperature decreases from 595 to 583°C with increasing cooling rate from 0.24 to 1.24 °C s^{-1} (Fig 4d). The increase in cooling rate is accompanied by increased heat extraction. Therefore, the melt is cooled to a lower temperature than the equilibrium melting point. Due to the increase in the cooling rates, the nucleation under cooling decreases.

The phenomenon of a decrease in the nucleation temperature with an increase in the solidification rate depends on the mobility of the clusters of atoms in the melt. These groups of the freezing atoms produce the fluctuation clusters and fluctuation embryos, which are the nucleation primers. The increase of the cooling rate with an increased amount of the nucleation primers is a well-established fact. This effect has influence on the grain size. Fig. 3, Table 2, Fig. 5a and b show the variation of the grain size, cooling rate and solidification range (temperature and time) as a function of vacuum applications. As seen on the picture at Fig. 3, the increase in vacuum level and cooling rate strongly decrease strongly grain size. Grain size decreases by increased cooling rate (cooling rate 1.24 °C s^{-1} grain size 0.18 mm), while it increases by decreased cooling rate (cooling rate 0.24 °C s^{-1} grain size 0.85 mm) (Fig. 5a). Therefore the alloy's design and process have a wide range of solidification rates (process parameters) to choose from.

Mechanical properties of the aluminum alloys are strongly dependent on the effect of grain size. The smaller particle size improves the tensile properties. Earlier research (Hasirci,2006) results show that, the increase in the vacuum level from 0 to 0.666 bar leads to the reduction of the grain size, which in turn has influence on the ultimate tensile strength (UTS) and hardness. The UTS and hardness increased, respectively, from 110 to 163 MPa from 60 to 77 HB by increased vacuum level (Fig. 5b).
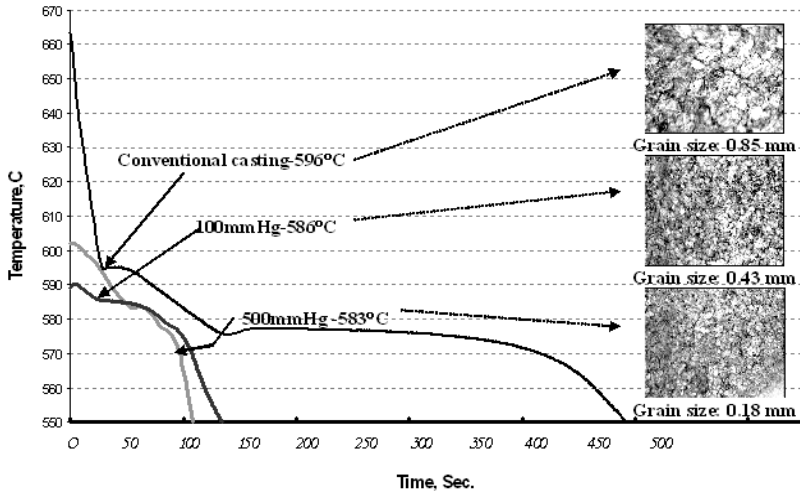
Fig. 3. Cooling curves and macro structures of Al-Si alloy obtained under 0, 0.133 and 0.666 bar vacuum conditions
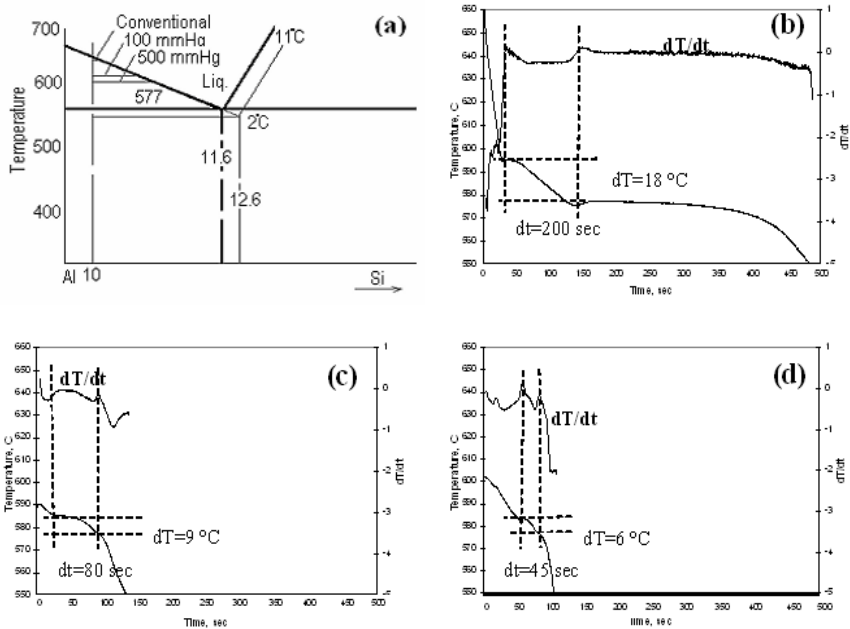
Fig. 4. Al-Si phase diagram (a), cooling and dT/dt curves of Al-Si alloy under 0 (b), 0.133 (c) and 0.666 bar (d) vacuum conditions.

6

Table 2. Various solidification properties and mechanical of AlSi alloy at various vacuum levels

	Vacuum Level (bar)		
	0	0.133	0.666
Cooling Rate, CR (dT/dt), (°C / sec.) - *(Change %)*	0.24- *(ref.)*	0.95 -*(↑74 %)*	1.24 -*(↑81 %)*
Effect of vacuum on cooling rate, Q (°C /sec.)	0*	0.71	1
Solidification Time, t (sec.) (from 650 to 550°C)	491 *(ref.)*	126 (↓74 %)	97 (↓ *81 %*)
Grain Size, (mm)	0.85	0.43	0.18
Solidification Range (for temperature), (°C)	20	10	8
Solidification Range (for time), (sec)	200	80	45
Tensile Strength, MPa	110	124	163
Hardness, HB	60	64	77
* Constant heat transfer of air: 0.0025			

(a)

(b)
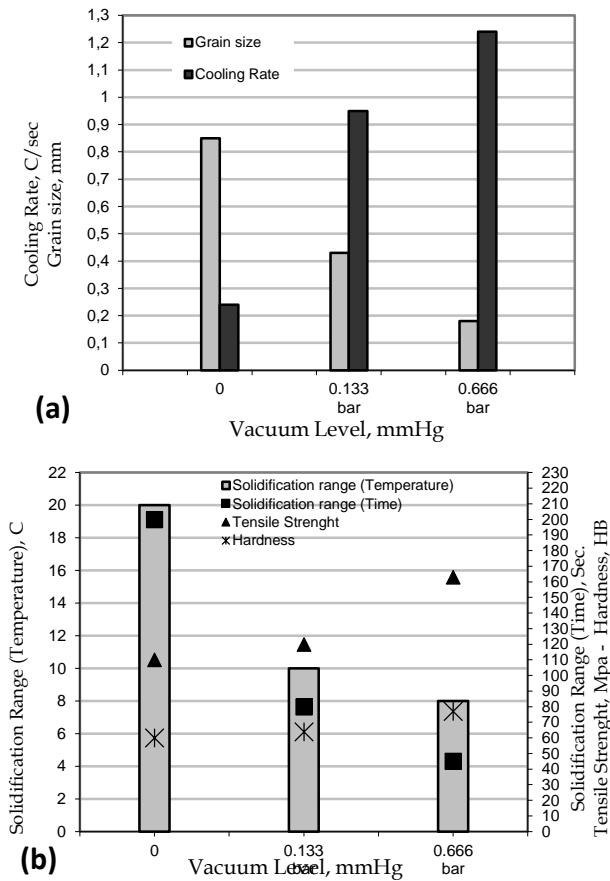
Fig. 5. Variation of cooling rate, grain size (a) and tensile strength, hardness, solidification temperature and time range (b) of the Al-Si alloy as a function of variation vacuum level

On the other hand, the cooling rate has significant influence on solidification temperature and time. Solidification temperature and time range decreased (respectively, from 12 °C and 155 sec to 8 °C and 45 sec) with increasing cooling rate (from 0.24 to 1.24 °C s^{-1}). Further, solidification starting temperature (approximately 13 °C) also decreased with increasing cooling rate.

4. CONCLUSIONS

The results are summarized as follows:

➢ Solidification parameters are affected by the vacuum level. The cooling rate, solidification time and temperatures vary with an increasing vacuum level.

➢ Increasing the vacuum level increases the cooling rate (81%) and significantly decreases the solidification (nucleate) range of AlSi alloy (temperature and time respectively 2 and 81 %) and eutectic temperature (2 ºC).

➢ These phenomena lead to an increased number of nucleuses that affect the size of the grains. Increasing the vacuum level significantly decreases grain size (80%).

➢ Solidification temperature and time range (respectively, from 12 °C and 155 sec to 8 °C and 45 sec) decreased as a result of increasing vacuum level.

REFERENCES

1) Campbell J. (1999). Casting. Butterworth –Heinemann, 1-55.

2) Güleyüpoglu S. (1997). Casting process design guidelines. Transaction of American Foundry Society, 97-83, 869-876.

3) Rasmussen N W. (2000). New filling/feeding process produces vertically-parted aluminum green sand castings. Modern Casting, 54-55.

4) Dash M and Malkhlouf M. (2001). Effect of key alloying elements on the feeding characteristics of aluminum - silicon casting alloys. Journal of Light Metals, 1, 251-265.

5) Lee Y W. Chang E. Lin Y L. and Yeh C H. (1990). Correlation of feeding and mechanical properties of A206 aluminum alloy plate casting, Transaction of American Foundry Society, 90-187, 935-941.

6) Loper Jr C R. and Prucha T E. (1999). Feed metal transfer in AL-Cu-Si alloys. Transaction of American Foundry Society, 90-165, 845-853.

7) Kuo J H. Hsu F L. and Hwang W S. (2001). Development of an interactive simulation system for the determination of the pressure-time relationship during the filling in a low pressure casting process. Science and Technology of Advanced Materials, 2, 131-145.

8) Hasirci H. (2006). Investigation of applicability of counter gravity direction casting processes in green sand mould and effect of process production casting part on structures and properties. Ph. D. Thesis, University of Gazi, Institute of Science and Technology, TURKEY.

9) Dobrzañski L A, Maniara R, and Sokolowski J H. (2000). The effect of cooling rate on microstructure and mechanical properties of AC AlSi9Cu alloy. Archives of Materials Science and Engineering, 28-2, 105-112.

10) Lee J H. Kim H S. Won CW. and Cantor B. (2002). Effect of the gap distance on the cooling behavior and the microstructure of indirect squeeze cast and gravity die cast 5083 wrought Al alloy. Materials Science and Engineering A; 338, 182-190.

11) Niu X P. Hu B H. Pinwill I. and Li H. (2000). Vacuum assisted high pressure die casting of aluminum alloys. Journal of Materials Processing Technology, 105, 119-127.

12) Shabestari S G. and Malekan M. (2005). Thermal Analysis Study of the Effect of the Cooling Rate on the Microstructure and

Solidification Parameters of 319 Aluminum Alloy. Canadian Metallurgical Quarterly ISSN 0008-4433, 44-3, 305-312.

13) Dobrzaski L A, Kasprzak W, Sokowski J, Maniara R and Krupiski M. (2005). Applications of the derivation analysis for assessment of the ACAlSi7Cu alloy crystallization process cooled with different cooling rate, COMMENT 2005 Proceedings of the 13th International Scientific Conference, Gliwice-Wisa, 147-150.

14) MacKay R. Djurdjevic M. and Sokolowski J H. (2000). The Effect of Cooling Rate on the Fraction Solid of the Metallurgical Reaction in the 319 Alloy. Transaction of American Foundry Society, 521-530.

15) Boileau J M, Zindel J W and Allison JE. (1997). The Effect of Solidification Time on the Mechanical Properties in a Cast A356-T6 Aluminum Alloy. Transactions of Automotive Engineers Society ISSN 0096-736X, 106-5, 63-74.

16) Bäckerud L, Chai G, and Tamminen J. (1992). Solidification Characteristics of Aluminum Alloys. Transaction of American Foundry Society, 2, 5-56.

DETERMINATION OF SURFACE ROUGHNESS THROUGH NOISE OF CUTTING TOOL IN MILLING OF AISI 1040 STEEL

Oğuz Girit

(Asst. Prof. Dr.), Marmara University, e-mail: ogirit@marmara.edu.tr
iD ORCID *0000-0003-2287-9936*
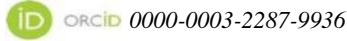
1. INTRODUCTION

The researchers, continues for reducing the time and the cost required for manufacturing. Automated production and minimal processing are one of the most important goals of modern manufacturing [1]. To achieve this goal, it is highly prioritized to develop techniques to minimize the needs for intermediate processes in production [2]. The technology is currently available to researchers and engineers in the manufacturing process [1]. The control system developed with the combination of existing technologies reduces both production time and cost [2]. One of the minor processes is the controlling the surface quality of the produced part [1]. Determining the surface quality of each part is both costly and a time consuming job [2]. Therefore, it is possible to reduce the time and cost allocated to quality control by improving prediction models and systems [2].

On Computer Numerical Control (CNC) machines, the correct sizing and surface quality can be achieved by the correct selection of machining parameters [1]. The machining parameters are parameters such as cutting, feed, spindle, spindle speeds, depth of cut [2]. The selection of these parameters is usually made either according to the experience of the operator, the manual of the machine or the tool catalogs [3]. Nevertheless, it is difficult to determine the feed and cutting speeds that can provide the surface roughness and tolerance values specified in the manufacturing drawings [4].

The tribological properties of the machined part surfaces are primarily influenced by the surface shape [5]. The surface roughness is not only an important factor in the traditional areas of tribology such as abrasion, friction and lubrication, but also at the same time in sealing, hydrodynamics, electricity, and heat transfer [6,7]. Surface roughness is the most important factor in the industry. Surface treatments are affected

by many variables [5]. Reduction of surface roughness is subject to factors such as the reduction of depth of cut, the use of low feed and high cutting speeds, the increase of the coolant flow, the tip radius of the cutting tool and the large chip angle values [3].

Kopac et al. emphasized what kind of results can be encountered in the working conditions of tempered AISI 1060 and AISI 4140 steels which are frequently used in practice and in the workings on the change of surface roughness as a result of random selection of machining parameters. In their work, low surface roughness values have been found to be achieved when using high-radius cutting tools for both steels [8].

In Yuan et al. research on turning, it has been revealed that the sharpness of a diamond cutting tool is one of the main factors affecting the machining deformations and the roughness of the machined surface [9]. Their pilot tests with aluminum alloy samples showed that the surface roughness of the workpiece, the microhardness of the workpiece, the permanent surface stresses and the dislocation densities changed depending on the tool tip radius [5]. The surfaces treated with the blunt tool were found to be stiffer than those machined with a sharp tool [4]. Eriksen observed the interactions between the different cutting speeds and advancing speeds, cutting tool tip radius and fiber direction of the thermoplastics reinforced with short fiber treated by turning [5].

It has been stated that it is possible to determine the optimum machining conditions experimentally, however it does not match the calculations of those theoretical parameters [7]. The surface roughness increases when the feed speed is above 0.1 mm / g, the surface roughness decreases when the tool tip radius decreases, the surface roughness deteriorates when the cutting speed reaches 500 m / min, the high cutting speed up to 1500 m / it is stated that the surface roughness of the processes is independent of the cutting speed [3].

In this study, one of the most important criteria in determining the surface quality in machining is the roughness value on the surface of the produced part [6]. In milling operations, the model was developed and roughness ratio was estimated by taking into account the shear forces and vibrations to estimate the surface roughness [10]. In addition, it is possible to estimate the surface roughness with the change in the pressure level of the sound generated during cutting [11]. In this study, the change in acoustic sound pressure during dry processing with DLC coated double groove carbide end mill in AISI 1040 steel was recorded by microphone and specialized software [6]. The relationship between the pressure change of recorded sound and average surface roughness (Ra) was examined and modeled using linear regression method [11]. In addition, the effect of the

cutting parameters on radial, tangential and axial forces was also investigated [12].

In the research, modern production is one of the most important targets of production, while also minimizing cost, increasing automation and minimizing processing for optimal efficiency [3]. To achieve this goal, it is highly prioritized to develop techniques to minimize the needs for intermediate processes in production. Technology therefore leads researchers and engineers in the production process [5]. The control system developed with the combination of existing technologies reduces both production time and cost. One of the minor processes is the controlling the surface quality of the produced part. Controlling the surface quality of each part is both costly and a time consuming job. Therefore, it is possible to reduce the time and cost allocated to quality control by improving estimation models and systems [3].

Ebner et al. measured the acustic sound at high cutting speeds in the milling machine [13]. Ghosh and colleagues (2007) attempted to estimate the CNC milling tool wear from the sound changes measured by the sensors in their work [13]. Matthew et al. concluded that; it has been shown that the cutting tool changes the sound pressure under various cutting conditions and gives effective results [14]. Mannan et al. studied the relationship between surface quality and the analysis of the noise produced when the cutting tool during chip removal resulting from tool wear [15].

In this study, AISI 1040 medium-carbon steel was recorded in dB with a specialized software program by listening to the change in acoustic sound pressure generated by the dry milling of the two-headed DLC coated carbide end mill. [6]. The relationship between the change in acoustic sound pressure and surface roughness is examined and modeled by linear regression. In addition, the forces generated in the dry milling are interpreted taking into account the cutting parameters [3].

2. MATERIALS AND METHODS

2.1. Material and Experiment

CNC machine used in experimental setup is a milling machine which is a series of O-M series with FANUC control which can perform three axis linear and circular interpolation and it can perform ISO format programming in metric and imperial units [16]. In this study, AISI 1040 medium carbon steel has been chosen as it is widely used. The mechanical and chemical properties of the AISI 1040 steel material, used as workpiece in the experimental work, are shown in Table 2. The force and acoustic sound were recorded on a desktop computer with a KISTLER 9443B dynamometer platform and a KISTLER 5019B amplifier combined with data acquisition. The setup of the experimental work is shown in Figure 1.
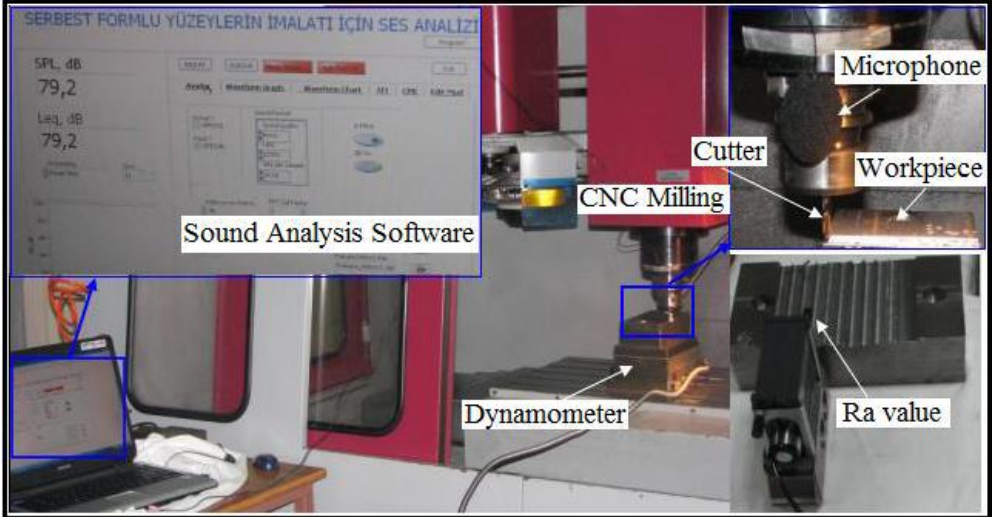
Figure 1. The experimental setup [3].
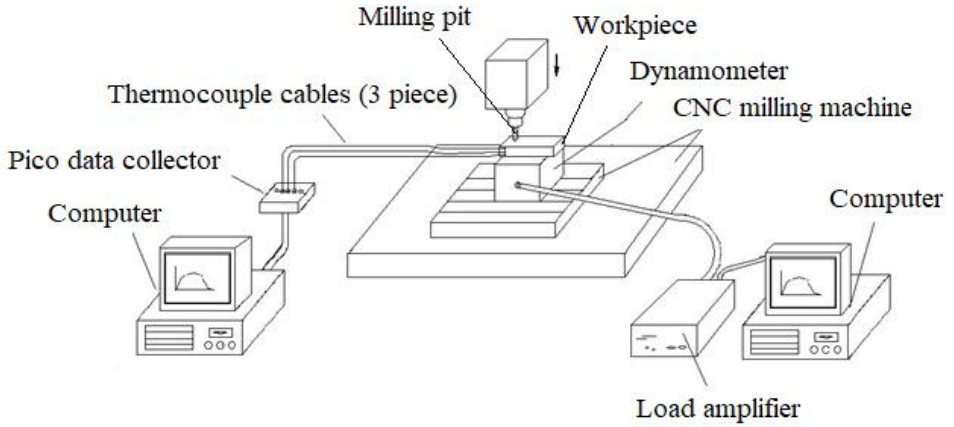
Figure 2. Schematic Presentation of Experiment Plan [3].

Table 1. CNC Milling Machine Technical Specifications [3].

Model Number	VMC – 850 / 550+APC
Table work surface	40‖ x 20‖ (1000 x 500 mm)
Movement boundaries	: 31.5‖ (800 mm) : 20‖ (500 mm) : 17.7‖ (450 mm)
Spindle Motor power	10 HP (30 min.) / 7.4 HP (cnot)
Table loading capacity	1980 Lbs (900 kg)
Machine floor area	92.5‖ x 98.4‖ (2350 x 2500)
Machine weight	12100 Lbs (5500 kg)

Table 2. Mechanical and chemical (%) properties of AISI 1040 steel material [12].

Hardness (Bhn)	Flowing (MPa)	Rupture (MPa)	Elongation (%)	Chemical structure (%)
170	353	518	25	Fe(98.07); C(0.329); Cr(0.036); Cu(0.2); Mn(0.69); Si(0.22); Ni(0.01); Co(0.02); Mo(0.02).

DLCM List 9330 end mills of NACHI company were used in this study (Figure 3). The cutting tools used in this study have a full length (L) = 60 mm, (l)= 20 mm, a stem diameter (d) = 10 mm, and a cutting mouth diameter (D) = 9 mm.
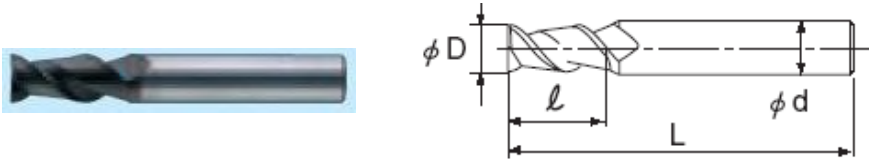
Figure. 3. The end mills used in the experiment [17]

2.2. Analysis Method

The primary purpose of this research; is to determine and formulate the relationship between the change in acoustic sound pressure and the maximum average surface roughness, depending on the cutting parameters that change during dry milling. In addition, it is the evaluation of the forces that occur during the chip lifting [18,19]. To achieve these goals;

✓ In each of the sixteen experiments, the sound received by the microphone, which is fixed at the nearest possible distance to the cutter attachment, is recorded by means of specialized software which converts the acoustic sound pressure change into numerical values. Calibrator used for microphone calibration (Figure 4) and measurements were made after the calibration factor was entered into the register. A sampling rate of 22050 was selected during the measurements [20].
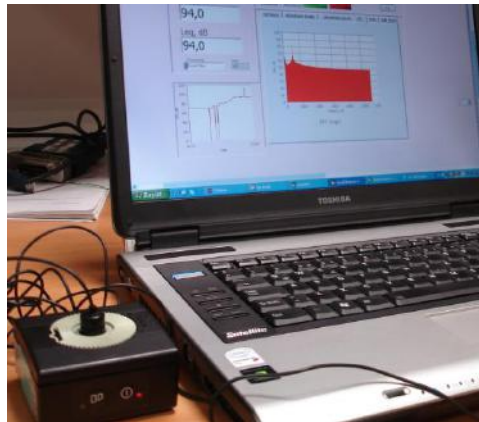
Figure 4. Microphone calibration [3].

✓ The forces were measured during the experiments. Parts of the build for force measurement are as follows; a quartz dynamometer, a three-channel charge-amplifier, an end connector for connection to a Kistler dynamometer, a program for the analysis of measurement information, an

ISA type A / D board for computer connection and interconnecting cables [21].

✓   Cutting forces measured in tangential, radial and axial directions are transformed into computer graphics using DynoWare software. After each test, Ra values of the average surface roughness at the working surface were measured by the MARH-Perthometer [21].

✓   The relationship between acoustic noise variation and average surface roughness is modeled by a linear regression model [22].

✓   The relationship between radial, tangential and axial forces and shear parameters is investigated [10].

3. EXPERIMENTAL DESIGN

Influence of the cutting parameters and the effect of cutting geometry and parameters on surface roughness Ra and cutting force N on milling of a AISI 1040 steel is discussed in this section [23]. Experimental design has been carried out by Taguchi method in this study because the traditional experiment design has been required to be highly complex, challenging and it has to be repeated too many times [22, 24, 25]. Taguchi method is beneficial for the experimental design of the machinability of AISI 1040 steel material. Having optimized parameters is also fruitful for keeping the response values at required levels [23]. In the experimental study; cutting speed v = 40-130 m / min, feed rate f = 30-120 mm / g, and chip depth, a = 0.75-3 mm. The L16 experimental design made according to the Taguchi Method and the results measured during the experimental study are shown in Table 3.

Table 3. L16 Experimental design and measurement results.

Control factors			Results of the measurement				
Experiment Number	v (m/min)	f (mm/min)	a (mm)	SPL (dB)	Ra (µm)	Fy (N)	Fx (N)	Fz (N)
1	40	30	0,75	83,3	0,51	65	63	23
2	40	60	1,50	88,0	0,58	172	151	56
3	40	90	2,25	94,4	0,83	265	235	81
4	40	120	3,00	104,8	1,25	382	320	122
5	70	30	1,50	85,6	0,46	73	65	37
6	70	60	0,75	90,3	0,61	79	70	21
7	70	90	3,00	96,6	0,89	252	217	71
8	70	120	2,25	99,5	1,01	232	213	68
9	100	30	2,25	85,7	0,47	94	76	51
10	100	60	3,00	88,3	0,57	178	138	43
11	100	90	0,75	94,6	0,82	87	78	17
12	100	120	1,50	98,8	0,81	155	127	39
13	130	30	3,00	88,1	0,56	106	85	67
14	130	60	2,25	88,4	0,57	128	117	59
15	130	90	1,50	95,7	0,75	121	114	45
16	130	120	0,75	98,7	0,97	87	82	24

4. EXPERIMENTAL RESULTS AND EVALUATION

4.1. Evaluation of Acoustic Sound Change and Ra Measurement Results

The change in the level of the acoustic sound obtained from the experimental studies according to the two most effective cutting parameters is given graphically in Figure 4. The sound pressure is expressed in terms of "dB SPL"; is a term that refers to the sound pressure level that acoustic sound waves apply to air molecules.

94 dB equals to SPL = 1 Pascal = 10 microbes. As seen in Figure 5, the increase in the progression rate has resulted in an increase in the acoustic volume. The change effect of the increase in chip depth on the acoustic sound pressure is significantly lesser than the effect of the progress rate.
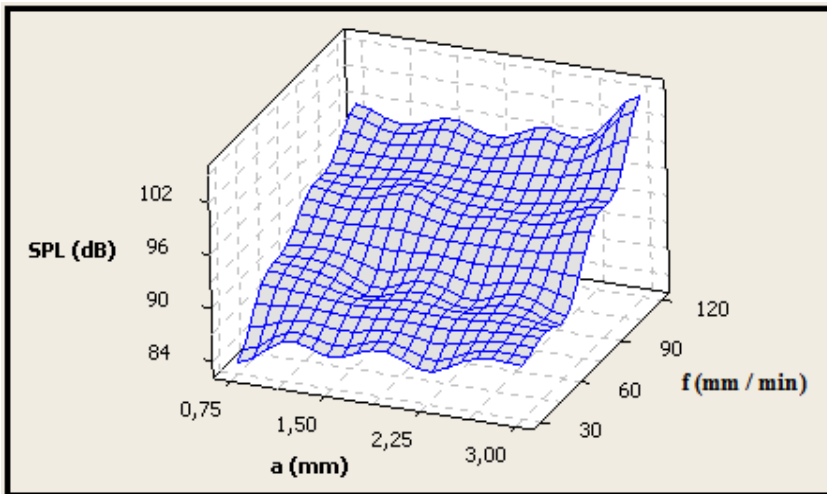
Figure 5. Change in acoustic sound level depending on chip depth and progress rate
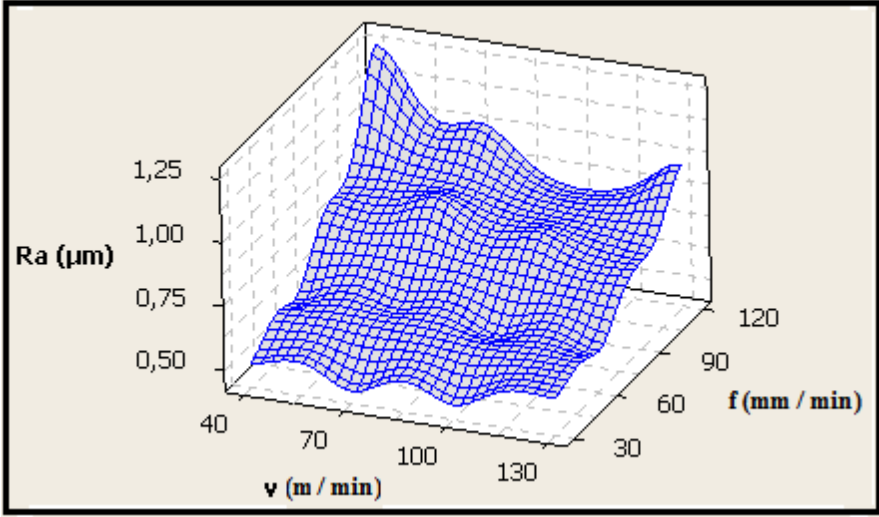
Figure 6. Change in average surface roughness depending on cutting speed and feed rate

As a result of sixteen experiments with different cutting parameters, the variation of the average surface roughness values obtained from the cut faces with respect to the two most important factors in the formation is given in Figure 6. The average surface roughness (Ra) is expressed as in equation numbered 1 [7].

$$R_a = \frac{1}{L}\int_0^L |Y(x)|dx$$

(1)

Where R_a is the mean deviation from line, Y is the ordinate of the profile curve, and L is the measured length.

As can be seen from Figure 6, a significant increase in the average surface roughness value is observed in correlation with the increase in the feed rate. The increase depending on the cutting speed is in the rate where it can be overlooked. However, the maximum average surface roughness was achieved at low shear rate and high feed rate. Linear regression analysis was performed to determine the relationship between the change in sound pressure level and the average surface roughness. The linear regression is expressed as shown below [7].

$$Y = \beta_0 + \beta_1 x_1 + ... + \beta_i x_i + \beta_n x_n + \varepsilon$$

(2)

Here Y expresses the answer, and if β_i is the answer then i shows the factor and the increase of the regression. As a result of the study using

20

Minitab software, the obtained regression equation and R2 (R-Sq) ratio are shown in Figure 7. According to the Pearson coefficient, if R^2 is 0.80 and above, the relationship between the dependent variable and the independent variable is assumed to be strong. In this case, the 0.93 ratio obtained in this study indicates a strong relationship and indicates that the regression analysis has been successfully applied.
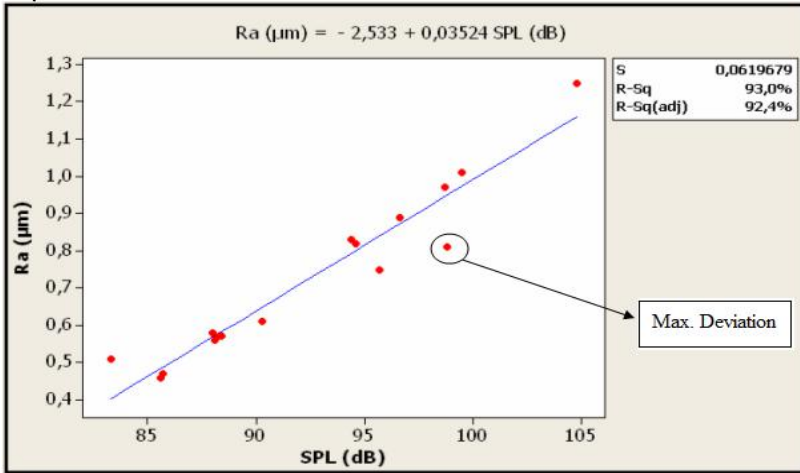
Figure7. Linear regression model for Ra

As shown in Figure 7, the maximum deviation is in Experiment 12. The deviation amount and residual rate in this experiment are given in Table 4.

Table 4. Maximum deviation and residual rate

Experiment	SPL (dB)	Ra (µm)	Fit	Residual
12	~ 99	0,81	0,949	-0.139

The study was carried out with the help of the sensitivity of the acoustic pressure changes and the same accuracy in the measurements of the average surface roughness and supports the studies done in the literature. The result is that during cutting at the milling, the acoustic sound produced by the cutting tool is in strong correlation with the average roughness of the surface obtained by the pressure of change at the end of cutting.

It is possible to interpret the results as a starting point to further reduce or completely eliminate surface quality control for a certain percentage of each produced part or produced parts, for firms that manufacture using the same method, cutting tool and workpiece material. It is also possible to increase the accuracy and reliability of this application by applying it to different parameters and workpiece materials.

4.2. Evaluation of Radial, Tangential and Axial Forces

Measurements of the shear forces generated during dry milling are another consideration in this work. During manufacturing similar workpiece material, it is important to determine the shear forces required by the cutting tool during tooling in regards to tool wear and, of course, workpiece surface quality.

In the study, Radial (F_y), Tangential (F_x) and Axial (F_z) forces that occurred during cutting were measured using Kistler dynamometer and amplifier. As expected, maximum forces were generated in the radial direction (Figure 8). It is seen that the most effective factor is the rate of progression in Figure 8, where two cutting parameters with dominant effect on the formation of radial force. In addition, the increase in chip depth has also increased the radial force.

From the perspective of the effect of the cutting parameters, the tangential force measurement results, which show a similar tendency to the radial force, are shown in Figure 9. In the formation of tangential force, the dominant two factors are the feed rate and chip depth. However, tangential force values were slightly less than radial force.
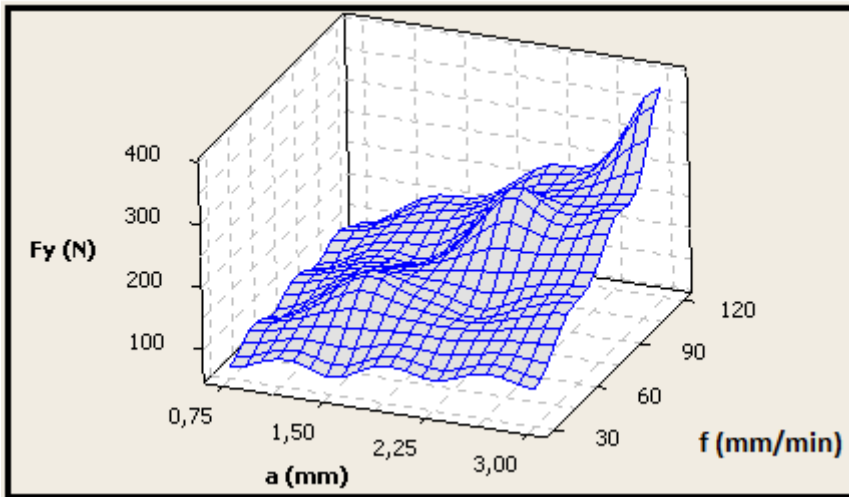
Figure 8. The effect of depth of cut and feed rate on radial force generation
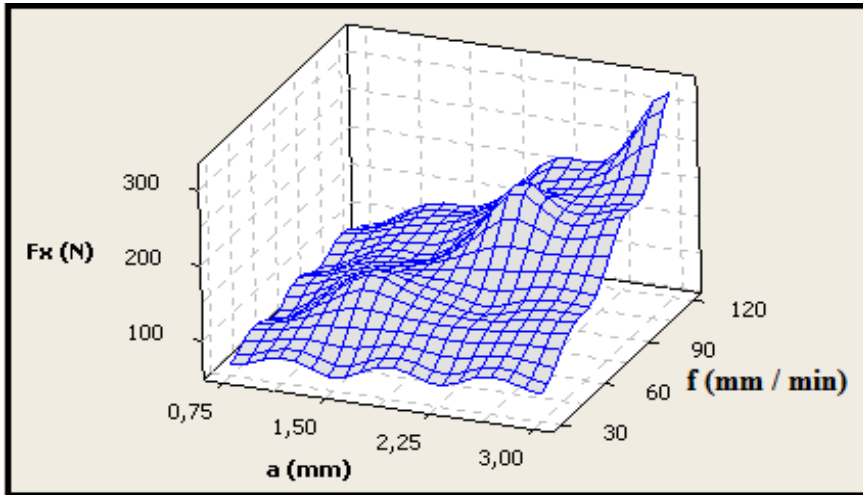
Figure 9. Effect of depth of cut and feed rate on tangential force generation

In the fore and aft circumferential, the forces generated in the axial direction are generally less than the forces generated in the radial and tangential direction. Because there is no advance in the axial direction, the force results which are less compared to the other two directions are presented in Figure 10. In Figure 10, which shows the two most effective factors in axial force generation, the feed rate and shear rate are influenced by the shear force. However, the difference between the chip depth and the cutting speed and the shear force effectiveness rates is negligible. The most effective factor in this case was the progress rate.
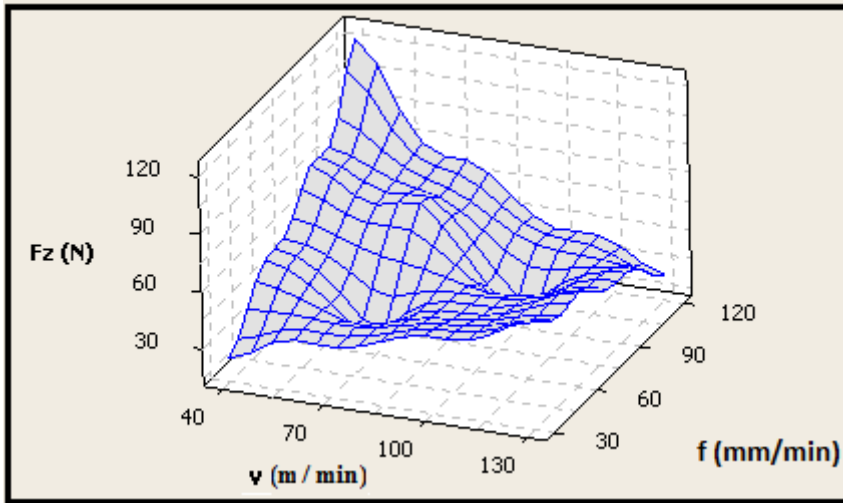
Figure 10. The effect of depth of cut and feed rate on the formation of axial force

5. CONCLUSIONS

In this study, AISI 1040 medium carbon steel with a two-spindle DLC coated carbide end milling is recorded with a microphone in dB by a specialized software and the relationship between the change in sound pressure and the average surface roughness are investigated. Below is the summary of the results:

(1) Linear regression analysis was performed to determine the relationship between the change in sound pressure level and the average surface roughness.

(2) It was found that the relation between linear regression modeled study, dependent variable (change in sound pressure level) and independent variable (mean surface roughness) were very strongly related to each other.

(3) The results obtained for the purpose of this study show that more comprehensive experimental studies can be done and modeled.

(4) It was concluded that tool feeding speed was the most effective factor in force formation during chip cutting process.
(5) Significant increase in the average surface roughness value is observed to be in correlation with the increase in the feed rate. The increase depending on the cutting speed is at a rate where it can be overlooked.

(6) The maximum average surface roughness was achieved at low shear rate and high feed rate.

24

(7) According to the Pearson coefficient, if R 2 is 0.80 and above, the relationship between the dependent variable and the independent variable is assumed to be strong. In this case, the 0.93 ratio obtained in this study indicates a strong relationship and indicates that the regression analysis has been successfully applied.

REFERENCES

[1] E. Yamaguti, J.F.A. Romero, A. Zanandrea, *ABCM Symposium Series Mechatronic.* **2,** 121 (2006).

[2] B.H. Amstead, P.F. Ostwald, M.L. Begeman. *Manufacturing Processes. 8th Edition.* Singapore: John Willey & Sons Inc 1987.

[3] A. Akay. *University of Marmara, Ins Pure and Applied Sci, Mecha. Eng. (Master Thesis),* İstanbul, Turkey (2009).

[4] T. Akasawa, H. Sakurai, M.T. Nakamura. *J. Mater. Proces. Technol.* **143-144:** 66 (2003).

[5] M. Kurt, E. Bagci, Y. Kaynak. *Int. J. Adv. Manuf. Technol.* **40**, 458 (2009). DOI 10.1007/s00170-007-1368-2

[6] J. Paulo Davim. *J. Mater. Proces. Technol.* **116,** 305 (2001). DOI: 10.1016/S0924-0136(01)01063-9

[7] I,S, Kannan, A. Ghosh. Procedia Mater. Sci. 5, 2615 (2014). DOI:10.1016/j. mspro. 2014.07.522

[8] J. Kopac, M. Bahor. *J. Mater. Proces. Technol.* **92–93**, 381 (1999).

[9] Z. J. Yuan, M. Zhou, S. Dong. *J. Mater. Proces. Technol.* **62,** :327 (1996).

[10] P.T. Mativenga, N.A. Abukhshim, M.A. Sheikh. *J. Eng. Manuf.* **220,** 657 (2005).

[11] S. Yıldız, B. Unsaçar. *Measurement.* **39,** 80 (2006).

[12] Computer Numerical Control (CNC) Machining Accelerator Toolkit For FANUC Series 30i-B, 31i-B, 32i-B, and 35i-B CNC Systems Rockwell Automation Publication. Luxemburg. (2012).

[13] I. D. Y. Ebner, J. F. A. Romero, A. Zanandrea, O. Saotome, J. O. Gomes. *ABCM Symposium Series in Mechatronic.* **2,** 121 (2006).

[14] S. C. Matthew, A. Mann, J. Gagliardi. *Applied Acoustics.* **43**, 333 (1994).

[15] M. A. Mannan, A.A. Kassim, M. Jing. *Pattern Recognition Letters.* **21,** 969 (2000).

[16] K. Nagatomi, K. Yoshida, K. Banshoya. *Mokuzai Gakkaishi.* **40,** 434 (1994).

[17] Nachi-Fujikoshi Corp. *www.nachi-fujikoshi.co.jp/eng/news/index.html*. Catalog. Accessed 29 May 2018

[18] B. Prashanth, K. Jayabalan. Inter. *J. Civil. Eng. Technol*. **8,** 115 (2017).

[19] N. Ghosh, Y.B. Ravi, A. Patra. *Mecha. Syst. Signal. Proces*. **21,** 466 (2007).

[20] V. Ostasevicius, V. Jurenas, V. Augutis. *Int. J. Adv. Manuf. Technol*. **88,** 2803 (2017).

[21] P. N. Botsaris, J. A. Tsanakas. *The International Conference of COMADEM, Prague.* 73 (2008).

[22] I. Korkut. *Gazi Üniversity, Graduate School of Natural and Applied Sciences, Doctora Thesis.* Ankara. (1996).

[23] M. Ay. *Acta Physica Polonica A,* **131**, 349 (2017).

[24] S. C. Carney, J. A. Mann, J. Gagliardi. *Applied Acoustics.* **43**, 333 (1994).

[25] R. K. Roy. *A primer on the taguchi method.* Van Nostrand Reinhold; New York (1990).

EFFECTS OF PROCESS PARAMETERS ON MECHANICAL PROPERTIES OF Al-Al$_2$O$_3$-B$_4$C HYBRID COMPOSITES BY USING GREY RELATIONAL ANALYSIS

Sare Çelik[1] & Türker Türkoğlu[2]

[1](Prof. Dr.), Balikesir University, e-mail: scelik@balikesir.edu.tr
ORCID *0000-0001-8240-5447*

[2](MSc.), Balikesir University, e-mail: turker.turkoglu@balikesir.edu.tr
ORCID *0000-0002-0499-9363*

1.INTRODUCTION

Material properties such as high specific stiffness, strength, and wear resistance are also strengthened by particle reinforced metal matrix composites. These characteristics are also preferred in many areas and in particular, aluminum metal matrix composites are responsible for the energy absorption of structural components in the automotive sector (Hedayatian, Momeni, Nezamabadi, & Vahedi, 2020; Kwon, Saarna, Yoon, Weidenkaff, & Leparoux, 2014; Sharma, Nanda, & Pandey, 2018).

Boron carbide (B$_4$C) with a high melting temperature has many superior properties such as high compressive strength, high hardness, chemical stability. In addition to these features, it is its negative feature that it gives brittleness to the materials of which it is a component. As well as high hardness and wear resistance, Alumina (Al$_2$O$_3$) decreases residual stress on fracture toughness (Alihosseini, Dehghani, & Kamali, 2017; Węglewski et al., 2019).

Metal matrix composites can be produced by a wide variety of production methods such as powder metallurgy, stir casting, friction stir processing (Avettand-Fènoël & Simar, 2016; Pang, Xian, Wang, & Zhang, 2018; Ramanathan, Krishnan, & Muraliraja, 2019). The most efficient process is known to be manufacturing with powder metallurgy (Yamanoglu, Daoud, & Olevsky, 2018). Compared to the stir casting method, the dispersion of the reinforcements in the matrix would increase the mechanical alloying of the matrix and reinforcement powders before the powder metallurgy process. By avoiding these possible cluster structures, it has been observed that the mechanical properties of the produced composites have also improved. Cluster morphologies act like

stress density areas that accelerate crack production and cause losses from mechanical properties (Bhoi, Singh, & Pratap, 2020).

Optimization provides to increase the benefits obtained by minimizing the costs in many areas such as design, analysis, and production in the industry. By analyzing the effects of factors on multi-response, the Grey Relational Analysis method can evaluate optimal process parameters for multiple experimental outcomes. Generally, Grey Relational Analysis is performed by combining with the Taguchi method (Kumar, 2020; Montgomery, 2017)

The volume percentage and size of the reinforcement are typically the factors influencing the properties of hybrid composites. Studies examining the effect of single/dual reinforcement size on mechanical properties remained limited. In the optimization and the production processes of composite materials, the optimum production parameters have been determined by combining the Grey Relational Analysis method with Taguchi in our study, since the Taguchi method was relatively insufficient in explaining the multi-response characteristics. By using these methods together, both individual response optimization and multiple response optimization of production parameters can be possible. In this study, the effect of single/dual size reinforcement and production parameters on microstructural and mechanical properties of composites were investigated and optimum process parameters were defined by Grey Relational Analysis (GRA) combined with the Taguchi Analysis.

2. MATERIALS METHOD

Pure Al (purity 99.5%) was used as a matrix material in the study. Al and Al_2O_3 powders have an average particle size of 60 μm, while B_4C powders have been selected to have a single/dual B_4C reinforced particle size (40 μm/40 μm+60 μm). Reinforcement content used in the study, it has been fixed 10 wt.% B_4C and 10 wt.% Al_2O_3. The powder metallurgy method is determined as the method of consolidation of powders. Samples were produced by the hot press and by grouping them according to temperatures of 500 °C-600 °C, ball milling treatment, and B_4C reinforcement type. Table 1 shows the process parameters. The hybrid composites were produced 15 mm in diameter and 10 mm in thickness.

Hardness measurements of hybrid composites load of 10 kg, applied for 10 seconds. In order to determine the average hardness values, 5 measurements were taken from each sample. The compression test was conducted by Zwick/Roel test machine at room temperature, loading speed of 1 mm/min. The compacted microstructure was also investigated by an optical microscope. Finally, experimental and numerical values were investigated using the Grey Relational Analysis (GRA) method combined with the Taguchi Analysis, and the results were presented comparatively.

Ball milling and B_4C reinforcement size type parameters used in the study have been defined as 0 and 1. In these definitions, it is defined as 1 if the ball milling operation has been conducted and 0 if it is not. B_4C reinforcement size (40 μm) has been expressed as 0, while B_4C reinforcement size (40 μm+60 μm) has been expressed as 1.

Table 1: Process Parameters

Sample	Ball milling	B_4C reinforcement size type (single/dual)	Sintering Temperature (°C)
1	0	0	500
2	0	0	600
3	1	0	500
4	1	0	600
5	0	1	500
6	0	1	600
7	1	1	500
8	1	1	600

3.RESULTS AND DISCUSSION

Hybrid composites for all production parameters have been successfully produced by the powder metallurgy method.

Microstructures were examined using an optical microscope and camera connected to it. In Figure 1, it is observed that the reinforcements are distributed uniformly within the matrix for all production parameters. However, it has been determined that there are partial agglomeration zones in the materials containing fine size reinforcement. It was stated in previous studies that the reason for this uniform distribution in the internal structure is the mechanical alloying process.
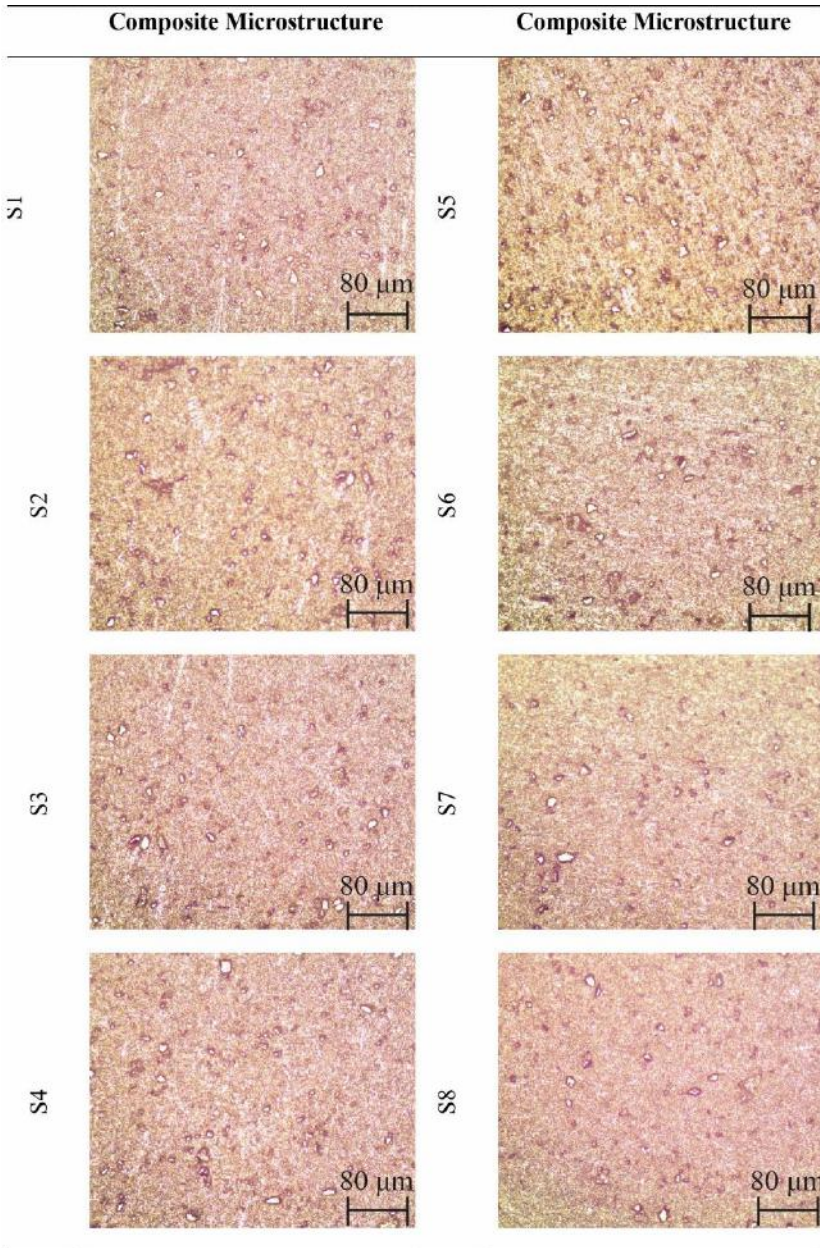
Figure 1: Optical microstructures of Hybrid Composite Samples

Figure 2 depicts the hardness values of the hybrid composites. As can be seen in Figure 2, it is seen that the maximum hardness is obtained from sample number 7. As a result of Vickers hardness tests; It is seen that the addition of B_4C and Al_2O_3 contributes significantly to the hardness of the composites. Compared to samples containing both pure Al and single-

particle size B$_4$C reinforcement, higher hardness values were obtained for composites with dual particle size B$_4$C. The reason for the hardness increase in hybrid composites, It is thought that ceramic reinforcements have higher hardness compared to aluminum metal (Asghar et al., 2018). Homogeneous dispersion of ceramic particles by mechanical alloying before hot pressing, and composite particle strength through the strengthening of the dislocation density (Fan et al., 2018).
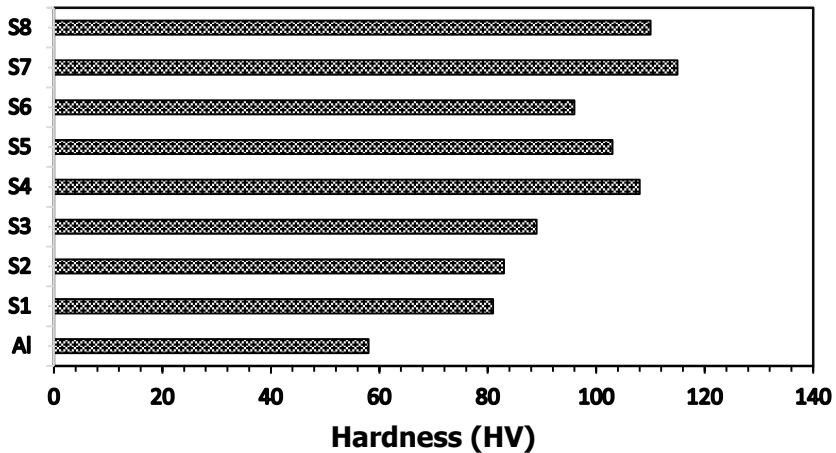
Figure 2: Hardness Values of Hybrid Composites

The compression behavior of hot-pressed composites is shown in Figure 3. These results have shown that; As the B$_4$C reinforcement type changed from single to dual structure, its compressive strength increased. This increase in the compressive strength of composites is due to the high compression strength values of ceramic reinforcements compared to the metal matrix, as well as the elastic modulus and thermal expansion mismatch between the reinforcement/matrix will cause dislocations (Lakshmikanthan, Bontha, Krishna, Koppad, & Ramprabhu, 2019). The strength of composites would be increased by this dislocation density increase. By acting as a load-bearing factor during deformation, rigid reinforcements are thought to contribute to the rise in strength (Hariharasakthisudhan & Jose, 2018).
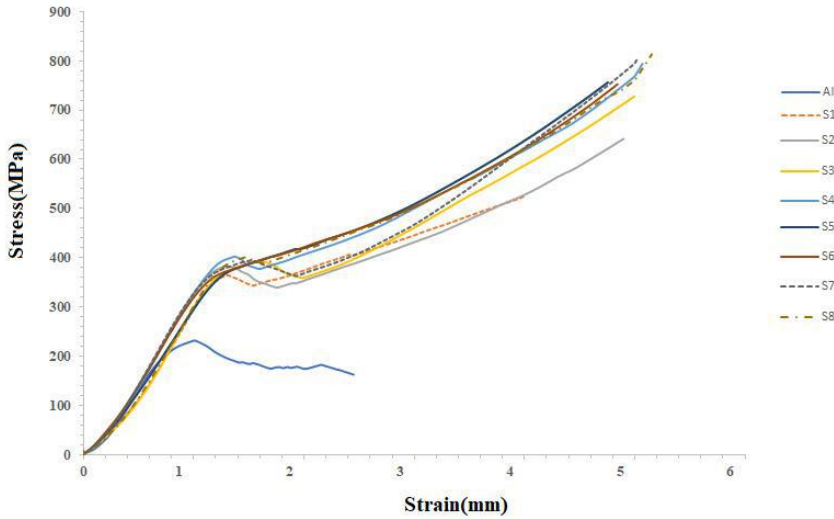
Figure 3: Compressive Strength of Hybrid Composites

In Grey Relational Analysis, it is possible to find the relationship between the parameters and outputs of the experiments designed with the Taguchi method, and the multiple performance characteristics by performing Analysis of Variance (ANOVA) at the same time (Haq, Marimuthu, & Jeyapaul, 2008; Montgomery, 2017). By combining these two methods, high accuracy parameter selections and result estimates can be evaluated (Hussain, Khan, & Sarmah, 2020; Jailani, Rajadurai, Mohan, Kumar, & Sornakumar, 2009). In order to find multi-response characteristics of process parameters such as hardness and compression strength, the optimum process parameters of Al-Al$_2$O$_3$-B$_4$C hybrid composites were determined by combining the Taguchi method and Grey Relational Analysis.

The factors used in the study and their levels are shown in Table 2. The experimental design consists of 3 factors and 2 levels. Taguchi's L8 orthogonal array was used under these conditions. S/N values of the designed experimental inputs and experimental results were determined with Minitab 16 (Statistical software). While the signal value obtained as a result of the analysis expresses the desired effect for the results, the N value indicates the undesirable effect for the results (Montgomery, 2017).

Grey Relational Analysis combined with the Taguchi method consists of the following process steps.

Step 1:

Determination of inputs and possible outputs in the production process.

Table 2: Parameters and Levels of the Experimental Process

Parameters	Level 1	Level 2
B_4C reinforcement size type	0	1
Ball milling	0	1
Temperature (°C)	500	600

Step 2:

Choosing the appropriate orthogonal arrays in the Taguchi method. In this study, L8 orthogonal array was chosen (Table 3.)

Table 3: Orthogonal design L_8 for responses

Sample	Factors			Responses	
	B_4C reinforcement size type	Ball Milling	Temp. (°C)	Hardness (HV)	Comp. St. (MPa)
1	0	0	500	81	524
2	0	0	600	83	641
3	0	1	500	89	727
4	0	1	600	108	794
5	1	0	500	103	755
6	1	0	600	96	751
7	1	1	500	115	805
8	1	1	600	110	813

Step 3:

Evaluating the outputs by performing the experimental analysis.

Step 4:

Choosing the appropriate one for the following formulas and calculating the S/N values.

i) If the results are to be maximized in the study; Larger the better approach should be chosen. As it was desired to maximize hardness and compressive strength values, Larger the better approach was chosen in this study by using Equation 1.

$$\frac{S}{N}\ Ratio\ = -10log_{10}\left(\frac{1}{n}\right)\sum_{i=1}^{n}\frac{1}{{y_i}^2} \tag{1}$$

ii) If the results are to be minimized in the study; Smaller the better approach should be chosen by using Equation 2.

$$\frac{S}{N}Ratio = -10log_{10}\left(\frac{1}{n}\sum_{i=1}^{n}y_i^2\right) \tag{2}$$

Step 5

Due to the different data values in the process, the calculated S / N Ratio values are normalized between 0 and 1. Normalization is a method of transformation that allows data to be distributed evenly and reduced to a range that is made possible. Table 4 presents S/N ratio and normalized S/N Ratio for hardness and compressive strength.

Table 4: S/N ratio and normalized S/N Ratio for Hardness and Compressive Strength

Sample	Response 1(Hardness)		Response 2 (Comp. St.)	
	S/N ratio	Normalized S/N ratio	S/N ratio	Normalized S/N ratio
1	38,1697	0	54,3866	0
2	38,3816	0,06959	56,1372	0,45883
3	38,9878	0,26873	57,2307	0,74545
4	40,6685	0,82081	57,9964	0,94616
5	40,2567	0,68556	57,5589	0,83149
6	39,6454	0,48475	57,5128	0,81940
7	41,2140	1	58,1159	0,97748
8	40,8279	0,8731	58,2018	1

In Equation 3, the larger the better approach has been formulated.

$$X_{ij}^* = \left(\frac{X_{ij} - min_j(X_{ij})}{max_j(X_{ij}) - min_j(X_{ij})} \right) \qquad (3)$$

In Equation 4, the smaller the better approach has been formulated.

$$X_{ij}^* = \left(\frac{max_j(X_{ij}) - X_{ij}}{max_j(X_{ij}) - min_j(X_{ij})} \right) \qquad (4)$$

Since it was desired to have maximum compressive strength and hardness values, Equation 3 was used for all target functions in the study.

Step 6

The Grey Relational co-efficient values of the normalized S / N values were calculated using the following formula (Equation 5).

$$\zeta_i(z) = \frac{\Delta_{min} + \zeta\Delta_{max}}{\Delta_{0i}(z) + \zeta\Delta_{max}} \qquad (5)$$

K is the coefficient value, defined in the range $0 \leq K \leq 1$

Step 7

Determination of Grey Relational Grade stages.

Grey relational grade is calculated by using Equation 6. Grey relational coefficients, grey relational grade, and rank values are displayed in Table 5.

$$\gamma_i = \frac{1}{n} \sum_{z=1}^{n} \zeta_i(z) \qquad (6)$$

Table 5: Grey Relational Coefficients, Grey Relational Grade and Rank Values

Sample	Grey relational coefficient		Grey relational grade	Rank
	Hardness	Comp. St.		
1	0,33333	0,333333	0,333	8
2	0,34955	0,480231	0,415	7
3	0,40608	0,662654	0,534	6
4	0,73617	0,902792	0,819	3
5	0,61392	0,747939	0,681	4
6	0,49249	0,734649	0,614	5
7	1	0,956913	0,978	1
8	0,79766	1	0,899	2

Step 8

Determination of optimum performance factors

On the basis of grey relational grade, processing parameters effect and optimum process parameters were calculated. In the light of these evaluations, the initial optimum process parameters were obtained as a combination of B_4C reinforcement size type. 1, Ball Milling 1, and sintering temperature 500 °C. Following these steps, when grey relational grade values were calculated by Taguchi analysis, it was observed that the highest effect on the process was achieved with Dual particle B_4C reinforced size and Ball Milled process.

Step 9

ANOVA for significant values

Further verification analysis was also performed through moreover ANOVA. The results of the ANOVA are presented in Table 6. From response Table 6, the Most effective parameters were determined effectively. B_4C reinforcement type and ball milling parameters were found to be significant on multi-performance characteristics. (P-value <0.05) Temperature is an important factor in sintering reactions in the composite production process by the powder metallurgy method. Although the temperature factor is expressed as insignificant in the optimization part of the study, it is concluded that the two sintering temperature values used in the study are sufficient for the composite production process since the obtained mechanical properties are appropriate.

Table 6: Results of Analysis of Variance (ANOVA)

Source	DF	Seq SS	F-value	P-value	R-sq
B$_4$C reinforcement type	1	0,14304	13,17	0,022	
Ball milling	1	0,17654	16,26	0,016	
Temperature (°C)	1	0,00603	0,56	0,497	
Error	4	0,04344			
Total	7	0,36905			88,23

4.CONCLUSIONS

Hybrid composites for all production parameters were successfully produced by the powder metallurgy method. Hardness analysis showed that the hardness of all composites increased compared to the hardness of the matrix phase, regardless of the reinforcement type and size. The hardness was maximized by the presence of B$_4$C in the composite content. The maximum hardness value was obtained from sample number 7 (B$_4$C particle size type: Dual, Sintering Temperature: 500 °C, Ball milled) as 115 HV. The compression strength values of hybrid composites increased with reinforcement. Compared to the monolithic aluminum material, an increase in compressive strength was achieved approximately 3 times. The presence of Dual B$_4$C increased strength depending on the density of dislocations. Grey relational analysis combined with Taguchi Experimental design has been successfully conducted in the production process of hybrid composites. Optimum parameters for multi-response characteristic; It has been obtained from dual size B$_4$C reinforcement, ball milling, and 500 °C hot pressed hybrid composite sample.B$_4$C reinforcement size type and Ball Milling have a significant effect on selected the multiple responses for the process.

REFERENCES

Alihosseini, H., Dehghani, K., & Kamali, J. (2017). Microstructure characterization, mechanical properties, compressibility and sintering behavior of Al-B$_4$C nanocomposite powders. *Advanced Powder Technology*, *28*(9), 2126–2134. https://doi.org/10.1016/j.apt.2017.05.019

Asghar, Z., Latif, M. A., Rafi-ud-Din, Nazar, Z., Ali, F., Basit, A., … Subhani, T. (2018). Effect of distribution of B$_4$C on the mechanical behaviour of Al-6061/B$_4$C composite. *Powder Metallurgy*, *61*(4), 293–300. https://doi.org/10.1080/00325899.2018.1501890

Avettand-Fènoël, M. N., & Simar, A. (2016). A review about Friction Stir Welding of metal matrix composites. *Materials Characterization*, *120*, 1–17. https://doi.org/10.1016/j.matchar.2016.07.010

Bhoi, N. K., Singh, H., & Pratap, S. (2020). Developments in the aluminum metal matrix composites reinforced by micro/nano particles – A review. *Journal of Composite Materials*, *54*(6), 813–833. https://doi.org/10.1177/0021998319865307

Fan, G., Jiang, Y., Tan, Z., Guo, Q., Xiong, D. bang, Su, Y., … Zhang, D. (2018). Enhanced interfacial bonding and mechanical properties in CNT/Al composites fabricated by flake powder metallurgy. *Carbon*, *130*, 333–339. https://doi.org/10.1016/j.carbon.2018.01.037

Haq, A. N., Marimuthu, P., & Jeyapaul, R. (2008). Multi response optimization of machining parameters of drilling Al/SiC metal matrix composite using grey relational analysis in the Taguchi method. *International Journal of Advanced Manufacturing Technology*, *37*(3–4), 250–255. https://doi.org/10.1007/s00170-007-0981-4

Hariharasakthisudhan, P., & Jose, S. (2018). Influence of metal powder premixing on mechanical behavior of dual reinforcement (Al$_2$O$_3$ (μm)/Si$_3$N$_4$ (nm)) in AA6061 matrix. *Journal of Alloys and Compounds*, *731*, 100–110. https://doi.org/10.1016/j.jallcom.2017.10.002

Hedayatian, M., Momeni, A., Nezamabadi, A., & Vahedi, K. (2020). Effect of graphene oxide nanoplates on the microstructure, quasi-static and dynamic penetration behavior of Al6061 nanocomposites. *Composites Part B: Engineering*, Vol 182. https://doi.org/10.1016/j.compositesb.2019.107652

Hussain, M. Z., Khan, S., & Sarmah, P. (2020). Optimization of powder metallurgy processing parameters of Al$_2$O$_3$/Cu composite through Taguchi method with Grey relational analysis. *Journal of King Saud*

University - Engineering Sciences, *32*(4), 274–286. https://doi.org/10.1016/j.jksues.2019.01.003

Jailani, H. S., Rajadurai, A., Mohan, B., Kumar, A. S., & Sornakumar, T. (2009). Multi-response optimisation of sintering parameters of Al-Si alloy/fly ash composite using Taguchi method and grey relational analysis. *International Journal of Advanced Manufacturing Technology*, *45*(3–4), 362–369. https://doi.org/10.1007/s00170-009-1973-3

Kumar, M. (2020). Mechanical and Sliding Wear Performance of AA356-Al_2O_3/SiC/Graphite Alloy Composite Materials: Parametric and Ranking Optimization Using Taguchi DOE and Hybrid AHP-GRA Method. *Silicon*. https://doi.org/10.1007/s12633-020-00544-9

Kwon, H., Saarna, M., Yoon, S., Weidenkaff, A., & Leparoux, M. (2014). Effect of milling time on dual-nanoparticulate-reinforced aluminum alloy matrix composite materials. *Materials Science and Engineering A*, *590*, 338–345. https://doi.org/10.1016/j.msea.2013.10.046

Lakshmikanthan, A., Bontha, S., Krishna, M., Koppad, P. G., & Ramprabhu, T. (2019). Microstructure, mechanical and wear properties of the A357 composites reinforced with dual sized SiC particles. *Journal of Alloys and Compounds*, *786*, 570–580. https://doi.org/10.1016/j.jallcom.2019.01.382

Montgomery, D. C. (2017). *Design and Analysis of Experiments Ninth Edition* (Ninth). Opgehaal van https://lccn.loc.gov/2017002355

Pang, X., Xian, Y., Wang, W., & Zhang, P. (2018). Tensile properties and strengthening effects of 6061Al/12 wt%B_4C composites reinforced with nano-Al_2O_3 particles. *Journal of Alloys and Compounds*, *768*, 476–484. https://doi.org/10.1016/j.jallcom.2018.07.072

Ramanathan, A., Krishnan, P. K., & Muraliraja, R. (2019). A review on the production of metal matrix composites through stir casting – Furnace design, properties, challenges, and research opportunities. *Journal of Manufacturing Processes*, Vol 42, bll 213–245. https://doi.org/10.1016/j.jmapro.2019.04.017

Sharma, S., Nanda, T., & Pandey, O. P. (2018). Effect of dual particle size (DPS) on dry sliding wear behaviour of LM30/sillimanite composites. *Tribology International*, *123*(November 2017), 142–154. https://doi.org/10.1016/j.triboint.2017.12.031

Węglewski, W., Krajewski, M., Bochenek, K., Denis, P., Wysmołek, A., & Basista, M. (2019). Anomalous size effect in thermal residual stresses in pressure sintered alumina-chromium composites.

Materials Science and Engineering A, *762*(July). https://doi.org/10.1016/j.msea.2019.138111

Yamanoglu, R., Daoud, I., & Olevsky, E. A. (2018). Spark plasma sintering versus hot pressing–densification, bending strength, microstructure, and tribological properties of Ti5Al2.5Fe alloys. *Powder Metallurgy*, *61*(2), 178–186. https://doi.org/10.1080/00325899.2018.1441777

CHAPTER IV

INFLUENCES OF AL AND ALTiB ADDITIONS ON THE MICROSTRUCTURE AND MECHANICAL PROPERTIES OF MgZnSn ALLOY POURED INTO GREEN SAND MOLD

Hasan Hasirci[1]

[1]*(Assoc. Prof. Dr.), Gazi University, e-mail: hasirci@gazi.edu.tr,*
0000-0001-5520-4383

1. INTRODUCTION

Magnesium alloys have low density and other benefits such as: a good vibration damping and the best from among all construction materials: high dimension stability, connection of low density and huge strength with reference to small mass, possibility to have application in machines and with ease to put recycling process, which makes probability to logging derivative alloys a very similar quality to original material (Carlson, B.E. 1997; Cao and Wessén, 2004:35A; Cao, P., Qian, M. and StJohn, D.H. 2004:5; Zhang, Z. R., and Tremblay, D. D. 2004: 385; Yang, M. and Pan, F. 2010:31; Liang, M. X., Xiang, W., Lin, L. X. and Lei, Y. 2010:201-6). A desire to create as light vehicle constructions as possible and connected with it low fuel consumption have made it possible to make use of magnesium alloys as a constructional material in car wheels, engine pistons, gear box and clutch housings, skeletons of sunroofs, framing of doors, pedals, suction channels, manifolds, housings of propeller shafts, differential gears, brackets, radiators and others (Dobrzański, L.A., Tański, T., Čížek, L. and Domagała J. 2008:31).

Magnesium alloys generally produced by sand casting, pressure die casting, permanent mold casting, squeeze casting, low pressure and counter gravity casting are preferred because of having light weight and good mechanical properties (Carlson, B.E. 1997; Zhang, Z. R., and Tremblay, D. D. 2004: 385; Kurnaz, S.C., Sevik, H., Açıkgöz, S. and Özel, A. 2011:509). These alloys can also be successfully sand cast providing some general principles be followed, which are dictated by the particular physical properties and chemical reactivity of magnesium (Carlson, B.E. 1997; Rzychoń, T., Kiełbus, A. and Lityńska-Dobrzyńska, L. 2013:83). Because, sand casting is easier and cheaper than other casting processes. Metal flow should be as smooth as possible to minimize oxidation. Because of the low density of magnesium, there is a relatively small pressure head in risers and sprues to assist the filling of molds. Sand molds

need to be permeable and the mold must be well vented to allow the expulsion of air.

In general, magnesium alloys are based on Mg–Al systems, which are relatively cheap, compared with other magnesium alloys available. It is well known, Al containing Mg alloys include the β-$Mg_{17} Al_{12}$ compound that detrimentally influences the mechanical properties such as tensile strength and impact resistance (Cao and Wessén, 2004:35A; Candan , S., Unal , M., Koc, E., Turen, Y. and Candan, E. 2010:509). One of the most efficient ways to decrease the detrimental effect of the β-$Mg_{17} Al_{12}$ phase on the mechanical properties is to addition third alloying element (Srinivasan, J. Swaminathan, M.K. Gunjan, U.T. Pillai, S. and Pai, B.C. 2010:527; Kim, B.H., Lee, S.W., Park, Y.H. and Park, I.M. 2010:493; Suresh, M., Srinivasan, A., Ravi, K.R., Pillai, U.T.S. and B.C. Pai. 2009:525). The problem with early magnesium alloy castings was that grain size tended to be large and variable, which often resulted in poor mechanical properties, micro porosity and, in the case of wrought products, excessive directional UTS of properties. Values of proof stress also tended to be particularly low relative to tensile strength. Alloying element is added to improve properties, especially grain refinement elements. Ca is an effective way to improve the mechanical properties of AZ91 alloys at elevated temperatures (Candan , S., Unal , M., Koc, E., Turen, Y. and Candan, E. 2010:509; Wenwen, D., Yangshan, S., Xuegang, M., Feng, X., Min, Z. and Dengyun, W. 2003:356; Wu, G., Fan, Y., Gao, H., Zhai, C. and Zhu, Y.P. 2005:408; Zhou, W., Aung, N.N. and Sun, Y. 2009:51; Guangyin, Y., Yangshan, S. and Wenjiang, D. 2001:308; Wang, F., Wang, Y., Mao, P., Lu, B. and Guo, Q. 2010:20). Other elements such as Sb, Bi and Pb to AZ91 alloy could also increase the tensile strength and creep resistance significantly (Candan , S., Unal , M., Koc, E., Turen, Y. and Candan, E. 2010:509; Srinivasan, J. Swaminathan, M.K. Gunjan, U.T. Pillai, S. and Pai, B.C. 2010:527; Zhou, W., Aung, N.N. and Sun, Y. 2009:51

Guangyin, Y., Yangshan, S. and Wenjiang, D. 2001:308). A recent study (Kim, B.H., Lee, S.W., Park, Y.H., Park J. I.M. 2010:493) showed that the presence of Sn contributed to the room and the elevated temperature strength of magnesium alloy attributed to the formation of dispersed short rod-like Mg2Sn phases. The addition of B in the form of Al-4B master alloy significantly refines the grain size of AZ91 leading to an improvement in the mechanical properties (Suresh, M., Srinivasan, A., Ravi, K.R., Pillai, U.T.S. and B.C. Pai. 2009:525). The beneficial effects of rare-earth (RE) on mechanical properties including strength and creep resistance of AZ91 alloys also have been reported (Candan , S., Unal , M., Koc, E., Turen, Y. and Candan, E. 2010:509). It is well known that Al–5Ti–B master alloy is an effective grain refiner in aluminum alloys, and it

could also refine the magnesium alloy, and TiB2 particles were found to nucleate the α-Mg grains. However, due to the low boron content, there is a relatively small amount of TiB2 particles present in the Al–5Ti–B master alloy. In this paper, the Ti to B atomic ratio is changed to improve the effectiveness of the master alloy and to eliminate the residual Ti so as to generate a larger amount of TiB_2 particles and produce a new Al–4Ti–5B master alloy (Wang, Y., Zeng X. and Ding,W. 2006:54; Chen, T.J., Wang, R.Q., Ma, Y. and Hao, Y. 2012:34; Ma, X., Wang, X., Li, X. and Yang, L. 2010:20; Xu, C., Lu, B., Lu, Z. and Liang, W. 2008:26).

The aim of the present study is to investigate the mechanical properties and the microstructure of alloyed with different and high amounts of Al and AlTiB of MgZnSn by surface coated and controlled atmosphere sand casting.

2. EXPERIMENTAL PROSEDURES

The alloys, with compositions listed in Table 1, were prepared using commercially pure magnesium and aluminum in a steel crucible with an electric resistance furnace protected by CO_2. Al and AlTiB were added as pure Al and Al5Ti1B master alloy. The casting parameters were as follows: the melt of matrix alloy was held at a 700 ºC casting temperature for homogenous mixture duration 20 min and casted at a normally gravity conditions. Cast samples were produced at coated green sand molds at protected atmosphere and size 20 mm diameter - 200 mm length. Casting procedures were carried out in a special bottom caster illustrated at Figure 1. Metallographic samples were first cut on a wire erosion machine. Grinding was performed using silicon carbide (SiC) grinding papers up to 1200 grit. Prior to polishing, the samples were rinsed with ethanol, and then polishing was performed with a 3 µm alumina solution.

Table 1. The chemical composition of the investigated alloys (mass fraction, %)

Alloy Number	Al	AlTiB	Zn	Sn	Mg
A1	2.5	-	1	1	Bal.
A2	5	-	1	1	Bal.
A3	10	-	1	1	Bal.
A4	15	-	1	1	Bal.
B1	-	2.5 (2.35 Al - 0.125Ti - 0.025B)	1	1	Bal.
B2	-	5 (4.7 Al - 0.25Ti - 0.05B)	1	1	Bal.
B3	-	10 (9.4 Al - 0.5Ti - 0.1B)	1	1	Bal.
B4	-	15 (14.1 Al - 0.75Ti - 0.15B)	1	1	Bal.

The specimens for scanning electron microscopy (SEM) were chemically etched in acetic picric (5 ml acetic acid, 6 g picric acid, 10 ml distilled water, 100 ml ethanol) to show grain boundaries and nital (4 ml nitric acid, 96 ml ethanol) for revealing structure. In addition, the distribution of alloying elements in the structure was verified by using an

SEM instrument (JEOL 6064LV) with an energy dispersive spectrometer (EDS). X-ray diffraction (XRD) analysis was also carried out to identify the phases present in the samples using a Rigaku D Max 1000 X-ray diffractometer with Cu Ka radiation. The grain size measurements were performed by using image analysis software (Imaje-J). The hardness values were determined by the Vickers hardness test with a load of 50 N. At least ten successive hardness measurements were made on each sample. The tensile test samples had a diameter of 8 mm and a length of 40 mm. The tensile tests were performed (ASTM E 8M-99) with a crosshead speed of 0.8 mm min−1 at room temperature. Each data represents at least average of five samples in tensile tests.
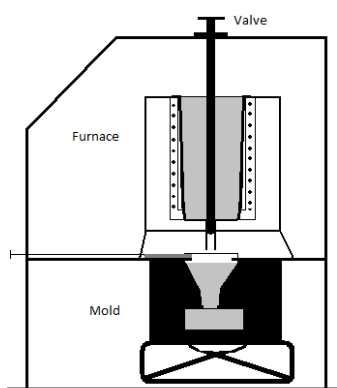
Fig. 1. Schematic illustration of special casting unit

3. RESULTS AND DISCUSSION

3.1. MICROSTRUCTURE AND CHARACTERIZATION

Fig. 2 shows the influence of different amounts of alloying elements addition into MgZnSn alloys on the grain size. It obviously shows that the grain size of A series alloys increases with increasing quantity of Al alloying element addition. The grain size of the a series decreases from 185 to 100 μm when the amount of Aluminum added increases from 2,5 to 15 wt%, respectively. With addition of AlTiB, the grain size of B series decreases from 150 to 55 μm when the amount of AlTiB added increases from 2,5 to 15 wt%, respectively. Several methods are available for grain refining magnesium alloys; however, the mechanisms involved are complex.

A study has shown the effect of Al addition (Cao, H. and Wessén, M. 2004:35). In this study, this has been achieved by remelting and solidifying the alloys in a gradient furnace. The drawing rate was varied from 0.3 to 6 mm/s, which yielded a wide variety of microstructures. The

results showed that homogeneous and reproducible samples could be produced, and that the tensile properties obtained showed a very small scatter. From the binary Mg-Al phase diagram, it follows that solidification begins with nucleation and growth of primary Mg α phase for hypoeutectic compositions (Al<33 wt pct). Under equilibrium conditions, Mg-Al alloys containing less than 12.7 wt pct Al will solidify into a fully α -phase structure with aluminum in solid solution. However, due to the slow diffusion rate of Al atoms in the β phase and to the relatively high drawing rates used in this investigation, solidification will proceed under non-equilibrium conditions. In fact, a certain amount of eutectic was detected even in the A1 alloys. The eutectic morphologies formed varied significantly between different Al contents. At the lowest Al content (Mg-3Al), the eutectic is predominantly completely divorced, and the $Mg_{17}Al_{12}$-β phase mainly appears in a compact globular form. With an increasing Al content, the eutectic liquid tends to solidify into more irregular eutectic islands consisting of $Mg_{17}Al_{12}$- β phase with dispersed β-phase particles inside. Consequently, the eutectic structure becomes less divorced with increasing Al content. In addition, due to the presence of these elements by an amount of Zn and Sn-rich phases are formed. At the others studies has shown the effect of AlTiB addition (Wang, Y., Zeng X. and Ding,W. 2006:54; Chen, T.J., Wang, R.Q., Ma, Y. and Hao, Y. 2012:34; Ma, X., Wang, X., Li, X. and Yang, L. 2010:20; Xu, C., Lu, B., Lu, Z. and Liang, W. 2008:26). AlTiB master alloys consist of Al_3Ti, AlB_x and TiB_2 particles, in which either the Al_3Ti and TiB_2 or both types of particles act as heterogeneous nucleation sites, like aluminum alloys (Chen, T.J., Wang, R.Q., Ma, Y. and Hao, Y. 2012:34; Ma, X., Wang, X., Li, X. and Yang, L. 2010:20; Xu, C., Lu, B., Lu, Z. and Liang, W. 2008:26). These particles are not melt into alloy, and thus they will make the core task on heterogeneous nucleant. According to the Al–Ti-B ternary phase diagrams, the AlTiB master alloys consist of Al_3Ti particles, respectively. In this study, Al_3Ti particles dissolve when the master alloys added into molten B series alloy. Therefore, the Ti and B are assumed to serve as heterogeneous nuclei of α-Mg.

SEM micrographs of some produced alloys at this study are shown in Fig. 3. As shown in Fig. 3(b-d) the addition of Al element modified the structure and decreased the grain size compared with Fig. 3(a). A similar trend is also observed in the alloys containing AlTiB (Fig. 3(e-h). SEM, EDS and XRD analysis of the various produced alloys are shown in Figs. 4 and 5. EDS, atomic ratio in Fig., proved it. 4(a) and (c) and XRD analysis of A1and B1 alloys that its microstructure mainly consists of primary α-Mg grains (point 1) with eutectic phases (Al riched α-Mg (point 3) + β-Mg_{17} Al_{12} (point 2) surrounding their boundaries. Fig. 4(b) and (d) shows that Al and AlTiB addition affected the morphology and

distribution of the β-Mg$_{17}$ Al$_{12}$, respectively. In the case of Al and AlTiB, eutectic morphology was changed to partially divorced eutectic, and the β-Mg$_{17}$ Al$_{12}$ phase was transformed from network to globular form.
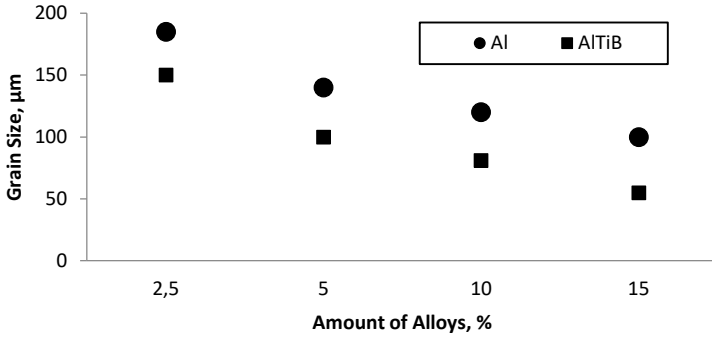
Fig. 2. The effect of alloying elements on grain size of MgZnSn alloys
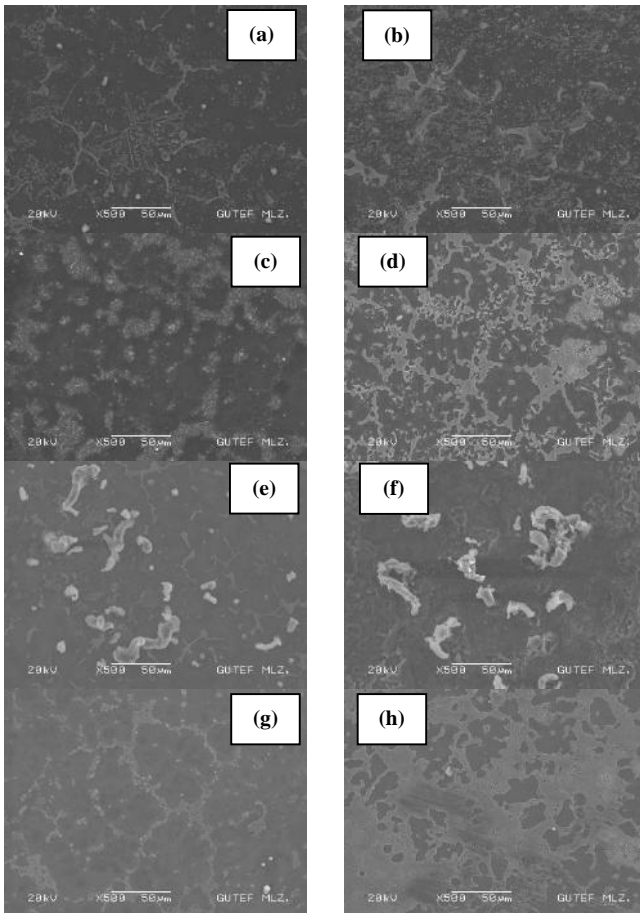
Fig. 3. SEM microstructures of: a) A1, b) A2, c) A3, d) A4, e) B1, f) B2,
g) B3 and h) B4 alloy
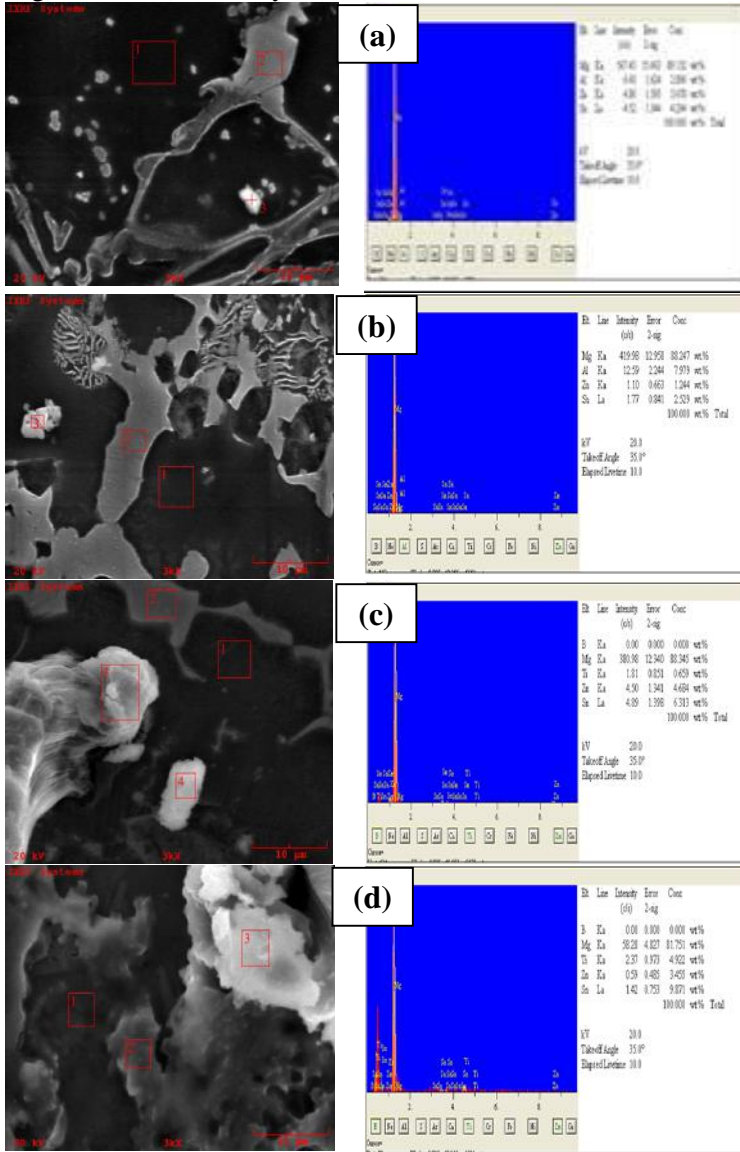
Fig. 4. SEM micrograph showing microstructure and EDS analysis of a)
A1, b) A4 and c) B1 and d) B4 alloy

Other hand, the addition of AlTiB changed the eutectic morphology
to partially divorced eutectic without changing the shape of the β-$Mg_{17}Al_{12}$
phase. The EDS mapping of B1 in Fig. 4(c) shows that Ti and especially

B have extremely low or unknown solubility in Mg lattice and it is likely that fine particles of pure Ti exist at around grain boundaries. Similar results were reported by studies (Chen, T.J., Wang, R.Q., Ma, Y. and Hao, Y. 2012:34; Ma, X., Wang, X., Li, X. and Yang, L. 2010:20; Xu, C., Lu, B., Lu, Z. and Liang, W. 2008:26). For the β-$Mg_{17}Al_{12}$ phase in B_4 alloys, titanium-containing particles may act as the heterogeneous nucleation site. Therefore, the one of the main effects of Ti and B on microstructure is the formation of partially divorced $Mg_{17}Al_{12}$ phase, as shown in Fig. 4(d). When the studies on grain refinement in Mg materials are examined, it will be seen that the grain refiner is generally used at low rates (0.1-2%). It is not seen in these studies what results will be obtained if the grain refiner is added at a high rate. One of the main objectives of this study is to demonstrate the effects of high AI and ALTiB content. The results showed that the increase in the addition amount was effective in reducing the grain size, and that these addition rates could be used safely and successfully.

The XRD spectrums (Fig. 5.a-b) of all the alloys show that Al addition did not result in the formation of Al containing any new phase. But, other XRD spectrums (Fig. 5.c-d) of all the alloys show that AlTiB addition result in the formation of containing at least some Ti and B containing new phase (as impurities of AlB, TiB, AlTi etc.). However, it can be seen in Fig. 5 (d) that α-Mg was detected in specimens and the amount and shape of phase was greatly reduced with increasing Ti and B with contained impurities of these alloys. In addition, β-$Mg_{17}Al_{12}$ was detected in specimens AlTi particles. β phase is smaller with increasing amounts of AlTi particles.
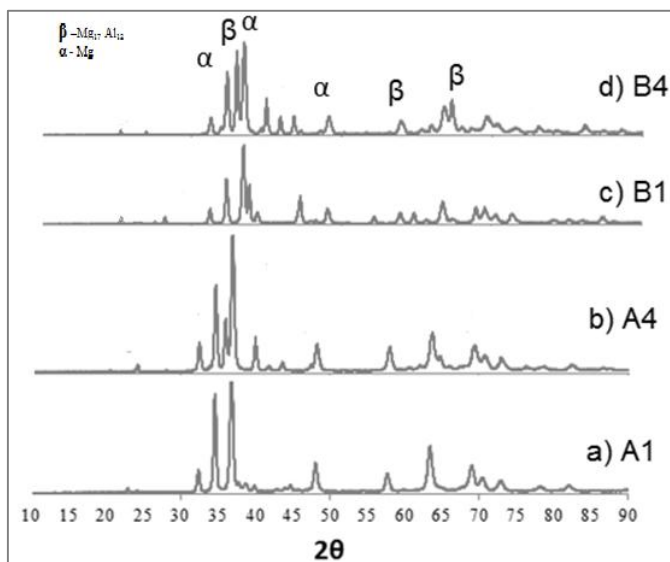

Fig. 5. The XRD spectrums of a) A1, b) A4, c) B1 and d) B4 alloy

3.2. MECHANICAL PROPERTIES

The results of hardness, ultimate tensile strength (UTS), yield strength (YS) and elongation measurements of the specimen are given in Table 2 and Figure 6. The hardness value of Al containing alloys increases with increasing alloying element concentration, and the hardness of A4 is improved by 59.2%. Then the hardness is relatively constant with more addition of Al. The hardness value of AlTiB containing alloys increased with increasing alloying element, and the hardness of B1 was improved by 59.5% due to the addition of 15 wt% AlTiB. In addition, the hardness values of Al min and maximum containing specimens was improved by respectively 33.4 and 33.7% due to the addition of AlTiB. Then the hardness keeps on stable with more addition of AlTiB. The main parameters affecting the hardness are the solubility of the alloying element, grain size and eutectic morphology. The reason for the hardness increment can be attributed to smaller grain size, insolubility of Al, Ti and B elements and homogeneous distributed eutectic areas. The UTS and YS of A1 are remarkably increased by Al up to 5 wt% and are improved by respectively 8 and 9% (specimen A1 and A2). Then the UTS and YS are decreased with increasing Al up to 15 (specimen A3 and A4). The UTS and YS of A1 are remarkably increased by AlTiB up to 15 wt%, and are improved19.5 % due to the addition of AlTiB (specimen B1, B2, B3 and B4). In addition, the UTS and YS values of minimum Al containing specimens were improved by 29.2 % due to the addition of 15 wt% AlTiB. The presence of brittle β-Mg17Al12 phase detrimentally influences the mechanical properties of Mg–Al alloys (Chen, T.J., Wang, R.Q., Ma, Y. and Hao, Y. 2012:34; Ma, X., Wang, X., Li, X. and Yang, L. 2010:20; Xu, C., Lu, B., Lu, Z. and Liang, W. 2008:26; Cao, H. and Wessén, M. 2004:35). It is thought that mechanical properties of Mg ally are affected by the change of the grain size and divorced eutectic structure. The reason that the mechanical properties increased due to the addition of 15 wt% was attributed to smaller grain size, the insolubility of Al and AlTiB elements and the homogeneously distributed eutectic areas.

It is known that, the β-Mg17Al12 phase is incompatible with the magnesium matrix, which results in an incoherent and fragile Mg/Mg17Al12 interface (Cao, H. and Wessén, M. 2004:35). The incoherence of the Mg/Mg17Al12 interface of A1 was decreased due to the network of brittle β-Mg17Al12 phase in the A1 destroys with addition of alloying elements. Hence, the elongation at fracture increment can be attributed to coarse grain size and divorced eutectic morphology. In another view of the Table 2, the UTS, YS and elongation at fracture of the alloys with AlTiB are higher than those of the Al alloys. In this study, Ti-B containing alloys include globular β-Mg17Al12 phase in the grain

boundaries, which can cause less stress concentration than Al containing alloys. Therefore, the UTS, YS and elongation at fracture of the alloys containing Ti-B was higher than those of the Al containing alloys.

Table 2. Changes of mechanical properties of MgZnSn alloy by addition Al and AlTiB

Alloy Number	Hardness, HV	UTS, MPa	YS, MPa	Elongation, %
A1	49,68	158,8	92	6
A2	57,78	174,6	102	5.2
A3	63,3	165,1	96	3.2
A4	79,1	168,2	98	2.4
B1	74,8	187	110	3.2
B2	79,3	190,4	118	4.1
B3	105	215	123	5.3
B4	119,3	223,5	130	5.8
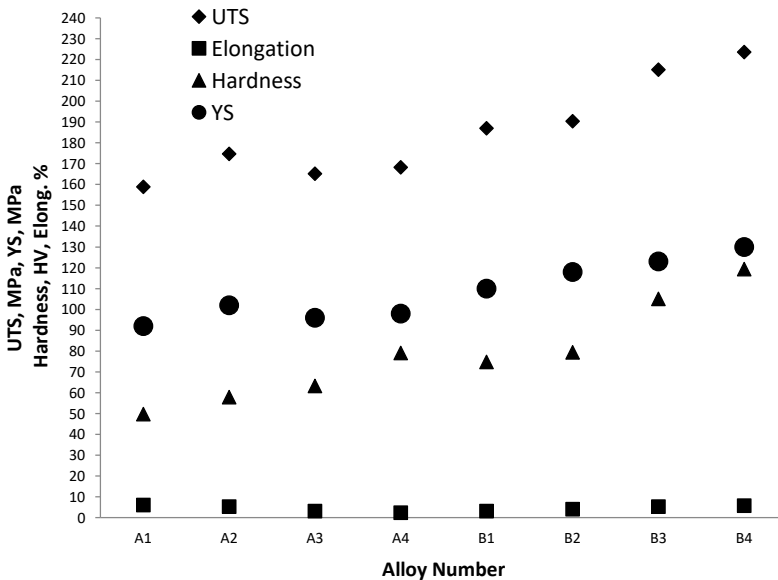
Fig 6. Mechanical properties of MgZnSn alloys

Examination of fracture surface of tensile specimens via SEM manifests the fracture behavior of the alloys, which is shown in Fig. 7. The alloy with Al and AlTiB exhibited different surface morphology compared to the base alloy A1. While it was seen the large, wide fracture areas on the

A1 (Fig. 7.a-d), some rod like morphology and small, narrow fracture areas were observed in Fig. 7(e-h).
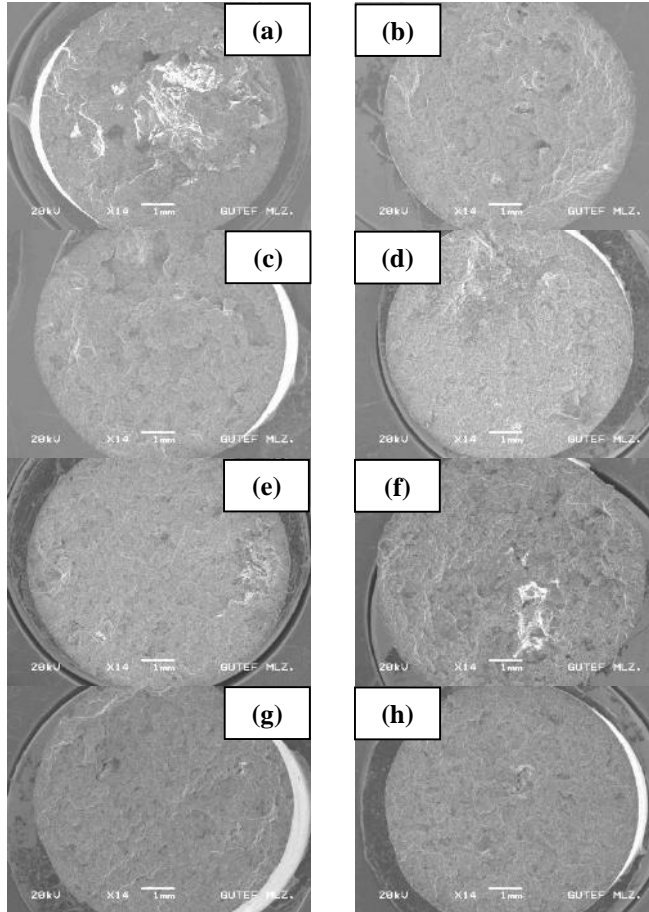
Fig. 7. SEM fractographs showing the morphology of fractured surfaces: (a) A1, (b) A2, (c) A3, (d) A4, (e) B1, (f) B2, (g) B3 and (h) B4 alloy.

4. CONCLUSIONS

In this study were obtained the following results.

The addition of Al and AlTiB alloying elements has a pronounced grain refining effect of MgZnSn alloy. The microstructure of MgZnSn alloying with Al generally consists of α-Mg and β-Mg$_{17}$Al$_{12}$ phases. The addition of AlTiB master alloy does not result in the formation of other new phases.

Metallographic studies showed that the addition of Al and AlTiB elements changed the microstructure of Mg alloy and resulted in a partially divorced eutectic. The addition of alloying elements did not result in the formation of Al containing any new phase, but AlTiB produced new phase (AlTi, AlB ect.).

The addition of AlTiB master alloy refines the grain of MgZnSn alloys to some extent. The average grain size is about 185 μm for the unrefined MgZnSn alloy and it decreases gradually with increasing AlTiB addition. A minimum of 55 μm for the grain size can be obtained at an optimum addition level (15% AlTiB). The grain size increases with further addition of AlTiB. Microstructures of MgZnSn alloys with Al5Ti1B addition are refined firstly and then coarsened with the increase of holding time. This reveals that the refinement efficiency of AlTiB fades increasingly after it is up to the optimum. TiB_2, with high melting point and hexagonal close-packed structure, is presumed to serve as the heterogeneous nuclei of α-Mg. The grain refinement of α-Mg mainly results from the existence of a large number of heterogeneous nucleation.

The hardness value of the alloys increased with both alloying elements. AlTiB addition was much more effective than Al on the hardness.

Al and AlTiB addition increased the UTS value of the alloys; the latter was much more effective than the former.

ACKNOWLEDGEMENT

REFERENCES

1) Carlson, B.E. (1997). Influence of processing variables and aluminum content on the microstructure and mechanical properties of Mg-Al Alloys. PhD Thesis, Materials Science and Engineering, University of Michigan.

2) Cao, H. and Wessén, M. (2004:35A). Effect of Microstructure on Mechanical Properties of As-Cast Mg-Al Alloys. Metallurgical and Materials Transactions A, 35A, 309—319.

3) Cao, P., Qian, M. and StJohn, D.H. (2004:51). Effect of iron on grain refinement of high-purity Mg–Al alloys. Scripta Materialia, 51, 125–129.

4) Zhang, Z. R., and Tremblay, D. D. (2004: 385). Microstructure and mechanical properties of ZA104 (0.3–0.6Ca) die-casting magnesium alloys. Materials Science and Engineering A 385, 286–291.

5) Yang, M. and Pan, F. (2010:31). Effects of Sn addition on as-cast microstructure, mechanical properties and casting fluidity of ZA84 magnesium alloy. Materials and Design, 31, 68–75.

6) Liang, M. X., Xiang, W., Lin, L. X. and Lei, Y. (2010:20). Effect of Al5Ti1B master alloy on microstructures and properties of AZ61 alloys. Trans. Nonferrous Met. Soc.China 20, 397–401.

7) Dobrzański, L.A., Tański, T. and Čížek, L. and Domagała J. (2008:31). Mechanical properties and wear resistance of magnesium casting alloys. Journal of Achievements in Materials and Manufacturing Engineering, 31 (1), 83-90.

8) Kurnaz, S.C., Sevik, H., Açıkgöz, S. and Özel, A. (2011:509). Influence of titanium and chromium addition on the microstructure and mechanical properties of squeeze cast Mg–6Al alloy", Journal of Alloys and Compounds. 509, 3190–3196.

9) Rzychoń, T., Kiełbus, A. and Lityńska-Dobrzyńska, L. (2013:83). Microstructure, microstructural stability and mechanical properties of sand-cast Mg–4Al–4RE alloy. Materials Characterization 83, 21–34.

10) Candan , S., Unal , M., Koc, E., Turen, Y. and Candan, E. (2010:509). Effects of titanium addition on mechanical and corrosion behaviours of AZ91 magnesium alloy. Journal of Alloys and Compounds, 509 (5), 1958-1963.

11) Srinivasan, J. Swaminathan, M.K. Gunjan, U.T. Pillai, S. and Pai, B.C. (2010:527). Effect of intermetallic phases on the creep behavior of AZ91 magnesium alloy. Mater. Sci.Eng. A 527, 1395–1403.

12) Kim, B.H., Lee, S.W., Park, Y.H. and Park, I.M. (2010:493). The microstructure, tensile properties, and creep behavior of AZ91,

AS52 and TAS652 alloy", J. Alloys Compd. 493, (2010), pp.502–506.

13) Suresh, M., Srinivasan, A., Ravi, K.R., Pillai, U.T.S. and B.C. Pai. (2009:525). Influence of boron addition on the grain refinement and mechanical properties of AZ91 Mg alloy. Mater. Sci. Eng. A 525, 207–210.

14) Wenwen, D., Yangshan, S., Xuegang, M., Feng, X., Min, Z. and Dengyun, W. (2003:356). Microstructure and mechanical properties of Mg–Al based alloy with calcium and rare earth additions. Mater. Sci. Eng. A 356, 1–7.

15) Wu, G., Fan, Y., Gao, H., Zhai, C. and Zhu, Y.P. (2005:408). The effect of Ca and rare earth elements on the microstructure, mechanical properties and corrosion behavior of AZ91D. Mater. Sci. Eng. A 408, 255–263.

16) Zhou, W., Aung, N.N. and Sun, Y. (2009:51). Effect of antimony, bismuth and calcium addition on corrosion and electrochemical behaviour of AZ91 magnesium alloy. Corros. Sci. 51, 403–408.

17) Guangyin, Y., Yangshan, S. and Wenjiang, D. (2001:308). Effects of Bismuth And Antimony Additions on the Microstructure And Mechanical Properties Of AZ91 Magnesium Alloy. Mater. Sci. Eng. A 308, 38–44.

18) Wang, F., Wang, Y., Mao, P., Lu, B. and Guo, Q. (2010:20). Effects of combined addition of Y and Ca on Microstructure and Mechanical Properties of Die Casting AZ91 Alloy. Trans. Nonferrous Met. Soc. 20, 311–317.

19) Kim, B.H., Lee, S.W., Park, Y.H., Park J. I.M. (2010:493). The Microstructure, Tensile Properties, And Creep Behavior of AZ91, AS52 and TAS652 alloy. Alloys Compd. 493, 502–506.

20) Y. Wang, X. Zeng and W. Ding, "Effect of Al–4Ti–5B Master Alloy On The Grain Refinement of AZ31 Magnesium Alloy", Scripta Materialia 54, (2006), pp.269–273.

21) Chen, T.J., Wang, R.Q., Ma, Y. and Hao, Y. (2012:34). Grain refinement of AZ91D magnesium alloy by Al-Ti-B master alloy and its effect on mechanical properties. Materials & Design, 34, 637-648.

22) Ma, X., Wang, X., Li, X. and Yang, L. (2010:20). Effect of Al5Ti1B master alloy on microstructures and properties of AZ61 alloys. Trans. Nonferrous Met. Soc.China 20, 397−401.

23) Xu, C., Lu, B., Lu, Z. and Liang, W. (2008:26). Grain refinement of AZ31 Magnesium alloy by Al-Ti-C-Y Master Alloy. Journal of Rare Earths, 26 (4), 604-608.

24) Cao, H. and Wessén, M. (2004:35). Effect of microstructure on mechanical properties of as-cast Mg-Al alloys", Metallurgical and Materials Transactions A, 35 (1), 309-319.

ADVANCED OXIDATION PROCESS TO DIFFERENT INDUSTRIAL WASTEWATERS: SONOFENTON

Şefika Kaya[1] & Yeliz Aşçı[2]

[1](PhD) Eskisehir Osmangazi University, email: sefikakaya@ogu.edu.tr
iD ORCID *0000-0001-8277-4365*

[2](Prof.PhD) Eskisehir Osmangazi University, email: yelizbal26@gmail.com
iD ORCID *0000-0001-5618-058X*

1. INTRODUCTION

In recent years, as industrialization has increased over time, the negative effects of increased production on the environment have become threatening to a clean environment. The inadequacy of traditional treatment methods in bringing the contaminants in wastewater to discharge standards, and the increasing costs with the removal of industrial wastewater show that the industries need advanced treatment technologies.

Advanced oxidation processes using Fenton's reagents generate hydroxyl radicals and destroy organic pollutants by converting them into harmless compounds such as CO_2, water and inorganic salts. The advantages of Fenton reagents are high efficiency, cheapness, usability at ambient temperature and pressure, non-toxicity, and ability to decompose different organic compounds (Villegas-Guzman et al., 2017; Nidheesh & Rajan, 2016). The classical Fenton process has several disadvantages such as large amount of sludge production and catalyst deactivation with iron complexing agents. In recent years advanced oxidation processes such as heterogeneous Fenton, photoFenton, sonoFenton, ozonation have been developed to overcome these problems (Shokoofehpoor et al., 2018).

Sound waves with a high frequency that the human ear cannot hear is called ultrasound. Ultrases is an acoustic wave in a solid, liquid or gas environment. Ultrasound is capable of generating high radicals in both low (20 kHz) and high frequency (>200 kHz) ranges (Dogu et al, 2017). In ultrasound waves, energy is transmitted by the vibration of the surrounding molecules, where the waves begin to spread, and operates according to the cavitation principle. Cavitation is an event that occurs in the liquid at very short intervals, characterized by growth and collapse of microbubbles or creating a space (Nunes et al., 2014). The heat from the cavity explosion

converts water into highly reactive hydrogen atoms and hydroxyl radicals ($\cdot$ OH). In the rapid cooling phase, hydroxyl radicals and hydrogen atoms come together to form hydrogen peroxide and molecular hydrogen, respectively. Thus, organic compounds in the environment are oxidized or reduced depending on the reactivity (Sivagami et al., 2019; Yang et al., 2014).

In the sonoFenton process, more hydroxyl radicals are formed because of Fenton reagents are used together with ultrasound (Al-Bsoul et al., 2020; Malakootian & Asadzadeh, 2020; Ammar, 2016).

$$Fe(II) + H_2O_2 \longrightarrow Fe(III) + \cdot OH + OH^- \quad (1)$$

$$H_2O_2 + US \longrightarrow 2\cdot OH \quad (2)$$

$$H_2O + US \longrightarrow \cdot H + \cdot OH \quad (3)$$

$$O_2 + US \longrightarrow 2\cdot O \quad (4)$$

$$H_2O + \cdot O \longrightarrow 2\cdot OH \quad (5)$$
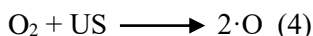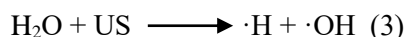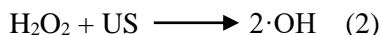
Textile industry produces large amounts of intense colored wastewater with high chemical oxygen demand, containing organic pollutants. The dyestuffs used are difficult to biodegrade, toxic and carcinogenic due to their complex chemical structure in water. Therefore, discharging textile industry wastewater procreates an significant environmental problem (Shahmoradi et al., 2019). In the production of sunflower oil, the waste water from the refining section contains a significant amount of oil, soap and NaOH. The first effect of this type of wastewater on receiving environments is that the water's contact with air is cut off and the amount of oxygen in the water decreases. Therefore, it is very important to treatment these waters (Saatci et al., 2002).

In this study, COD removal eficiencies from textile industry wastewater and sunflower oil industry wastewater were investigated by sonoFenton process. The parameters such as iron ion concentration, hydrogen peroxide concentration and reaction time were investigated and optimum experimental conditions were determined.

2. MATERIALS AND METHODS
2.1. Materials

Experimental studies were carried out with sunflower oil industry and textile industry wastewater. The sunflower oil industry wastewater was supplied from an oil production factory in Eskişehir. This wastewater is the exit water sent to the treatment unit as wastewater after neutralization process in production. Textile industry wastewater was provided from the reactive dyeing process water of an factory in Bursa. The characterization of industrial wastewaters were represented in Table 1. Iron(II) sulphate

heptahydrate (FeSO$_4$.7H$_2$O) was obtained from Merck. Hydrogen peroxide (30% w/w) was purchased by Sigma-Aldrich.

Table 1: Characterization of industrial wastewaters.

	Sunflower oil industry wastewater	**Textile industry wastewater**
pH	9.5	9
COD, mg/L	7100	2535

2.2. SonoFenton process

Sonics VCX 750 brand ultrasonic homogenizer was used in sonoFenton process experiments. Ultrasonic homogenizer has 20 kHz and 750 W operating characteristics. Firstly, the pH of the wastewater sample was adjusted in experimental studies. Then, Fe(II) and H$_2$O$_2$ solutions were added to the sample. The device was started by dipping the 13 mm probe of the device into the sample to a depth of approximately 4 cm. At the end of the experiment, the clear part of the sample was taken and necessary measurements were made.

Figure 1: SONICS VCX 750 ultrasonic homogenizer and 13 mm probe.

2.3. Analysis

In the COD analysis, Hach Lange LCK 514 brand 13 mm diameter COD test kits suitable for spectrophotometer device were used. 2 ml sample was put into the kits and kept in Hach Lange LT 200 brand thermoreactor at 148ºC for 2 hours. Then, the COD removal efficiency was calculated by making measurements in the spectrophotometer.

3. RESULTS AND DISCUSSIONS
3.1. Effect of the Fe(II) concentration

Since iron ions enable the generation of hydroxyl radicals by catalyzing the hydrogen peroxide, it is an important parameter in oxidation processes. Experimental studies were carried out at 50, 100, 150, 200, 250 and 300 ppm Fe(II) concentrations to examine the effect of iron ion on COD removal efficiency. Other parameters were kept constant as the pH 2, H_2O_2 concentration 200 ppm and reaction time 120 minutes. The experimental results were reported in Figure 2.
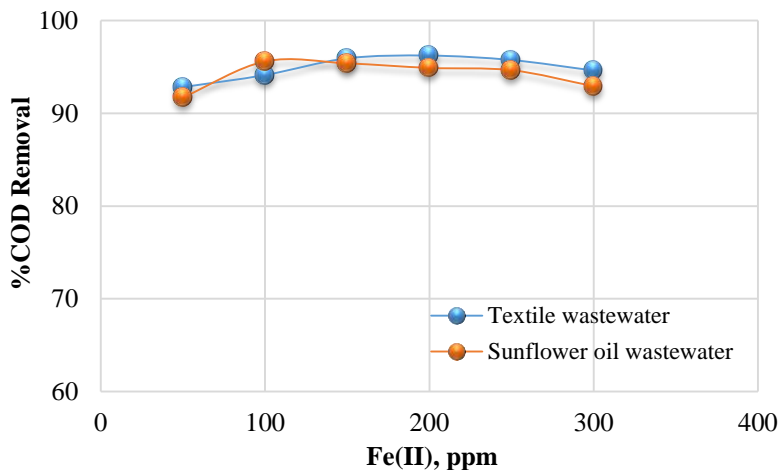
Figure 2: Effect of the Fe(II) concentration on sonoFenton process (pH=2, H_2O_2=200 ppm, reaction time 120 minutes).

When Figure 2 was examined, it was seen that COD removal efficiencies increased with increasing iron ion concentration. The COD removal efficiency from textile industry wastewater reached 96.2% at 200 ppm Fe(II) concentration. In the sunflower oil industry wastewater, 95.6% COD removal was achieved at 100 ppm Fe (II) concentration. The optimum iron ion concentrations were determined as 200 ppm for textile industry wastewater and 100 ppm for sunflower oil industry wastewater. Since there is not enough iron ions to produce hydroxyl radicals by catalyzing hydrogen peroxide in the environment at low concentrations of iron ions, less ·OH radicals are produced. In this case, the small amount of ·OH radicals produced does not react effectively with organic pollutants in the wastewater (Hashemi & Sagharlo,2020; Mehrdad et al., 2017). Although high concentrations of iron ions initially increase COD removal, it later creates a scavenging effect on the ·OH radical (Xu & Wang, 2011).

$$Fe(II) + H_2O_2 + H^+ \longrightarrow Fe(III) + \cdot OH + H_2O \quad (6)$$

$$Fe(II) + \cdot OH \longrightarrow Fe(III) + OH^- \quad (7)$$
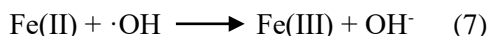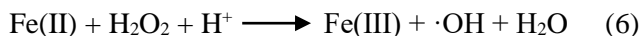
3.2. Effect of the H_2O_2 concentration

In order to determine the optimum H_2O_2 concentration, different concentrations of H_2O_2 solutions (50, 100, 150, 200, 250 and 300 ppm) were prepared and experiments were conducted. The other parameters as pH, iron ion concentration and reaction time were kept constant and the results were indicated in Figure 3.
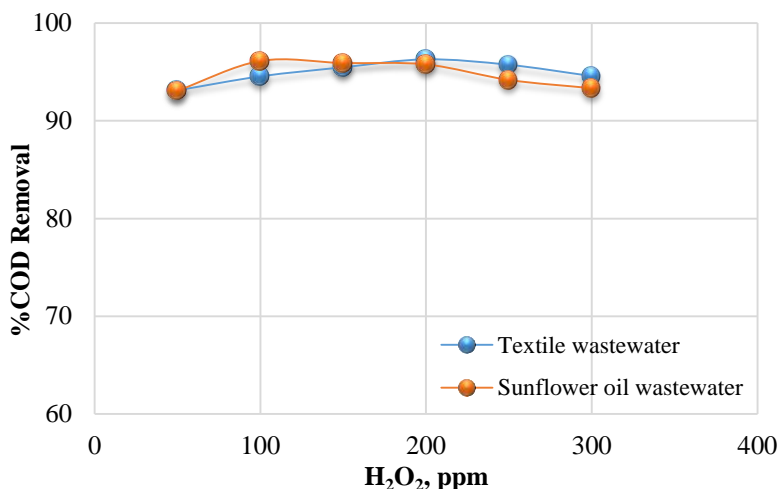
Figure 3: Effect of the H_2O_2 concentration on sonoFenton process (pH=2, Fe(II)=200 ppm for textile wastewater, Fe(II)=100 ppm for sunflower oil wastewater, reaction time 120 minutes).

Another important parameter affecting oxidation processes is the hydrogen peroxide concentration. Hydrogen peroxide reacts with iron ions to produce hydroxyl radicals with high oxidation potential. Increasing the hydrogen peroxide concentration increases hydroxyl radical generation and consequently increases the removal efficiency (Ahmadzadeh & Dolatabadi, 2018; Wang et al., 2010). However, at high hydrogen peroxide concentrations, hydrogen peroxide reacts with hydroxyl radicals and the hydroperoxyl radical ($H_2O\cdot$) is formed. The hydroperoxyl radical has a lower reaction rate and oxidation potential than the hydroxyl radical (Verma & Haritash, 2019; Malakootian et al., 2019).

$$H_2O_2 + \cdot OH \longrightarrow H_2O + H_2O\cdot \quad (8)$$

According to Figure 3, COD removal efficiencies increased with increasing hydrogen peroxide concentration for both wastewater. The maximum COD removals were attained at 200 ppm hydrogen peroxide concentration for textile industry wastewater and 100 ppm hydrogen peroxide concentration for sunflower oil industry wastewater.

3.3. Effect of the reaction time

In order to determine the effect of reaction time on COD removal, experimental studies were performed at different reaction times ranging from 5-240 minutes (constant pH, hydrogen peroxide and iron ion concentration).
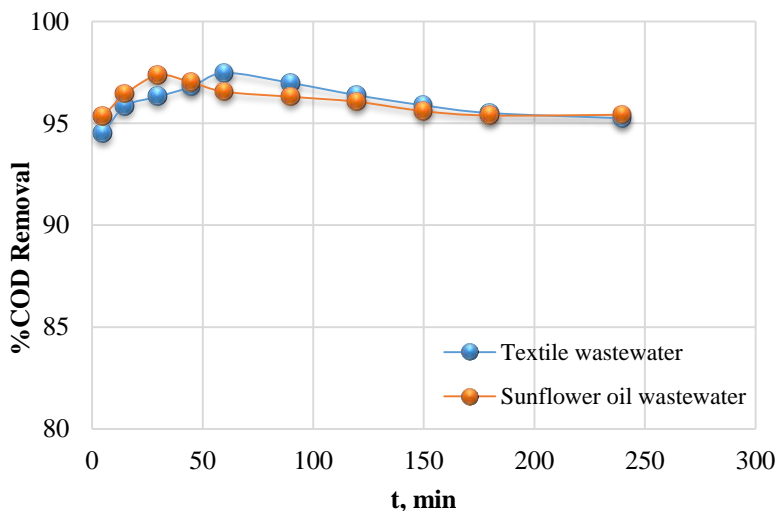
Figure 4: Effect of the reaction time on sonoFenton process (pH=2, Fe(II)=200 ppm and H_2O_2=200 ppm for textile wastewater, Fe(II)=100 ppm and H_2O_2=100 ppm for sunflower oil wastewater).

As shown in Figure 4, the COD removal efficiency from sunflower oil industry wastewater in the sonoFenton process increased in the first 30 minutes and then remained constant by decreasing. The maximum COD removal efficiency was reached in the 30th minute of the reaction as 97.4%. The efficiency of COD removal from textile industry wastewater has increased up to 60th minutes with increasing reaction time. After this the COD removal efficiency was began to decrease and remained constant. The optimum reaction time was determined as 60 minutes, when 97.5% COD removal was carried out.

In sonoFenton process, the presence of both iron ions and sound waves in the reaction medium enables more hydroxyl radical generation. Therefore, high COD removal efficiencies are obtained at low reaction times (Gharaee et al., 2019). Shokri (2018), Chakma et al. (2015) and Zhong et al. (2011) reported the optimum reaction time as 60 minutes in their sonoFenton study. In similar studies, Lim et al. (2017) and Saeed et al. (2015) presented the optimum reaction time as 30 minutes.

4. CONCLUSION

In this study, the treatment of two different industrial wastewater with different COD values were investigated. SonoFenton process studies were carried out with textile industry wastewater and sunflower oil industry wastewater. The COD removal efficiencies from wastewaters were investigated and optimum experimental conditions (such as iron ion concentration, hydrogen peroxide concentration and reaction time) were determined. Under optimum experimental conditions (iron ion concentration 200 ppm, hydrogen peroxide concentration 200 and reaction time 60 minutes) 97.5% COD removal efficiency has been achieved for textile industry wastewater. The optimum conditions for sunflower oil industry wastewater were obtained as iron ion and hydrogen peroxide concentrations 100 ppm and reaction time 30 minutes. Under these conditions 97.4% COD removal efficiency was reached. In the sonoFenton process, Fenton reagents are used together with ultrasound. Thus, more hydroxyl radicals are produced and higher removal efficiency is acquired in a short time. As a result, using the sonoFenton method in the treatment of industrial wastewater is a highly innovative and highly efficient alternative method.

5. ACKNOWLEDGMENTS

REFERENCES

Ahmadzadeh, S. and Dolatabadi, M. (2018). Removal of acetaminophen from hospital wastewater using electro-Fenton process. Environmental Earth Sciences volume 77, 53.

Ammar, H. B. (2016). Sono-Fenton process for metronidazole degradation in aqueous solution: effect of acoustic cavitation and peroxydisulfate anion. Ultrasonics Sonochemistry, 33, 164-169.

Al-Bsoul, A., Al-Shannag, M., Tawalbeh, M., Al-Taani, A. A., Lafi, W. K., Al-Othman, A. and Alsheyab, M. (2020). Optimal conditions for olive mill wastewater treatment using ultrasound and advanced oxidation processes. Science of The Total Environment, 700, 134576.

Chakma, S., Das, L. and Moholkar, V. S. (2015). Dye decolorization with hybrid advanced oxidation processes comprising sonolysis/Fenton-like/photo-ferrioxalate systems: a mechanistic investigation. Separation and Purification Technology, 156, 596-607.

Dogu, İ., Yalcin, M., Ileri, B. and Ayyildiz, O. (2017). Sono-Electrochemical Treatment of Leather Wastewater, Çanakkale Onsekiz Mart University. Journal of Graduate School of Natural and Applied Sciences, 3(1), 1-23.

Gharaee, A., Khosravi-Nikou, M. R. and Anvaripour, B. (2019). Hydrocarbon contaminated soil remediation: A comparison between Fenton, sono-Fenton, photo-Fenton and sono-photo-Fenton processes. Journal of Industrial and Engineering Chemistry, 79, 181-193.

Hashemi, M. and Sagharlo, N. G. (2020). Optimization and evaluation of the efficiency of sono-Fenton and photo-Fenton processes in the removal of 2, 4, 6 trinitrotoluene (TNT) from aqueous solutions. Journal of Advances in Environmental Health Research, 8, 38-45.

Lim, C. H., Ang, J. J., Lau, S. and Tay, M. G. (2017). Optimization of hydroxyl radical production using electro-Fenton method for chemical oxygen demand reduction in diluted palm oil mill effluent. Water and Environment Journal, 31, 578-583.

Malakootian, M., Khatami, M., Ahmadian, M. and Asadzadeh, S. N. (2019). Biogenic silver nanoparticles/hydrogen peroxide/ozone: efficient degradation of Reactive Blue 19. BioNanoscience, 10, 1-8.

Malakootian, M. and Asadzadeh, S. N. (2020). Oxidative removal of tetracycline by sono Fenton-like oxidation process in aqueous media. Desalination and Water Treatment, 193, 302-401.

Mehrdad, A., Farkhondeh, S. and Hasaspoor, F. (2017). Kinetic study of sonocatalytic degradation of Methylene blue by sonofenton process. Journal of Applied Chemistry, 12(45), 83-90.

Nidheesh, P.V. and Rajan, R. (2016). Removal of rhodamine B from a water medium usinghydroxyl and sulphate radicals generated by iron loaded activated carbon. RSC Advances. 6, 5330-5340.

Nunes, M. A., Mello ,P. A., Bizzi, C. A., Diehl, L. O., Moreira, E. M., Souza, W. F., Emanuela, C., Gaudino, E. E, Cravotto, G. and Flores, E. M. (2014). Evaluation of nitrogen effect on ultrasound-assisted oxidative desulfurization process. Fuel Processing Technology, 126, 521-527.

Saatci, Y., Arslan, E. I., Ipek, U. and Cici, M. (2002). Reduction of Pollution Loads of Wastewater from Sunflower Seed Oil Factory. Anadolu University Journal Of Science And Technology, 3, 49-58.

Saeed, M. O., Azizli, K., Isa, M. H. and Bashir, M. J. K. (2015). Application of CCD in RSM to obtain optimize treatment of POME using Fenton oxidation process. Journal of Water Process Engineering, 8, 7-16.

Shahmoradi, B. Maleki, A. and Byrappa, K. (2015). Removal of disperse orange 25 using in situ surface-modified iron-doped TiO_2 nanoparticles. Desalination and Water Treatment, 53 (13), 3615-3622.

Shokoofehpoor, F., Chaibakhsh, N. and Gilani A. G. (2018). Optimization of sono-Fenton degradation of Acid Blue 113 using iron vanadate nanoparticles. Journal Separation Science and Technology, 54, 2943-2958.

Shokri, A. (2018). Application of Sono–photo-Fenton process for degradation of phenol derivatives in petrochemical wastewater using full factorial design of experiment. International Journal of Industrial Chemistry, 9, 295-303.

Sivagami, K., Anand, D., Divyapriya, G. and Nambi, I. (2019). Treatment of petroleum oil spill sludge using the combined ultrasound and Fenton oxidation process. Ultrasonics Sonochemistry, 51, 340-349.

Verma, M. and Haritash, A. K. (2019). Degradation of amoxicillin by Fenton and Fenton-integrated hybrid oxidation processes. Journal of Environmental Chemical Engineering, 7, 102886.

Villegas-Guzman, P., Giannakis, S., Rtimi, S., Grandjean, D., Bensimon, M., de Alencas-tro, L.F., Torres-Palma, R. and Pulgarin, C. (2017). A green solar photo-Fenton processfor the elimination of bacteria and micropollutants in municipal wastewatertreatment using

mineral iron and natural organic acids. Applied Catalysis B: Environmental.219, 538-549.

Wang, N., Zhu, L., Wang, M., Wang, D. and Tang, H. (2010). Sono-enhanced degradation of dye pollutants with the use of H_2O_2 activated by Fe_3O_4 magnetic nanoparticles as peroxidase mimetic. Ultrasonics Sonochemistry, 17, 78-83.

Xu, L. and Wang, J. A. (2011). Heterogeneous Fenton-like system with nanoparticulate zero-valent iron for removal of 4-chloro-3-methyl phenol. Journal of Hazardous Materials, 186(1), 256-64.

Yang, B., Zuo J., Tang X., Liu F., Yu X., Tang X., Jiang H. and Gan L. (2014). Effective Ultrasound Electrochemical Degradation of Methylene Blue Wastewater using A Nanocoated Elect-rode. Ultrasonic Sonochemistry, 21 (4), 1310-1317.

Zhong, X., Royer, S., Zhang, H., Huang, Q., Xiang, L., Valange, S. and Barrault, J. (2011). Mesoporous silica iron-doped as stable and efficient heterogeneous catalyst for the degradation of CI Acid Orange 7 using sono–photo-Fenton process. Separation and Purification Technology, 80, 163-171.

TEMPLATED CARBONS WITH NATURAL ZEOLITE: SYNTHESIS AND CHARACTERIZATION[*]

Emine Sıla Yiğit[1] & Fatma Tümsek[2]

[1] *Eskişehir Osmangazi Universirty, e-mail: eminesilayigit@gmail.com*
ORCID *0000-0001-6326-8379*

[2]*(Assoc. Prof. Dr.), Eskişehir Osmangazi University, e-mail: ftumsek@ogu.edu.tr*
ORCID *0000-0003-2064-6215*

INTRODUCTION

Carbon materials are used in separation processes such as water and air purification, adsorption, catalysis or energy storage. The high surface area and large pore volume of these materials and their high mechanical stability and inert properties increase their use (Chen et al., 2011). The hydrophobic nature of carbon surfaces are the most important properties for many applications (Santos et al., 2010). Porous carbon materials can be classified into three groups according to their pore diameters as those with pore size less than 2 nm microporous, those with pore size between 2-50 nm mesoporous, and those with pore size greater than 50 nm macroporous (Upare et al., 2011).

Activated carbons are the most widely used carbon materials and they are produced by various methods from carbonaceous raw materials. The pore structure of carbon material is one of the most important properties that determine its use in a specific process. Optimization of experimental parameters during the carbonization/activation steps allows the structural properties of the carbons to be designed.

However, despite great efforts and a lot of research done to control pore size and pore size distribution, the complexity of the carbon structure prevents the obtaining of carbons with a pore structure that can be precisely controlled by conventional activation processes. Recent developments in industrial technology have opened up new application areas for porous carbons and this has required carbons with a specific

---

[*] It is produced from the thesis titled "Templated Synthesis and Characterization of Porous Carbon from Natural Zeolite and Sugar".

porous structure. To meet such a requirement, many new approaches have been proposed to control the pore structure (Kyotani, 2000).

Research into the template synthesis of porous carbon materials has been ongoing since the first work of Knox et al in 1986, when they presented the concept of planned porous carbon with template synthesis. Since then, such porous carbon materials with uniform sizes of micropore, mesopore and macropore have been synthesized using a variety of inorganic templates. For this aim, a significant number of studies have recently focused on the preparation of a designed carbon material using a template material (Kyotani, 2000; Barata-Rodriques et al., 2003; Böhme et al., 2005; Sakintuna and Yürüm, 2006; Santos et al., 2010).

This method consists mainly of the following steps: (a) the impregnation of a carbon source into the template material, (b) the carbonization, and (c) the removal of the template material from the structure. When this synthesis procedure is followed, the carbon formed in the pores of the template transforms into a carbon framework, while the volume covered by the template forms the pores of the resulting carbon material. In other words, the carbon formed is the reverse copy of the template material (Xia et al., 2011). Depending on the material used as the template, carbons with different structure and pore size distribution can be prepared. Silicas, zeolites, clays and pillared clays are inorganic materials that can be used as templates (Santos et al., 2010). Polymers, sucrose, phenolic resin or furfuryl alcohol are generally used as carbon resources (Böhme et al., 2005).

Zeolites, which contain three-dimensional regular channels in their structures, are substances with molecular sieve properties used for adsorption and catalytic purposes. The carbons obtained by using zeolites as templates offer the advantage of having large surface areas and micropore volumes without the activation process required to open new accessible micropore structures (Sakintuna et al., 2004). The use of natural zeolite is important in that it is a cheap and abundant resource in our country. The use of sugar as a carbon source also offers an economical way to produce porous carbon by template synthesis, since sugar is a natural and relatively inexpensive chemical.

The aim of this work is to obtain porous carbons with a certain pore size distribution, which is particularly important in areas such as gas separation, storage and catalysis. Accordingly, it is aimed to realize the template synthesis of porous carbons using natural zeolite as inorganic template and sugar as carbon source. The synthesis of porous carbons was carried out at different sugar concentrations and different carbonization temperatures. Thus, the effects of these synthesis

parameters on the carbon product formed were revealed. Characterization of the formed carbons was carried out by scanning electron microscopy (SEM), transmission electron microscopy (TEM), X-ray diffraction (XRD), elemental analysis and nitrogen adsorption.

MATERIAL AND METHOD

A natural zeolite belonging to Balıkesir/Bigadiç region was used as a template material in the preparation of the samples. Sugar used as a carbon source is crystalline granulated sugar. For the synthesis of porous carbons, a suspension containing 10 g of zeolite and 90 mL of distilled water was prepared and mixed for 10 minutes. Then, 1 mL of concentrated H_2SO_4 and 100 grams of sugar solutions prepared with 1%, 5% and 10% sugar by mass were added into the suspensions and stirred for half an hour and kept at room temperature for 72 hours. The samples were dried in the oven at 100 °C for 24 hours and ground, and subjected to carbonization process at different temperatures (500 °C, 600 °C, 700 °C and 800 °C). Carbonization was carried out at a heating rate of 10 °C/min and under N_2 flow of 50 mL/min for 1 hour. The samples obtained were mixed with 20 mL of concentrated HF per 1g sample and kept for 24 hours. The filtered samples were washed with distilled water and dried at 100 °C for 24 hours. Identification of the porous carbons was made according to sugar percent and carbonization temperature. First number represents the sugar percentage and the second represents the carbonization temperature used in the synthesis. For example, 10-700 defines carbon obtained at 10% sugar and 700 ºC calcination temperature.

Characterization processes of the obtained porous carbons by Nitrogen (N_2) adsorption, XRD analysis, SEM and TEM imaging and elemental analysis were performed.

The surface areas, pore volumes and pore size distribution of porous carbons were determined using N_2 adsorption-desorption isotherms measured at 77 K with an automatic adsorption tool (Quantachrome, Autosorb 1C). In order to prepare the samples before analysis, the carbon samples were heated at 250 ºC for 3 hours under high vacuum. Nitrogen adsorption/desorption isotherms were determined in the 1.10^{-4}-1 relative pressure range. Surface areas were calculated according to the BET method from the isotherm data in the range of 0.05-0.2 relative pressure. Micropore volume was determined according to the t-plot method. The total volume of micro and mesopores was determined at 0.99 value of relative pressure and the mesopore volume was found by subtracting the micropore volume from the total pore volume. The pore size distributions of the samples were determined from the desorption branch of the isotherm according to the BJH method.

X-ray diffraction analysis was made by Panalytical Empyrean diffractometer with CuKα radiation at the rate of 1°/min in the range of 0°-80°.

The surface morphology was investigated by a scanning electron microscopy (SEM) (Jeol, JSM5600LV) and a transmission electron microscopy (TEM) (FEI Tecnai G2 Spirit Bio(TWIN)). Elemental analysis of carbon samples were performed by a LECO, CHNS-932 elemental analyser.

RESULTS AND DISCUSSION

Characterization of solids and understanding of surface area and porosity is achieved by obtaining the adsorption isotherm. The sequential adsorption of known nitrogen volumes on the adsorbent is allowed. In this way, point-by-point adsorption isotherms are obtained by measuring equilibrium pressures. The adsorption/desorption isotherm of nitrogen gas on the 10-700 carbon is given in Figure 1.
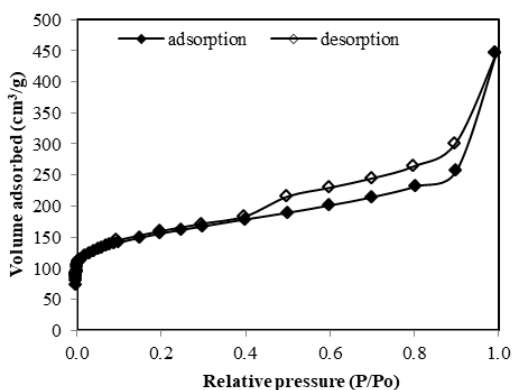
Figure 1. Adsorption/Desorption Isotherm for Carbon10-700

The isotherms obtained for all carbon samples are similar to the isotherm given in Figure 1. When the isotherms are examined, it is similar to type IV according to the IUPAC classification. These isotherms present a H3 type hysteresis loop between the adsorption and the desorption branches. Type IV isotherms are generally obtained in aggregated powders with non-rigid slit-shaped pores. Multi-layer adsorption occurs on the solid surface up to high values of relative pressure. When capillary condensation occurs, the adsorbed gas becomes liquid, and therefore desorption isotherm proceeds in a different path than the adsorption isotherm (Rouquerol et al., 1999).

The pore size distributions of the carbons determined from the desorption isotherm according to the BJH method are given in Figure 2.

According to the pore size distributions given in Figure 2, it is seen that the pores are mostly in the range of 3-5 nm (30-50 Å). This corresponds to the mesopores according to the IUPAC classification, which indicates the presence of a mesopore framework in the template carbons.

The specific surface areas and the pore properties are presented in Table 1.The surface areas of the carbons increased up to 700°C with the increase in the carbonization temperature, and the increase in the temperature to 800°C decreased the surface area value a little. With the increase in the sugar percentage, the surface area values increased. According to the results of nitrogen adsorption, carbon with the highest specific surface area of 566 m^2/g was obtained at 700°C for 10% sugar and it was determined that the increase in carbonization temperature up to 700°C significantly increased the surface area. In the literature, the surface area has been determined as 397 m^2/g for porous carbon prepared at 700°C by using natural zeolite template and furfuryl alcohol carbon source (Sakintuna and Yürüm, 2006). With the increase in the sugar percentage, the surface area values increased, as the 1% sugar ratio was increased to 5%, the surface area value increased from 141m^2/g to 552 m^2/g. As a result of the increase in the sugar ratio from 5% to 10%, the surface area increased to 566 m^2/g.
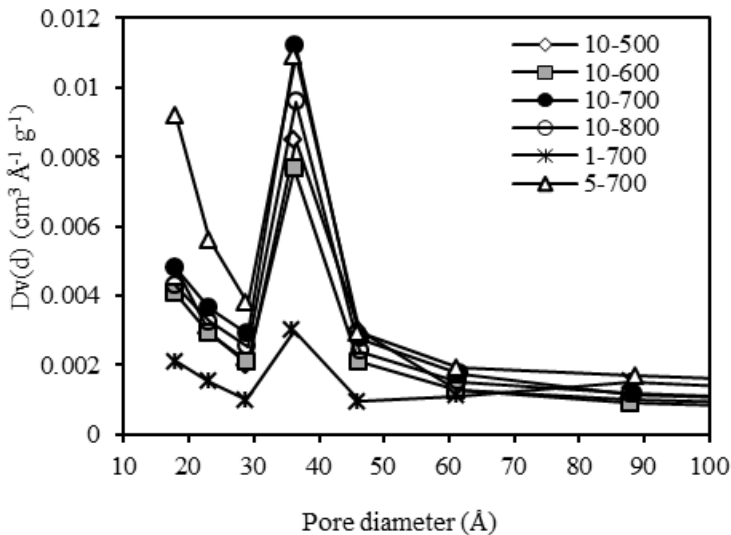

Figure 2. Pore Size Distribution of Templated Carbons

Table 1. The Specific Surface Area and Pore Properties of Templated Carbons

Carbon	S_{BET} (m^2/g)	V_{micro} (cm^3/g)	V_{meso} (cm^3/g)	V_t (cm^3/g)	D_p (nm)
10-500	352	0.1187	0.1298	0.2485	2.83
10-600	430	0.1315	0.3631	0.4946	4.61
10-700	566	0.1818	0.5108	0.6926	4.89
10-800	502	0.1496	0.4554	0.6050	4.83
1-700	141	0.0118	0.3853	0.3971	11.3
5-700	552	0.1741	0.6658	0.8399	6.09

The carbonization temperature and sugar percentage had a similar effect on the pore volumes of the samples. The pore volumes of the carbons produced at different carbonization temperatures are compared in Figure 3, and the pore volumes of the carbons produced with different sugar percentages are compared in Figure 4. While the increase in the carbonization temperature slightly increased the micropore volume, the mesopore and thus the total pore volume significantly increased. Micropore volume in carbon produced using 1% sugar is very small; almost all of the total pore volume is due to mesopores. Increasing sugar to 5% increased both micro and mesopore volume. When the sugar ratio increased to 10%, the micropore volume increased and the mesopore and total pore volume decreased. Accordingly, it can be concluded that the mesopore volume increases with the increase of the carbonization temperature, and the increase in the sugar ratio increases the micropore volume.
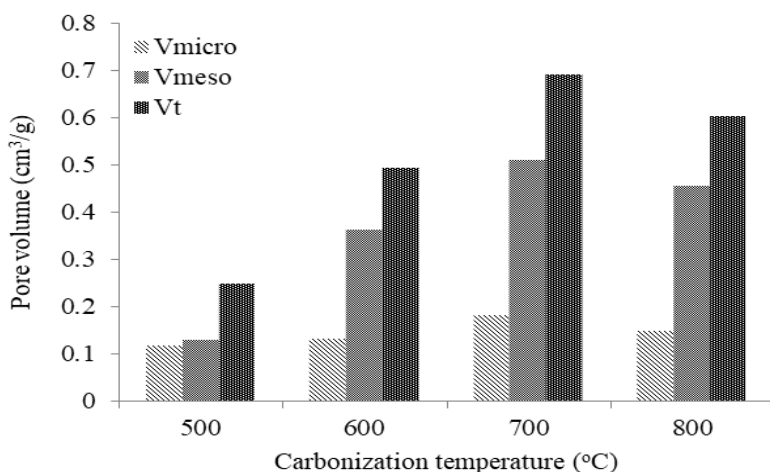
Figure 3. Comparison of Pore Volumes of Carbons at Different Carbonization Temperature
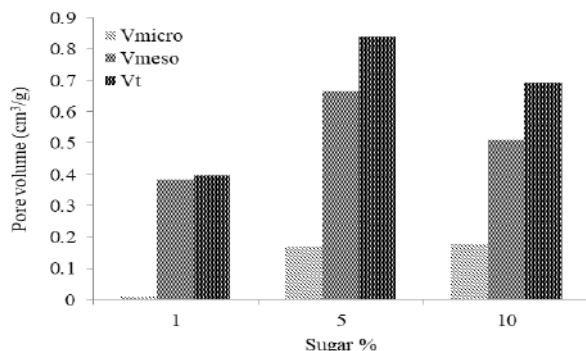
Figure 4. Comparison of Pore Volumes of Carbons at Different Sugar Ratio

XRD spectra for templated carbons are given in Figure 5. The peaks of $2\theta = 8°$, $15°$, $29°$ and $32°$ are seen in the spectra for all carbons. It has also been observed in the literature that carbons produced using different carbon sources with the zeolite template give similar XRD spectra (Barata-Rodrigues et al., 2003; Sakintuna and Yürüm, 2006). These peaks indicate that the zeolite framework is duplicated. The broad peak seen in the 20-30 range was characteristic of disordered carbon structures and represents the (002) reflection of graphite due to the stacking nature of the aromatic layers (Sakintuna and Yürüm, 2006).
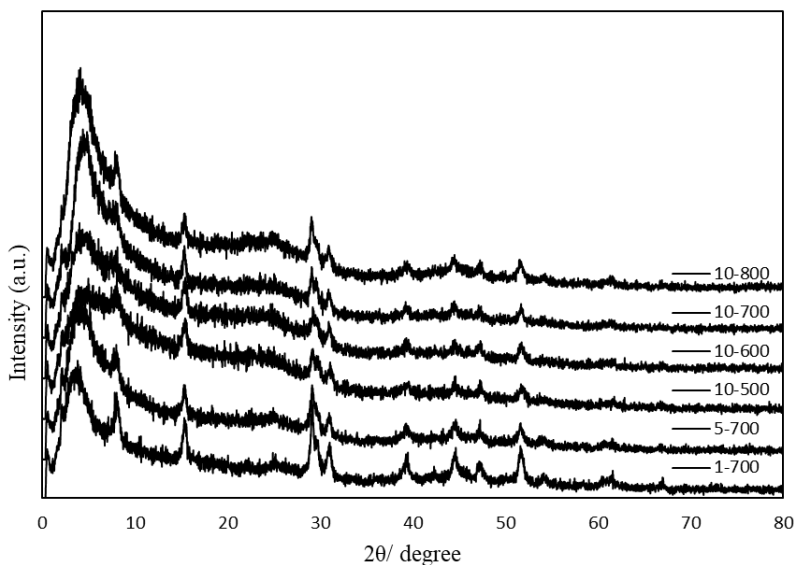
Figure 5. XRD Spectra of Templated Carbons

Surface morphology of the samples is observed by SEM imaging (Figure 6). SEM images provide information about the surface morphology and pores of carbons. When SEM images are examined, the surface morphologies of all produced carbons are similar. Structures defined as flower-like for zeolite patterned carbons in the literature were observed in SEM images (Sakintuna et al., 2004). In addition, the porous structure can be selected from the images.

TEM images of the 10-700 carbon are given in Figure 7. From the TEM image, it can be said that the pores are approximately spherical. In addition, it can be seen that there are regular, similar pore structures as well as irregular regions.
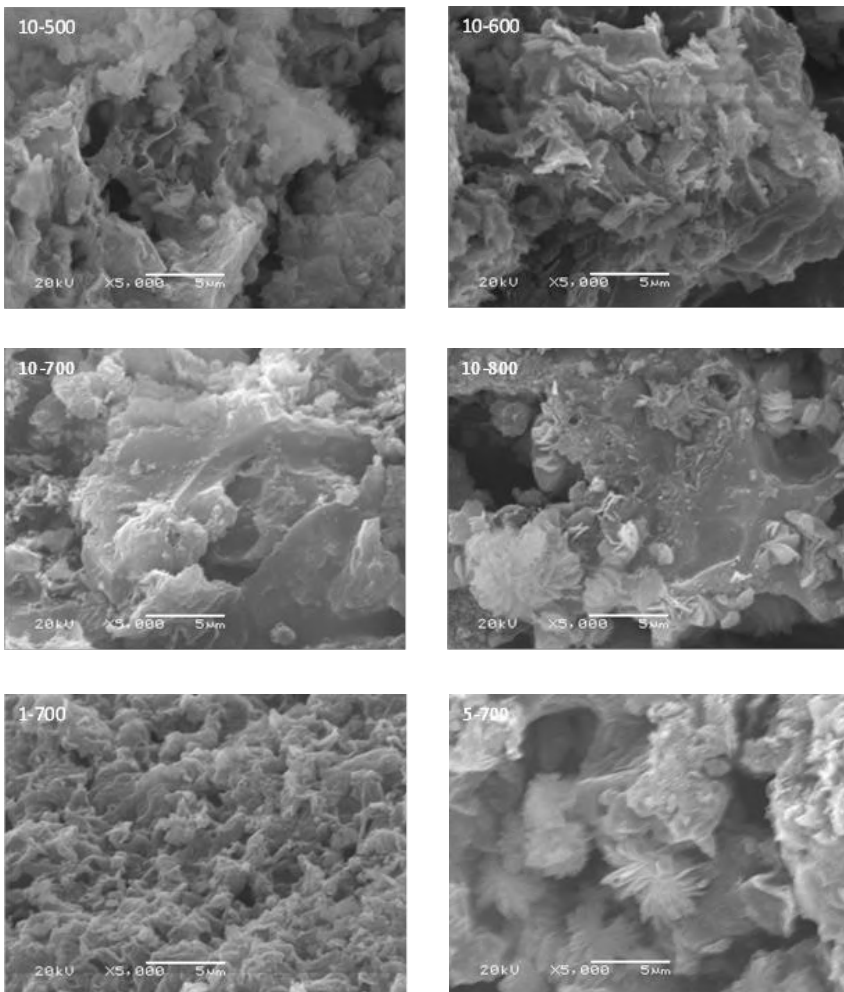
Figure 6. SEM Images of Templated Carbons
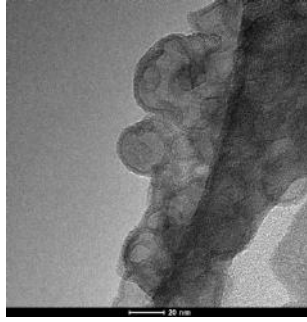
Figure 7. TEM Image of 10-700 Carbon

Elemental analysis results are given in Table 2.According to the elemental analysis result, the% C value for carbons produced using 10% sugar at different carbonization temperatures varies around 60%. It was concluded that the carbonization temperature did not significantly change the carbon percentage. In addition, with the increase in carbonization temperature, a decrease from 3% to 1% is observed in the H% value. The increase in the sugar percentage increased the carbon percentage significantly, as expected.

Table 2. Elemental Analysis of Templated Carbons

Carbon	C%	H%	O%
10-500	57,66	2,95	39,39
10-600	62,08	2,45	35,47
10-700	59,47	1,92	38,61
10-800	58,22	1,19	40,59
1-700	11,45	1,46	87,09
5-700	49,69	1,37	48,94

In this study, the preparation of template porous carbons using natural zeolite and sugar by template synthesis and the investigation of the structural and physical properties of these carbons are explained. The obtained carbons present offer large surface areas and pore volumes and can be used for a variety of applications such as adsorption, catalysis, gas separation.

ACKNOWLEDGMENTS

REFERENCES

Barata-Rodrigues, P.M., Mays, T.J., Moggridge, G.D. (2003). Structured carbon adsorbents from clay, zeolite and mesoporous aluminosilicate templates, *Carbon*, 41, 2231–2246.

Böhme, K., Einicke, W.D. and Kepel, O. (2005). Templated synthesis of mesoporous carbon from sucrose-the way from the silica pore filling to the carbon material, *Carbon* 43, 1918-1925.

Chen, L.F., Liang, H.W., Lu, Y., Cui, C.H., Yu, S.H. (2011), Synthesis of an attapulgite clay@carbon nanocomposite adsorbent by a hydrothermal carbonization process and their application in the removal of toxic metal ions from water, *Langmuir*, 27(14), 8998-9004.

Knox, J.H., Kaur, B., Millward, G. R. (1986), Structure and Performance of Porous Graphitic Carbon in Liquid-Chromatography, *J. Chromatogr*, 352, 3-25.

Kyotani, T. (2000). Control of pore structure in carbon, *Carbon*, 38, 269-286.

Rouquerol, F., Rouquerol, J. Sing, K. (1999), *Adsorption by Powders and Porous Solids*, London: Academic Press.

Sakintuna, B., Aktaş, Z., Yürüm, Y. (2004), Templated synthesis of porous carbons and flower-like carbon fluorides using natural zeolite, *Prepr. Pap. -Am. Chem. Soc., Div. Fuel Chem.*, 49(2), 696-697.

Sakintuna, B., Yürüm, Y. (2006), Preparation and characterization of mesoporous carbons using a Turkish natural zeolitic template/furfuryl alcohol system, *Microporous and Mesoporous Materials*, 93, 304-312.

Santos, C., Andrade, M., Vieira, A.L., Martins, A., Pires, J., Freire , C. and Carvalho, A.P. (2010), Templated synthesis of carbon materials mediated by porous clay heterostructures, *Carbon*, 48, 4049–4056.

Upare, D.P., Yoon, S., Lee, C.W. (2011), Nano-structured porous carbon materials for catalysis and energy storage, *Korean J. Chem. Eng*., 28(3), 731-743.

Xia, Y., Yang, Z., Mokaya, R. (2011), Templated Porous Carbon Materials: Recent Developments, Bruce, D.W., Walton, R. O'Hare D. (Eds.) in *Porous Materials* (p. 217-280), Hoboken, NJ, USA: Wiley.

MEMORY CIRCUIT ELEMENTS AND APPLICATIONS

Kamil Orman[1] & Yunus Babacan[2]

[1] *Erzincan Binali Yıldırım University, e-mail: korman@erzincan.edu.tr*
ORCID *0000-0002-7236-9988*

[2] *Erzincan Binali Yıldırım University, e-mail: ybabacan@erzincan.edu.tr*
ORCID *0000-0002-6745-0626*

INTRODUCTION

Resistors, capacitors and inductors as passive circuit elements connect the relationships between voltage-current, charge-voltage and flux-current respectively. But the connection of the flux and charge is missing until Chua's original paper [1]. Chua called the new circuit element, memristor (memory+resistor), which provides the missing relationship between flux and charge as shown in Fig.1 [1].
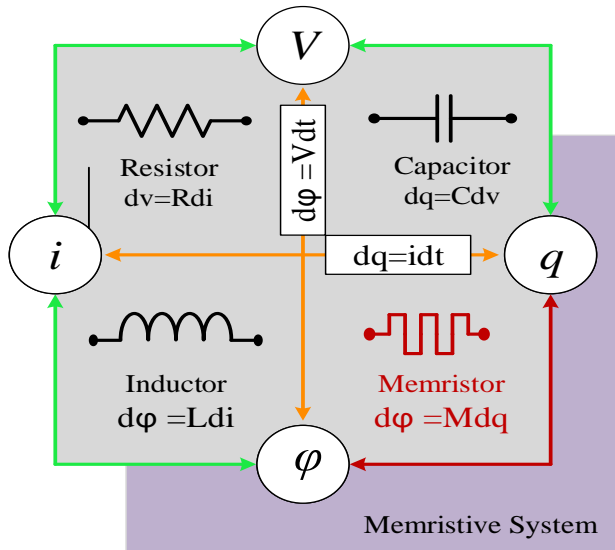
Fig. 1. The fundamental two-terminal circuit elements.

But, Chua's paper [1] didn't attract researchers' attention until 2008 [2]. Memristor did not implemented until this year because of the lack

of the advanced technology. Materials at nano-scales are suitable to realized memristive devices. Researchers interested in the effect of the memristor on the classical designed circuits. That is why emulator circuits were designed [3-18] because of the fact that physical implemented memristor did not obtained easily. The current-voltage relationship of memristor can be defined by

$$V = \left[M\left(x_1, x_2, \ldots x_n \right) \right] i \tag{1}$$

where V and i are voltage and current respectively. M is memristance (resistance of memristor), x_i's are state variables. The memristance $(R_{Memristor}(x))$ which depends on the history exhibits non-linear characteristics when applied appropriate frequency and voltage/current signals.

$$V(t) = R_{Memristor}(x) i(t) \tag{2}$$

The memristor has two main structures: doped region and undoped region. Doped region exhibits low resistance thanks to rich electrons and undoped region exhibits high resistance because of the lack of the electrons. Memristance is as follow:

$$R_{Memristor}(x) = \left[R_{ON} x + R_{OFF} \left(1 - x \right) \right], \; (x = \frac{w}{D}) \tag{3}$$

The change of the x value is

$$\frac{dx}{dt} = \frac{\mu_v R_{ON}}{D^2} i(t) \tag{4}$$

Where μ_v is electron mobility memristor, w and D denote the doped area and thickness of the memristor area, respectively and R_{ON} and R_{OFF} denote resistances for high and low dopant concentrations areas, respectively. Researcher were added a function $(f(x))$ which is called window function to take into account the nonlinear kinetics of dopants and boundary limit effects of memristor [2,4,19-20]. The equation (4) is rearranged as follows,

$$\frac{dx}{dt} = \frac{\mu_v R_{ON}}{D^2} i(t) f(x) \tag{5}$$

The first f(x) window function which is linear model was presented by HP research team [2].

$$f(x) = \frac{x(1-x)}{D} \qquad (6)$$

The HP window function is very simple but inadequate. That is why Joglekar showed the new model as below [19],

$$f(x) = 1 - (2x - 1)^{2p} \qquad (7)$$

Biolek improved the Joglekar model [4],

$$f(x) = 1 - (x - stp(-i))^{2p} \qquad (8)$$

Prodromakis presented versatile model take into account nonlinear kinetics of dopants [20],

$$F(x) = j(1 - \left[(w - 0.5)^2 + 0.75 \right]^p) \qquad (9)$$

Memristors exhibit pinched hysteresis voltage-current characteristics at low frequencies when applied sinusoidal signal and behave linear resistor at higher frequency signal because of the fact that the interior electrons are not follow higher frequency signal. The voltage-current curves with various frequency sinusoidal signals are shown in Fig.2.
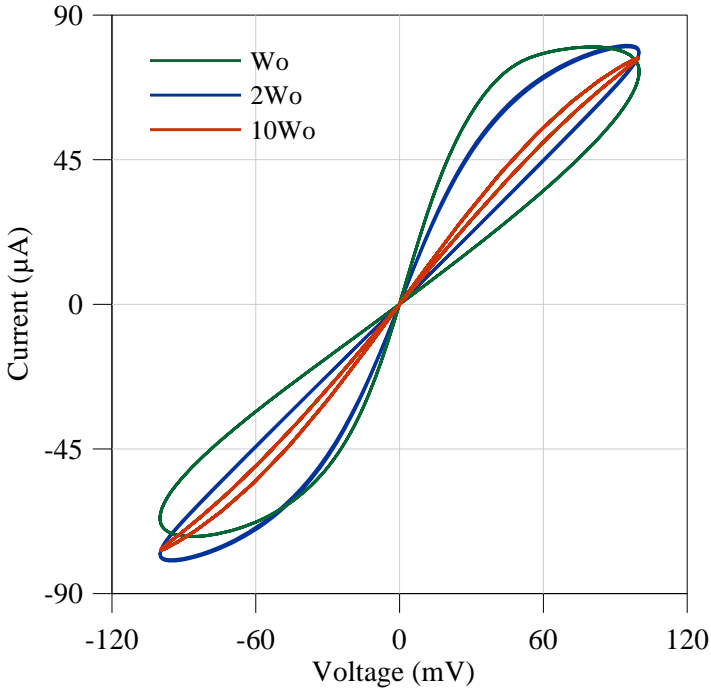
Fig. 2. The voltage-current relationship of memristor with various frequencies.

Stanley Williams mentioned how they found the missing memristor with details [21] and they fabricated the memristors as a multiple crossbar arrays. Both the scanning tunneling microscope image and crossbar structure of the memristor is as shown in Fig.3.

The memristive behavior depends on the length of the doped region. When the signal applied to the memristor, the doped region changes depend on the direction and value of the applied signal. The detailed photo is shown in Fig.3b for TiO_{2-x} memristor.

(a)   (b)
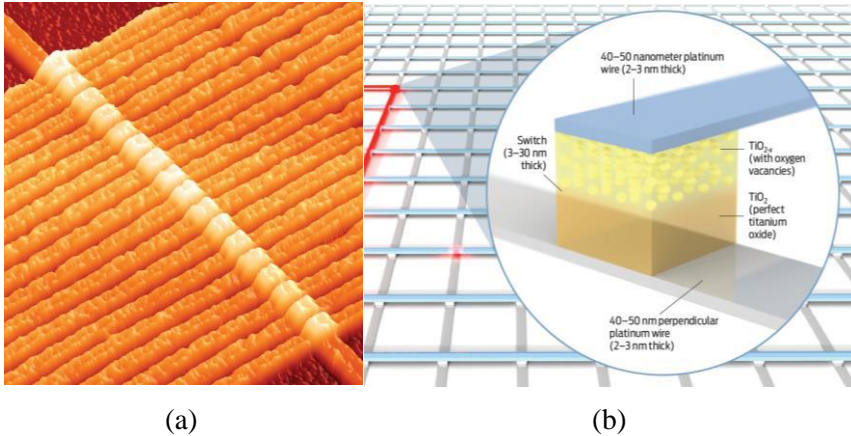
Fig. 3. a) The scanning tunneling microscope image of the memristor b) The crossbar architecture is a fully connected mesh of perpendicular wires [21].

The voltage-current curve for the first memristor which was realized using TiO_2 sandwich structure by HP research team is shown in Fig.4 [2].
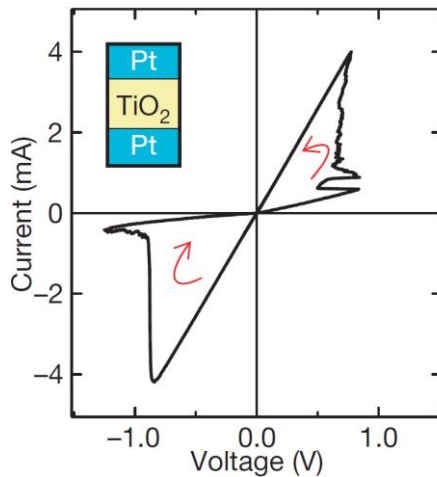
Fig. 4. The voltage-current relationship of the TiO_2 memristor [2].

MEMRISTOR and BEYOND

Di Ventra and co-workers extended the notion of memristive systems to capacitive and inductive elements whose properties depend on the state and history of the system [22]. All these new hypothetical mem-elements show pinched hysteretic loops charge-voltage for the memcapacitor, and current-flux for the meminductor. Memcapacitors and meminductors are history dependent capacitor and history dependent inductor, respectively. Many researchers study on memcapacitor and meminductor circuit elements with non-linear behavior and their circuit symbols are shown in Fig.5 [22].
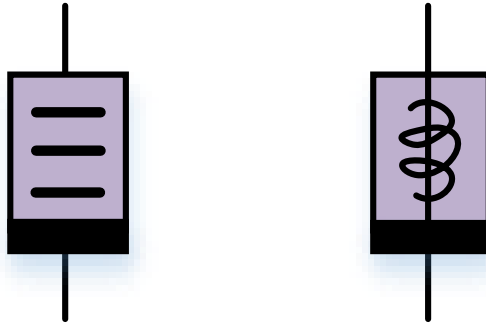
Fig. 5. Symbols of memcapacitor and meminductor [22].

Chua extended the two terminal passive circuit elements, *periodic table of circuit elements*, as shown in Fig.6 [23]. He categorized all elements as resistors, capacitors, inductors and negative resistance according to relationships between voltage and current. Resistor, capacitor and inductor are the ratio of voltage and current, the ratio of derivation of voltage and current, the ratio of voltage and the derivation of current, respectively. The details were introduced in [24]

$$V^{(\alpha)}(t) = \begin{cases} \dfrac{d^a V(t)}{dt^a}, & \text{if } \alpha = 1, 2, ...\infty \\ V(t), & \text{if } \alpha = 1, 2, ...\infty \\ \displaystyle\int_{-\infty}^{t} V(\tau)d\tau, & \text{if } \alpha = -1 \\ \displaystyle\int_{-\infty}^{t}\int_{-\infty}^{\tau\alpha}....\int_{-\infty}^{\tau 2} V(\tau_1)d\tau_1 d\tau_2 ....d\tau_\alpha, & \text{if } \alpha = -2, -3, ..., \infty \end{cases}$$

(10)

$$
i^{(\beta)}(t) = \begin{cases} \dfrac{d^{\beta}i(t)}{dt^{\beta}}, & \text{if } \beta = 1, 2, \ldots \infty \\[2mm] i(t), & \text{if } \beta = 1, 2, \ldots \infty \\[2mm] \displaystyle\int_{-\infty}^{t} i(\tau)d\tau, & \text{if } \beta = -1 \\[2mm] \displaystyle\int_{-\infty}^{t}\int_{-\infty}^{\tau\alpha}\ldots\int_{-\infty}^{\tau 2} i(\tau_1)d\tau_1 d\tau_2 \ldots d\tau_{\beta}, & \text{if } \beta = -2, -3, \ldots, \infty \end{cases}
$$

$$(11)$$

The α and β values are orders of the voltage $(V^{(\alpha)})$ and current $(I^{(\beta)})$ respectively. For example, the circuit element is a resistor when α and β values equal to zero, or the circuit element is capacitor when $\alpha = 0$ and $\beta = -1$
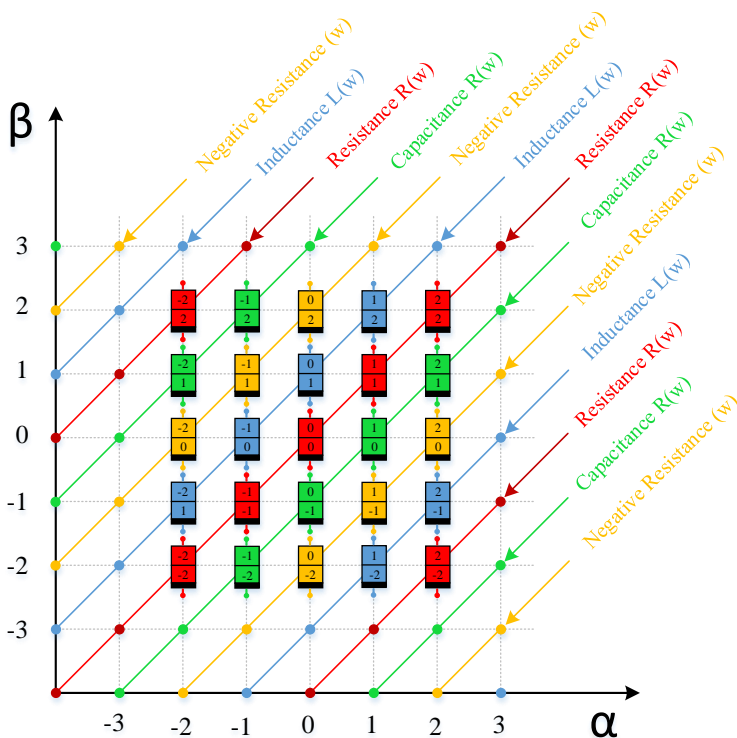
Fig. 6. The periodic table of all two-terminal circuit elements. Resistors line, capacitors line, inductors line and negative resistance line are red, green, blue and yellow respectively.

MEMRISTOR WITH SPIKE-TIMING DEPENDENT PLASTICITY

Synapses which are cleft between presynaptic and postsynaptic neuron is shown in Fig.7. and play a fundamental role in learning and memory mechanisms. Spike-Timing-Dependent Plasticity (STDP) which is a form of Hebbian learning mechanism is an important synaptic learning rule and based on relative timing between pre-spike and post-spike [25]. There are many studies about STDP learning rule both computational models [26-28] and circuit implementations [29-37].
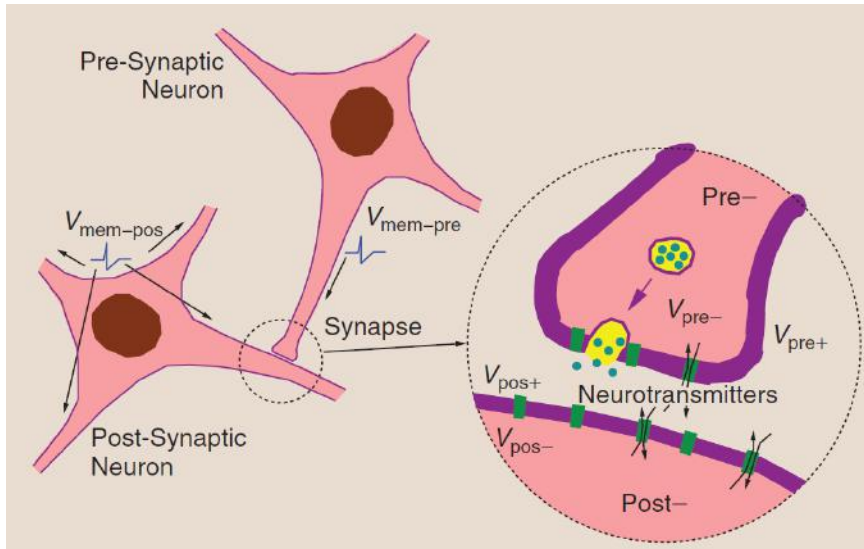
Fig. 7. Illustration of synaptic action [38].

Neurons start fire when signals reach the threshold level, and this fired signal called *spike*. The conductance of the synapse changes according to the value, frequency and direction of spikes. If the pre-spike precedes the post-spike, synapses undergo long term potentiation (LTP). The connection between neurons becomes stronger. If the post-spike precedes the pre-spike, synapses undergo long term depression (LTD), i.e., the connection between neurons becomes weaker. Namely, long term potentiation (LTP) is expressed as increase in synaptic transmission, long term depression (LTD) is expressed as decrease in synaptic transmission. The experimental data was presented by Bi and Poo as shown in Fig.8. [25,39].
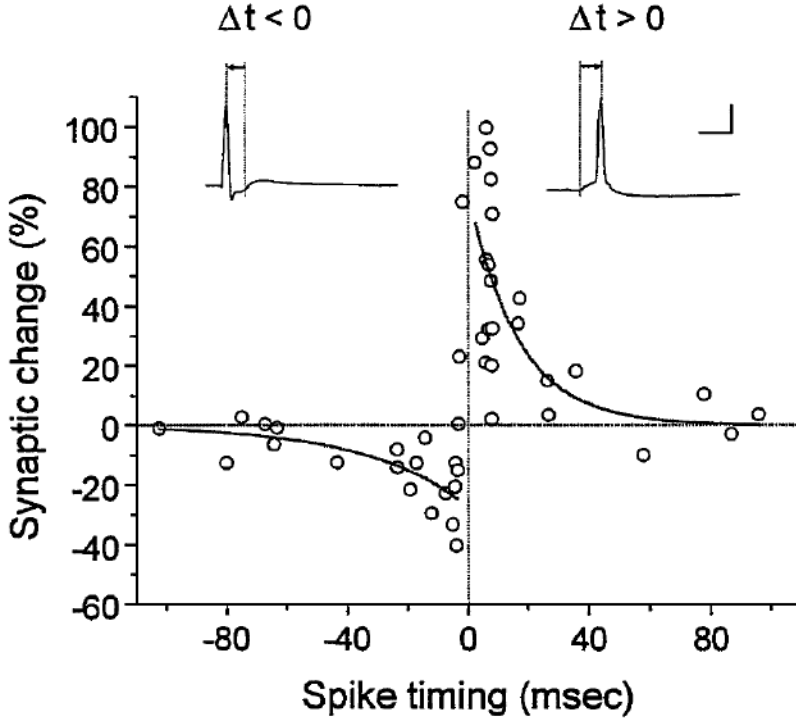
Fig. 8. Experimental STDP data of a biological synapse. If the pre-spike precedes the post-spike ($\Delta t>0$), the conductance of synapse increases. Otherwise, the conductance of synapse decreases ($\Delta t<0$) [39].

The total synaptic change induced with pairs of pre-spike and post-spike [39-40].

This rule for pair based STDP rule is given by,

$$\Delta w = \begin{cases} \Delta w^+ = A^+ e^{\left(\frac{-\Delta t}{\tau_+}\right)}, & if \ \Delta t > 0 \\ \Delta w^- = A^+ e^{\left(\frac{-\Delta t}{\tau_-}\right)}, & if \ \Delta t \leq 0 \end{cases} \tag{12}$$

Memristors are passive, history dependent, polarized and frequency dependent circuit elements. Synapses have also all these properties that is why researchers spend effort to show the connection of between synapses and memristor both experimentally and theoretically. Various circuit implementations which consist of many circuit blocks, transistors and active circuit elements exist in literature [29-37]. But only one memristor exhibit synaptic characteristics so this advantage provides to memristor new application area: Neuromorphic circuits. But proposed

memristor models were lack of the some synaptic characteristics. Li and his co-workers suggested memristor SPICE model account for STDP behavior with both volatile and non-volatile characteristics [41]. Babacan and Kacar also proposed fully floating memristor emulator which is accounting for STDP behavior as shown in Fig.9 [18].
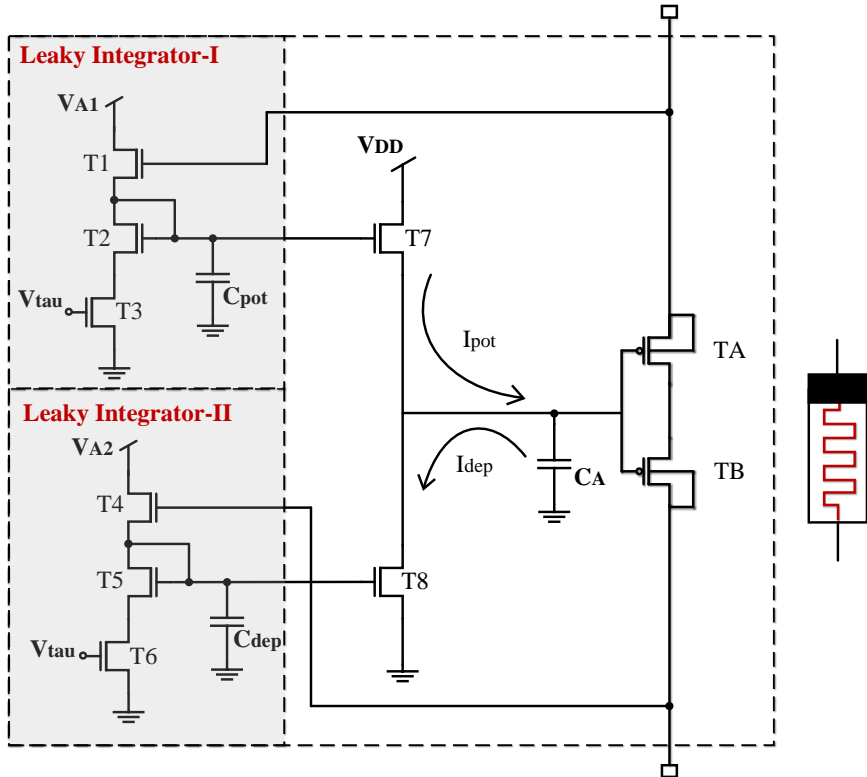
Fig. 9. Memristor emulator circuit accounting for Spike timing dependent plasticity [18].

The physical demonstration of the STDP behavior of memristor was demonstrated previously [42-44]. So memristor with STDP behavior is important to design memristor based neuromorphic circuits. This circuit exhibits both memristive characteristics which are pinched hysteresis loop, resistance change depends on the signal directions and STDP behavior as shown in Fig.10.
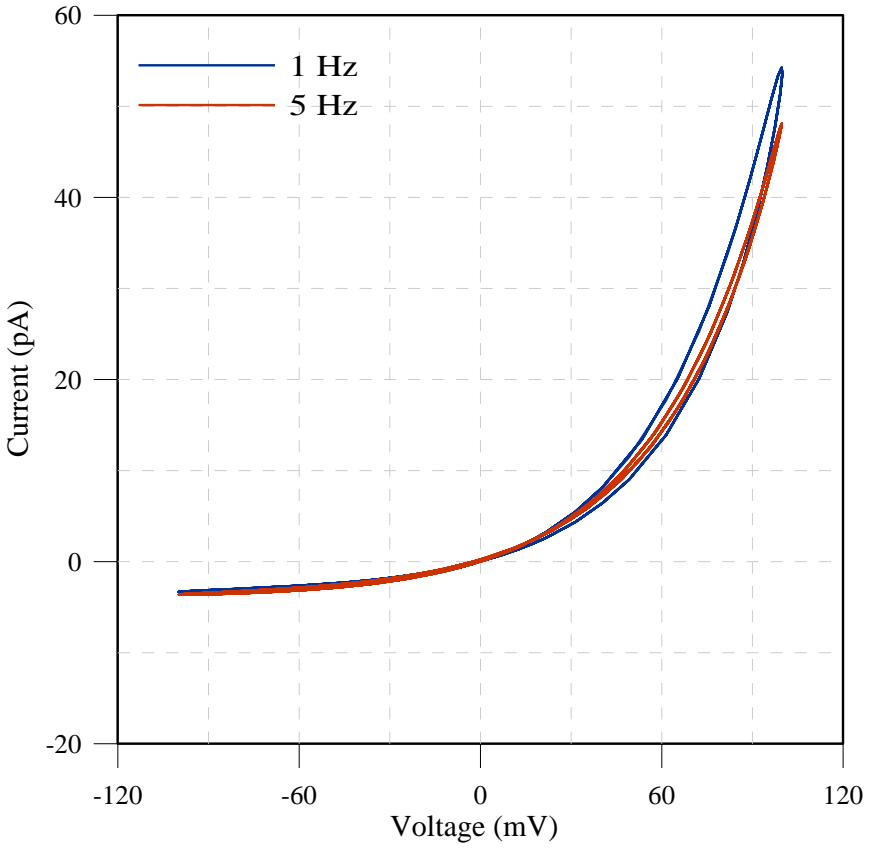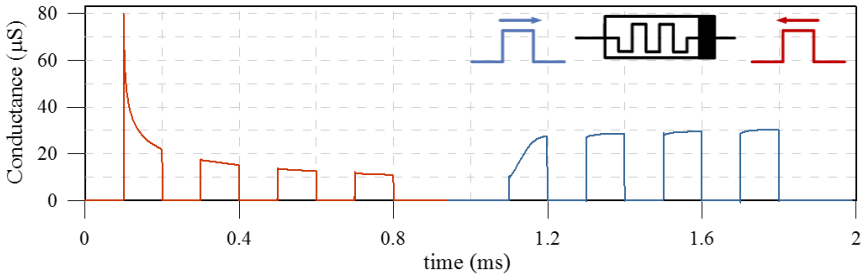
Fig. 10. a) Voltage - Current characteristics of memristor and b) Variations of the memristor conductance for each pulse along the time [18].

Spike timing dependent plasticity characteristics of the memristor emulator circuit is shown in Fig.11. Conductance of the memristor emulator circuit changes (ΔG) as a function of time difference of post-spike and pre-spike ($\Delta t = t_{post} - t_{pre}$). The STDP learning rule requires that the

changes of the synapse conductance to be a function of the time elapsed between the arrival of the pre-spike and the post-spike [15]. Both LTP and LTD mechanism are obtained from fully floating memristor emulator as shown in Fig.11.
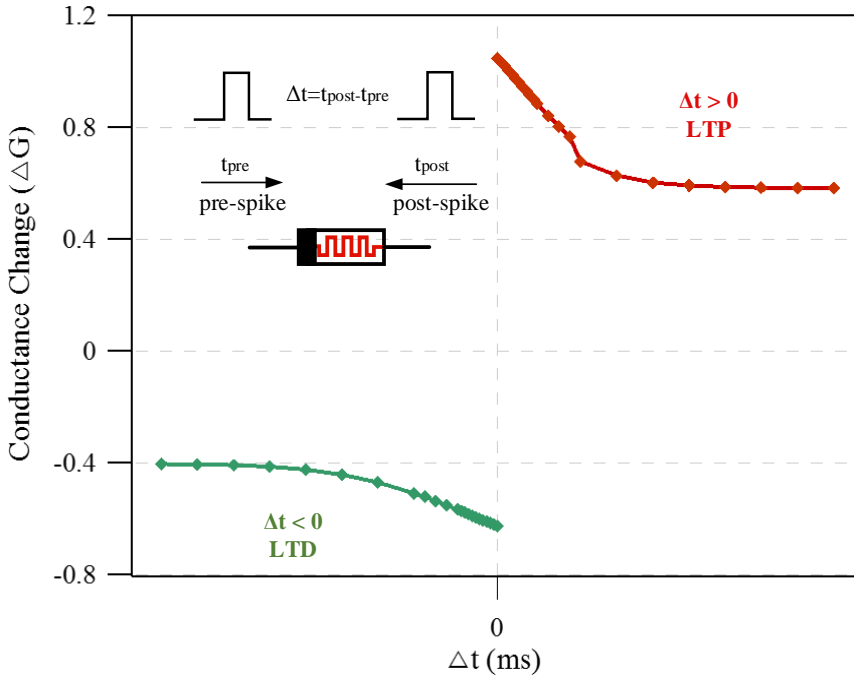
Fig.11. Variations of the memristor conductance for each pulse along the time. Blue line represents increasing of the conductance and red line represents decreasing of the conductance. The relative change is defined as $\Delta G = (G_{after} - G_{before})/G_{before}$, where G_{before} is the conductance of the memristor before the pre-spike and post-spike pair, and G_{after} is the conductance of the memristor after the pre-spike and post-spike pair [18].

ACTIVE CIRCUIT ELEMENT BASED MEMRISTORS

Since the initial fabrication of memristor [2], various SPICE based memristor models/circuits [3-18] have been presented. The emulators which have been built using active circuit elements [11-18] doesn't have mathematical details because of the fact that it is hard to analyses these type of the circuit elements. Especially, the presented emulators [3-18] perform the key properties of memristor which are pinched hysteresis loop and history dependent behavior but researchers didn't explain mathematically how these circuits behave as a memristor. From this point, pathological elements (i.e., nullators, norators, and the voltage mirror-current mirror pairs) which open up the possibility to model the active

87

devices offer potential advantages to solve the fundamental mathematical transfer function of memristor emulator circuits based on active circuit elements. Traditionally, active circuit elements are modelled with voltage/current controlled voltage/current sources. But this model technique gives rise to problems such as increased circuit complexity. Modelling and understanding the conductance mechanism of memristor emulator is already difficult and the conductance mechanism can be controlled so hard when memristor is modelled using active circuit elements. Kim and co-workers [14] presented –one of the well-known OpAmp based memristor emulator circuit as shown in Fig. 12. But mathematical analyses were not given to explain its conductance and pinched hysteresis loop characteristics.
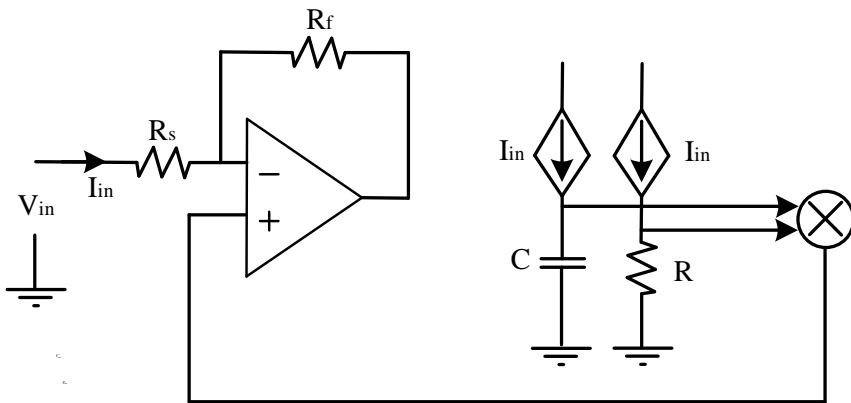
Fig. 12. Voltage controlled memristor emulator which is presented by Kim and co-workers [14].

Yener and Kuntman proposed four DDCC based memristor emulator as shown in Fig.13 and presented its chaotic circuit application [15]. Some mathematical equations were given but memristive mechanism couldn't explained with details.
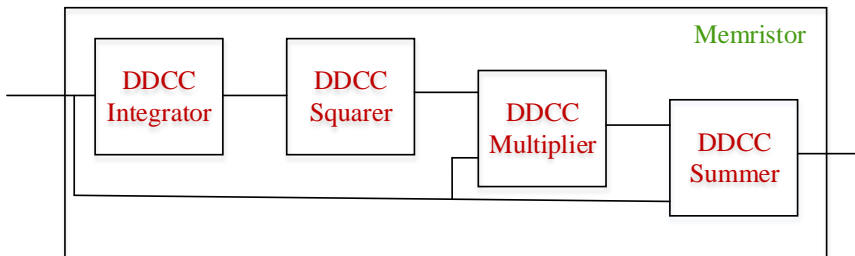
Fig.13. Block schematics of the DDCC based memristor emulator which is presented by Yener and Kuntman [15].

Another memristor emulator circuit based on the active circuit element which is the differential difference current conveyor (DDCC) was given by Yesil and co-workers as shown in Fig.14. [16]. Both conductance mechanism and pinched hysteresis behavior were not given with details in this study as well.
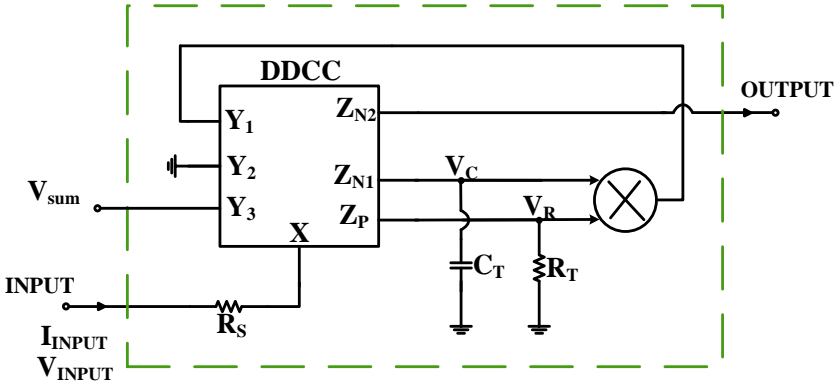
Fig.14. DDCC based memristor emulator which is presented by Yesil and co-workers [16].

Previous memristor models are lack of the very important property: fully floating structure. Babacan and Kacar suggested a novel fully floating memristor model based on OTA active circuit element as shown in Fig.15 [17]. The circuit is simpler than previous emulator circuits but detailed mathematical analyses also were not given such as previous studies.

Various memristor emulators were suggested and some of them have hard switching characteristics [13], smooth switching characteristic [14-18], and account for STDP characteristics [18]. All suggested models have two important properties: 1. All circuits based on active circuit elements, 2. Do not have detailed mathematical explanation about their conductance mechanisms. Memristors exhibit different characteristics because of the fact that they consist of different material structures. For example HP research group show titanium memristor which exhibits hard-switching behavior [2], after five years, the research group implemented vanadium oxide memristor which has threshold voltage [45]. The other research groups presented memristor with STDP behavior [42-44] but all experimental implemented emulators are lack of the clear explanations and models. If conductance mechanism of emulators can be explained clearly, more realistic models can be designed and each important property such as threshold, STDP behavior can be controlled.
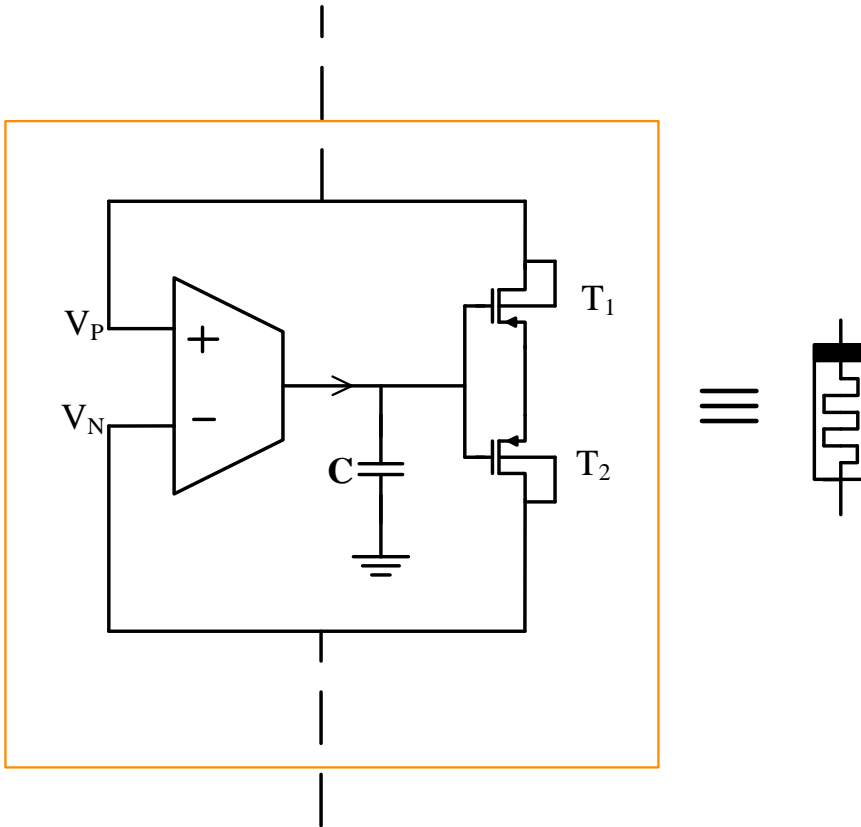
Fig.15. Fully floating memristor emulator based on OTA [17].

PATHOLOGICAL ELEMENTS and MEMELEMENTS

Pathological elements are gaining the popularity because of their capability of modelling active circuits. All proposed memelements consist of transistors and active circuit elements. We will refer some memristor emulators based on active circuit elements and transistors in this section. All models and circuits which are based on active elements lack of the detailed mathematical analyses. The characteristics of memelements depend on their material structure. For example, some memelements exhibit smooth voltage-current curve, other memelements exhibit hard-switching characteristics. Or the voltage-current curve with threshold voltage can be obtained when using appropriate materials. But there is no detailed mathematical study how the memristor exhibit its hysteresis curve and how we can control or improve mathematically its voltage-current behavior depend on the material structure. From this point, pathological elements provide unique advantages to obtain and improve the transfer

function of memelements. Various pathological elements such as voltage mirror and current mirror become important to avoid the use of the resistors in the nullor representation of building block. The nullator and narrator are one port elements and defined by V=I=0, and V, I are arbitrary, respectively.

Voltage mirror is a two port network element and defined by,

$$V_1 = -V_2 \tag{13}$$

$$I_1 = I_2 = 0 \tag{14}$$

The circuit symbol of the voltage mirror is shown in Fig.16.
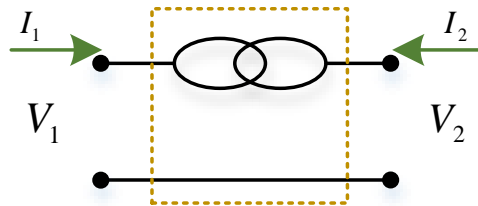
Fig.16. The voltage mirror symbol.

The all voltages and currents for current mirror are arbitrary.

$$V_1 \, and \, V_2 \, are \, arbitrary$$
$$I_1 = I_2 \, are \, also \, arbitrary \tag{15}$$
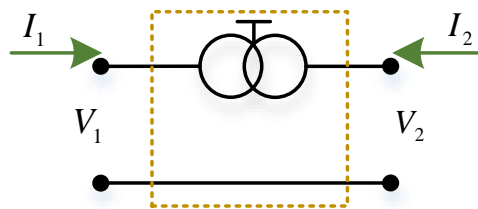
Fig.17. The current mirror symbol.

The nullor which is a two port network element is shown in Fig.18. and consists of an input nullator and an output norator. The voltage and current of a nullator and norator take zero and independently arbitrary value, respectively.
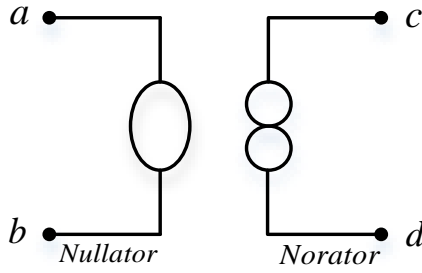
Fig.18.The nullor element [2].

The operational amplifier (Opamp) is realized from a nullor when one of the norator terminals is connected to the ground. The nullor element provides ability to model active devices [46-47]. Transistors which can be operated in saturation region, linear region and subthreshold region have crucial importance in all memelement circuit design. Transistors are not operated in only one region in circuit applications, sometimes operated in both saturation and linear region or other probabilities. In this situation the analyses of transistors become very hard especially operated in subthreshold region. Therefore the pathological models of transistors provide important advantage to analyses the transistor based circuit. The MOS transistor was modeled with nullor element as shown in Fig.19.
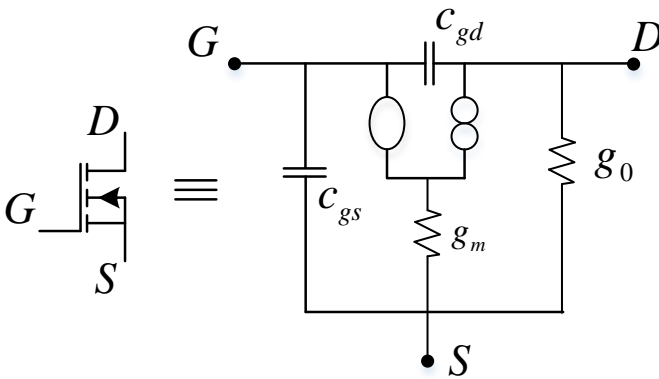
Fig.19.The MOS transistor model using nullor [48].

Active circuit elements have elusive properties to design emulator or new circuit components. Because memristor is passive circuit elements and cannot be modeled using only passive circuit elements. At this point, pathological elements occupy very important place. Sánchez-López introduced grounded pathological elements based fully differential active device models as shown in Fig.20. [49].
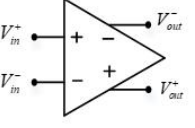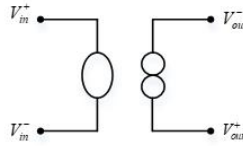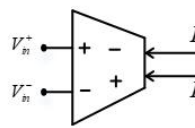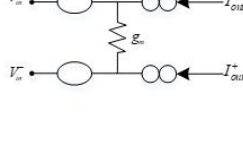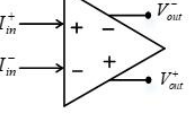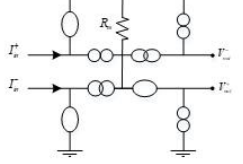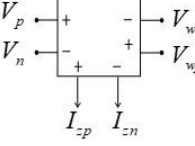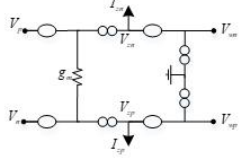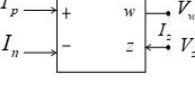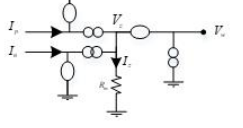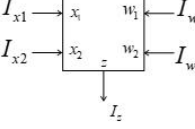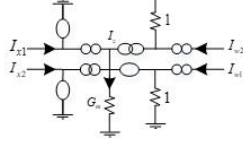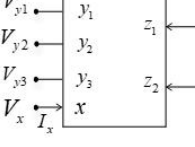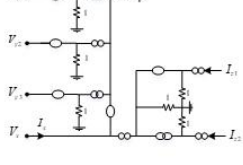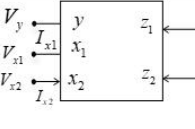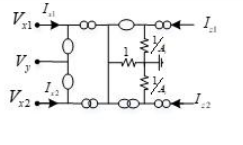
Active Device	Behavior Equation	Pathological Element-Based Model	Name
(circuit symbol)	$V_{out}^+ - V_{out}^- = A_v\left(V_{in}^+ - V_{in}^-\right)$	*(circuit diagram)*	Fully-Differential Operational Amplifier (**FD-Opamp**)
(circuit symbol)	$I_{out}^+ - I_{out}^- = g_m\left(V_{in}^+ - V_{in}^-\right)$	*(circuit diagram)*	Fully-Differential Operational Transconductance Amplifier (**FD OTA**)
(circuit symbol)	$\begin{bmatrix} V_{in}^+ \\ V_{in}^- \\ V_{out}^+ \\ V_{out}^- \end{bmatrix} = \begin{bmatrix} 0 & 0 \\ 0 & 0 \\ R_m & -R_m \\ -R_m & R_m \end{bmatrix}\begin{bmatrix} I_{in}^+ \\ I_{in}^- \end{bmatrix}$	*(circuit diagram)*	Fully-Differential Operational Transresistance Amplifier (**FD OTRA**)
(circuit symbol)	$\begin{bmatrix} I_{zp} \\ I_{zn} \\ V_{wp} \\ V_{wn} \end{bmatrix} = \begin{bmatrix} g_m & -g_m & 0 & 0 \\ -g_m & g_m & 0 & 0 \\ 0 & 0 & 1 & 0 \\ 0 & 0 & 0 & 1 \end{bmatrix}\begin{bmatrix} V_p \\ V_n \\ V_{zp} \\ V_{zn} \end{bmatrix}$	*(circuit diagram)*	Fully-Balanced Voltage Differencing Buffered Amplifier (**FB-VDBA**)
(circuit symbol)	$\begin{bmatrix} I_z \\ V_w \end{bmatrix} = \begin{bmatrix} 0 & 1 & -1 \\ 1 & 0 & 0 \end{bmatrix}\begin{bmatrix} V_z \\ I_p \\ I_n \end{bmatrix}$	*(circuit diagram)*	Current-Differencing Buffered Amplifier (**CDBA**)
(circuit symbol)	$\begin{bmatrix} I_z \\ I_{w1} \\ I_{w2} \end{bmatrix} = \begin{bmatrix} 1 & -1 & 0 \\ 0 & 0 & G_m \\ 0 & 0 & -G_m \end{bmatrix}\begin{bmatrix} I_{x1} \\ I_{x2} \\ V_z \end{bmatrix}$	*(circuit diagram)*	Current Differencing Transconductance Amplifier (**CDTA**)
(circuit symbol)	$\begin{bmatrix} V_x \\ I_{z1} \\ I_{z2} \end{bmatrix} = \begin{bmatrix} 0 & 1 & -1 & 1 \\ 1 & 0 & 0 & 0 \\ -1 & 0 & 0 & 0 \end{bmatrix}\begin{bmatrix} I_x \\ V_{y1} \\ V_{y1} \\ V_{y3} \end{bmatrix}$	*(circuit diagram)*	Differential Difference Current Conveyor (**DDCC±**)
(circuit symbol)	$\begin{bmatrix} V_{x1} \\ V_{x2} \\ I_{z1} \\ I_{z2} \end{bmatrix} = \begin{bmatrix} 0 & 0 & 1 \\ 0 & 0 & 1 \\ A_i & -A_i & 0 \\ -A_i & A_i & 0 \end{bmatrix}\begin{bmatrix} I_{x1} \\ I_{x2} \\ V_y \end{bmatrix}$	*(circuit diagram)*	Differential Current Conveyor (**DCCII±**)

Fig.20. Pathological element-based active circuit elements [49].

We referred the active circuit elements based memristor emulator circuits [11-18] and now we modified these circuits using pathological elements. First of all, the circuit which was designed by Kim and co-workers is modified as shown in Fig.21. Authors didn't give details of the mathematical analyses of the circuit because of the complexity of the circuit. But the analyses are less complex when use the pathological elements.
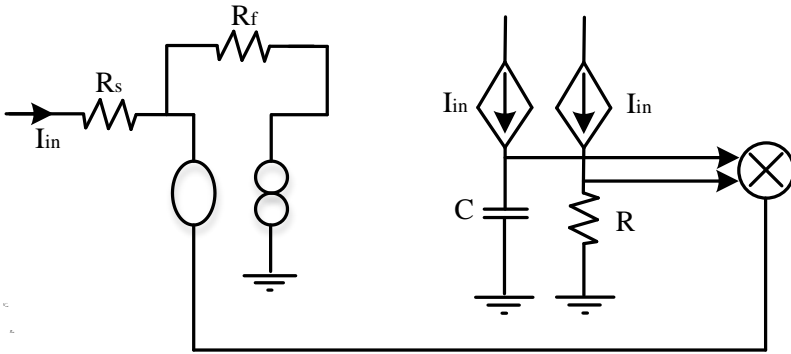
Fig.21. Memristor emulator based on OTA [17].

The other circuit which is based on DDCC active circuit element was designed by Yesil et al. [16], this circuit has semi-floating characteristics and strong voltage-current hysteresis curve. The schematic of the circuit is shown in Fig. 22 when rearranged using the pathological circuit elements.
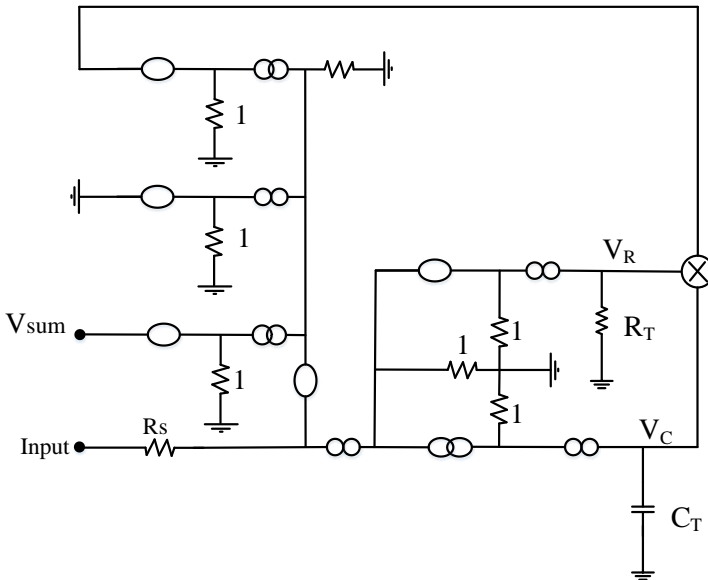
Fig.22. DDCC based memristor emulator which is presented by Yesil and co-workers [16].

Babacan and Kacar designed fully floating memristor emulator based on OTA active circuit element, and its pathologic circuit element based new schematic is shown in Fig.23a.
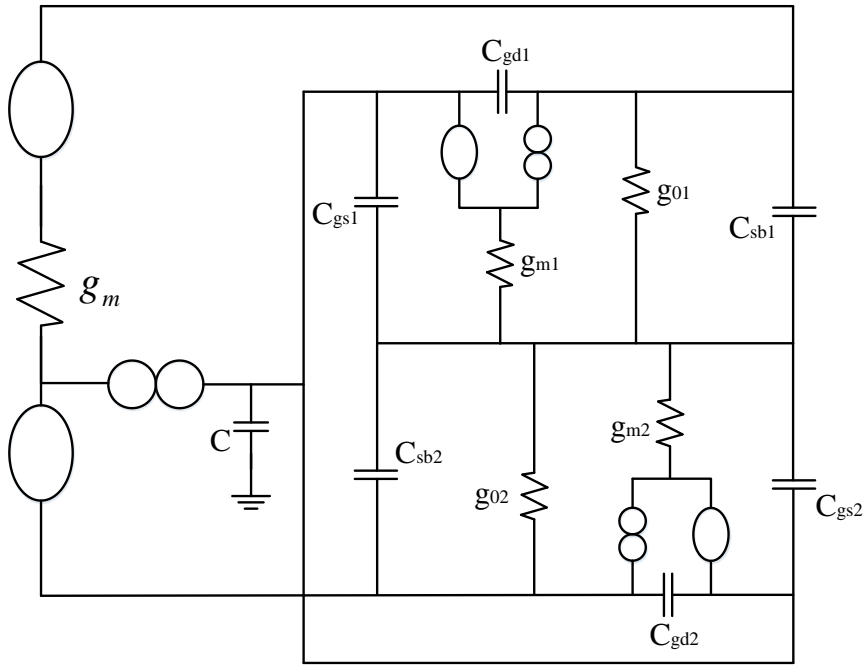
(a)
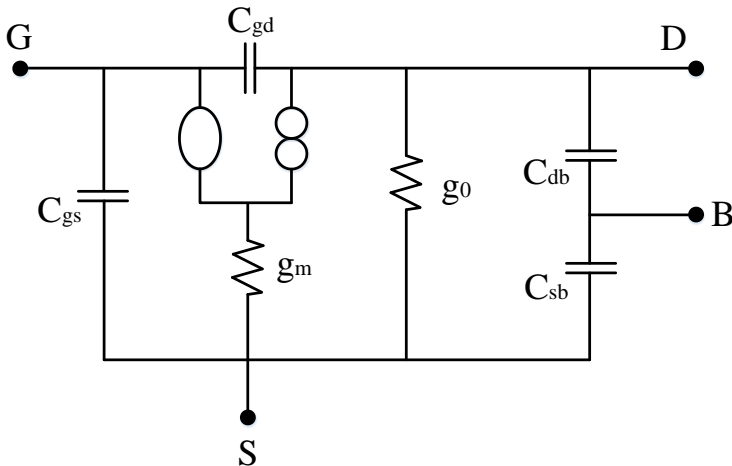
(b)

Fig.23. a) Fully floating memristor emulator based on OTA [17] and b) Pathological element equivalents of the MOS transistor [48].

The bulk terminals were connected to the drain terminals of the transistors that is why the pathological element based MOS transistor model [48] are rearranged using bulk terminals as shown in Fig.23b. All active circuit element based circuits lack of the detailed analyses for this reason their pathological equivalent is presented.

The detailed analyses are able to be done when using new forms. Because all circuits can be perform memristive effect but researchers didn't control the memristive effect when look at the mathematical equations or transfer function. And also the active circuit element based emulators can be improved when all analyses are known.

Author analyzed the memory consumption and computation time for nodal based and pathological elements based equations. Less processing time and memory consumption are required to solve the pathological elements based equations via nodal analyses as shown in Table 1.

Table 1: CPU-time and memory Consumption to solve the transfer function [49].

Equation	CPU-time (sec)	Memory (bytes)
(9)	0.05	147,634
(10)	1.81	56,169,210
(11)	0.02	289,854
(12)	0.03	215,738
(13)	8.66	211,591,018
(14)	8.70	209,594,926

The equations (9), (15), (16) and (10), (19), (20) are obtained from pathological element based analyses and nodal analyses, respectively. System requirements are less to solve the equations (9), (15), (16) [49]. Memristor and memristor based circuits candidate to build fast and ultra-low power dissipation systems. For this reason, the system analyses should be done in very short time using minimum energy.

CONCLUSION

In this chapter, memristive elements, pathological circuit elements and pathological equivalents of the memristor emulators were referred. Memristors which have nonlinear characteristics are new passive circuit element and there are several techniques to model memristive characteristics. Especially active circuit element based memristor emulators are more successful among all emulators. Classical nodal

analyses of active circuits are difficult so all presented active circuit element based memristor emulators are lack of the detailed mathematical analyses. To know the transfer function of memristor is important because of the fact that synaptic learning mechanism-Spike-Timing Dependent Plasticity (STDP), associative learning mechanism and similar complex operations can be implemented with memristor as presented before. Therefore, the detailed mathematical analyses are essential to analyze and improve the memristor and memristor based circuits. And also a nodal analysis consumes more energy and time to solve the transfer function of the circuit. That is why pathological circuit elements become significant candidate to analyze, solve and improve the memristive elements and memristor based circuit characteristics.

REFERENCES

[1] Chua LO (1971) Memristor-the missing circuit element. IEEE Transactions on Circuit Theory, 507-519.

[2] Strukov DB, Snider GS, Stewart DR and R. S. Williams (2008) The missing memristor found, Nature, 80–83.

[3] Wang Y and Liao X (2016) Stability analysis of multimode oscillations in three coupled memristor-based circuits, AEU-International Journal of Electronics and Communications, 1569-1579.

[4] Biolek Z, Biolek D and Biolkova V (2009) SPICE model of memristor with nonlinear dopant drift, Radioengineering, 210-214.

[5] Shin S, Zheng L, Weickhardt G, Cho S, Kang SM (2013) Compact circuit model and hardware emulation for floating memristor devices, IEEE Circuits and Systems Magazine, 42-55.

[6] Zhang Y, Zhang X and Yu J (2009) Approximated SPICE model for memristor. International Conference on Communications, Circuits and Systems, ICCCAS.

[7] Biolek D, Biolek Z, and Biolkova V (2009) SPICE modeling of memristive, memcapacitative and meminductive systems, Circuit Theory and Design, European Conference on IEEE.

[8] Williams RS, Pickett MD and Strachan JP (2013) Physics-based memristor models, IEEE International Circuits and Systems (ISCAS).

[9] Yang JJ, Strukov DB and Stewart DR (2013) Memristive devices for computing, Nature nanotechnology, 13-24.

[10] Kvatinsky S, Friedman EG, Kolodny A and Weiser UC (2013) TEAM: threshold adaptive memristor model, Circuits and Systems I: Regular Papers, IEEE Transactions on, 211-221.

[11] Abuelmaatti MT, Khalifa ZJ (2015) A continuous-level memristor emulator and its application in a multivibrator circuit, AEU-International Journal of Electronics and Communications, 771-775.

[12] Sanchez-Lopeza C, Carrasco-Aguilar MA, Muniz-Montero C (2015) A 16 Hz–160 kHz memristor emulator circuit, AEU-International Journal of Electronics and Communications, 1208-1219.

[13] Babacan Y, Kacar F, Gurkan K (2016) A spiking and bursting neuron circuit based on memristor, Neurocomputing, 86-91.

[14] Kim H et al. (2012) Memristor emulator for memristor circuit applications, IEEE Transactions on Circuits and Systems I: Regular Papers, 2422-2431.

[15] Yener Ş and Kuntman H (2012) A new CMOS based memristor implementation, Applied Electronics International Conference, pp.345-348, 2012.

[16] Yesil A, Babacan Y and Kacar F (2014) A new DDCC based memristor emulator circuit and its applications, Microelectronics Journal.

[17] Babacan Y and Kacar F (2016) Floating Memristor Emulator with Subthreshold Region, Analog Integrated Circuits and Signal Processing, 1-5.

[18] Babacan Y and Kacar F (2017) Memristor Emulator with Spike-Timing-Dependent-Plasticity, International Journal of Electronics and Communications, 16-22.

[19] Joglekar YN, Wolf SJ (2009) The elusive memristor: Properties of basic electrical circuits, *Eur. J. Phys.,* 30 (4), 661 -675.

[20] Peh, T, Papavassiliou, BP, Toumazou C, Prodromakis T (2011) A Versatile Memristor Model With Nonlinear Dopant Kinetics, IEEE Transactions on Electron Devices, 3099–3105.

[21] William SR (2008) How We Found The Missing Memristor, IEEE Spectrum, 29-35.

[22] Di Ventra M, Pershin Y, Chua LO (2009) Circuit Elements With Memory: Memristors, Memcapacitors, and Meminductors, Proceedings of the IEEE.

[23] Chua LO, Nonlinear Circuit Foundations for Nanodevices, Part I: The Four-Element Torus, Proceedings of the IEEE.

[24] Chua LO (1980) Device modeling via nonlinear circuit elements, IEEE Trans. Circuits Syst., vol. CAS-27, pp. 1014-1044.

[25] Bi GQ and Poo MM (1998) Synaptic modifications in cultured hippocampal neurons: dependence on spike timing, synaptic strength, and postsynaptic cell type, J. Neuroscience, 10464-10472.

[26] Song S, Miller K and Abbott L (2000) Competitive Hebbian learning through spike-timing-dependent synaptic plasticity, Nature Neuroscience, 919-926.

[27] Iannella N and Tanaka S (2006) Synaptic efficacy cluster formation across the dendrite via STDP, Neuroscience Letters, 24-29.

[28] Iannella N, Launey T and Tanaka S (2010) Spike timing-dependent plasticity as the origin of the formation of clustered synaptic efficacy engrams, Neuroscience.

[29] Azghadi M, Al-Sarawi S, Iannella N and Abbott D (2013) A new compact analog VLSI model for spike timing dependent plasticity, IFIP/IEEE 21st Int. Conf. Very Large Scale Integr., 7-12.

[30] Azghadi M, Al-Sarawi S, Iannella N and Abbott D (2014) Tunable low energy, compact and high performance neuromorphic circuit for spike-based synaptic plasticity, Plos One.

[31] Azghadi M, Al-Sarawi S, Iannella N and Abbott D (2012) Design and implementation of BCM rule based on spike-timing dependent plasticity, 2012 international joint conference on neural networks (IJCNN), 1-7.

[32] Cameron K, Boonsobhak V, Murray A, and Renshaw D (2005) Spike timing dependent plasticity (STDP) can ameliorate process variations in neuromorphic VLSI, IEEE Transactions on Neural Networks, 1626-1627.

[33] Koickal T, Hamilton A, Tan S, Covington J, Gardner J, and Pearce T (2007) Analog VLSI circuit implementation of an adaptive neuromorphic olfaction chip, IEEE Transactions on Circuits and Systems I: Regular Papers, 60-73.

[34] Azghadi M, Al-Sarawi S, Iannella N and Abbott D (2012) Efficient design of triplet based spike-timing dependent plasticity, 2012 international joint conference on neural networks (IJCNN), 1-7.

[35] Azghadi M, Al-Sarawi S, Iannella N and Abbott D (2011) Novel VLSI implementation for triplet-based spike-timing dependent plasticity, In Proceedings of the 7th international conference on intelligent sensors, sensor networks and information processing, 158-162.

[36] Indiveri G, Chicca E, and Douglas R (2006) A VLSI array of low-power spiking neurons and bistable synapses with spike-timing dependent plasticity, IEEE Transactions on Neural Networks, 211-221.

[37] Tanaka H, Morie T, and Aihara K (2009) A CMOS spiking neural network circuit with symmetric/asymmetric STDP function, IEICE Trans. Fund. Electr., Commun. Comput. Sciences, 1690-1698.

[38] Serrano-Gotarredona T, Prodromakis T, Linares-Barranco B (2013) A Proposal for Hybrid Memristor-CMOS Spiking Neuromorphic Learning Systems, IEEE Circuits and Systems Magazine, 74-88.

[39] Bi G, Poo MM (2001) Synaptic modification by correlated activity: Hebb's postulate revisited, Annu. Rev. Neuroscience, 139-166.

[40] Gerstner W, Kempter R, Hemmen JL and Wagner HA (1996) A neural learning rule for sub-milisecond temporal coding, Nature, 76-78.

[41] Li Q, Serb A, Prodromakis T and Xu H (2015) Memristor SPICE Model Accounting for Synaptic Activity Dependence, PLoS One, 1–12.

[42] Jo SH, Chang T, Ebong I, Bhadviya BB, Mazumder P, et al. (2010) Nanoscale memristor device as synapse in neuromorphic systems. Nano letters; 10: 1297–1301.

[43] Wang ZQ, Xu HY, Li XH, Yu H, Liu YC, et al. (2012) Synaptic learning and memory functions achieved using oxygen ion migration/diffusion in an amorphous InGaZnO memristor. Advanced Functional Materials; 22: 2759–2765.

[44] Li Y, Zhong Y, Xu L, Zhang J, Xu X, et al. (2013) Ultrafast Synaptic Events in a Chalcogenide Memristor. Scientific Reports, 3: 1619.

[45] Pickett MD, Medeiros-Ribeiro G, Williams S (2012) A scalable neuristor built with Mott memristors, Nature Materials.

[46] Bruton LT (1980) RC Active Circuits, Englewood Cliffs, NJ: Prentice- Hall, chapter 2 and 3.

[47] Davis AC (1967) The significance of nullators, norators and nullors in active network theory, Radio and Electronic Engineer, pp. 256–267.

[48] Sanchez-Lopez C, Tlelo-Cuautle E (2009) Symbolic Behavioral Model Generation of Current-Mode Analog Circuits, IEEE International Symposium on Circuits and Systems, ISCAS.

[49] Sanchez-Lopez C, Fernández FV, Tlelo-Cuautle E, Sheldon X-DT (2011) Pathological Element-Based Active Device Models and Their Application to Symbolic Analysis, IEEE Transactions On Circuits And Systems—I: Regular Papers, 58(6).

CHAPTER VIII

SMART CAMPUSES AND CAMPUS SECURITY

Murat Dener[1]

[1](Assoc. Prof. Dr.), Gazi University, e-mail: muratdener@gazi.edu.tr
iD ORCID *0000-0001-5746-6141*
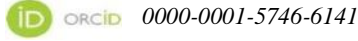
1. INTRODUCTION

According to the data of the Higher Education Institution, there are 203 universities in our country, including 129 state universities and 74 foundation universities. Considering that our existing universities have at least one campus and some universities have more than one campus, it can be seen that there are nearly 1000 campuses in our country. In addition, approximately eight million students in total, including approximately three million students at the associate degree level, approximately four and a half million students at the undergraduate level, and approximately four hundred thousand students at the graduate level, study at these campuses. This increases the importance of our campuses. Now, there is a need for smart campus solutions that leave traditional campus environment approaches and include innovative solutions. Smart campus refers to an intelligent infrastructure where smart sensors and actuators collaborate to gather information and interact with the machines, vehicles and users of a university campus. Creating a smart campus in universities around the world is gaining importance. Because the university community has become more mobile, student numbers are more unpredictable and funding has become more uncertain. Investment in management knowledge is required to focus campus strategies on resource efficiency and sharing, and to improve decision making.

This study focused on the smart campus and campus security. In the second part, smart solutions that can be found in the smart campus are presented, and in the third part, the techniques and technologies required to realize these systems are explained. In the fourth section, current studies on smart campus and campus security are mentioned. In the last section, the results of the study are given.

2. SMART SYSTEMS

Smart campus, educational institutions' advanced services, decision making, campus sustainability, etc. is a new trend that allows it to combine smart technologies with physical infrastructure.

Smart environments are systems that allow remote monitoring and management of heating, cooling, ventilation, lighting and security systems in the environment. These systems include water, electricity, natural gas, internet etc. consumed in the environment. It may include measurement of services. The internet control of electrical and electronic devices in the environment such as refrigerators, ovens, fans, washer / dryers [1] is also included in the concept of smart environment. Remote management of curtains and blinds, garage, garden and doors, television / projection and sound system, solar panels, gas leak controllers can also be included in this system. In advanced smart environment systems, remote control of the water and food of animals, monitoring the position of the inhabitants and turning on and off doors and lights accordingly, health monitoring systems for the elderly and the disabled can also be found.

Smart buildings are designed with the use of smart media technologies in the size of office buildings, production and service buildings, and residential blocks. Main services include heating, cooling, humidification, lighting, ventilation, water and hot water distribution, security and alarm system, gas control, fire control. Intelligent building technologies have become indispensable for controlling energy and operating costs, which have become important as buildings grow. Today, smart buildings can monitor the residents of the building by watching their magnetic ID cards, and they can reduce energy costs in unused parts of the building with automatic door and lighting systems [1].

Moreover, the following systems and more should be found in smart campus systems. These;

3d printing, Adjusting the temperature of the building, Air quality tracking, Carbon dioxide levels in classrooms and offices, Collection management and security system, Control of electronic devices in homes, Crowd management, Culture and tourism movements, Cyber security, Data-based crime prevention programs, Deformation and vibration sensors, Detection of hazardous gases, Detection of unauthorized entries, Detection of weapon sounds, Document tracking system, Drinking water monitoring, Drones for risk assessment, Dynamic pricing, Education digitalization, Emergency applications, Emergency response and disaster services, Energy management, Energy usage tracking, Face reading, Fingerprint reading, Fire systems, Following noise pollution, Health management, Heating-cooling systems, Indoor air quality, Indoor navigation, Intelligent systems for the disabled, Intrusion detection

systems, Library management, Lighting control systems, Locating systems for doctors in the hospital, Measuring the humidity and pollution levels of the specified areas, Monitoring noise levels, Monitoring of environment information, Monitoring of institutional vehicles, Online education,

Patient monitoring systems, Person and object tracking systems, Pollution control, Robots, Smart bike rental, Smart buildings, Smart classes, Smart education, Smart energy, Smart infrastructure, Smart junction, Smart Lamps, Smart lighting, Smart management, Smart offices,

Smart Parking, Smart public administration, Smart society, Smart tourism and entertainment, Social media data from students analysis systems, Speed warning security systems, Sports-social activities management, Student attendance-registration system, Swimming pool remote measurement, Traffic control, Traffic light control systems, Vehicle tracking systems, Waste management, Water management, Weather, air pollution detection systems, Wi-fi - station, Wireless monitoring of infrastructure.

3. TECHNICAL AND TECHNOLOGIES

Some of the techniques and technologies that should be known in terms of developing the mentioned smart systems and ensuring security are as follows: Information security, Cloud computing, Big data and data analytics, Internet of Things, Robotics, Artificial Intelligence and Machine Learning, Blockchain, Augmented reality, Sensor technologies, 5G and beyond connection technologies.

Information security is the process of ensuring the integrity of the information from the sender to the recipient in an environment where the information is continuously accessible, without being corrupted, changed or captured by others and transmitting it securely. TS ISO / IEC 27001 has been prepared in order to establish and document an information security management system and to provide the basic principles of the concept of information security. The basic principles of the concept of information security can be briefly illustrated by (CIA) acronym. These abbreviations are as follows: Protection of confidentiality (ensuring that access to information is available only to authorized persons). Integrity (protection of information and information processing methods, accuracy and completeness). Accessibility (ensuring that authorized personnel have access to information and related assets when necessary).

Cloud computing is a set of software, system or platform-based services that can be accessed and managed entirely over the internet instead of local resources. It is a computing model that can be used independently of place and time. This model; It offers fast access to all kinds of data

processing resources, including data storage areas, computer networks, servers and applications, and can be easily configured. Cloud computing and storage solutions offer businesses and individual users the opportunity to develop and manage business through secure and high-processing data centers spread around the world.

Big data and data analytics are all data collected from various sources such as social media posts, blogs, photographs, videos, and log files, converted into meaningful and processable form. In particular, it is used by institutions such as companies, educational institutions and hospitals to personalize information about end users and provide them with better quality services. Approaches such as statistics science, modern computing methods, computer science, artificial intelligence techniques, machine learning algorithms and mathematics are used to obtain value from high volume data. With big data analytics supported by different disciplines, institutions are supported to make more effective decisions.

Internet of Things refers to the connection of objects used in daily life to the internet. With the connection of the objects we see around us to the internet, communication between objects takes place and as a result, systems that help people and tools that increase the quality of life can emerge.

Robotics is a multi-disciplinary science that deals with the design, manufacture and use of robots. It is mostly preferred in places where people's work will be risky and in the industry.

Artificial Intelligence and Machine Learning is a computer science branch that works to create intelligent computers that can display intelligent behaviors unique to humans, such as artificial intelligence reasoning, language understanding, learning, and problem solving. Machine Learning, on the other hand, refers to the scientific expression of thinking and intelligent behavior mechanism and the concretization of this mechanism in machines.

Blockchain is a designed technology where everyone can upload programs, programs can be executed automatically, the current and previous states of each program can be seen by everyone at all times and the applications running on it are cryptologically secured.

Augmented reality includes many techniques, tools and methods used to create a rich environment between reality and virtuality. It enables the real world to be enriched with graphics, sound and animations developed in computer environment. Unlike Virtual Reality, the main purpose in Augmented Reality is not to create virtual environments that imitate the real world; to enrich the real world in real-time and interactively with virtual environments developed in computer environment.

Sensor technologies are the name given to the sense organs of sensor, automatic control systems. Just like people perceive what is happening in their environment with their sense organs, machines also perceive values such as temperature, pressure, speed and so on through their sensors. Devices that detect changes in the physical environment around us instead of people are called sensors. Sensors are devices that can detect physical changes and convert them into electrical signals very quickly. These signals emerging in the sensors are controlled by the microprocessor. In this way, it becomes possible to use sensors for many different purposes [2].

5G and beyond connection technologies, 5G, are intended to be able to operate in a highly heterogeneous environment characterized by the presence of a wide variety of access technologies, multi-layer networks, multiple device types, and multiple user interaction diversity. With 5G, a much more flexible, sustainable and programmable structure will dominate the next generation core network architecture compared to today. With 5G, it is aimed to support higher bandwidth, lower latency and high amount of data [3].

4. CURRENT STUDIES

The web of science database on smart campus and campus security was scanned and important studies were presented here.

In the study [4], a new approach called wisdom campus has been put forward. According to the authors, the wisdom campus is the ultimate form of university computing, the further expansion and elevation of the digital campus. Wisdom campus integrates cloud computing, mobile internet, big data, knowledge management and other emerging information technologies.

In the study [5], students with insufficient financial means can be identified with big campus data. The proposed system can also alert the counselors to provide psychological support to students in distress. The system has significantly increased the efficiency and quality of student management and reduced the workload of university staff.

The study [6] provides a comprehensive data set on electrical energy consumption at the university. The total amount of electricity consumed at Covenant University in Nigeria was measured, monitored and recorded on a daily basis over a one-year period.

In the study [7], it is stated that new buildings and infrastructures in Bogor Agricultural University cause a decrease in green open area and increase in carbon dioxide emission. The aim of the study is to estimate the amount of carbon stock using remote sensing technology to support the low emission program.

The study [8] presents a comparison of energy generation costs from gas-powered turbine and diesel-powered distributed electric power types at Covenant University in Nigeria.

In the study [9], a strong data discovery is made on the daily internet data traffic generated in a university campus.

In the study [10], information is produced about the use of smart campus tools to improve the effective and efficient use of campuses. It is stated that in order to use the resources of universities as effectively as possible, it is necessary to benefit from smart campus tools. This problem can be solved using.

In the study [11], cyber-physical system perspective is presented for the smart water management system on campus.

In the study [12], participation management system was developed as an Android application running on a smart tablet with the near field communication standard.

In this study [13], cyber security and wireless sensor network concepts as well as internet of things for smart campus are reviewed.

In the study [14], a database and smart campus mobile terminal application were designed to manage and monitor the use of campus energy in order to reach the smart campus.

In the study [15], to solve the problem of poor service quality, the user's query range is introduced to present a new anonymous zoning scheme.

In the study [16], an Energy Management System is recommended for optimum operation of the Savona Campus Smart Polygeneration Micro Grid in order to minimize overall production costs.

In the study [17], a different virus spread model was created for a smart campus network, considering the differences between individuals, and a method of extending the individual evolution process to the evolutionary process of the whole network was proposed.

The study [18] proposes a susceptibility classification method based on multi-specific fusion for Tibetan microblogs.

In the study [19], an effective and practical computational outsourcing protocol that protects privacy for the local binary model feature over large encrypted images is proposed.

In the study [20], a multi-source multimedia conference system supported by cloud computing called Multimedia conference system technology is designed and implemented.

The study [21] proposes an intelligent campus care and guidance framework for students with facial recognition based on deep learning through Internet of Things technologies.

The study [22] examined the design of an intelligent bus positioning system based on the Internet of Things to improve bus delivery vehicles, increase the efficiency of bus operations and implement a smart campus.

In the study [23], a student achievement prediction framework including data processing and student achievement prediction is designed.

In the study [24], a mutual authentication protocol developed in mobile RFID for smart campus is revealed by analyzing and examining existing smart campus authentication protocols.

In the study [25], a smart campus automatic settlement PLC control system was designed for the Internet of Things.

The study [26] introduces and analyzes the current research state of the smart campus and the challenges in integrating various service data into the smart campus.

In the study [27], a reliable edge caching and bandwidth allocation scheme is presented for mobile users.

In the study [28], the smart campus hospital environment is monitored, then real-time transmission, storage, and imaging data are analyzed to intelligently define the smart campus hospital environment.

In the study [29], the characteristics of Weibo's communication and the public opinion formation process of the microblog and its communication mechanism are analyzed.

The study [30] analyzes the salient features of the smart campus from the perspective of technology, business and construction mode and proposes a smart campus architecture model.

The study [31] presents a new deep topical correlation analysis approach for social media that provides robust and accurate topic detection.

In the study [32], under the background of the 5G network, the basic technologies of the smart campus network teaching platform are discussed.

The study [33] proposed a new authentication protocol for smart campuses, including Telecare Drug Information Systems.

The study [34] addresses classroom shortages caused by the gap between enrollment and attendance on a real university campus. Classrooms are equipped with Internet of Things (IoT) sensors to measure real-time usage, using AI to predict attendance, and optimal allocation of rooms to courses to minimize space waste.

In the study [35], it is aimed to investigate the underlying communication networks for remote monitoring of electric vehicles charging stations in a smart campus parking lot.

In the study [36], a Deep Neural Network based emotional awareness campus virtual assistant was developed.

The study [37] optimizes the existing wireless video surveillance system based on the Internet of Things to strengthen school security and create a wireless smart campus.

The study [38] aims to design a framework for local energy trade with electric vehicles in smart car parks where electric vehicles can exchange energy by buying and selling prices.

In the study [39], an architecture is proposed for creating and running responsive smart classes.

In the study [40], an IoT architecture that can transparently manage different communication protocols in smart environments is presented and research has been conducted for monitoring and controlling distributed energy resources in a smart campus.

The study [41] reveals a comprehensive architecture that defines various components and their interoperability in an intelligent education environment.

In the study [42], it was stated that green campus is a concept implemented by campuses where policies are directed to ecological perspectives. They conducted research on water security in green campuses.

In the study [43], Zigbee, LoRa, Bluethooth and WiFi were selected as the most popular IoT protocols, and their performance was tested and compared by establishing a network on the university campus.

The study [44] proposes a blockchain-based energy trading platform for electric vehicles in smart campus parking lots.

The study [45] looks at a university campus in the center of Lisbon, which requires a significant amount of electricity and natural gas to support internal activities. The idea is to meet some of the energy consumption of the campus with excess energy from solar systems installed in surrounding residential buildings. The goal is to find the number and type of solar equipment that maximizes the annual reduction of energy costs of the campus where both residents and campus are viewed as a virtual storage space.

The study [46] developed a new indoor positioning system combined with the outdoor positioning system to support seamless indoor and outdoor navigation and direction finding.

In the study [47], the differences between the network in the traditional campus and the network in the smart campus are analyzed and compared, and suggestions are made on how to create a smart campus from cloud computing and internet of things perspectives.

In the study [48], campus network security is examined.

The study [49] proposes a Bluetooth Low Energy based student positioning framework to automatically record student participation in classrooms.

The study [50] proposes a technical architecture for the future Smart Campus, consisting of 5G and IoT networks, complemented by distributed computing and data analytics.

The study [51] aims to accelerate the information-generation process of data collection and analysis for smart campus, current research and current problems in smart campus planning.

In the study [52], the current literature is examined and a smart campus outline based on smart city concepts is proposed.

The study [53] presents a case study in which emerging areas and related technologies are explored to benefit communities and actively engage their members as central players in such an intelligent environment.

The study [54] proposes a plan that can facilitate building a smart and friendly campus.

The study [55] explains the development of the smart campus using the Internet of Things (IoT) technology.

The study [56] presents the key features of this platform, with a special emphasis on the functionality, services and potential offered by the IoT platform, as well as the technological challenges encountered and solutions adopted.

In the study [57], it is proposed to use a LoRaWAN fog computing-based architecture to connect to IoT nodes deployed on the campus of A Coruña University in Spain.

The study [58] addresses the need to educate students on how to design complex sensor-based IoT ecosystems.

The study [59] explores the challenges of long-term real-world Internet of Things (IoT) deployment on a university campus.

The study [60] integrates a large data framework that can analyze data regardless of its format and provide effective responses to each process.

In the study [61], the data produced by students in search of patterns that allow students to be classified according to their needs are analyzed. Once these needs are identified, it is possible to make decisions that contribute to each student's learning; Artificial intelligence has been used for this.

The study [62] proposes a new disaster management system such as Named Data Networking Disaster Management, in which a producer transmits a fire warning message to neighboring consumers.

In the study [63], combining big data technology and cloud computing technology in smart campus construction to make campus database system and campus management system mutually.

In the study [64], firstly, the capabilities of existing IoT applications were determined. Then, it was stated how the information from IoT applications should be used in organizational decision making processes.

In the study [65], it is proposed to develop an IoT-based energy monitoring system prototype for the buildings in the Institut Teknologi Sumatera campus area.

In the study [66], the application of smart room technology based on Internet of Things is recommended to increase energy efficiency.

The study [67] deals with the security management of the campus network to analyze the weakness of the campus network in threat management.

5. CONCLUSIONS

Smart campuses are of great importance in social, financial and environmental terms. Considering the technologies required to realize the smart system, it can be clearly seen that there is no restriction in the realization of the systems. In other words, the desired smart system can be fulfilled with these technologies. The important thing is to pass right thinking and dreaming right. We can think of the campus as a city. Students spend 24 hours on campus from morning to evening, even at universities with dormitories. They meet all their needs, including education, health, sports and social, within the campus. There are hundreds of academic and administrative staff on campus, together with students. Having a command of this large living space is also attractive for managers. The answer to questions such as how many people are on campus, or how many vehicles, how much energy is consumed today and in which units, the status of the waste on campus, the amount of water consumed and the quality of

drinking water, the conditions in campus classrooms and offices, and more. will be able to reach easily. Considering the judgment that you cannot improve what you cannot measure, everything on the campus will be measured and necessary measures will be taken, unnecessary waste will be prevented. Even if these systems bring a high financial burden in the first place, they will pay for themselves over time. Internet of Things platforms for Smart Cities are technologically complex, and using them on a large scale involves high costs and risks. For this reason, pilot plans are particularly important in this context, which allow the proof of concept to be validated, to experiment with different technologies and services, and to fine-tune them before moving them to real scenarios.

REFERENCES

1. Mutlu, M.E. (2018). New Communication Technologies, Anadolu University Publications, E-ISBN 978-975-06-3046-0.

2. Pehlivanoglu, M. (2020), What is a Sensor?, https://muhendis gelisim.com/sensor-nedir/.

3. 5GTR Forum Working Groups (2018), 5G and Beyond, White Book, Information Technologies and Communication Authority.

4. Wang, H.Y. (2018). A research on the security of wisdom campus based on geospatial big data, 6th International Conference on Computer-Aided Design, Manufacturing, Modeling and Simulation (CDMMS 2018), 1967, DOI: 10.1063/1.5038997.

5. Wu, F., Zheng, Q.H., Tian, F., Suo, Z.H., Zhou, Y.A., Chao, K.M., Xu, M., Shah, N., Liu, J., Li, F. (2020). Supporting poverty-stricken college students in smart campus, Future Generation Computer Systems-The International Journal of Escience, 111, 599-616.

6. Popoola, S.I., Atayero, A.A., Okanlawon, T.T., Omopariola, B.I., Takpor, O.A. (2018). Smart campus: Data on energy consumption in an ICT-driven university, Data In Brief, 16, 780-793.

7. Lavista, L., Prasetyo, L.B., Hermawan, R. (2016). Dynamics change of the above carbon stocks in Bogor Agricultural University, Darmaga campus, 2nd International Symposium on Lapan-Ipb Satellite (Lısat) for Food Security and Environmental Monitorıng, 33, 305-316.

8. Okeniyi, J.O., Atayero, A.A., Popoola, S.I., Okeniyi, E.T., Alalade, G.M. (2018). Smart campus: Data on energy generation costs from distributed generation systems of electrical energy in a Nigerian University, Data In Brief, 17, 1082-1090.

9. Adeyemi, O.J., Popoola, S.I., Atayero, A.A., Afolayan, D.G., Ariyo, M., Adetiba, E. (2018). Exploration of daily Internet data traffic generated in a smart university campus, Data In Brief, 20, 30-52.

10. Valks, B., Arkesteijn, M., Den Heijer, A. (2019). Smart campus tools 2.0 exploring the use of real-time space use measurement at universities and organizations, Facilities, 37(13), 961-980.

11. Abhishek, M.B., Shet, N.S.V. (2019). Cyber physical system perspective for smart water management in a campus, Desalination and Water Treatment, 147, 296-307.

12. Kamada, S., Ichimura, T., Shigeyasu, T., Takemoto, Y. (2014). Registration system of cloud campus by using android smart tablet, Springerplus, 3, DOI: 10.1186/2193-1801-3-761.

13. Sanchez-Torres, B., Rodriguez-Rodriguez, J.A., Rico-Bautista, D.W., Guerrero, C.D. (2018). Smart Campus: Trends in cybersecurity and future development, Revista Facultad De Ingenieria, Universidad Pedagogica Y Tecnologica De Colombia, 27(47), 93-101.

14. Zheng, W.B., Yang, Z., Feng, L., Fu, P., Shi, J.L. (2019). APP Design of Energy Monitoring in Smart Campus Based on Android System, International Journal of Online and Biomedical Engineering, 15(5), 18-27.

15. Sun, R.X., Xi, J.W., Yin, C.Y., Wang, J., Kim, G.J. (2018), Location Privacy Protection Research Based on Querying Anonymous Region Construction for Smart Campus, Mobile Information Systems, 2018, DOI: 10.1155/2018/3682382.

16. Bracco, S., Brignone, M., Delfino, F., Procopio, R. (2017). An Energy Management System for the Savona Campus Smart Polygeneration Microgrid, IEEE Systems Journal, 11(3), 1799-1809.

17. Wang, L., Yao, C.H., Yang, Y.Q., Yu, X.H. (2018). Research on a Dynamic Virus Propagation Model to Improve Smart Campus Security, IEEE Access, 6, 20663-20672.

18. Qiu, L.R., Lei, Q., Zhang, Z. (2018). Advanced Sentiment Classification of Tibetan Microblogs on Smart Campuses Based on Multi-Feature Fusion, IEEE Access, 6, 17896-17904.

19. Xia, Z.H., Ma, X.H., Shen, Z.X., Sun, X.M., Xiong, N.N., Jeon, B. (2018). Secure Image LBP Feature Extraction in Cloud-Based Smart Campus, IEEE Access, 6, 30392-30401.

20. Zhang, W., Zhang, X.C., Shi, H.L. (2018). MMCSACC: A Multi-Source Multimedia Conference System Assisted by Cloud Computing for Smart Campus, IEEE Access, 6, 35879-35889.

21. Chen, L.W., Chen, T.P., Chen, D.E., Liu, J.X., Tsai, M.F. (2018). Smart Campus Care and Guiding With Dedicated Video Footprinting Through Internet of Things Technologies, IEEE Access, 6, 43956-43966.

22. Feng, X.J., Zhang, J.L., Chen, J.H., Wang, G.Q., Zhang, L.Y., Li, R.Z. (2018). Design of Intelligent Bus Positioning Based on Internet of Things for Smart Campus, IEEE Access, 6, 60005-60015.

23. Qu, S.J., Li, K., Zhang, S.H., Wang, Y.C. (2018). Predicting Achievement of Students in Smart Campus, IEEE Access, 6, 60264-60273.

24. Zheng, L.J., Song, C.L., Cao, N., Li, Z.X., Zhou, W.F., Chen, J.Y., Meng, L.L. (2018). A New Mutual Authentication Protocol in Mobile RFID for Smart Campus, IEEE Access, 6, 60996-61005.

25. Guo, G.Z. (2018). Design and Implementation of Smart Campus Automatic Settlement PLC Control System for Internet of Things, IEEE Access, 6, 62601-62611.

26. Yang, A.M., Li, S.S., Ren, C.H., Liu, H.X., Han, Y., Liu, L. (2018). Situational Awareness System in the Smart Campus, IEEE Access, 6, 63976-63986.

27. Xu, Q.C., Su, Z., Wang, Y.T., Dai, M.H. (2018). A Trustworthy Content Caching and Bandwidth Allocation Scheme With Edge Computing for Smart Campus, IEEE Access, 6, 63868-63879.

28. Liang, Y., Chen, Z.X. (2018). Intelligent and Real-Time Data a Acquisition for Medical Monitoring in Smart Campus, IEEE Access, 6, 74836-74846.

29. Nan, F., Suo, Y.N., Jia, X.Y., Wu, Y.Y., Shan, S.J. (2018). Real-Time Monitoring of Smart Campus and Construction of Weibo Public Opinion Platform, IEEE Access, 6, 76502-76515.

30. Xu, X., Wang, Y.S., Yu, S.J. (2018). Teaching Performance Evaluation in Smart Campus, IEEE Access, 6, 77754-77766.

31. Peng, J., Zhou, Y.Y., Sun, X.S., Su, J.S., Ji, R.R. (2019). Social Media Based Topic Modeling for Smart Campus: A Deep Topical Correlation Analysis Method, IEEE Access, 7, 7555-7564.

32. Xu, X., Sun, M.Y., Yang, S.C., Yu, S.J., Manogaran, G., Mastorakis, G., Mavromoustakis, C.X., Li, D. (2019). Research on Key Technologies of Smart Campus Teaching Platform Based on 5G Network, IEEE Access, 7, 20664-20675.

33. Safkhani, M., Vasilakos, A. (2019). A New Secure Authentication Protocol for Telecare Medicine Information System and Smart Campus, IEEE Access, 7, 23514-23526.

34. Sutjarittham, T., Gharakheili, H.H., Kanhere, S.S., Sivaraman, V. (2019). Experiences With IoT and AI in a Smart Campus for Optimizing Classroom Usage, IEEE Internet Of Things Journal, 6(5), 7595-7607.

35. Ahmed, M.A., El-Sharkawy, M.R., Kim, Y.C. (2020). Remote Monitoring of Electric Vehicle Charging Stations in Smart Campus Parking Lot, Journal of Modern Power Systems and Clean Energy, 8(1), 124-132.

36. Chiu, P.S., Chang, J.W., Lee, M.C., Chen, C.H., Lee, D.S. (2020). Enabling Intelligent Environment by the Design of Emotionally Aware Virtual Assistant: A Case of Smart Campus, IEEE Access, 8, 62032-62041.

37. Zhou, Z.Q., Yu, H., Shi, H.S. (2020). Optimization of Wireless Video Surveillance System for Smart Campus Based on Internet of Things, IEEE Access, 8, 136434-136448.

38. Ahmed, M.A., Kim, Y.C. (2018). Energy Trading with Electric Vehicles in Smart Campus Parking Lots, Applied Sciences-Basel, 8(10), DOI: 10.3390/app8101749.

39. Huang, L.S., Su, J.Y., Pao, T.L. (2019). A Context Aware Smart Classroom Architecture for Smart Campuses, Applied Sciences-Basel, 9(9), DOI: 10.3390/app9091837.

40. Pasetti, M., Ferrari, P., Silva, D.R.C., Silva, I., Sisinni, E. (2020). On the Use of LoRaWAN for the Monitoring and Control of Distributed Energy Resources in a Smart Campus, Applied Sciences-Basel, 10(1), DOI: 10.3390/app10010320.

41. Atif, Y., Mathew, S.S., Lakas, A. (2015). Building a smart campus to support ubiquitous learning, Journal of Ambient Intelligence and Humanized Computing, 6(2), 223-238.

42. Wimala, M., Zirads, B., Evelina, R. (2019). Water Security in Green Campus Assessment Standard, 2018 International Conference on Green Energy and Environment Engineering (CGEEE 2018), 93, DOI: 10.1051/e3sconf/20199302003.

43. Del-Valle-Soto, C., Valdivia, L.J., Velazquez, R., Rizo-Dominguez, L., Lopez-Pimentel, J.C. (2019). Smart Campus: An Experimental Performance Comparison of Collaborative and Cooperative Schemes for Wireless Sensor Network, Energies, 12(16), DOI: 10.3390/en12163135.

44. Silva, F.C., Ahmed, M.A., Martinez, J.M., Kim, Y.C. (2019). Design and Implementation of a Blockchain-Based Energy Trading Platform for Electric Vehicles in Smart Campus Parking Lots, Energies, 12(24), DOI: 10.3390/en12244814.

45. Rech, S., Casarin, S., Silva, C.S., Lazzaretto, A. (2020). University Campus and Surrounding Residential Complexes as Energy-Hub: A MILP Optimization Approach for a Smart Exchange of Solar Energy, Energies, 13(11), DOI: 10.3390/en13112919.

46. Torres-Sospedra, J., Avariento, J., Rambla, D., Montoliu, R., Casteleyn, S., Benedito-Bordonau, M., Gould, M., Huerta, J. (2015). Enhancing integrated indoor/outdoor mobility in a smart campus,

International Journal of Geographical Information Science, 29(11), 1955-1968.

47. Huang, C. (2017). On Study of Building Smart Campus under Conditions of Cloud Computing and Internet of Things, 1st International Global on Renewable Energy and Development (IGRED 2017), 100, DOI: 10.1088/1755-1315/100/1/012118.

48. Huang, M., Luo, W.B., Wan, X. (2019). Research on Network Security of Campus Network, 2018 International Symposium on Power Electronics and Control Engineering (ISPECE 2018), 1187, DOI: 10.1088/1742-6596/1187/4/042113.

49. Puckdeevongs, A., Tripathi, N.K., Witayangkurn, A., Saengudomlert, P. (2020). Classroom Attendance Systems Based on Bluetooth Low Energy Indoor Positioning Technology for Smart Campus, Information, 11(6), DOI: 10.3390/info11060329.

50. Jurva, R., Matinmikko-Blue, M., Niemela, V., Nenonen, S. (2020). Architecture and Operational Model for Smart Campus Digital Infrastructure, Wireless Personal Communications, 113(3), 1437-1454.

51. Luo, L. (2018). Data Acquisition and Analysis of Smart Campus Based on Wireless Sensor, Wireless Personal Communications, 102(4), 2897-2911.

52. Min-Allah, N., Alrashed, S. (2020). Smart campus-A sketch, Sustainable Cities and Society, 59, DOI: 10.1016/j.scs.2020.102231.

53. Prandi, C., Monti, L., Ceccarini, C., Salomoni, P. (2020). Smart Campus: Fostering the Community Awareness Through an Intelligent Environment, Mobile Networks & Applications, 25(3), 945-952.

54. Dong, X., Kong, X.J., Zhang, F.L., Chen, Z., Kang, J.L. (2016). OnCampus: a mobile platform towards a smart campus, Springerplus, 5, DOI: 10.1186/s40064-016-2608-4.

55. Sari, M.W., Ciptadi, P.W., Hardyanto, R.H. (2017). Study of Smart Campus Development Using Internet of Things Technology, IAES International Conference on Electrical Engineering, Computer Science and Informatics, 190, DOI: 10.1088/1757-899X/190/1/012032.

56. Alvarez-Campana, M., Lopez, G., Vazquez, E., Villagra, V.A., Berrocal, J. (2017). Smart CEI Moncloa: An IoT-based Platform for People Flow and Environmental Monitoring on a Smart University Campus, Sensors, 17(12), DOI: 10.3390/s17122856.

57. Fraga-Lamas, P., Celaya-Echarri, M., Lopez-Iturri, P., Castedo, L., Azpilicueta, L., Aguirre, E., Suarez-Albela, M., Falcone, F., Fernandez-Carames, T.M. (2019). Design and Experimental Validation of a LoRaWAN Fog Computing Based Architecture for IoT Enabled Smart Campus Applications, Sensors, 19(15), DOI: 10.3390/s19153287.

58. Tabuenca, B., Garcia-Alcantara, V., Gilarranz-Casado, C., Barrado-Aguirre, S. (2020). Fostering Environmental Awareness with Smart IoT Planters in Campuses, Sensors, 20(8), DOI: 10.3390/s20082227.

59. Gilman, E., Tamminen, S., Yasmin, R., Ristimella, E., Peltonen, E., Harju, M., Loven, L., Riekki, J., Pirttikangas, S. (2020). Internet of Things for Smart Spaces: A University Campus Case Study, Sensors, 20(13), DOI: 10.3390/s20133716.

60. Villegas-Ch, W., Molina-Enriquez, J., Chicaiza-Tamayo, C., Ortiz-Garces, I., Lujan-Mora, S. (2019). Application of a Big Data Framework for Data Monitoring on a Smart Campus, Sustainability, 11(20), DOI: 10.3390/su11205552.

61. Villegas-Ch, W., Arias-Navarrete, A., Palacios-Pacheco, X. (2020). Proposal of an Architecture for the Integration of a Chatbot with Artificial Intelligence in a Smart Campus for the Improvement of Learning, Sustainability, 12(4), DOI: 10.3390/su12041500.

62. Ali, Z., Shah, M.A., Almogren, A., Din, I.U., Maple, C., Khattak, H.A. (2020). Named Data Networking for Efficient IoT-based Disaster Management in a Smart Campus, Sustainability, 12(8), DOI: 10.3390/su12083088.

63. Tang, Z.J. (2017). On Study of Application of Big Data and Cloud Computing Technology in Smart Campus, 1st Internatıonal Global on Renewable Energy and Development (IGRED 2017), 100, DOI: 10.1088/1755-1315/100/1/012026.

64. Valks, B., Arkesteijn, M.H., Koutamanis, A., den Heijer, A.C. (2020). Towards a smart campus: supporting campus decisions with Internet of Things applications, Building Research and Information, DOI: 10.1080/09613218.2020.1784702.

65. Yuliansyah, H., Corio, D., Yunmar, R.A., Aziz, M.R.K. (2019). Energy Monitoring System Based on Internet of Things Toward Smart Campus in Institut Teknologi Sumatera, International Conference on Science, Infrastructure Technology and Regional Development, 258, DOI: 10.1088/1755-1315/258/1/012008.

66. Yuliansyah, H., Corio, D., Yunmar, R.A., Aziz, M.R.K. (2019). Smart-Room Technology Implementation Based on Internet of Things Toward Smart Campus in Institut Teknologi Sumatera, International Conference on Science, Infrastructure Technology and Regional Development, 258, DOI: 10.1088/1755-1315/258/1/012053.

67. Zhou, D.R. (2019). Research on the Security Early Warning Model of Campus Network Based on Log, 2018 4th International Conference on Environmental Science and Material Application, 252, DOI: 10.1088/1755-1315/252/4/042080.

CHAPTER IX

DRONE TECHNOLOGY IN PRECISION AGRICULTURE

Ilker Huseyin Celen[1] & Eray Önler[2] & Hasan Berk Özyurt[3]

[1] (Prof.Dr), *Tekirdag Namik Kemal University, e-mail:, icelen@nku.edu.tr.*
ORCID 0000-0003-1652-379X,

[2] (Dr.), *Tekirdag Namik Kemal University, e-mail: erayonler@gmail.com*
ORCID 0000-0001-7700-3742

[3] (RA.), *Tekirdag Namik Kemal University, e-mail: b.ozyurt94@gmail.com*
ORCID *0000-0003-0775-1723*

1.INTRODUCTION

The ongoing rapid and uncontrolled urbanization process in the world, globalization trends, increasing planning needs, developments in information technologies and the inevitability of environmental management have made the sustainable development approach mandatory today.

Agricultural production areas are decreasing, while the population in the world is increasing very rapidly. As a result, the food need to feed the population could not be met, bringing the concept of food safety to the agenda. Nowadays, as arable lands are decreasing, in order to meet the food needs of the world population; wider international cooperation, sustainable agricultural development, environmental approaches, use of advanced technology in agricultural production, etc. issues need to be focused intensively. For this reason, agricultural production systems based on information and technology, which enable the determination, analysis and management of factors that vary in time and spatial in the field, have started to be used widely for optimum gain, production efficiency, sustainability and environmental protection.

In agricultural production using precision agriculture method, optimum use of available resources, maximization of yield and minimum environmental damage are aimed. In the precision farming method, the agricultural area is not considered homogeneous but heterogeneous. It helps to reduce the waste of pesticides to be used especially for the control of weeds, diseases and pests. In addition, it enables the plants to get as much nutrient as they need, resulting in more efficient production. In other

words, it can be considered as a management strategy to increase production and quality by using information technologies. This aspect differs from traditional agriculture. In the precision farming method, the change on the land can be detected precisely by using local data. In this way, farmers can have more information on their land and apply it in land management. Detailed data on agricultural production areas can be obtained by using appropriate technologies. With the detection of variability on the land, fertilizers, chemicals and water can be used in agricultural production as required. In this way, the optimization of agricultural inputs is provided (Shibusawa, 1998).

The emergence and development of many technologies such as the global positioning system (Global Positioning System, GPS), geographic information system (GIS), smaller computer components, remote sensing, automatic control, advanced data processing methods, telecommunications have benefited this technology (Gibbons, 2000). The basis of these applications is to determine the current situation in the field correctly and to make applications according to the need. Precision agricultural technologies are used in seeds, fertilizers, pesticides, etc. applications, taking into account the temporal and spatial differences according to plant and soil characteristics. This ensures more efficient and environmentally friendly use of inputs. It is an approach that enables the use of new technologies in agriculture. Thanks to these practices, the development of the rural population, whose main source of economic income is agriculture, can be continued by increasing the efficiency per unit area and reducing migration to the city. Precision agricultural technology applications also allow to obtain the desired optimum yield.

The main target in agriculture; is to create a structure based on adequate and balanced nutrition of the society, using natural resources sustainably and containing advanced technology. Considering that the world population will exceed 9 billion by 2050 and the urbanization rate will increase to 70%, this structure has a strategic priority. Techniques that increase productivity and industrial applications come to the fore every day. In the near future, artificial intelligence will be used effectively in the agriculture sector and the use of nanotechnology will gain importance.

Agricultural research shows that innovative agriculture, agriculture 4.0 and precision agriculture practices will be used more in the future. Because with the development of machine-machine communication, drone applications, autonomous tractors, sensor technologies, cloud technology and augmented reality applications, agriculture and. technology relationship is increasing. As a result, a data-driven agricultural ecosystem has started to emerge. While data-driven agriculture helps farmers to make decisions and use opportunities effectively, automation systems ensure that agricultural lands are used effectively.

When the farmer is guided with the right information, he/she can maximize the earnings and the quality of the product he obtains when he uses the right tools and applies agricultural inputs (fertilizers, pesticides, water, etc.) at the right rate and time. Thus, more production can be achieved with less input by using the resources correctly and effectively. Digitalization in agriculture will play an important role in supporting farmers' workloads as well as in dramatically transforming lives in rural areas..

Internet of things applications used in agriculture are expected to reach a volume of 30 billion dollars by 2023 on a global scale. The intensive use of information technologies in different fields has led to the creation of digital data. Developing hardware possibilities and data processing solutions have made it easier to obtain information from this data.

In the near future, it will be a priority to create digital systems and develop digital literacy strategies and programs in the agricultural ecosystem. Thus, farmers will have the opportunity to obtain and market better products with the information flow and digital solutions obtained from the field. Researchers' priority areas of study include developing data exchange, data use and data analysis opportunities to generate added value in agriculture and to evaluate digital solution opportunities.

The use of Unmanned Aerial Vehicle (UAV) in precision agriculture applications started in the 1950s. Various analyzes can be made with these UAVs and efficiency can be increased by finding suitable solutions as a result of the evaluation (Rango et al., 2006). It is seen that different applications are made according to the agricultural product grown in agricultural production studies with UAVs. It is seen that UAVs are used in different agricultural applications with different sensors. For example, monitoring the maturity of coffee seeds (Herwitz et al., 2003), monitoring winter wheat production using various fertilizers (Hunt et al., 2010), determining and monitoring the productivity of rice fields (Swain, 2010), monitoring vineyards, healthy and diseased determination of areas (Turner, et al., 2011) etc. Information obtained by using UAVs with different sensors (e.g. soil moisture, surface temperature, photosynthesis activity, weed or pest infestation, etc.) are used for reduction of the total cost of agricultural production, increase of production efficiency, accurate harvest estimation, reduction and adaptation of climate change , environmental sustainability issues.

2.Unmanned Aerial Vehicle Development

According to the Global Air Traffic Management Operational Concept Doc. 9854, unmanned aerial vehicles are defined as vehicles that are regulated and do not have a pilot. In other words, and in the simplest

definition, UAV (UAV: Unmanned Aerial Vehicle) is defined as an aircraft that can go automatically, with GPS control, without a pilot (Dictionary.com, 2016). Today, UAVs are aircrafts that are sent by a pilot on the ground to perform a task with a remote control (Figure 1) or that are automatically flown by loading a previously made flight program. The historical development of UAVs is very old (Kahveci & Can, 2017).

UAVs are defined as "drone" or "UAV / UAS (Unmanned Aerial Vehicle / Systems)" in the international literature and they actually mean the same except for certain technical features. From a technical point of view, the drone refers to unmanned aerial or marine vehicles that can go automatically, while "UAV" refers to an aircraft that can fly unmanned, has an engine, can be controlled and is itself a non-weapon like a "cruise" missile. This definition has been expanded a little more and the abbreviation UAS (Unmanned Aircraft / Aerial Systems) has been used. The UAS definition includes the small aircraft and its related components (ground control station and communication line) under 25 kg that can be used without a pilot. In this context, the definition of "UAV / UAS" is divided into two different classes. These are RPAS (Remotely Piloted Aircraft Systems) and "Autonomous (Automated) UAS". In the definition of "RPAS", the aircraft is controlled by remote control by the pilot (operator) on the ground. In the RPAS concept, auxiliary equipment such as launch pad, command & control connections are also included. In the definition of "Automatic UAS", there is no pilot intervention, it is fully computer controlled and fully automatic. In conclusion; The terms "Drone", "UAV / UAS" and "RPAS" are widely used synonymously by users and there are no clear lines between them in international use. However, as far as legislation is concerned, the use of "Automatic UAS" is excluded from this definition as it is prohibited in almost all countries, including the EU (Kahveci and Can, 2017).

Figure 1: UAV automatic flying (Anonymous, 2020a)

Air balloons are known as the ancestor of unmanned aerial vehicles (Figure 2). The history of unmanned aerial vehicles is based on the discovery of hydrogen gas by Henry Cavendish in 1766 (Anonymous, 2016a). With the realization that hydrogen gas is lighter than air, air

balloons construction has begun. The first balloons made were used in unmanned flight trials in order to make manned flights. In the 19th century, air balloons were used for military and scientific purposes. The first use of UAVs for scientific purposes; French Physicist Jean Baptiste Biot and French Chemist Joseph Louis Gay Lussac reached an altitude of 4 km in 1804 during the researches on the composition of air and the earth's magnetic field (Anonymous, 2016b). During the American civil wars (1861-1865), it was used by soldiers to attack with unmanned air balloons by mounting flame-throwing guns (Anonymous, 2016c). French Meteorologist Leon Philippe Teisserenc de Bort made meteorological measurements at various heights using unmanned air balloons with measuring instruments in 1902 (Anonymous, 2016d). Japan used fire bomb loaded motorized air balloons that could fly from high altitudes in the attacks against America in 1945 (Anonymous, 2016e). America used balloons equipped with cameras to take images for military purposes in the 1950s (Davies and Harris, 1988).

People interested in the field of aviation carried out studies involving primitive flight experiments to build steam powered airplanes and keep them in the air between 1850 and 1900 (Anonymous, 2016f). The wing-propeller and gasoline-powered bombs produced by the American Navy in 1918, which can travel up to 60 miles from a previously determined route, are considered to be one of the pioneering work in the production of today's modern unmanned aerial vehicles. In 1944, the Germans developed bombs that could fly long distances by reaching a speed of 400 km / h with a jet engine and could be controlled by radio waves. For a while, the necessity and benefits of these tools began to be questioned and studies slowed down. The fact that Israel used unmanned aerial vehicles against Syria in the Lebanon war in 1982 and achieved a great success attracted attention again on this technology (Anonymous, 2016g). It was later used for surveillance and reconnaissance purposes during the 1990 Gulf War. Since 2002, America has started to use predator unmanned aerial vehicles, which are among the modern drones of today, in war operations against terrorism. All unmanned aerial vehicles built up to the last 10 years consist of fixed wing ones. Later, rotary-wing, vertically movable, helicopter-like unmanned aerial vehicles equipped with HD cameras were produced. Today, UAVs with powerful autonomous control systems, ranging from the size of a passenger plane to the size of an insect, can be produced. UAV technology has been put into civilian use after 2010 and its usage areas are increasing day by day as the relevant legal regulations are made.
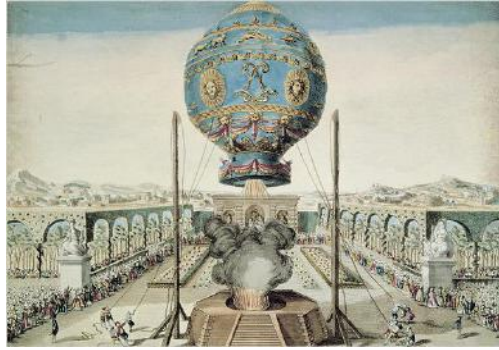
Figure 2: First air balloon at the history (Anonymous, 2020b)

The fact that 25% of the participating companies formed UAV technology companies at the Intergeo fair held in Hamburg in October 2016 clearly reveals the place of UAV in the sector (Torun 2016). Since the first half of the 2000s, many research and application studies on UAV photogrammetry, UAV remote sensing, processing and analysis of UAV data, verification of UAV data have been increasingly continuing all over the world. There are many publications on UAV photogrammetry in the world.

3. Technical Aspects of UAVs

Figure 3. Rotary wing drones (Anonymous, 2020c)

Drone; It is an unmanned aerial vehicle that uses aerodynamic forces to hold the vehicle in the air and is flown by an external pilot either by pre-programmed or ground command (Figure 3) . Today, UAVs with powerful autonomous control systems, ranging from the size of a passenger plane to the size of an insect, can be produced. UAV technology was put into civilian use after 2010, and its usage areas have increased as the relevant legal regulations are made. Unmanned aerial vehicle; It is an integrated system consisting of three components: pilotless aircraft system, remote pilotage control system and command-control communication environment between these two. Considering the details of this system, it consists of the main body (skeleton, wing, propeller, engine and battery),

126

control unit (electronic sensors, communication electronics, GNSS), sensors compatible with the purpose of use and hardware and software for flight planning.

There are multirotor drones with different numbers of motors. These are generally three rotors (tricopter), four rotors (quadrocopter), six rotors (hexacopter), eight rotors (octocopters). Since Tricopter drones have only 3 motors, they have a cost advantage despite their low weight carrying and maneuverability (Figure 4). Quadcopters have 4 rotors. Two rotors rotate clockwise while the other two rotors rotate counterclockwise (Figure 5). Quadcopters are the most preferred drone structure in terms of both cost and functionality. Hexacopters, on the other hand, have all the advantages of quadcopters, but they have the potential to carry more load and climb to higher altitudes due to their more rotors. For balanced and stable flight, three of the six rotors in Hexacopters rotate clockwise while the other three rotors rotate counterclockwise (Figure 6).

A drone is steered vertically with propellers attached to rotors. Each propeller has a variable and independent speed allowing a full range of motion. One drone motor is used per propeller. A faster motor rotation provides more flight power but requires more power from the battery, resulting in reduced flight time.

The most important basic feature of UAVs is to have a light body or chassis with a drone skeleton on which all components are fixed. It is very important for the body to be light in order to achieve high flying times. Usually balsa, foam, etc. in UAVs. materials with very low specific gravity are used. As the power requirement increases, more powerful motors or longer propellers are used.
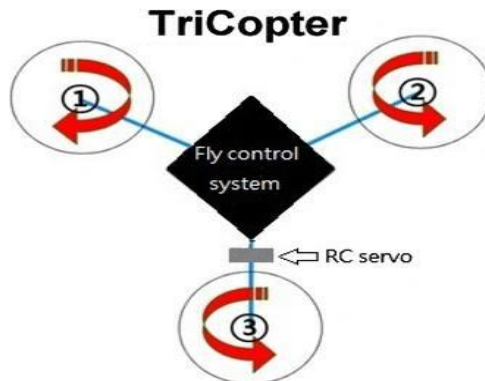
Figure 4: Rolling direction of the propellers at tricopter (Zou et al., 2012)
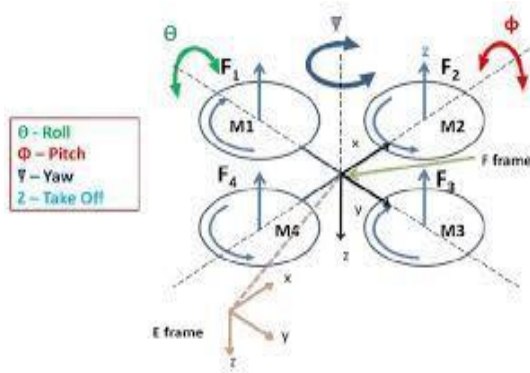
Figure 5: Quadrocopter Control Frames (Kurak and Hodzic, 2018)
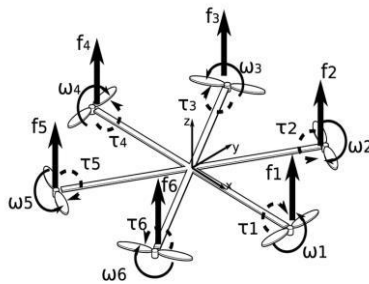
Figure 6: The body frame of an hexacopter (Artale et al. 2013)

The structure of the propellers affects the load the drone can carry, the speed it can fly and its maneuverability. There is a direct proportion between the propeller length and the load it can lift. However, as the propeller gets longer, its acceleration capability decreases. The maneuverability of the aircraft increases as the speed change capability is more flexible in drones with short propellers. However, in order to achieve the same lifting power, a higher rotor rotation speed is required for short propeller drones. This causes a higher load on the electric motor and shortens its service life.

Figure 7: Drone propeller

Control signals are received from the pilot through the radio receiver. The Flight Controller used in UAVs is a built-in computer that interprets these signals sent from the pilot and sends the relevant inputs to the Electronic Speed Control Device to control the UAV.

Flight control devices are a circuit board used in unmanned aerial vehicles systems and qualified as the brain of the flight system (Figure 8). It generally contains one or more sensors to control the unmanned aerial vehicle. It also receives the commands sent from the radio control system and controls the motors in order to keep the drone in the air according to these commands. Basically, its function is to control the speed of the motors to which the propellers are connected and the direction of rotation in accordance with the incoming commands. Today, almost all flight control devices have basic sensors such as Gyro (Gyroscope) and Acc (Accelerometer). It may also include some baramotric pressure sensors and more advanced sensors such as a magnetometer (compass), GPS, LIDAR etc. (Uz, 2019).
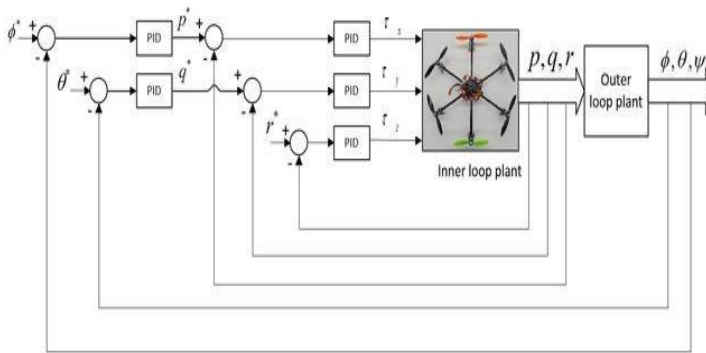
Figure 8: Drone control system structure (Poksawat and Wang, 2017)

The Electronic Speed Controller (Figure 9)supplies a controlled current to each motor to produce the correct rotation speed and direction. It supports the electric motor to move in the opposite direction and at the same time to perform sudden braking.

Figure 9: Electronic speed controller (Anonymous, 2020e)

Generally, lithium polymer batteries are used because of their high power density and rechargeable feature (Figure 10). In addition, sensors

such as accelerometers, gyroscopes, GPS and barometers can be used for positional measurements. Cameras with many different features are often installed for navigation and aerial photography.
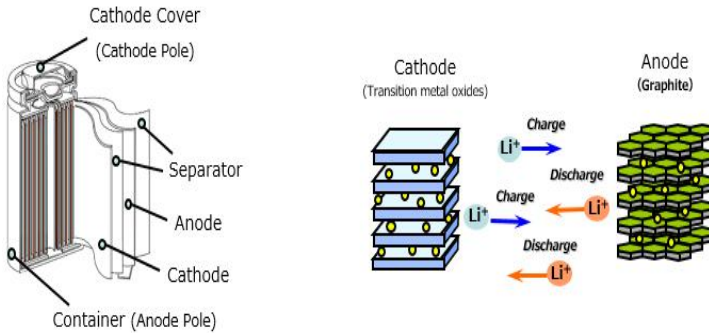
Figure 10: Lithium based batteries (Anonymous, 2020f)

Drones can be controlled manually with a radio transmitter controller (Figure 11). With the help of the levers on this controller, the rotation speed and direction of the propellers are changed, allowing the drone to perform various maneuvers. With the screens on some remote controls, datas of various sensor and camera images can be monitored. In addition, built-in sensors can provide useful settings such as automatic altitude and fixed UAV position. The drone can also be flown autonomously. The route and landing point of the drone can be determined with a software.

Figure 11: Drone radio controllers (Anonymous, 2020g)

Depending on the technological development, the use of smartphones and tablets instead of the control unit, the reduced costs of various sensors (GPS, Wi-Fi receivers, MEMS INS sensors, visible band, multi-spectral, thermal, hyper-spectral cameras, etc.) UAV production costs have decreased. With the development of minimalized hardware solutions in GNSS technology, location determination can be made more accurately in navigation applications performed with PPK (Post Processed Kinematic) GNSS (Colomina et.al, 2014). The top five sectors where UAV finds the most common application on a global scale; real estate and construction, photogrammetry (aerial measurement), film / aerial

photography, agriculture and aerial monitoring (tracking) activities. UAV photogrammetry has made room for itself in agriculture, mining, aerial photography and real estate sectors.

There are differences in terms of mathematical and statistical models between UAV photogrammetry (Structure from Motion-SfM) and traditional photogrammetry (Figure 12). UAV photogrammetry focuses on efficiency rather than accuracy. However, traditional photogrammetry seeks solutions with global consistency, model validity, accuracy of measurements, compatibility and basically a holistic / global mathematical model. This important difference limits the use of UAV photogrammetry as a means of measuring from the air, creating a 3D digital surface model and creating an orthophoto. The replacement of UAV photogrammetry to traditional photogrammetry may be possible with advances in two areas. The first of these is the harmonization of the mathematical / statistical model and their applications used in UAV photogrammetry with traditional photogrammetry (Figure 12). The other is that the sensor and lens designs that enable traditional photogrammetry to create a global solution can also be applied to UAVs (Draeyer et.al, 2014, Torun 2016, UAS PIEngineering 2012). On the other hand, the model and calculation approaches that improve with UAV photogrammetry contribute to the increase of the computational efficiency of traditional photogrammetry.
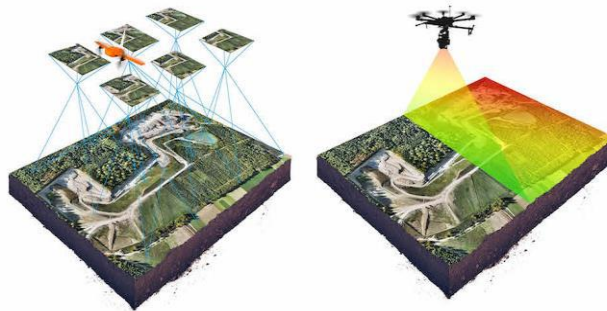
Figure 12: UAV Photogrammetry (Anonymous, 2020h)

In the UAV photogrammetry (Structure from Motion-SfM) approach, which has found a wide application area with the contribution of the developments in the field of computer vision, the following calculation and processing process is performed;

- Creating dense point clouds (sparse / frequent) by matching with multi-dimensional feature vectors (feature vector),

- Thus, creating a triangular surface network or a pyramidal solid model (TIN / TEN model, TIN: Triangulated Irregular Network; TEN: Tetrahedronized Irregular Network),

- Creating an object surface or solid object model with reconstruction from TIN / TEN surface and 3D model,

- Texturing the created surface (photogrammetry and orthophoto in remote sensing) (Cryderman et.al 2015, Draeyer et.al, 2014, UAS PIEngineering 2012).

UAV photogrammetry is especially used in agriculture, mining, aerial photography and real estate sectors. Because of the need for more precise work and measurements due to ownership rights, the use of UAV is progressing more slowly but continuously in map-cadastre and planning works. Meanwhile, with the experience gained from the applications, the need to establish quality assurance and infrastructure in the field of measurement using UAV is rapidly increasing.

UAVs and Agriculture

Agriculture is a labor-intensive branch of production in which the product is usually grown in a short period of time. Producers make use of vehicles ranging from simple tools to complex and self-propelled machines in the production, which is compressed into a period of 2-3 months. The purpose of production is to carry out and control agricultural activities in a short period of time. For this, various sources of information are used in agricultural production and business management. Along with the developing technology, information technologies have increased the efficiency of the machinery and have been used effectively in agriculture.

Unmanned aerial vehicles have recently begun to be used in civilian areas, apart from defense and security areas. It is used in many areas such as agriculture, fire fighting, transportation, natural life surveillance, aerial shooting, post-earthquake damage and radiation detection. The use of UAVs in agriculture are passive applications for disease and pest detection, water stress detection, yield / maturity estimation, weed flora detection, water resources control and monitoring of workers based on remote sensing and plant monitoring techniques.

Climate change has a great impact on the food industry. Developing technology is expected to overcome this effect by minimizing it as much as possible. The agri-food sector must adapt to these changes and make correct, effective and reliable decisions. Unmanned aerial vehicles, which can keep up with these changes, have a high potential of use in the future, can support the agricultural sector, have emerged as a solution to all these problems.

UAVs can fly manually by a pilot on the field or software can be used to enable it to follow a certain route. UAVs can easily access many data by using various sensors like multispectral cameras used in UAVs (nutrient deficiency, pest damage, fertilizer needs and water quality,

Multispectral imaging and processing, mapping invisible reflections from plants, stress analysis, etc.), hyperspectral cameras (Plant nutrients, plant diseases, water quality and Mineral and surface chemical composition analysis), LIDAR sensors (This sensor using laser, the collection of altitude data that can create three-dimensional models of your farm), thermal cameras (surface temperature of land and plants).

When some of the studies conducted on agricultural fields using UAVs are examined, it is seen that different applications are made according to the agricultural product grown: Monitoring the maturity of coffee seeds, monitoring winter wheat fields grown using different fertilizers, determining and monitoring the productivity and total vitality areas of the rice fields, different sensor systems on the UAVs. There are different applications such as monitoring the vineyards, determining healthy and diseased areas. Some UAV models can scan and monitor 500 acres of land in a single flight. This monitoring can be through video recording or taking pictures at regular intervals. Negative situations such as crushing of agricultural products and disease transmission may be encountered in monitoring practices by entering the field. In monitoring studies using drones, disease detection and water puddles formed as a result of irrigation can be detected without damaging the product (Şener et al.2018a, Şener 2018b, Şener 2019). Drone technology (especially in large agricultural areas) can be used in different applications such as soil analysis, determination of the condition of the product, protection of agricultural products from pests and wild animals, irrigation and application of environmentally friendly solutions instead of pesticides. At the same time, it can give farmers a more detailed and purposeful picture of their fields with the sensors and digital imaging capabilities in their systems. This information will also be useful for improving crop yield and farm productivity.

Drones that provide the necessary insulation and protection can also be used in liquid fertilizer applications. Similarly, drones used in spraying applications can be sprayed more precisely and economically. In addition, crop damage and soil congestion can be reduced since the tractor will not travel on the land. Spraying only previously determined diseased areas provides benefits in terms of reducing environmental pollution as well as reducing costs.

In addition to existing uses, it can also be used for precision fertilizer planning, weed and disease control, tree and land mapping, crop spraying, plant pollination control.

Nutrient-deficient areas in the field can be detected from the air using drones equipped with cameras with advanced sensors. Various software are used to create an application map from the captured images.

By using these software, fertilization program can be created to meet the varying nutritional requirements of agricultural products in different parts of the land. The purpose of the global positioning systems is to determine the latitude, longitude and altitude coordinates of the field and / or equipment according to the spatial and temporal data. Variable amounts and doses of pesticides and fertilizers are applied to the field according to the mapping principle created by this system. Positioning systems are divided into two groups as ground-based and satellite-based (Keskin & Görücü-Keskin, 2012).

Using techniques similar to manure planning, drone operators can accurately assess weed and disease levels in arable crops (Figure 13). It can collect data by identifying different characteristics of weeds and affected areas. By analyzing this information, preventive determinations and control can be made for products sensitive to weed species and diseases. Especially in orchards, it provides convenience to producers in terms of identifying and labeling trees infected with various diseases.

In addition to disease control by using UAVs (Figure 14), orchard producers can benefit from accurate calculations of areas and tree and row spacing reports. The same is true in forestry and timber production. The ability to cover large terrains is a great advantage for mapping in general. Hundreds of hectares of land can be mapped in a day with the help of detailed systems that exactly define the boundary features. With the obtained data, a 3D computer model is created to detect ground features and possible changes. This information can be used to give field measurements for application purposes or to support the machine software to help the operator avoid hazards such as electrical wiring, flooding, changes in waterways or drainage equipment.

Figure 13: Drone for weed mapping (Anonymous, 2020i)

Today, due to the decline in the number of bees, concerns have been raised about the future of plant pollination, which is the basis of horticulture and agricultural production worldwide. Using a drone weighing only 15 grams, the researchers were able to fertilize the flowers without harming the plant. Researchers are continuing their research into

plant pollination, with the autopilot version that the plant grower can free to run the business alone.

Figure 14: Drone in spraying application (Anonymous, 2020j)

The mapping and imaging capabilities of drone platforms with a range of sensors can be used throughout the production process to better plan production and thus increase efficiency . Before the vegetation cycle starts, data can be obtained for potential yields using UAV technology, and the main point here is that this yield is obtained from the land soil quality, color and three-dimensional images (Figure 15). As a result of the analysis, the UAVs also provide the information of the exact harvest time for the field. In addition to this information, it also helps to control the water flow. During the vegetation period, UAVs are used to monitor the planned area and to find a solution quickly when any problem occurs.
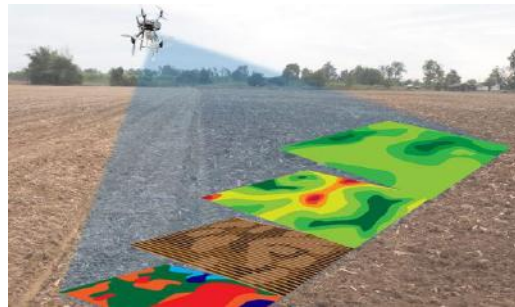
Figure 15. Drone for mapping (Anonymous, 2020k)

UAVs offer the option of producing with a new perspective and approach in terms of developing agriculture, increasing efficiency, and making correct land control.

UAVs are now replacing traditional pesticide sprayers used by farmers in agriculture. Spraying rates are 40 times faster than conventional pesticide sprayers. It saves 90% water and 30-40% pesticide with smart spraying systems.

UAVs provide more precise and reliable information by predicting the risks in large-scale lands, increasing the yield and ensuring the optimum level of product quality. Locations with permanent cloud

persistence or high turbidity become traceable and high resolution data can be obtained.

It increases productivity by reducing the workload and time required in the management of large-scale lands. It provides an economically effective traceability of inaccessible areas that are difficult to work due to its topography.

Since reliable results are obtained, it can be used easily in scientific researches. Despite the bad environment and weather conditions, the stable use of UAVs is proof that there will be significant progress in agriculture compared to traditional methods. For this reason, UAVs are a promising technology and alternative to old methods in low cost, comprehensive and reliable data collection. Usage areas and the research opportunities it creates indicate that UAVs will be increasingly used in the future and will be constantly on the agenda.

UAV technology can collect data in agricultural areas faster, more accurately and at lower cost. Today, negative effects and results of plant protection applications made with conventional methods. For example, in conventional spraying applications with a tractor, a small part of the sprayed liquid can hold on the plant, while the rest flows into the soil. In addition, it causes serious yield losses as it causes soil congestion and crushing of agricultural products during tractor spraying.

With the decisions based on the analysis of the data obtained from the sensors, exact accuracy in fertilizer applications can be effective in efficiency and can reduce costs. This opportunity is valid not only for macronutrients but also for micronutrients. With the same approach, product losses can be minimized by monitoring the initiation and spread stages of pests and diseases in an easy, cheap and timely manner. Naturally, early diagnosis provides opportunity to use minimum insecticide and pesticide, reduces environmental damage and brings cost reduction.

Beyond easy adaptation to the topography, UAV technology offers a very rapid application opportunity compared to airborne spraying. With spectral or thermal sensors, it can prevent possible drought damage by guiding the producer about irrigation with analysis based on leaf-soil moisture.

Another area of use is active applications that include precise chemical application, pest removal and livestock control. UAVs started to be used for agricultural purposes under the leadership of Japan in the 1980s with the request of the development of an unmanned helicopter for spraying from Yamaha company (Anonymous, 2016j). Later, it started to take part in agriculture in order to overcome the problems caused by satellite and air platforms in remote sensing (Tekin et al., 2015).

With the help of the developments in imaging systems in agriculture in recent years, UAVs are widely used especially in remote sensing studies. It is necessary to take images with cameras with various features in order to use UAVs for the detection of disease factors, pest detection, determination of harvest time and yield estimation. Studies can be made to produce weed maps in the season or late season with images taken from aerial platforms or satellite (Koger et al., 2003; De Castro AI et al., 2012). The properties of the sensors of the cameras used in these images are important. Visual sensors that provide us with the closest image to the real image, Lidar sensors that enable us to carry the vegetation to three-dimensional environment, thermal sensors that distinguish objects based on temperature difference and multispectral and hyperspectral sensors that can measure reflections in different wavelengths of light are used. In particular, sensors using infrared wavelength reflections are widely used in remote sensing studies. Differentiation due to differences in spectral characteristics of plants is achieved by using various indices. With these differences, a healthy plant and an unhealthy plant, a cultivated plant with weeds, a mature plant and an immature plant, a plant under water stress and a plant that does not need watering and a nutrient deficient plant can easily be demonstrated from the differences in spectral indices. Color tones and even colors of plants may change according to their health conditions. When the human eye detects the changes / damages in plants, it is quite late to perform the necessary applications, but with the data collected in the visible light spectrum and near-infrared (NIR) spectrum, these differences can be detected long before the symptoms that the human eye can perceive.
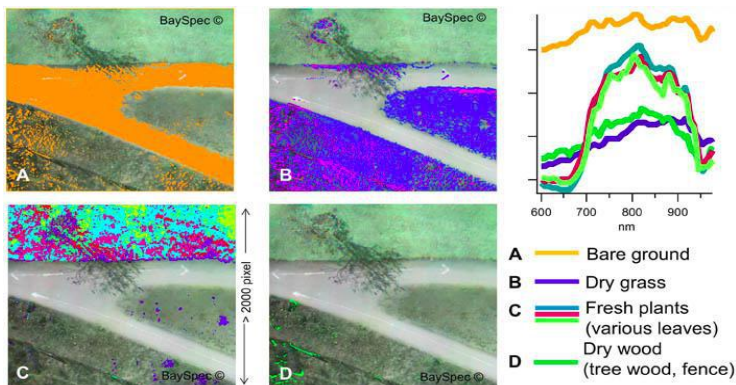
Figure 16: UAV Hyperspectral Camera Anonymous, 2020l)

Scientists have developed many indices for determining natural phenomena and observing the changes that occur by taking advantage of the measurements made with the help of white light and near infrared sensors. With the help of these indices, the quality and quantity of vegetative vegetation are evaluated (Bannari et al., 1996). However, NDVI

(Normalized Difference Vegetation Index) index is mostly used among these indices. This index is expressed as a normalized differential plant index. NDVI is a digital indicator, using visible and near infrared wavelengths of the electromagnetic spectrum. Index is formulated on the principle of not reflecting other objects at near infrared wavelengths, where vegetation reflects too much light. When plants are dehydrated or stressed, they reflect less light at near infrared spectrum, while reflecting the same amount of light at visible wavelength. Therefore, when these two types of data are combined, the presence of vegetation and health conditions can be determined. Different indices based on similar approaches have been and continue to be developed. Normalized Difference Vegetation Index (NDVI), Green Normalized Difference Vegetation Index (GNDVI), and Normalized Difference Red Edge Index (NDRE) are some of the indexes developed.

Crop yield is determined by instant monitoring and mapping systems during harvest or by yield measurement methods after harvest. Crop yield is determined by instant display and mapping systems during harvest or by yield measurement methods after harvest. These measurement methods include sensors (such as flow sensor, moisture sensor, work width sensor, harvest head) and a computer environment (Keskin and Görücü-Keskin, 2012). In parallel with the developments in image technology in recent years, precise and spectral cameras can be installed on UAVs to determine parameters such as the distribution of the plant in the field, plant health and frequency. In this way, mapping is carried out by making predictions about yield before harvest and even during plant development, without waiting for harvest or post-harvest. Lelong ve ark. (2008) İHA'ların küçük parsellerdeki buğday için miktarsal ölçümünde kullanılması konusunda araştırma yapmışlardır. As a result of the research, they determined the relationships between leaf area index-NDVI (Normalized Difference Vegetation Index) and nitrogen uptake-GNDVI (Green Normalized Difference Vegetation Index) with the help of UAV. Berni et al. (2009) measured leaf area index, chlorophyll content, water stress and plant temperature using thermal and multispectral image sensors on the UAV. Geipel et al. (2014) made a mid-season product yield estimation with the help of spectral and spatial modeling based on aerial images and product surface models taken with the help of UAVs.

Soil characterization and mapping systems are particularly important for variable level fertilizer applications (Figure 15). In this system, soil fertility (plant nutrients), physical (soil type, compaction, organic matter content, etc.) and chemical (soil pH level, cation exchange capacity) characteristics, and irrigation and drainage characteristics are taken into account (Sharp and Visible-Sharp, 2012). Before the automatic soil sampling tools were developed and became widespread, the necessary

analyzes to determine the soil properties were made by taking soil samples from the field and taking them to the laboratory. However, thanks to special cameras and sensors mounted on the UAV in recent years, mapping operations have been carried out in a shorter time. Gago et al. (2015) examined the plant-water relationships in the plant-scale study of scanning images obtained from different types of UAVs such as unmanned helicopters, multirotors, and fixed wings, and concluded that UAVs are useful in irrigation management. Aldana-Jague et al. (2016) conducted research on 2 hectares of land with drones equipped with multispectral cameras (flying at 120 m altitude) to determine the amount of organic carbon in the soil and reported that it has a potential use area. Neely et al. (2016) reported that soil properties affect crop yield and quality, and that they can predict crop yield at the end of the season by installing multispectral cameras on the UAV.

In the crop and field conditions monitoring systems, it is aimed to monitor the plant and field status on foot or by vehicle and to obtain border maps. Although applications with vehicles are faster than applications by foot, technological developments show that UAVs can also be used in this area. Data obtained on a foot or off-road vehicle, in limited areas or over a long period of time, is then loaded into the computer and evaluated. In applications made with UAVs, it is displayed with the help of software. The use of UAVs not only saves time with higher resolution images at low altitudes, but also offers the opportunity to monitor larger areas in a short time and take precise measurements by scanning the entire field surface. Zarco-Tejada et al. (2013) reported that UAVs equipped with high-resolution hyperspectral cameras can be used to determine the content of leaf carotenoid in vineyards. Mesas-Carrascosa et al. (2015) reported that UAV images can be used to determine soil and green parts (crops and weeds) for weed management specific to the region during the growing season. Ehsani and Maja (2013) stated that human-based observations on product health may lead to loss of time, cost increase and human errors, whereas UAV observations will be more effective. Zorlu (2016) monitored the development process of the cotton plant with UAVs and made evaluations about its development. The purpose of remote sensing systems is to measure and monitor from a certain height and distance without contacting the field and / or plant. Measurement and monitoring heights can vary from a pole planted in the field to the satellite in space. Measurement and imaging from the pole can be fixed or mounted on an off-road vehicle. While the measurements and images taken from the satellite can be monthly, weekly or daily, it is possible to take measurements and images with UAVs at desired altitudes and at the desired time - day and hour. Maps obtained by taking up-to-date images at the desired time and area used in many areas can be used as an alternative to satellite images. In the next stage, it can assist in fertilization, land

reclamation, urban planning, land use and planning. Stehr (2015) reported that the image taken from 15 cm resolution UAV cameras is 40,000 times better than the average satellite data and 44 times better than the best commercial satellite image. Matese et al. (2015) compared the NDVI images obtained from a vineyard by using UAVs, planes and satellites as remote sensing platforms. They reported that UAVs are suitable in small areas, 5 ha is the threshold, and satellite images can be viewed at a lower cost in areas above 5 ha. Ehsani and Maja (2013) concluded that low altitude UAVs are better than traditional aerial images when using thermal and visible / near infrared images in distinguishing healthy and stressed trees.

Classification of UAVs

Today, UAVs in many different shapes, sizes, configurations and characters are produced (Table 1). Classifications based on flight range, altitude and wing structure are mostly used (Table 2). (Blyenburgh, 1999; Bento, 2008; Şahin, 2011).

Table 1. NATO UAS Classification (Szabolcsi, 2016)

NATO UAS CLASSIFICATION						
Class	Category	Normal Employment	Normal Operating Altitude	Normal Mission Radius	Primary Supported Commander	Example Platform
Class III (> 600 kg)	Strike/Combat"	Strategic/National	Up to 65,000 ft	Unlimited (BLOS)	Theatre	Reaper
	HALE	Strategic/National	Up to 65,000 ft	Unlimited (BLOS)	Theatre	Global Hawk
	MALE	Operational/Theatre	Up to 45,000 ft MSL	Unlimited (BLOS)	JTF	Heron
Class II (150 kg – 600 kg)	Tactical	Tactical Formation	Up to 18,000 ft AGL	200 km (LOS)	Brigade	Hermes 450
Class I (< 150 kg)	Small (>15 kg)	Tactical Unit	Up to 5,000 ft AGL	50 km (LOS)	Battalion, Regiment	Scan Eagle
	Mini (<15 kg)	Tactical Subunit (manual or hand launch)	Up to 3,000 ft AGL	Up to 25 km (LOS)	Company, Platoon, Squad	Skylark
	Micro ** (<66 J)	Tactical Subunit (manual or hand launch)	Up to 200 ft AGL	Up to 5 km (LOS)	Platoon, Squad	Black Widow

UAVs are divided into two groups according to the wing type as fixed wing and rotary wing . Although fixed-wing (aircraft) UAVs perform fast and long-range missions, they cannot stay fixed in the air on the target and cannot be used very close to the target surfaces. Due to their high degree of control, rotary wing (helicopter) UAVs fly very close to the target surface, but are used for shorter times and distances (Jurdak et al., 2015). Fixed-wing UAVs are more advantageous to use than rotary-wing UAVs with features such as simple construction, easier maintenance and

repair, long flight time, more area coverage in one flight and higher flight speed (Anonymous, 2016i).

Table 2: Classification of UAVs (Govorcin et al., 2014)

Name of category	Acronym	Weight [kg]	Range [km]	Flight Altitude [m]	Endurance [hours]
Micro	Micro	<5	<10	250	1
Mini	Mini	25-150	<10	150-300	<2
Close Range	CR	25-150	10-30	3000	2-4
Short-Range	SR	50-250	30-70	3000	3-6
Medium Range	MR	to 1250	70-200	5000	6-10
Medium Range Endurance	MRE	to 1250	>500	8000	10-18
Low Altitude Deep Penetration	LADP	to 350	>250	50-9000	0,5-1
Low Altitude Long Endurance	LALE	<30	>500	3000	>24
Medium Altitude Long Endurance	MALE	to 1500	>500	14 000	24-48

Factors Affecting UAV Market Development

Although it creates uncertainty in long-term projection due to national and international (ICAO, FAA, EU) legislative formations that regulate the market and implementation, it is seen that the growth in the market will be at the level of 10%. The speed of development of the UAV sector is influenced by the UAV testing and certification made by the authorized national / international organizations, legal restrictions on privacy, collision avoidance and developments in complex airspace management systems.

It is estimated that the UAV market, which was 10.1 Billion USD as of 2015, will grow to 14.9 Billion USD in the 2015-2020 period with a growth of 8.12%. Here, the biggest share in demand is formed by the defense and security sectors, including the military, security and emergency situations. More than 65% of the UAV market is the USA. Israel, China, Britain, Australia, Canada, France and Turkey are the other important market players. In terms of employment, it will create a new job opportunities in the world in the next 10 years (Juul, 2015, UAV Market, 2015).

Leading manufacturers that create a market with their innovations in the sector are generally companies that have started as start-ups in the last 10-15 years. For example, DJI (China), Parrot (France) AeroVironment (USA) in the USA, 3D Robotics (USA), Titan Aerospace (USA), Aurora Flight Sciences (USA) are the leading companies in the industry (Canis, 2015). In addition to the UAV software developed by the manufacturers, open source UAV software platforms for flight planning, flight control, sensor control and data transfer are developed by open source platforms including Intel and Linux. In addition, the rapid development in the UAV sector has revealed the need for standardization. In this framework, the

study has been initiated to make the UAV software developed by ETHZ the basic standard. The UAV technology developed by Google will open up a new area of use as well as being very large-sized (larger than passenger aircraft) for mapping, communication and internet access, taking its power from solar energy, and having the ability to navigate beyond the Troposphere, in the Stratosphere (~ 20 km).

Today, the use of UAVs can pose security threats, as revealed in various instances (UAVs that landed in the White House by mistake in 2015, UAVs flying around airports). In UAVs for defense and military purposes, the number of accidents obtained with open source information in the 2007-2014 period is over 200. In this respect, it is imperative that UAVs be examined in terms of safety. While it is an essential need to establish the legal infrastructure of the UAV sector only due to accidents that have occurred or are likely to happen; beyond that, insurance, trade, certification, security etc. The fact that there is a need for more comprehensive legislation covering areas cannot be ignored.

In addition to national legislation, UAV regulations are based on the International Civil Aviation Convention set forth by the Chicago Conference (UN Chicago Convention-1944) and the International Civil Aviation Organization (ICAO) publications established on this basis (1947) and international conventions (Cary, et.al., 2011, UAS ICAO, 2011). Following the regulation published by ICAO in 2011 in terms of creating UAV legislation; USA, EU, Australia, Sweden, UK, Canada etc. Some countries have followed their legislative practice and experience.

RESULTS

The use of UAV has been increasing due to technological developments and increases in labor costs in recent years. It should be expected that UAVs will become more widespread as the legal regulations regarding their use are completed.

The use of UAVs in agriculture can be profitable for large farms. Drone applications and use with a state-supported organization will be suitable for these farmers. These tools should be expected to become more widespread with their efficiency-enhancing and time-saving advantages.

In the past, UAVs were mostly produced for military missions. It has evolved in parallel with the technological developments in time and has come to the present day and started to be used in various applications for civilian purposes since 2010.

Thanks to the camera and battery technology developed in recent years, high resolution images can be obtained from hundreds of hectares of field in a single flight time with UAVs. These studies can be carried out in a shorter time without the need for human and labor. In addition, it

provides the opportunity to receive images even in cloudy weather conditions where images cannot be taken from satellites.

Unlike other sectors, there is no need for additional equipment other than special camera and sensor devices in the use of UAVs in agriculture. In fact, research has shown that 85% savings are achieved in forest seeding applications by adding additional cameras - sensors to vehicles that are out of use in military use. However, legal restrictions and security reservations (private life, terrorist activities, etc.) remain as an obstacle to their spread.

LITERATURE

1. Aldana-Jague; E., Heckrath, G., Macdonald, A., van Wesemael, B., van Oost, K. (2016). UASbased soil carbon mapping using VIS-NIR (480-1000 nm) multi-spectral imaging: Potential and limitations. Geoderma 275: 55-66.

2. Anonymous (2020a). https://img.militaryaerospace.com/files/base/ebm/mae/image/2019/02/content_dam_mae_online_articles_2019_02_heron_uav_26_feb_2019.png?auto=format&w=720. Access Date: 12.11.2020

3. Anonymous (2020b). https://www.laodikeiaballoons.com/the-experience/history-of-balloning. Access Date: 12.11.2020

4. Anonymous (2020c). https://www.popularmechanics.com/technology/gadgets/g2983/the-best-drones-review/ . Access Date: 12.11.2020

5. Anonymous (2020e). https://www.amazon.in/Robodo-Electronics-Controller-Brushless-Quadcopter/dp/B00MTJ8QP6. Access Date: 12.11.2020

6. Anonymous (2020f). https://industrial.panasonic.com/content/data/BT/pictures/lp3_lithium-ion_01_e.jpg. Access Date: 12.11.2020

7. Anonymous (2020g). https://encrypted-tbn0.gstatic.com/images?q=tbn%3AANd9GcTxRoBwvSpDZBgNNwyG_upc6dVn83dLJoIp1A&usqp=CAU. Access Date: 12.11.2020

8. Anonymous (2020h). https://wingtra.com/drone-photogrammetry-vs-lidar/ Access Date: 12.11.2020

9. Anonymous (2020i). https://track32.nl/portfolio/drone-for-mapping-weed-populations/. Access Date: 12.11.2020

10. Anonymous (2020j). https://meticulousblog.org/top-10-companies-in-agriculture-drone-market/. Access Date: 12.11.2020

11. Anonymous (2020k). https://nias-uas.com/create-map-drone-data-real-time/. Access Date: 12.11.2020

12. Anonymous (2020l). https://www.bayspec.com/spectroscopy/oci-uav-hyperspectral-camera/. Access Date: 12.11.2020

13. Anonymous (2016a). http://www.notablebiographies.com/CaCh/Cavendish-Henry.html. Access Date: 29.11.2016.

14. Anonymous (2016b). Access Date: 29.11.2016 http://wwwgroups.dcs.st-and.ac.uk/history/Biographies/Biot.html

15. Anonymous, 2016c. ballooning/civil-warballooning.html?referrer=https://www.google.com.tr/ Access Date: 29.11.2016

16. Anonymous (2016c). http://www.history.com/news/attack-ofjapans-killer-wwii-balloons-70-years-ago. Access Date: 29.11.2016

17. Anonymous (2016d). https://en.wikipedia.org/wiki/Timeline_of_aviation_%E2%80%93_19th_century. Access Date: 30.11.2016

18. Anonymous (2016e). http://www.rubincenter.org/2010/09/rodman-2010-09- 07/ Access Date: 30.11.2016

19. Anonymous (2016f). http://www.dohenydrones.com/newsfixed-wing-versus-rotary-wing Access Date: 30.11.2016

20. Anonymous (2016g). http://newatlas.com/uav-cropdusting/27974/ Access Date: 30th November 2016

21. Anonymous (2010). Unmanned aircraft systems: Terminology, definitions and classification, Joint doctirin note3/10, United Kingdom Ministry of Defence, May 2010, 21pp, United Kingdom.

22. Artale, V., Ricciardello, A., Milazzo, C. (2013). Mathematical Modelling of Hexacopter, Applied Mathematical Sciences 7(97):4805-4811.

23. Bannari, A., Morin, D., Bonn, F., Huete, A. R.(1995) 'A Review of Vegetation Indices', Remote Sensing Reviews, 13: 1, 95-120.

24. Bento, M.F. (2008) Unmanned Aerial Vehicle (An Overview). (www.insidegnss.com/auto/janfeb08- wp.pdf (Access Date: May 2016)).

25. Berni, J.A.J., arco-Tejada, P.J., Suarez, L., Fereres, E. (2009). Thermal and narrowband multispectral remote sensing for vegetation monitoring from an unmanned aerial vehicle. IEEE Transactions on Geoscience and Remote Sensing 47(3): 722-738.

26. Blyenburgh, P. V. (1999). UAVs: an Overview. Uninhabited Aerial Vehicles (UAVs), Air and Space Europe Vol:1, No:5/6. pp. 43-47

27. Canis, B. (2015): Unmanned Aircraft Systems 8UAS): Commercial Outlook for New Industry, Congressional Research Service, CRS Report, 7-5700, R44192

28. Cary, L, Coyne, J. (2011): ICAO Unmanned Aircraft Systems (UAS), Circular 328, 2011-2012 UAS Yearbook - UAS: The Global

Perspective – 9th Edition - June 2011 - Blyenburgh & Co © - www.uvs-info.com - Page: 112/216

29. Colomina, I., Molina, P. (2014): Unmanned Aerial System for Photogrammetry and Remote Sensing, Isprs Journal Of Photogrammetry And Remote Sensıng, June 2014

30. Dean, H., Fujikawa, S. J., Linden, D. S., Daughtry, C. S., McCarty, G. W., Hunt, R. (2010). Acquisition of NIR-Green-Blue Digital Photographs from Unmanned Aircraft for Crop Monitoring. Remote Sensing, 290-305.

31. De Castro A., I., Jurado-Expósito M., Peña-Barragán J., M., López-Granados, F. (2012) Airborne Multi-spectral Imagery for Mapping Cruciferous Weeds in Cereal and Legume Crops. Precis Agric 13(3): 302–321. doi: 10.1007/s11119-011-9247-0.

32. Dictionary.com, 2016, http://dictionary.reference.com/browse/uav?s=t, Access Date: 14th January 2016.

33. Draeyer B., Strecha, C. (2014): White paper: How accurate are UAV surveying methods? Pix4D White paper, February 2014

34. Ehsani, R., Maja, J.M. (2013). The rise of small UAVs in precision agriculture. Resource 20(4): 18- 19.

35. Gago, J., Douthe, C., Coopman, R.E., Gallego, P.P., Ribas-Carbo, M., Flexas, J., Escalona, J., Medrano, H. (2015). UAVs challenge to assess water stress for sustainable agriculture. Agricultural Water Management 153:9-19.

36. Geipel, J., Link, J., Claupein, W. (2014). Combined spectral and spatial modeling of corn yield based on aerial images and crop surface models acquired with an unmanned aircraft system. Remote Sensing 6 (11): 10335-10355.

37. Gibbons, G., 2000. Turning a farm art into science an overview of precision farming. URL: http://www.precisionfarming.com.

38. Govorcin, M., Pribicevic, B., Dapo, E. (2014). Comparison And Analysis Of Software Solutions For Creation Of A Digital Terrain Model Using Unmanned Aerial Vehicles. 14th International Multidisciplinary Scientific Geoconference Sgem 2014 - Geoconference On Informatics

39. Jurdak, R., Elfes, A., Kusy, B., Tews, A., Hu, W., Hernandez, E., Kottege, N., Sikka, P. (2015). Autonomous surveillance for biosecurity. Trends in Biotechnology 33(4): 201-207.

40. Juul, M. (2015): Civil drones in the European Union, European Parliment, EPRS | European Parliamentary Research Service, Octover 2015

41. Haser, A.B., 2010. Bu insansız hava aracından daha önce yapmamış mıydık?, Bilim ve Teknik Dergisi, Aralık sayısı.

42. Herwitz, S. R., Johnson, L., Dunagon, S., Higgins, R., Sullivan, D., Zheng, J., Lobitz, B., Leung, J., Gallmeyer, B., Aoyagi, M., Slye, R., Brass, J., Witt, G. (2003). Coffee field ripeness detection using high resolution imaging systems on a solar-powered UAV, Proc. 30th Symp. Rem. Sens. Environ., TS-12.3, 3 pp., Honolulu, HI.

43. Kahveci, M., Can, N. (2017). S.Ü. Müh. Bilim ve Tekn. Derg., c.5, s.4, ss. 511-535. İnsansız Hava Araçları: Tarihçesi, Tanımı, Dünyada Ve Türkiye'deki Yasal Durumu. Selcuk Univ. J. Eng. Sci. Tech., v.5, n.4, pp. 511-535, ISSN: 2147-9364 (Elektronik) DOI: 10.15317/Scitech.2017.109

44. Keskin, M., Gorucu-Keskin, S. (2012). Hassas Tarım Teknolojileri. Hatay. Mustafa Kemal Üniversitesi Yayınları No:35. 210 s.

45. Koger, C., H., Shaw, D.R., Watson, C., E, Reddy, K.,N. (2003) Detecting Late Season Weed Infestations in Soybean (Glycine max). Weed Technol 17: 696-704. doi:10.1614/WT02-122.

46. Kurak, S., Hodzic, M. (2018). Control and Estimation of a Quadcopter Dynamical Model. Periodicals of Engineering and Natural Sciences, Vol:6, No:1, 63-75

47. Lelong, C.C.D. Burger, P., Jubelin, G., Roux, B., Labbe, S., Baret, F. (2008). Assessment of unmanned aerial vehicles imagery for quantitative monitoring of wheat crop in small plots. Sensors 8:3557-3585.

48. Mesas-Carrascosa, F.J., Torres-Sanchez, J., Clavero-Rumbao, I., Garcia-Ferrer, A., Pena, J.M., BorraSerrano, I., Lopez-Granados, F. (2015). Assessing optimal flight parameters for generating accurate multispectral orthomosaicks by UAV to support site-specific crop management. Remote Sensing 7: 12793-12814.

49. Neely, H.L., Morgan, C.L.S., Stanislav, S., Rouze, G., Shi, Y., Thomasson, J.A., Valasek, J., Olsenholler, J. (2016). Strategies for soil-based precision agriculture in cotton. Proc. SPIE 9866, Autonomous Air and Ground Sensing Systems for Agricultural Optimization and Phenotyping.

50. Poksawat, P., Wang, L. (2017). Automatic Tuning of Hexacopter Attitude Control Systems with Experimental Validation. 21st

International Conference on System Theory, Control and Computing Conference.

51. Rango, A., Laliberte, A., Steele, C., Herrick, J. E., Bestelmeyer, B., Schmugge, T., Jenkins, V. (2006). Using Unmanned Aerial Vehicles for Rangelands: Current Applications and Future Potentials. Environmental Practice, 159-168.

52. Shibusawa, S. (1998). Precision Farming and Terra-mechanics. Fifth ISTVS Asia-Pacific Regional Conference in Korea, October 20-22.

53. Stehr, N. (2015). Drones: The newest technology for precision agriculture. Nat.Sci.Educ. 44:89-91. Şahin, M. (2011). Sabit Kanatlı Mini İnsansız Hava Aracının Geliştirilmesi Ve Ağaçlandırma Çalışmalarında Kullanımı. Erciyes Üniv. Fen Bil. Ens. Yüksek Lisans Tezi, Kayseri,91 s.

54. Szabolcsi, R. (2016). Beyond Training Minimums – A New Concept of the UAV Operator Training Program. International conference Knowledge Based Organization.

55. Swain, K. C., Thomson, S. J., Jayasuriya, H.P.W. 2010. Adoption of an Unmanned Helicopter for Low-Altitude Remote Sensing to Estimate Yield and Total Biomass of a Rice Crop.

56. Şahin, M. (2011). Sabit Kanatlı Mini İnsansız Hava Aracının Geliştirilmesi Ve Ağaçlandırma Çalışmalarında Kullanımı. Erciyes Üniv. Fen Bilimleri Ens. Yüksek Lisans Tezi, Kayseri, 91 s

57. Şener, M., Pehlivan, M., Tekiner, M., Alkan, C., Ozden, U.E., Erdem, T., Celen I.H., Seren, A, Aydın, S.A., Kolsuz, H.U., Seyrek, K, Gurescı, G., Kose G., Turan, L. (2019). Monitoring of irrigation schemes by using thermal camera mounted UAVs, Fresenıus Envıronmental Bulletın, Vol. 28:6, Pp. 4684-4691.

58. Şener, M., Boyraz Erdem, D., Alkan, C., Celen, I.H., Erdem, T. (2018a). Unmanned Aerial Vehicle (UAV) for Monitoring Agricultural Activity, Journal of Scientific and Engineering Research, vol. 5, pp. 137-139.

59. Şener, M., Pehlivan, M., Tekiner, M., Alkan, C., Ozden, U.E., Erdem, T., Celen I.H., Seren, A, Aydın, S.A., Kolsuz, H.U., Seyrek, K, Gurescı, G., Kose G & Turan, L. (2018b). Unmanned Aerial Vehicle (UAV) based remote sensing for crop pattern mapping, Turkey, Fresenıus Envıronmental Bulletın, Vol. 27, Pp. 8831-8837.

60. Torun, A. (2016): Integrating Geospatial Technologies: Reflections on Intergeo 2016, GIM International, November.

61. UAV Market (2015): The Global UAV Market 2015–2025, Ref Cpde: DF0060SR, Jan 2015 UAS ICAO (2011): Unmanned Aircraft Systems (UAS), Cir 328 AN/190, International Civil Aviation Organization UAS PIEngineering (2012): Aspects of Accuracy in UAS Photogrammetry, White Paper Version 1.0.4PIEneering Ltd.

62. Uz, U. (2019). Hexacopter Yapısında Bir İnsansız Hava Aracı İle Elektronik İlaçlama/Sulama Sisteminin Oluşturulması. T.C. İstanbul Gelişim Üniversitesi Fen Bilimleri Enstitüsü Umut Uz Yüksek Lisans Tezi Mekatronik Mühendisliği Anabilim Dalı, 95 sayfa., İstanbul.

63. Zorlu, F. (2016). İnsansız Hava Aracı ile Pamuk Bitkisinin Gelişim Sürecindeki Değişimlerin İzlenmesi ve Değerlendirilmesi. Harran Üniversitesi Fen Bilimleri Ens. Yüksek Lisans Tezi, Şanlıurfa, 56s.

64. Zou, J., Su, K., Tso, H. (2012). The modeling and implementation of tri-roto flying robot. Artificial Life and Robotics, 17, 86-91.

65. Turner, D., Lucieer, A., Watson, C. (2011). Development of an Unmanned Aerial Vehicle (UAV) for hyper resolution vineyard mapping based on visible, multispectral, and thermal imagery

HISTORICAL RELIABILITY EVALUATION OF POWER DISTRIBUTION SYSTEMS BASED ON MONTE CARLO SIMULATION METHOD[*]

Mohammed Wadi[1] & Abdulfetah Shobole[2]

[1]*(Asst. Prof.) Istanbul Sabahattin Zaim University, e-mail: mohammed.wadi@izu.edu.tr*
iD ORCID *0000-0001-8928-3729*

[2]*(Asst. Prof.) Istanbul Sabahattin Zaim University, e-mail: abdulfetah.shobole@izu.edu.tr*
iD ORCID *0000-0002-3180-6504*

1. INTRODUCTION

It is crucial to assess power systems' reliability to get the most accurate and appropriate planning, operation, and maintenance decisions. Historical assessment and predictive assessment are widely used methods to assess the reliability of a distribution network. Predictive reliability assessment is classified into two methods, analytical method and simulation method. Besides, analytical methods can be categorized into Markov modeling and network modeling groups (Koster et al., 1978). Simulation methods are considered the most flexible methods. However, it is computationally-burden. Since the historical reliability assessment based on actual data, which is exceptionally crucial in reliability analysis and can be a reference for comparison with other reliability assessment techniques (A. A. Chowdhury, 2005), it is preferable by most utilities rather than a predictive assessment. Thus, the utilities continually need to preserve and collect the data for plans and studies. The actual collected data would improve the system analyses in the future and the system's overall reliability. The significance of reliability studies for utility operators is crucial to determine the parts that are experiencing repeated failures, the areas of the highest amount of energy not supplied, and the areas of weak protection system (Wilson et al., 2006).

Many valuable works have been presented on historical reliability assessment (Allan, 1994)(Kim & Singh, 2010)(Baharum et al., 2013)(Abunima et al., 2018). Baharum et al. (Baharum et al., 2013), assessed the historical reliability based on the collected from an electricity distribution company in Baghdad, Iraq, and the two-parameter Weibull

---

[*] Reliability Assessment of Closed Ring Power Distribution Systems

function. The statistical measures obtained by this analysis revealed the weakest parts such as transformers and circuit breakers. In (Feng, 2006), the actual data of 13 utilities in Canada are used to perform historical reliability analysis to determine the performance and assess the financial risk for their power distribution networks. Besides, it is established the regulations that are required to specify the reward/penalty levels. In (Wallnerström, 2008), the actual data for one Swedish power distribution network for three years (2004 -2006) are used to perform historical reliability analysis. The obtained result verified that the annual outage cost per customer was more than 500 €. In (A. A. Chowdhury, 2005), the actual data for two Canadian power distribution networks are utilized to improve the performance-based regulation in a deregulated environment to investigate the level of service reliability of these networks.

(Billinton & Pan, 2004) introduced a historical reliability assessment based on actual reliability data taken from the Canadian Electricity Association (CEA) service continuity reports. The study presented package of reward/penalty structure based on the historic reliability record could be integrated into a performance-based regulation plan. Historic reliability data are therefore, extremely crucial for distribution system risk assessment and remedial work in this new regime.

Monte Carlo Simulation (MCS) for reliability assessment in power systems also have been appeared in the literature (Thoemmes et al., 2010)(Schoemann et al., 2014)(Wijekularathna et al., 2019)(Godha et al., 2011)(Al-Wafi et al., 2016)(Bakkiyaraj & Kumarappan, 2010).

MCS techniques based on non-sequential state transition sampling reliability evaluation of power systems is proposed(Bakkiyaraj & Kumarappan, 2010). This method is applied to Roy Billinton Test System (RBTS) and verified its effectiveness compared with the sequential simulation. In (Godha et al., 2011) MCS to assess the costs due to electric supply interruptions in distribution power system. Feeder 1 of RBTS Bus-2 is utilized to carry out the simulation and to confirm the applicability of MCS.

The sequential time MCS is presented to assess distribution systems' reliability due to severe weather (Cadini et al., 2017). MCS in combining with stochastic models for describing uncertain weather conditions with a cascading failure model based on a DC approximation of the power flows and a proportional re-dispatch strategy is proposed. The sequential time MCS method was tested by IEEE14 reference power system. The obtained results show that rare, but highly severe (in terms of duration and intensity), weather events may have, in general, a significant impact on the distributions of the reliability performance indices of a power transmission grid.

Also, in (Silva et al., 2016), the Quasi-Sequential MCS is also used to assess the distributed generation's such as photovoltaic connection on the power quality indices of distribution networks impact on system reliability. The method was tested by a real distribution feeder with 1560 nodes. The obtained results show that PV penetration can cause about 31% of improvements in the voltage conformity indices, and increases the lifespan of the voltage regulators as a result of a reduction about 20% in the number of tap changes.

This Chapter introduces historical reliability analysis for a real 4-feeder power distribution network in Istanbul. Then, MCS is utilized to estimate its future reliability. The obtained results from historical and MCS are analyzed and compared.

In this Chapter, the following essential issues shall be discussed:

• The value of reliability assessment analyses in planning, design, and maintenance of power distribution networks;

• Evaluating the reliability of actual 4-feeder power distribution network in Istanbul via historical assessment;

• Evaluating the reliability based on the MCS method;

• Comparing the historical and MCS methods results;

• They are presenting several vital recommendations for power utilities and electric companies to improve their systems' reliability.

2. RELIABILITY CALCULATIONS

The components of any electric system are connected in two ways, series, and parallel. Similarly, power distribution networks' components are connected in series, parallel, or combination of series and parallel. Calculation of load point (LP) indices, i.e., failure rate (λ), mean outage time (r), and the mean annual unavailability (U), is mandatory to calculate the system reliability indices. SAIFI that defined as the total number of customer interruptions by the total number of customers served, SAIDI defined as the total customer interruption duration by the total number of customers served, CAIDI that defined as the total customer interruption duration by the total number of customer interruptions, ASAI defined as the customer hours of available service by customer hours demand, expected energy not supplied (ENS) is defined as the product sum of average LP demand and the average outage time per year, and average expected energy not supplied (AENS) is defined as the expected ENS by the total number of customers served are the most crucial system reliability indices (Ali A. Chowdhury & Koval, 2009). Tables 1 and 2 present the formulas to calculate LP indices for series and parallel systems, respectively (Mohammed Wadi et al., 2017).

Table 1: LP reliability indices for series systems

# Series Component	λ_s [failure/year]	r_s [hour]	$U_s = \lambda_s r_s$ [hour /year]
n Component	$\sum_{i}^{n} \lambda_i$	$\dfrac{\sum_i \lambda_i\ r_i}{\sum_i \lambda_i}$	$\sum_{i} \lambda_i\ r_i$

Table 2: LP reliability indices for parallel systems

λ_p [failure/year]	r_p [hour]	$U_p = \lambda_P r_P$ [hour /year]
$\dfrac{\lambda_1\lambda_2(r_1 + r_2)}{1 + \lambda_1 r_1 + \lambda_2 r_2}$ $\lambda_1\lambda_2(r_1 + r_2)\ if\ \lambda_i r_i \ll 1$	$\dfrac{r_1 r_2}{r_1 + r_2}$	$\lambda_1\lambda_2 r_1 r_2$
$\lambda_1\lambda_2\lambda_3(r_1 r_2 + r_2 r_3 + r_3 r_1)$	$\dfrac{r_1 r_2 r_3}{(r_1 r_2 + r_2 r_3 + r_3 r_1)}$	$\lambda_1\lambda_2\lambda_3 r_1 r_2 r_3$

3. DISTRIBUTION NETWORK STRUCTURE IN TURKEY

Generally, the topology of electric distribution systems is a radial configuration or mesh configuration, but radial-operated such as the distribution network given in Figure 1. Besides, a substantial part of Istanbul's local electric distribution company is also ring-designed but radial-operated, as shown in Figure 2. Power distribution utilities have been attempting to develop their networks by modifying them into closed-ring in lieu of radial networks based on state-of-the-art bidirectional protection, control, and communication devices (Suthapanun et al., 2015), (Xu & Zou, 2010). Likewise, automatic power electronic converter switches in lieu of manual-operated switches play a vital role in such networks (Pattabiraman et al., 2019).

There are many attempts from the Scientific and Technological Research Council of Turkey (TUBITAK) to modify the distribution system's automation and configuration in Turkey. TUBITAK-UZAY (Ozay et al., 1999) proposed new functions for fault detection and service restoration for BEDAS in Istanbul, known as the TUBITAK Distribution Automation System (TUDOSIS).

4. DESCRIPTION OF SYSTEM CONFIGURATION

The historical data for the 4-Feeder sector of the real power distribution network in Istanbul are utilized to evaluate its reliability. The 4-feeder system consists of four 34.5 kV distribution feeders, twenty-four buses, 40 distribution lines, 62301 customers, and a total load up to 200 MW, as shown in Figure 2.
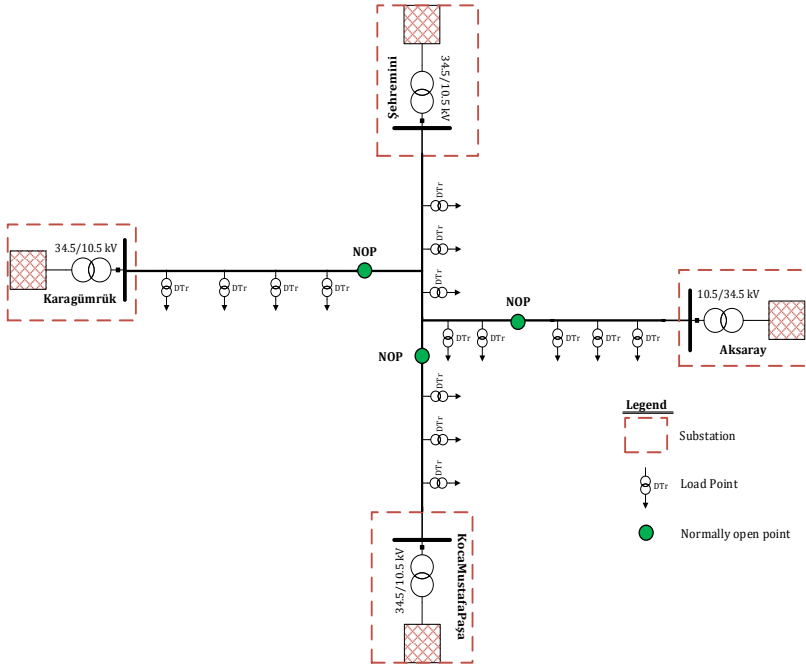
Figure 1. Electric distribution section meshed-designed radial-operated
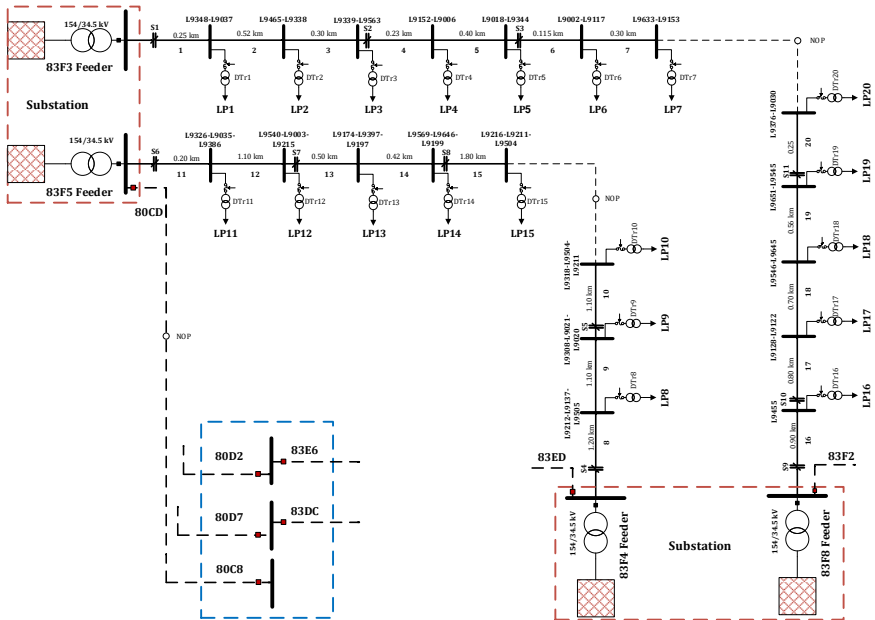
Figure 2. Single line diagram of the 4-Feeders distribution system

For the 4-feeder system depicted in Figure 2, the historical assessment reliability can be evaluated based on the following data (Wadi et al., 2020):

- The failure data of each component,
- The outage time and the switching time data for each component,
- Average load and peak load for each LP,
- The number of customers at each LP,
- The length of the feeder's sections and laterals,

These are collected from local power distribution utilities in Istanbul and organized as depicted in Tables 3-7.

Table 3: Feeder's sections and laterals length data in km

SN*	F1[+]: 83F3	S. N	F2: 83F4	S. N	F3: 83F5	S. N	F4: 83F8
1	0.25	8	1.20	11	0.20	16	0.90
2	0.52	9	1.10	12	1.10	17	0.80
3	0.30	10	1.10	13	0.50	18	0.70
4	0.23	28	0.595	14	0.42	19	0.56
5	0.40	29	0.313	15	1.80	20	0.25
6	0.115	30	0.331	31	0.086	36	0.316
7	0.30			32	0.272	37	0.127
21	0.11			33	0.222	38	0.335
22	0.252			34	0.156	39	0.208
23	0.181			35	0.397	40	0.221
24	0.152						
25	0.273						
26	0.10						
27	0.217						

* **SN:** Section Number, [+]**F$_i$:** Feeder Number

Table 4: 4-Feeder load points load in kW

Load Point	Average Load/Customer	Peak load/ Customer
1-7, 11-15	2.50	3.125
8-10, 16-20	3.00	3.750

5. HISTORICAL RELIABILITY ASSESSMENT OF 4-FEEDER SYSTEM

The reliability indices for any system are classified into two groups, LP indices such as λ, *r*, and U. Furthermore, system indices such as System SAIFI, SAIDI, CAIDI, ASAI, ENS, and AENS as given in (Wadi et al., 2018). The historical assessment results from 2012 to 2014 are summarized in Tables 7 and 8. Besides, Figures 3, 4, 5, and 6 graphically show the obtained results.

Table 5: 4-Feeder customer data

Load Point	No. of Customers	Load Point	No. of Customers
1	3305	11	3281
2	1447	12	3571
3	866	13	4742
4	2378	14	6335
5	640	15	8023
6	209	16	2611
7	549	17	2866
8	5439	18	2103
9	5216	19	663
10	7322	20	735

Table 6: 4-Feeder switches locations

Feeder	Section No.
F1	*S (1,1), S (2,4), S (3,6)
F2	S (4,8), S (5,10)
F3	S (6,11), S (7,13), S (8,15)
F4	S (9,16), S (10,17), S (11,20)

*S (x, y): Switch location, where x is the number of switches, while y the number of sections

Examining Figure 3 shows that Feeder F4-83F8 has the smallest SAIFI, 0.0305, and 0.0611 interruption /customer for the years 2012-2013 and 2013-2014, respectively. Therefore, this feeder can be considered the most reliable feeder, and its customers encounter the least occurrence of sustained interruptions among all the feeders. On the other hand, the Feeder F3-83F5 has the highest SAIFI, 0.4679, and 0.2366 for 2012-2013 and 2013-2014.

Table 7: Feeders and system indices for the period 2012-2013

Feeders/Indices	SAIFI	SAIDI	CAIDI	ASAI	AENS
F1-83F3	0.1825	0.3499	1.9178	0.99996006	0.87
F2-83F4	0.0797	0.0964	1.2105	0.99998899	0.24
F3-83F5	0.4679	0.4952	1.0582	0.99994347	1.24
F4-83F8	0.0305	0.0285	0.9333	0.99999675	0.07
System-Average	0.1901	0.2425	1.2754	0.99988927	0.61

Table 8: Feeders and system indices for the period 2013-2014

Feeders/Indices	SAIFI	SAIDI	CAIDI	ASAI	AENS
F1-83F3	0.1245	0.0692	0.5557	0.99999210	0.17
F2-83F4	0.1408	0.1286	0.9133	0.99998532	0.32
F3-83F5	0.2366	0.1458	0.6162	0.99998336	0.36
F4-83F8	0.0611	0.0326	0.5333	0.99999628	0.08
System-Average	0.1408	0.0940	0.6681	0.99995706	0.24

Based on the 4-Feeder distribution power systems, the average failure and repair data for each component can be extracted by historical assessment. These data are indispensable to predict the system's reliability at any time using simulation assessment methods such as MCS. This analysis noticed that most failures were with the lines, and the most occurred faults are the earth fault and the phase-to-ground fault. Circuit breakers rarely experience faults, and the only failure with CB was taken place at 9540 current transformer (CT) related to the feeder F1-83F3 due

to the explosion of CB. Likewise, the failure of transformers also rarely occurred, for this system at 34.5/0.4 kV 9569 CT related to the feeder F3-83F5 registered one failure due to rats. Table 9 summarizes the reliability data. In this historical reliability analysis, only the distribution transformers, CBs, and distribution lines components are considered. The other components, such as relays, sectionalizers, and buses, are considered 100% reliable.
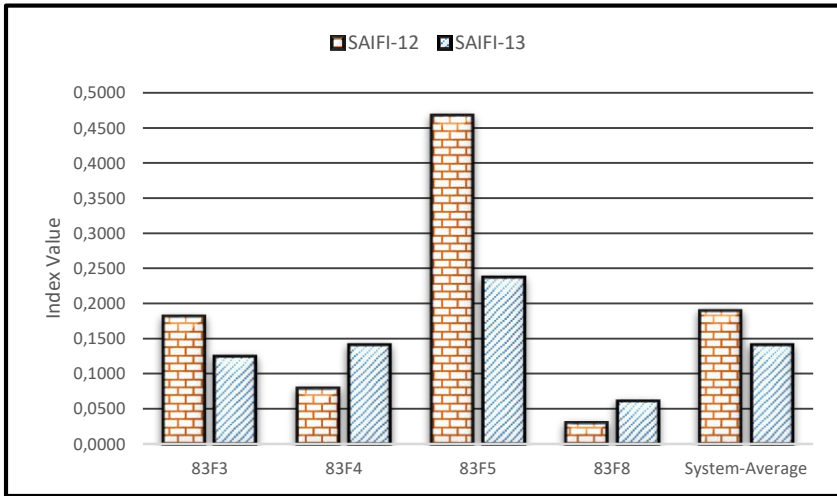
Figure 3. Feeder s and system SAIFI index for the period 2012-2014
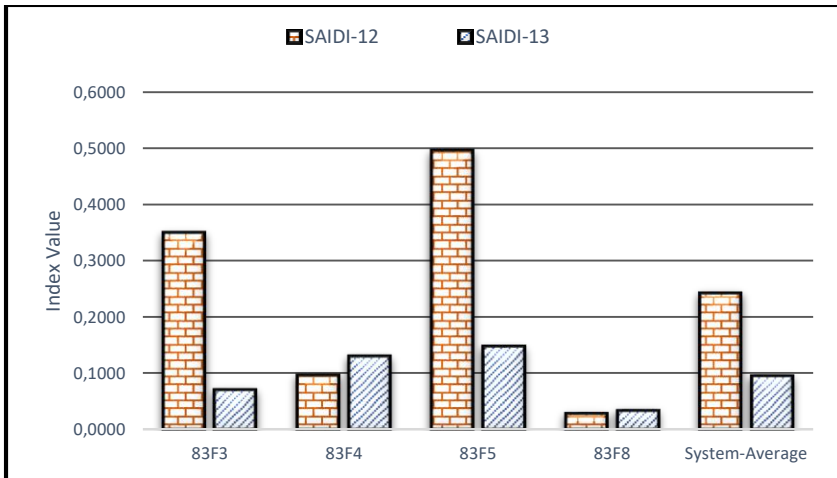
Figure 4. Feeders and system SAIDI index for the period 2012-2014

In the same manner, the feeder F4-83F8 has the least interruption duration with 0.0285 and 0.0326 *SAIDI* index for the years 2012-2013 and 2013-2014, respectively, as given in Figure 4. However, the feeder F3-

83F5 has the highest interruption duration with 0.4952 and 0.1458 SAIDI index for the years 2012-2013 and 2013-2014, respectively. Figure 5 provides a whole picture of the system by showing each feeder's reliability compared to others. It can be noticed that the feeder F4-83F8 has the highest reliability value, of 0.99988927 and 0.99995706 for the years 2012-2013 and 2013-2014, respectively.
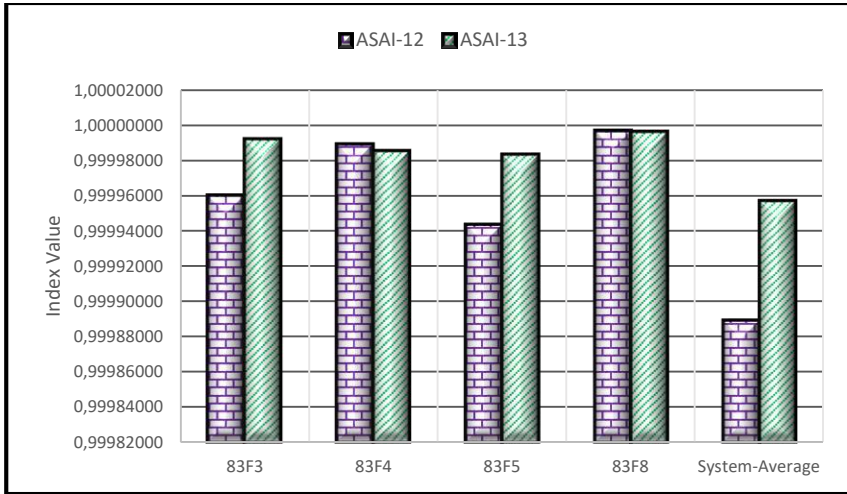
Figure 5. Feeders and system ASAI index for the period 2012-2014

Table 9: System reliability data for the period 2012-2014

Component	λ	r
34.5/0.40 kV Transformer	0.025	3.0
34.5/0.4 kV Circuit Breakers	0.025	2.0
34.5 kV Lines	0.050	1.5
0.4 kV Lines	0.125	1.0

It is crucial to calculate the ENS and AENS indices of different customers to estimate the interruptions costs. Figure 6 explains the AENS for the 4-Feeder distribution power system, and it is found that the feeder F3-83F8 is achieving the least AENS, i.e., 0.61 and 0.24 kWh/year/customer for the years 2012-2013 and 2013-2014, respectively.
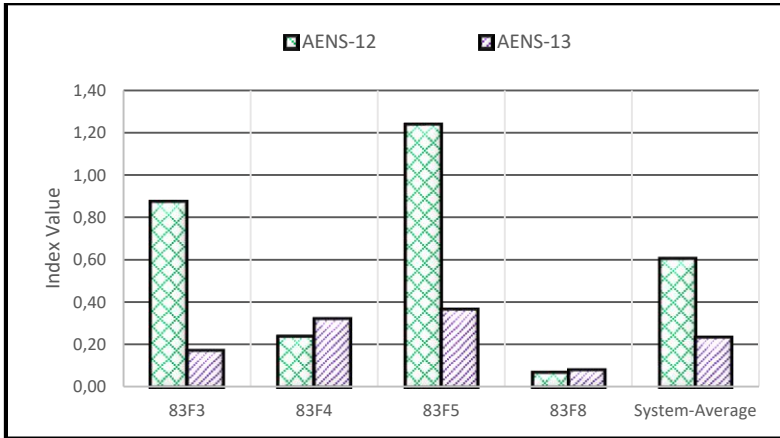
Figure 6. Feeders and system AENS index for the period 2012-2014

6. RELIABILITY ASSESSMENT VIA MONTE CARLO SIMULATION

Monte Carlo simulation method occupies a distinctive standing in a lot areas, such as nonlinear mathematical problems, stochastic simulation, medical diagnostic, engineering system analysis, and reliability assessment (Wadi et al., 2020). MCS introduces a powerful approach to evaluate the reliability of any system (Zhang et al., 2011). MCS's primary task to assess power systems' reliability is to generate an artificial history of faults for each component in the power system, i.e., lines, transformers, and circuit breakers. The failure process was frequently modeled using Weibull or Exponential distribution, while Lognormal or Exponential distribution for modeling repair process (Martinez-Velasco & Guerra, 2016). In this analysis, Exponential distribution is used for modeling both Time-to-Failure (TTF) and repair to time (TTR) as in equation (1) (Haroonabadi & Haghifam, 2011)

$$TTF = -\frac{1}{\lambda}\ln(n), \quad TTR = -\frac{1}{\mu}\ln(n) \tag{1}$$

where: n is a random number between 0 and 1

MCS is used to generate the TTF and TTR for each component based on random numbers and usually uniform random numbers (Wadi et al., 2018) (M. Wadi et al., 2017) (Wadi & Baysal, 2017). It is crucial to expand the simulation time to be tens or hundreds of thousands of years to obtain accurate and robust results.

In distribution power systems, MCS is used to generate random samples of λ and μ of each component, such as transformers, lines, circuit breakers, and relays. Upon the two parameters, TTF and TTR are

calculated. Then, reliability indices such as SAIFI, SAIDI, and others can be calculated. Hence, these reliability indices are aggregated to generate the probability distributions for each component. These probability distributions provide an essential tool to expect the reliability of any component at any time. Besides, the process of the MCS method in power distribution systems as given in Figure 7 (Shobole et al., 2017) (Guo et al., 2016), and can be described as follows:

1. Start with the first sample year,
2. Randomly an artificial hourly history of faults is generated for each component to calculate TTF and TTR based on their formulas as depicted in Eqn. (3). In this paper, two states for each component energized and de-energized are considered,
3. Start at time one (first hour), determine the fault locations,
4. Identify interrupted customers (i.e., LPs) and their TTR values,
5. Return to step 2 until each hour in a year has been examined,
6. Carry out a counter to obtain the total interrupted customer-numbers and total interrupted customer-hours,
7. Calculate SAIFI and SAIDI for this sample year,
8. Return to step 1 until predetermined stopping condition (i.e., number of iterations 10000 times) is fulfilled,
9. Aggregate calculated reliability indices to generate probability distributions,
10. Repeat steps 2-9 for the following sample year until a predetermined number of sample years (i.e., 100 years) is fulfilled.

In this analysis, the following operating conditions are considered;

- All feeder sections and lateral distributors' failures are included.
- All protection devices and sectionalizers are assumed to be 100% reliable.
- Not all the feeder sections have sectionalizer, while all laterals have fuses at the lateral point.
- All customers are residential.
- All 34.5 kV feeders' sections and 0.4 kV lateral distributors are overhead lines.
- The average time for repair is 2 hours.
- The average failure rate for 34.5 kV lines is 0.05 failure/year, while 0.4 kV lines is 0.125 failure/year.

Table 10 draws the obtained results of MCS reliability assessment and comparison with average system reliability indices based on historical reliability assessment. Figure 8 graphically explains the difference in system reliability indices between both methods.

Table 10: Comparison between historical and MCS assessments

Indices	Historical Assessment	MCS Assessment
SAIFI	0.165	0.1163
SAIDI	0.168	0.4382
CAIDI	1.017	3.767
ASAI	0.99992316	0.99956999
AENS	0.42	0.25
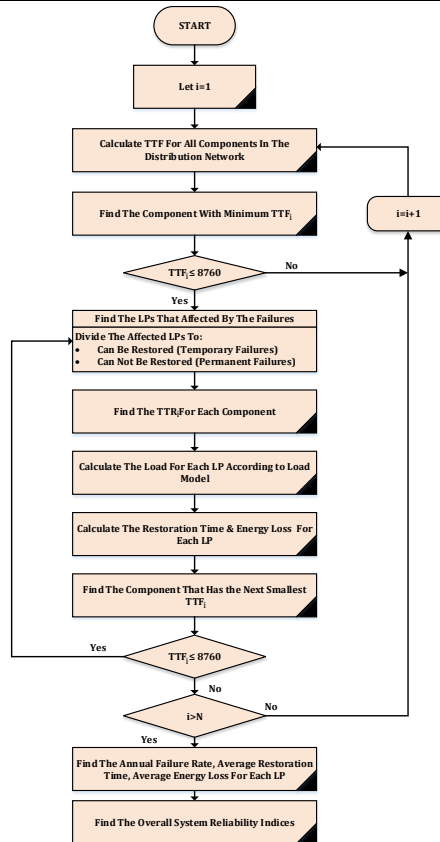
Figure 7. MCS flowchart for reliability assessment in distribution power systems

Table 10 shows that there is, to some extent, a difference between the results of historical reliability analysis and MCS analysis. This difference is because of the historical reliability assessment based only on three years of data. The simulation in this study depends on the average

values of failure and repair rates to construct the artificial history for distribution transformers and lines. Three years, i.e., 2012 – 2014, are used to create the TTF and TTR probability distribution function. The minimum advised period for suitable reliability assessment is five years of reliability data, while ten years is the best for accurate reliability assessment and expectation (Shobole et al., 2017a) (Chojnacki, 2012) (Guo et al., 2016). Moreover, it is necessary to notice that the maximum difference was in CAIDI, which can be explained due to the sensitivity of this index to SAIFI and SAIDI. In other words, any change in SAIFI, SAIDI, or both causes dramatically change in CAIDI (Arya et al., 2012) (Moazzami et al., 2013).
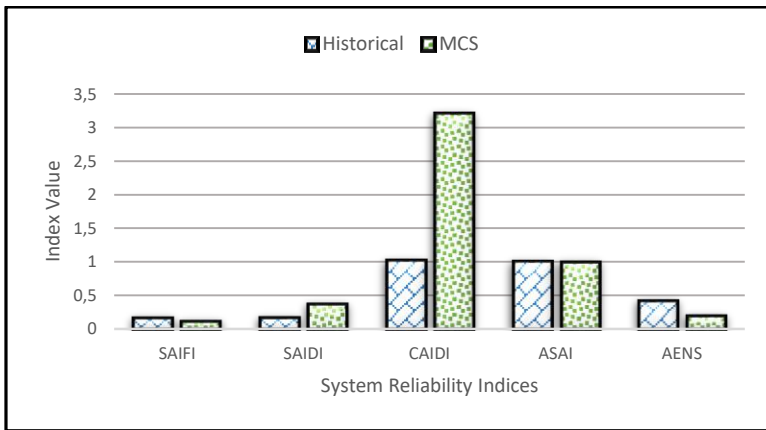
Figure 8. Comparison between historical and MCS reliability assessment

7. CONCLUSION

Collecting reliability data in databases is crucial for energy utilities to conduct reliability assessment whenever the need arises. Historical reliability assessment also can be taken as a reference for other reliability assessment methods. Besides, it is a crucial tool in the planning, design, and maintenance processes of power systems. In this Chapter, the historical reliability assessment for the 4-Feeder power distribution system is assessed and analyzed. MCS reliability analysis is performed based on the average reliability values extracted from the historical reliability assessment. The comparison results verify that MCS is a powerful tool to assess the reliability of power systems. This study found that the feeder F3-83F5 experiences the most significant frequency and duration of interruption with 0.4679 and 0.2366 for the SAIFI index.

Similarly, 0.4952 and 0.1458 the SAIDI index for the years 2012-2013 and 2013-2014, respectively. On the contrary, the feeder F4-83F8 experiences the least frequency and duration of interruption with 0.0305 and 0.0611 for the SAIFI index and 0.0285 and 0.0326 for the SAIDI index for the years 2012-2013 and 2013-2014, respectively. Ultimately, the

reliability assessment is a powerful tool to define the power system's weakness and then decide the relevant remedial actions needed to achieve the required service reliability levels. Generally, power utilities and electric companies can consider the following recommendations to improve their systems' reliability;

• Continuous and accurate registration of different failures and interruptions by preparing certain forms, including all data required for reliability assessment.

• Training the crew of maintenance to fill out the forms of reliability on time, the date of fault, the cause of failure, and the exact period for repair and restoration.

• Preparing a smart mobile application instead of filling out forms; to increase registration speed and the accuracy of the collected data.

• Organizing the collected data into databases to simplify future reliability studies.

• Increase the number of sectionalizers at feeder sections to reduce the number of customers being interrupted.

• Replacing manual sectionalizers with automated ones to reduce the time of restoration.

• Installing insulators and anti-bird cones on the top of poles impede birds from access to distribution transformers and connections.

• To ward off the rodents, it is essential to use tightly sealed cabinets, poison materials, or ultrasonic devices.

REFERENCES

Abunima, H., Teh, J., Lai, C. M., & Jabir, H. J. (2018). A systematic review of reliability studies on composite power systems: A coherent taxonomy motivations, open challenges, recommendations, and new research directions. *Energies*, *11*(9), 1–37. https://doi.org/10.3390/en11092417

Al-Wafi, E., Al-Subhi, A., & Al-Muhaini, M. (2016). Reliability assessment of a practical power system using Monte Carlo simulation. *2015 Saudi Arabia Smart Grid, SASG 2015*, 1–6. https://doi.org/10.1109/SASG.2015.7449276

Allan, R. (1994). Power system reliability assessment-A conceptual and historical review. *Reliability Engineering and System Safety*, *46*(1), 3–13. https://doi.org/10.1016/0951-8320(94)90043-4

Arya, L. D., Choube, S. C., Arya, R., & Tiwary, A. (2012). Evaluation of reliability indices accounting omission of random repair time for distribution systems using Monte Carlo simulation. *International Journal of Electrical Power and Energy Systems*, *42*(1), 533–541. https://doi.org/10.1016/j.ijepes.2012.04.064

Baharum, A., Alwan, F. M., & Hasson, S. T. (2013). A case study of reliability and performance of the electric power distribution station based on time between failures. *Mathematical Problems in Engineering*, *2013*. https://doi.org/10.1155/2013/583683

Bakkiyaraj, R. A., & Kumarappan, N. (2010). Evaluation of composite reliability indices based on non-sequential Monte Carlo simulation and particle swarm optimization. *2010 IEEE World Congress on Computational Intelligence, WCCI 2010 - 2010 IEEE Congress on Evolutionary Computation, CEC 2010*. https://doi.org/10.1109/CEC.2010.5586274

Billinton, R., & Pan, Z. (2004). Historic performance-based distribution system risk assessment. *IEEE Transactions on Power Delivery*, *19*(4), 1759–1765. https://doi.org/10.1109/TPWRD.2004.832404

Cadini, F., Agliardi, G. L., & Zio, E. (2017). A modeling and simulation framework for the reliability/availability assessment of a power transmission grid subject to cascading failures under extreme weather conditions. *Applied Energy*, *185*, 267–279. https://doi.org/10.1016/j.apenergy.2016.10.086

Chojnacki, A. L. (2012). The use of extended Petri nets in analyzing the reliability of MV / LV distribution transformer stations. *Elektronika*

Ir Elektrotechnika, *5*(5), 17–22. https://doi.org/10.5755/j01.eee.121.5.1645

Chowdhury, A. A. (2005). Distribution system risk assessment based on historical reliability performance. *2005 IEEE International Conference on Electro Information Technology*, *2005*, 1–7. https://doi.org/10.1109/eit.2005.1626967

Chowdhury, Ali A., & Koval, D. O. (2009). Power Distribution System Reliability: Practical Methods and Applications. *Power Distribution System Reliability: Practical Methods and Applications*, 1–531. https://doi.org/10.1002/9780470459355

Feng, Z. (2006). Electric Distribution System Risk Assessment Using Actual Utility Reliability Data. *Master Thesis*, *March*.

Godha, N. R., Deshmukh, S. R., & Dagade, R. V. (2011). Application of Monte Carlo simulation for reliability cost/worth analysis of distribution system. *2011 International Conference on Power and Energy Systems, ICPS 2011*, *December*, 22–24. https://doi.org/10.1109/ICPES.2011.6156644

Guo, H., Levi, V., & Buhari, M. (2016). Reliability assessment of smart distribution networks. *Proceedings of the 2015 IEEE Innovative Smart Grid Technologies - Asia, ISGT ASIA 2015*, 1–6. https://doi.org/10.1109/ISGT-Asia.2015.7387037

Haroonabadi, H., & Haghifam, M. R. (2011). Generation reliability assessment in power markets using Monte Carlo simulation and soft computing. *Applied Soft Computing Journal*, *11*(8), 5292–5298. https://doi.org/10.1016/j.asoc.2011.05.031

Kim, H., & Singh, C. (2010). Reliability modeling and simulation in power systems with aging characteristics. *IEEE Transactions on Power Systems*, *25*(1), 21–28. https://doi.org/10.1109/TPWRS.2009.2030269

Koster, J. K., Cohn, L. H., Mee, R. B. B., & Collins, J. J. (1978). Late Results of Operation for Acute Aortic Dissection Producing Aortic Insufficiency. In *Annals of Thoracic Surgery* (Vol. 26, Issue 5). https://doi.org/10.1016/S0003-4975(10)62926-8

Martinez-Velasco, J., & Guerra, G. (2016). Reliability Analysis of Distribution Systems with Photovoltaic Generation Using a Power Flow Simulator and a Parallel Monte Carlo Approach. *Energies*, *9*(7), 537. https://doi.org/10.3390/en9070537

Moazzami, M., Hemmati, R., Haghighatdar Fesharaki, F., & Rafiee Rad,

S. (2013). Reliability evaluation for different power plant busbar layouts by using sequential Monte Carlo simulation. *International Journal of Electrical Power and Energy Systems*, *53*, 987–993. https://doi.org/10.1016/j.ijepes.2013.06.019

Ozay, N., Guven, A. N., Buyuksemerci, A., & Fettahlioglu, M. (1999). Design and implementation of a feeder automation system for distribution networks. *International Conference on Electric Power Engineering, PowerTech Budapest 1999*, *February 1999*, 122. https://doi.org/10.1109/PTC.1999.826553

Pattabiraman, S., Sampath, K., Kannan, M., Ganesan, R. G., & Narayanan, K. (2019). Reliability Improvement in Radial Distribution System through Reconfiguration. *2019 IEEE PES Innovative Smart Grid Technologies Asia, ISGT 2019*, 1963–1967. https://doi.org/10.1109/ISGT-Asia.2019.8881119

Schoemann, A. M., Miller, P., Pornprasertmanit, S., & Wu, W. (2014). Using Monte Carlo simulations to determine power and sample size for planned missing designs. *International Journal of Behavioral Development*, *38*(5), 471–479. https://doi.org/10.1177/0165025413515169

Shobole et al. (2017b). Valuation of reliability assessment for power systems in terms of distribution system, a case study. *2017 6th International Conference on Renewable Energy Research and Applications, ICRERA 2017*, *Nov. 5-8*, 1114–1118. https://doi.org/10.1109/DISTRA.2017.8191227

Silva, E. N. M., Rodrigues, A. B., & Da Guia Da Silva, M. (2016). Stochastic assessment of the impact of photovoltaic distributed generation on the power quality indices of distribution networks. *Electric Power Systems Research*, *135*, 59–67. https://doi.org/10.1016/j.epsr.2016.03.006

Suthapanun, C., Jirapong, P., Bunchoo, P., & Thararak, P. (2015). Reliability assessment tool for radial and loop distribution systems using DIgSILENT PowerFactory. *ECTI-CON 2015 - 2015 12th International Conference on Electrical Engineering/Electronics, Computer, Telecommunications and Information Technology*. https://doi.org/10.1109/ECTICon.2015.7206929

Thoemmes, F., MacKinnon, D. P., & Reiser, M. R. (2010). Power analysis for complex mediational designs using Monte Carlo methods. *Structural Equation Modeling*, *17*(3), 510–534. https://doi.org/10.1080/10705511.2010.489379

Wadi, & Baysal, M. (2017). *Reliability Assessment of Radial Networks Via Modified Rbd Analytical Technique*. *35*(4), 717–726.

Wadi, Baysal, M., Shobole, A., & Tur, M. R. (2018). Reliability Evaluation in Smart Grids via Modified Monte Carlo Simulation Method. *7th International IEEE Conference on Renewable Energy Research and Applications, ICRERA 2018*, *5*, 841–845. https://doi.org/10.1109/ICRERA.2018.8566982

Wadi et al. (2020). Historical and Monte Carlo Simulation-Based Reliability Assessment of Power Distribution Systems. *Sigma Journal of Engineering and Natural Sciences*, *38*(3), 1527.

Wadi, Mohammed, Baysal, M., & Shobole, A. (2017). Comparison between open-ring and closed-ring grids reliability. *2017 4th International Conference on Electrical and Electronics Engineering, ICEEE 2017*, 290–294. https://doi.org/10.1109/ICEEE2.2017.7935836

Wallnerström, C. J. (2008). On Risk Management of Electrical Distribution Systems and the Impact of Regulations On (RCM). In *Thesis Licentiate Stockholm Electrical Systems* (Issue January 2008).

Wijekularathna, D. K., Manage, A. B. W., & Scariano, S. M. (2019). Power analysis of several normality tests: A Monte Carlo simulation study. *Communications in Statistics: Simulation and Computation*, *0*(0), 1–17. https://doi.org/10.1080/03610918.2019.1658780

Wilson, A., Graves, T., Hamada, M., & Reese, C. S. (2006). *Advances in System Reliability Assessment*.

Xu, H., & Zou, H. (2010). Research on complex multi-state distribution system reliability modeling and assessment methods based on Bayesian networks and random set theory. *2010 China International Conference on Electricity Distribution, CICED 2010*, *1*.

Zhang, X., Bie, Z., & Li, G. (2011). Reliability assessment of distribution networks with distributed generations using Monte Carlo method. *Energy Procedia*, *12*(December), 278–286. https://doi.org/10.1016/j.egypro.2011.10.038

APPENDIX

$$SAIFI = \frac{Total\ Number\ of\ Customer\ Interruptions}{Total\ Number\ of\ Customers\ Served} = \frac{\sum_i \lambda_i\ N_i}{\sum_i N_i}$$

$$SAIDI = \frac{Sum\ of\ Customer\ Interruption\ Durations}{Total\ Number\ of\ Customers\ Served} = \frac{\sum_i U_i\ N_i}{\sum_i N_i}$$

$$CAIDI = \frac{Sum\ of\ Customer\ Interruption\ Durations}{Total\ Number\ of\ Customer\ Interruptions} = \frac{\sum_i U_i\ N_i}{\sum_i \lambda_i\ N_i}$$

$$ASAI = \frac{Customer\ Hours\ of\ Available\ Service}{Customer\ Hours\ Demanded} = \frac{\sum_i\ N_i \times 8760 - \sum_i U_i\ N_i}{\sum_i\ N_i \times 8760}$$

$$ENS = Total\ Energy\ not\ Supplied\ by\ the\ System = \sum_i L_i\ U_i$$

$$AENS = \frac{Total\ Energy\ not\ Supplied}{Total\ Number\ of\ Customers\ Served} = \frac{\sum_i L_i\ U_i}{\sum_i N_i}$$

where:
N_i: is the number of customers of load point i
8760: is the number of hours in a calendar year
L_i: is the average load connected to load point i

NOMENCLATURE

AENS:	Average Energy Not Supplied (kWh/customer/year)
ASAI:	Average System Availability Index
BEDAS:	Bosporus Electric Distribution LTD Company
CAIDI:	Customer Average Interruption Duration Index (hour/failure)
CEA:	Canadian Electrical Association
CT:	Central Transformer
DTr:	Distribution Transformer
ENS:	Energy Not Supplied (MWh /year)
LP:	Load Point
MC:	Monte Carlo
MCS	Monte Carlo Simulation
RBTS	Roy Billinton Test System
S:	Switch
SAIFI:	System Average Interruption Frequency Index (interruption/customer)
SAIDI:	System Average Interruption Duration Index (hour/interruption)
S. N.	Section Number
TTF:	Time to Failure
TTR:	Time to Repair
TUBITAK:	The Scientific and Technological Research Council of Turkey
TUDOSIS:	TUBITAK Distribution Automation System
U:	Average Annual Outage (hour/year)
λ:	Average Failure Rate (failure/year) for lines and cables (failure/year.km)
μ	Average Repair Rate (hour/year)

NETWORK DISTANCE COEFFICIENT EFFECT ON DETERMINING TRANSPORTATION FACILITY LOCATION

Emre Demir[1]

[1]*(Asst. Prof.), Antalya Bilim University, e-mail: emre.demir@antalya.edu.tr*
iD ORCID *0000-0003-0013-4482*
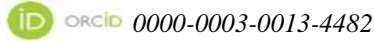
1. INTRODUCTION

Design in engineering can be identified as a decision-making procedure to make solutions satisfying some specific needs. Most of the engineering design problems contain multipart objective functions along with several decision variables. Feasible solutions must be found for every kind of designs characterized by potential decision variables of design parameters. At this point, optimization becomes a great option to discover the most appropriate solution among the solutions of the problem under specific conditions. For such purposes, an optimization technique tries to find the most suitable solution among all available feasible solutions. Traditional search methods have been used for a long time for getting solutions of engineering design problems. However, in real design problems, there can be a lot of decision variables effecting on objective function which those can make the problem very complicated. Therefore, there is a strong requirement to apply operative optimization approaches (Parkinson et al. 2013; Aydogdu 2017). One kind of such effective optimization methods is implementing a metaheuristic algorithm. Metaheuristic algorithms are prescribed as advanced and global search operators (Yang 2010). Many methods possess results through trial and error which can be titled as a standard search engine. A standard search engine finds numerous possibilities for the final solution. However, metaheuristic algorithm can greatly reduce the number of possibilities of a standard search engine. This provides convenience and reliability to many researchers. A couple of examples of well-known metaheuristic algorithms are particle swarm optimization (PSO) based on social behavior of bird flocking and fish schooling, firefly algorithm (FA), harmony search algorithm (HSA) based on music improvisation process.

Engineering designs and decision-making procedures are commonly encountered in transportation, especially in the aviation sector. It continues to develop rapidly in Turkey as in the whole world. The demand for aviation, which is of great importance in freight and passenger transportation, is

increasing day by day. According to the General Directorate of Civil Aviation, the fact that more passengers are carried than in the past shows that almost everyone in Turkey has started to become accessible to aviation (SHGM 2020). As a result of the increasing demand, the opportunities in the aviation sector increases. In addition, the number of aircrafts using the airports in Turkey or landing and taking off at the airports in the country increases day by day. Civil aviation in Turkey has made great strides in aviation infrastructure in recent years. As new airports were put into service, the number of domestic and international flights increased rapidly. Although the rules in aviation are very strict, there may be crashes or accidents of various sizes due to running into some setbacks (Uslu and Dönmez 2017). Although these crashes or accidents occurring in the chain of faults are tried to be minimized, loss of life and property during the accident is at a high level. In such cases, emergency intervention aims at minimizing financial losses, and most importantly, minimizing injuries and fatality rates. One of the ways to minimize losses in airline accidents is rapid interventions during or after the accident. When health, rescue or engineering service is provided quickly, the time lost will be minimized and thus losses and expenses will be reduced. When it comes to emergency response, airline transportation and the properties of the airports in our country have an important place.

Location analysis can be performed to minimize losses. As an example, Demir and Kockal (2019) determined the location of a facility that is planned to serve the entire transportation network in order to minimize financial losses. In another study (Demir 2018a), analyses were made to select the airport with the most suitable location that can be used within the borders of the country. The traffic rates of the airports were taken into account using the Weizsfeld algorithm (WA) in line with the Weber problem (WP). Then, Istanbul Sabiha Gokcen Airport was proposed as the airport that can provide service to all airports in Turkey. However, in this research, the following novelties are introduced. 1) Crow search algorithm (CSA) has never been used for evaluating an optimum facility location for the airports in a country. Therefore, the evaluation of finding an optimum facility location for the airports in Turkey will be held by using CSA. 2) Although other algorithms such as WA have been used for evaluating a facility location for the airports (Demir 2018b) and for a cement plant (Demir and Kockal 2019); network distance matrix and network distance coefficient were not included. Euclidean distance matrix between the nodes were used as inputs rather than highway network distance matrix depicting the costs between the nodes of a particular network. In this study, however, highway network distance matrix indicates the transportation costs between the nodes of the airports network in the country. It is thought that the use of up-to-date optimization opportunities together with up-to-date data will contribute to the national development by making the supply or transportation needs faster in emergency situations.

This text is planned as follows. In the second part, the method to be used is explained. Data collection and the attributes are introduced in the third section. Also a design example is submitted in the same section to demonstrate the analysis. Next, the findings that are encountered in line with the analyses and discussion are presented. In the last part, a general evaluation is made within the framework of the results.

2. METHODOLOGY

The problem of this study comes from finding the most convenient aid facility location considering the travel matrix between the airports in the country. Therefore, the objective with the parameters are described as follows (2.1, 2.2).

$$\text{Min} \sum_{i=1}^{n} k * a_i * \sqrt{\left|X_i - X_f\right|^2 + \left|Y_i - Y_f\right|^2} \tag{2.1}$$

$$k = \left. d_{i,j} \middle/ \sqrt{\left|X_i - X_j\right|^2 + \left|Y_i - Y_j\right|^2} \right. \tag{2.2}$$

where;
i, j : node i and node j respectively
k : coefficient for distance cost
a_i : weight coefficient of node i
X_i : x coordinate for node i
Y_i : y coordinate for node j
X_f : x coordinate of the final node
Y_f : y coordinate of the final node
$d_{i,j}$: network distance between node i and node j

When i and j are equal to one another, k can be accepted as 1 which is a non-factor in formula (2.1). In this study, the CSA created by observing the behavior of crows is used for optimization of a facility location. Crows are members of smart bird species. Observations suggest that crow flocks' behaviors have several similarities with optimization parameters. According to a behavior type of crows, they follow the other birds and steal their food, thus they find food sources. Moreover, crows hide their food to protect them and try to fool other bird species. In this case, one can say that crows are researchers, the environment is search area, positions of crow show a possible solution, and quality of food source can be convenience function. Using this behavioral similarity, CSA tries to simulate the crow's smart behavior to find solutions for optimization problems. Considering all such behaviors, a population-based metaheuristic algorithm is created. In this way, basic CSA principles can be described as follows: crows live in flocks, they memorize

locational positions of places used for hiding objects, they follow birds to steal their belongings, and they shelter their cache from theft (Askarzadeh 2016).

A d-dimensional environment with an input of a number of crows is assumed in CSA. The number of crows which is flock size is N and the position of crow i during iteration in search space is specified by a vector $x^{i,iter}(i = 1,2,...,N; iter = 1,2,...,iter_{max})$ where $x^{i,iter} = [x_1^{i,iter}, x_2^{i,iter},...,x_d^{i,iter}]$. Here $iter_{max}$ is the maximum number of iterations. Crows have memory to find the location of its hiding place. The location of hiding place of the crow i is shown by $m^{i,iter}$. In fact, each crow memorizes that the location of its best experience. Crows move around in the neighborhood to find a better food source (i.e. hiding places of food). One can assume that crow j wants to go to its hiding place $m^{j,iter}$ during the iteration. In iteration, crow i decides to follow crow j to find the hiding place of crow j. In this situation, the following two cases may be seen.

Case-1: As crow i follows crow j, crow j does not notice this move. Therefore, crow i can merge to the hiding location of crow j. For case-1, crow i gains a new position which is obtained as using the following equation (2.3).

$$x^{i,iter+1} = x^{i,iter} + r_i * fl^{i,iter} * (m^{j,iter} - x^{i,iter}) \qquad (2.3)$$

where r_i is a randomly chosen number using a uniform distribution between 0 and 1. $fl^{i,iter}$ shows the flight length of crow i at iteration $iter$.

Case-2: Crow j knows that it is followed by crow i. Therefore, crow j wants to cheat crow i by heading to another location of the search field to prevent the cache. Case-1 and Case-2 can be combined as in (2.4).

$$x^{i,iter+1} = \begin{cases} x^{i,iter} + r_i * fl^{i,iter} * (m^{i,iter} - x^{i,iter}) & r_j \geq AP^{j,iter} \\ a\ random\ position & otherwise \end{cases} \qquad (2.4)$$

where r_j is a number chosen randomly with a uniform distribution between 0 and 1. $AP^{j,iter}$ represents awareness probability of crow j at iteration $iter$. Generally, metaheuristic algorithms contain two main components which are intensification and diversification. Intensification is basically concentrating on searching in a local area by being aware of there is a good solution available in that particular region. Diversification is to creating a wide variety of solutions to explore a global scale search area. When discovering the best solutions in metaheuristic algorithms, the right balance must be constructed between intensification and diversification. In the case of CSA, the algorithm is mainly controlled by and awareness probability (AP) when considering the balance between intensification and diversification. Low values for AP increases intensification. In addition to this, an increased AP value decreases the probability of searching good solutions in the neighborhood. Also the search is continued on a global scale. In other words,

letting large AP values in CSA increases diversity of solutions. Given an AP value, general steps of CSA are as follows.

Firstly, in step-1, problem and parameters are initialized. Optimization problem, decision variables and constraints are defined. Adjustable parameters of CSA such as flock size (N), flight length (fl) awareness probability (AP), and maximum number of iterations ($itermax$), are submitted.

Secondly, step-2 initializes location of crow and memory of a crow. A number of crows such as N crows which are the members of the flock, are randomly placed in a d-dimensional search area. Each crow indicates a possible solution of the problem and d is inserted as the number of decision variables. When a memory is assigned to a crow, that crow has no experience at the first. That means it does not remember an experience from its previous moves. Moreover, it is assumed that crows hide their food at their starting positions.

Thirdly, step-3 evaluates fitness function. By adding the decision variable values into the objective function, quality value of the locations of crows are computed. Later step-4 generates new position. As a crow would like to discover a new location, it randomly selects on of the flocks such as crow j. The crow follows crow j to reveal a new food location (m^j) hidden by the crow j. This process repeats for all crows. Accordingly, checking the applicability of new positions takes place in step-5. That means after new positions are produced for each crow, the validity of them is inspected. If the position is feasible, the crow position is updated. Otherwise, the position of crow cannot be updated and thus it remains in the same position as it stands before the move.

After deciding on the applicability of new positions, fitness function for new positions is evaluated as step-6. In this step, the fitness function values are computed for new positions of each crow. Then the memory should be updated as changes happened in step-7. Using the equation (2.5) where f () indicates the objective function value, the crows update their memories. When the fitness function value of the crow's new position is more appropriate than the fitness function value of the memorized position, the memory of the crow is updated in accordance with the new location.

$$m^{i,iter+1} = \begin{cases} x^{i,iter+1} & f(x^{i,iter+1}) \ is \ better \ than \ f(m^{i,iter}) \\ m^{i,iter} & otherwise \end{cases} \qquad (2.5)$$

Last but not least, the ending process criterion should be checked as step-8. In this manner, step-4 and step-7 are repeated until $iter_{max}$ is attained. When the ending criterion or the finish criterion is met, the most convenient position in objective function value is reported. Thus, this is the solution of the optimization problem.

3. THE CASE STUDY

In this section, the data will be processed under two main headings. The first is the preparation of geographic data and the second is the preparation of transport data. Then, by using such processed data, the procedures and methods in this study are applied.

3.1. LOCATION DATA

Location information is very important in the analysis of location optimization problems. In this study, location data is carefully collected. The costs such as distances between the airports are one of the main variables to be used in the optimization method in this study. In that respect, geographical coordinate information of fifty-five airports actively used in civil aviation in Turkey has been of interest. The State Airports Authority (DHMİ) website shares many information about the airports of the country. The website offers location information in degrees, minutes, seconds for latitudes and longitudes which is a common global geographic positioning system (DHMİ 2020). However, because the optimization method used in this research will operate on a plane-based system, it has become necessary to establish a plane coordinate system. For this reason, projection changes were made in order to transfer the coordinates of all airports to a horizontal plane. Mercator projection which can be used worldwide in plane-based maps was preferred to be used in optimization processes. It is not completely possible to geometrically position the latitude and longitude coordinates in the Mercator projection, since there is a special shape of our planet called geoid. Although the Earth is flattened from the top and bulged from the sides and this makes challenging positioning problems, the Mercator projection is one of the best projections for conversions. Therefore, Snyder (2012), Demir (2018b), Demir and Kockal (2019) used such practices in their studies.

3.2. TRANSPORTATION DATA

Transportation network data is one of the most important elements of this study. Moreover, traffic data related to the network data is very crucial for the analysis. Traffic data were obtained thanks to the DHMİ website, which regularly stores data on the number of aircraft using the airports on a monthly basis and presents them for research (DHMİ 2020). The most up-to-date traffic data can be collected through the website. The following time period of the traffic data is examined: From the full service time of Istanbul Airport (i.e. from May 2019) to the measures taken by the Ministry of Interior against the Coronavirus disease (COVID-19) pandemic. In short, the ten-month time period from May 2019 to February 2020 is under the scope of evaluation. It is assumed that the services provided at the fifty-five airports within the scope of the assessment were performed under normal conditions in this ten-month period. The traffic data during this period were included in

the analysis. Traffic data of a particular airport will demonstrate the weight coefficient of the airport which is a kind of importance factor. The total traffic data of ten months for a particular airport are recorded to form the specific weight coefficient of that airport. Thus, the weight coefficients to be used in the problem were provided. For example, Table-1 shows the aircraft traffic data of six airports as a sample in the six-month period between September 2019 and February 2020. In the analysis, ten-month period of data from May 2019 to February 2020 were investigated. Such data is very crutial to possess the information of a_i (i.e. weight coefficient of node i) in network.

Table-1. Monthly aircraft traffic data of six airports as a sample (DHMİ 2020)

| Airport | Data Period | | | | | | Ten months total |
	09/19	10/19	11/19	12/19	01/20	02/20	
Erzurum	5,455	6,023	6,623	7,047	444	850	42,509
Gaziantep	14,574	16,263	17,993	19,573	1,714	3,341	115,265
Adiyaman	1,372	1,534	1,708	1,850	139	275	10,674
Agri	1,774	1,972	2,152	2,320	174	346	13,746
Amasya	969	1,074	1,171	1,273	98	196	7,740
Balikesir	16,921	18,925	20,661	22,165	1,762	3,481	127,931

Network distance matrix data is also constituted by the data depicting the relationship between the nodes in network. That type of data represents the costs between the nodes in terms of distance values. Distance values between the nodes provides a detailed information about the positions of the airports in the network. Such information has been recorded by measuring the highway distances between each airport in the country. As a sample, Table-2 demonstrates a part of the whole distance matrix, which consists the distances in kilometers between five randomly chosen airports. Such information is very essential in order to decide on the coefficient k (i.e. the coefficient for distance cost).

Table-2. Distances between five airports in kilometers.

| Airport	Antalya	Adana	Trabzon	Diyarbakir	Zonguldak
Antalya	–	599	1223	1115	703
Adana	599	–	843	524	742
Trabzon	1223	843	–	574	817
Diyarbakir	1115	524	574	–	1142
Zonguldak	703	742	817	1142	–

4. RESULTS AND DISCUSSION

Data collection, transfers and data processing were performed on a computer with an Intel® Core ™ i5-2410M CPU @ 2.30GHz, 6GB of installed memory, and a 64-bit operating system. The optimization process based on the transportation data and the weight coefficients of the transportation network nodes was calculated with CSA method. The coding in which the algorithm is reflected was run. Thus the values under the "optimum location" heading in Table-3 were obtained. These values indicate the latitude and longitude indicators of the optimum location respectively. They are found in degrees but that can be turned into other measurement types. The values point at the vicinity of Inegol in Bursa region where the terrain is relatively suitable for a possible construction. If another option is thought, the nearest airport facility can be offered as the ideal airport (Table-3). With the assistance of the assessment made in congruity with the optimum location appeared in Table-3, it is found that there is no air terminal office at the optimum location. In any case, a thick street network as of now exists, which depicts that the landscape is generally appropriate for a potential development. In this way, a facility can be situated at the optimum location. Another alternative could be allocating the optimum location to the closest air terminal office which is now being used. In accordance with this, it is assessed that the nearest air terminal, Bursa Yenisehir Airport, can offer support to all air terminals if there should arise an occurrence of crises regarding access distance or actual distance to optimum location coordinates.

Table-3. Optimum location and the nearest ideal airport

	Optimum Location	**Ideal Airport**
Latitude ($\lambda°$)	39.97647	40.25583
Longitude ($\Phi°$)	29.41965	29.56194
Place	Vicinity of Inegol, Bursa	Bursa Yenisehir Airport

Underpinned the available traffic data of the airports and geographical location data, in line with all these analyses, the ideal airport place is recommended for positioning the necessary equipment and personnel. In addition, the geographical location of the ideal location which is recommended to provide service in emergency situations and the ideal airport are shown visually on the map in Figure-1.

Figure-1. The optimum location and the ideal airport according to CSA.
(Note: This figure has been mapped with the help of Google Maps.)
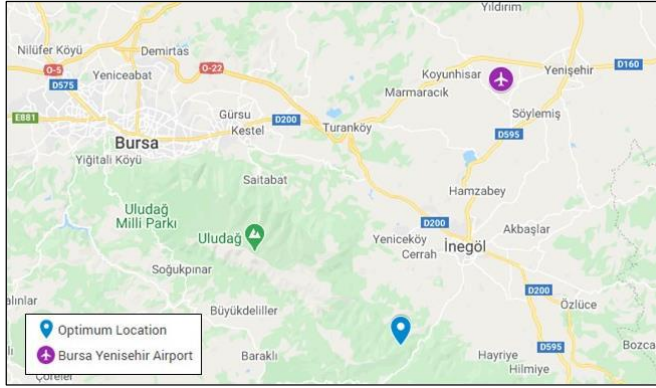
5. CONCLUSION

It is crucial to reduce the loss of life and reduce the costs in emergency by urgently intervening. Recently, Istanbul Airport as a new large airport started to serve the region. Therefore, the traffic data have been collected for a while by observing the new situation. Up-to-date data should be evaluated by considering up-to-date optimization method. In addition to the new airline traffic data, the highway network distances between the airports in use in the country play a key role in the analysis. The network distance matrix is introduced for the optimization process. Moreover, the weight coefficients of the airports based on traffic data greatly contributed to detect the outputs. If the center of gravity of the network nodes had been found only, the specific importance of airports with heavy air traffic would have been ignored. Since the network distance matrix and the weight coefficients of the airports were taken into consideration, the analysis provided the most convenient and ideal results to be applied to reality. Considering the optimum location coordinates found in this study and presented in Table-3, there are currently no airport facilities that these coordinates point at. Therefore, the closest airport in terms of access distance or physical distance to these coordinates was determined by finding the shortest network distance between two points. With the help of the evaluation made in conformity with the optimum location value shown in Table-3, it is discovered that there is no airport facility at the optimum location. However, a dense road network already exists, which describes that the terrain is relatively suitable for a possible construction. Therefore, a facility can be located at the optimum location. Another option could be assigning the optimum location to the nearest airport facility which is already in use. In line with this, it is evaluated that the closest airport to the optimum location computed, Bursa Yenisehir Airport, can provide service to all airports in case of emergencies. Thus, it is evaluated that the airport closest to the

179

optimum location can serve the airports within the country in case of emergency.

In this study, as a result of the analysis made considering the traffic data and location data collected, Bursa Yenisehir Airport was proposed for the positioning of the equipment and personnel that may be needed for emergency response. It is considered that assigning this airport, where aid facilities can be established, aims at minimizing the loss of life during or after disasters such as any natural disaster or accident. As a result of this study and in line with the recommendations of the research, it is expected that progress will be made in minimizing the loss of life and reducing time and expense loss. Thus, a significant contribution is expected to result in regional and countrywide development.
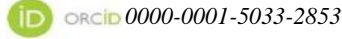
REFERENCES

Askarzadeh, A. (2016). A novel metaheuristic method for solving constrained engineering optimization problems: crow search algorithm. *Computers & Structures*, *169*, 1-12.

Aydogdu, I. (2017). Cost optimization of reinforced concrete cantilever retaining walls under seismic loading using a biogeography-based optimization algorithm with Levy flights. *Engineering Optimization*, *49*(3), 381-400.

Demir, E. (2018a). Havalimanlarında kalkış öncesi, acil durumlarda, yardım alınabilecek en uygun lokasyonun Weber problemine uyarlanarak belirlenmesi. *Türk Coğrafya Dergisi*, (70), 81-85.

Demir, E. (2018b). Approach for siting a support facility for transporting supplies in emergency cases in the Republic of Bulgaria. In *MATEC Web of Conferences* (Vol. 234, p. 06001). EDP Sciences.

Demir, E., & Kockal, N. U. (2019). Iterative methodology on locating a cement plant. *Journal of Inequalities and Applications*, *2019*(1), 1-8.

DHMİ, (2020), Devlet Hava Meydanları İşletmesi Genel Müdürlüğü Havalimanları karşılaştırmalı istatistikleri, <https://www.dhmi.gov.tr/sayfalar/istatistik.aspx>, accessed on 18 April 2020.

Parkinson, A. R., Balling, R., & Hedengren, J. D. (2013). Optimization methods for engineering design. *Brigham Young University*, *5*, 11.

SHGM, (2020), Sivil Havacılık Genel Müdürlüğü Faaliyet Raporu 2019, <http://web.shgm.gov.tr/documents/sivilhavacilik/files/pdf/kurumsal/faaliyet/2019.pdf>, accessed on 15 April 2020.

Snyder, J. P. (2012). *MAP PROJECTIONS: A Working Manual (us Geological Survey Professional Paper 1395)*. WWW MILITARYBOOKSHOP Company U.

Uslu, S., & Dönmez, K. (2017). Hava Trafik Kontrol Kaynaklı Uçak Kazalarının İncelenmesi. *Mehmet Akif Ersoy Üniversitesi Sosyal Bilimler Enstitüsü Dergisi*, *9*(18), 271-287.

Yang, X. S. (2010). *Engineering optimization: an introduction with metaheuristic applications*. John Wiley & Sons.

CHAPTER XII

SUSTAINABLE GROUNDWATER REMEDIATION WITH BIOBARRIERS USING AGRICULTURAL OR PLANT PRODUCTION RESIDUES

Emre Burcu Özkaraova[1]

[1](Assoc. Prof. Dr.) Ondokuz Mayıs University, e-mail: ozkaraova@omu.edu.tr

ORCID 0000-0001-5033-2853

INTRODUCTION

The World's population is estimated to be 7.7 Billion people (UN, 2019). Clean drinking water and food supplies are among the major requirements. Despite the differences in cultural habits in consumption and state of development, agricultural activities and livestock production increased during the last century. The expansion and intensification of agricultural activities caused to the detoriation of soil and water resources (Mateo-Sagasta et al., 2017). Various contaminants, including nitrogenous compounds, pesticides, growths regulators, veterinary antibiotics have been detected (Menz et al., 2015). Intensified agricultural activities also resulted in higher production of agricultural residues and wastes (Obi et al., 2016). Residues/wastes from the harvesting and processing of agricultural yields like crops, fruits, vegetables and animals are accepted as crop residues and animal wastes, respectively (Obi et al., 2016; Sabiiti, 2011). The estimated amount of agricultural residues and/or wastes Worldwide is about 998 million tons per year (Agamuthu 2009). Therefore, the management of agricultural residues/wastes based on the 4 R principles (reduce, reuse, recycle, recover) is of most importance. These residues have been accepted as a resource and have been used for many purposes besides conventional utilizations for biogas, energy, compost and animal feed (Sabiiti, 2011; Zhang et al., 2012a).

Aiming the reduction of biodecomposable materials to be disposed off at landfills, research continues for the reuse, recycling and utilization of agro-residues like corn cob, straw and stover, olive and apricot stones, rice and nut husk, nut shells etc. for potential uses in water purification (El Nadi et al., 2014; Ghazy et al., 2016; Góngora-Echeverría et al., 2017). These were also used as filling materials in permeable reactive barrier systems and in-situ bioreactors (e.g. biowalls). Permeable reactive barrier (PRB) is an in-situ sustainable groundwater remediation technology that has been widely used and studied in groundwater

remediation in the last two decades with its convenient, efficient and inexpensive features (Obiri-Nyarko et al., 2014; USEPA, 2012). Especially when the location of the contaminant source is uncertain or contaminant release is slow, PRB systems are favored. The concept of PRB systems involves the underground placement of a reactive zone perpendicular to the contaminated groundwater plume (Obiri-Nyarko et al., 2014). This reactive treatment zone contains reactive materials placed on the underground surface for the remediation during the passive flow of contaminated water (USEPA, 2012). The groundwater flows normally under its natural gradient naturally forming a passive treatment system (Figure1). As can be seen from Table 1, the main advantage of these systems are their low cost as they do not require aboveground facilities or energy inputs and generally rely on the natural water flow in situ to bring contaminants into contact with reactive materials (Liu et al., 2006). While some of the reactive media remove pollutants through oxidative and reductive chemical or biological processes, others work by providing conditions favorable for pollutant immobilization such as precipitation, adsorption and co-precipitation (USEPA, 1998). The reactive materials are chosen according to the treatment strategy determined with respect to the type and concentration of pollutants and overall contaminant mass flux.
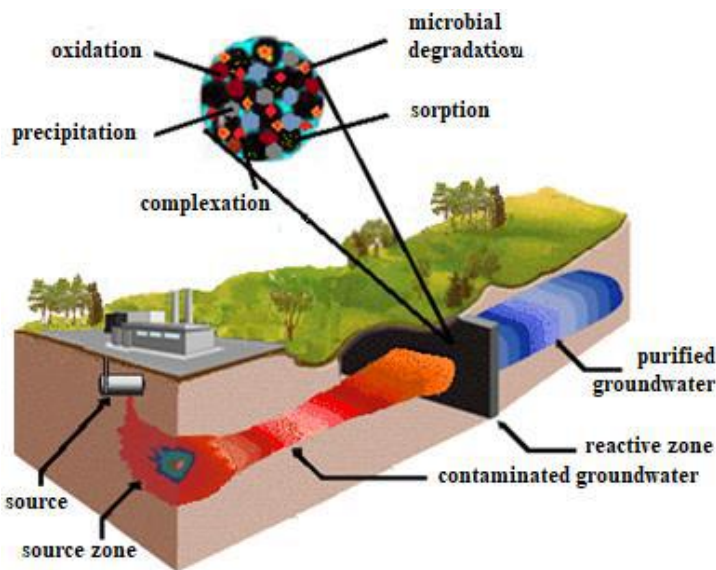

Figure 1. Schematic presentation of a conventional permeable reactive barrier system

Laboratory experiments, pilot and field studies have shown that different pollutants can be treated with appropriate reactive materials. These reactive materials are selected depending on the abiotic and/or

biotic processes needed in the treatment zone to remove the target contaminants dissolved in the groundwater. The selected process will initiate the type and function of permeable reactive barrier (Figure 2).

Table 1. Advantage and disadvantages of the PRB system (Maitra, 2019; Thiruvenkatachari et al., 2008)

| Advantage	Disadvantages
Relatively inexpensive due to low energy cost, low maintenance and monitoring cost, with the exception of initial installation cost	Requires detailed geological and hydrogeological site characterization and accurate plume delineation
Allows treatment of wide range of pollutants	Restricted to treatment of dissolved pollutants
Allows treatment of multiple pollutants/ multiple plumes with sequenced and/or multiple PRBs	Plumes at great depth require different PRB configurations (e.g. alloys of permeable wells)
Allows usage of sustainable and cheap reactive materials	Aquifer systems with too high or low hydraulic conductivities may result in higher installation costs
Aboveground usage is not restricted and does not influence PRB performance	Below ground structures (e.g. services, foundation) may influence installation and performance
No cross-media contamination as contaminants remain below ground	Limitations due to reduction in pore size (clogging) by precipitates etc.
Requires occasional monitoring of PRB performance and maintenance	May require long-term monitoring under extreme conditions (presence of persistent pollutants and low hydraulic conductivity)
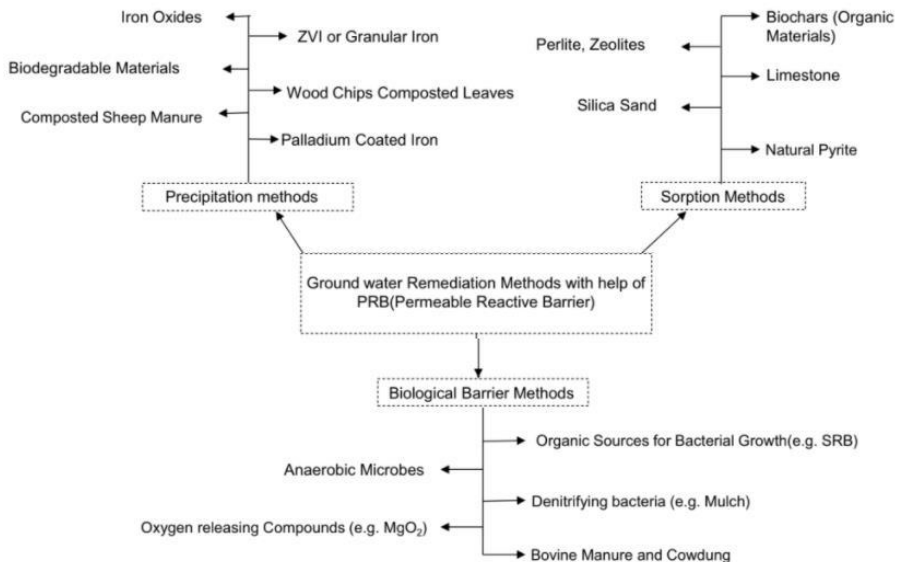
Figure 2. Mechanisms within the permeable reactive zone of PRB (Thakur and Kumar, 2021)

Materials tested included zeolite and apatite to treat radionuclides, activated carbon to remove polycyclic aromatic hydrocarbons (PAHs) and other volatile organic compounds (VOCs), zero valent iron to treat energetic compounds, chlorinated solvents and arsenic, granular peat moss, peat, mulch and many other reactive materials to address other contaminants like BTEX, pesticides, heavy metals, nitrobenzene and mine drainage (NAVFAC, 2020; ITRC, 2011; Rasmussen et al., 2002).

Systems consisting of a reactive zone stimulating biotic processes are called permeable reactive biobarriers, biowalls or bioreactors. They can be installed to intercept and remediate plumes, reduce contaminant discharges at key locations and/ or to treat residual contaminants in the plume. The biotic processes can be under aerobic, anoxic and anaerobic conditions depending of the mechanism. With the selection of appropriate electron donors, oxygen releasing compounds, nutrients and other indirect reagents, the transformation/degradation of inorganic (e.g. nitrate, sulfate, perchlorate) and organic contaminants (e.g. chlorinated hydrocarbons, energetic materials (e.g. RDX and HMX) can be triggered (ITRC, 2011; Newell, 2008). Oxygen or nitrate releasing compounds (e.g. calcium oxide (CaO), calcium peroxide (CaO_2), magnesium peroxide (MgO_2), percarbonate ($Na_2CO_3 \cdot 1.5\ H_2O_2$), persulfate ($Na_2S_2O_8$) etc.) have been used to maintain an aerobically active zone for the treatment of petroleum hydrocarbons such as PAH, BTEX and MTBE (Liang et al., 2011; Liu et al., 2006; Liu et al., 2019). Various plant and crop residues like sawdust, straw, maize cobs have been evaluated as potential substrates for the removal of nitrate in groundwater with denitrification biowalls (Addy et al., 2016; Cameron and Schipper, 2010; Warneke et al., 2011; Zhang et al., 2012b). Similarly, citrus peel, straw, garden compost, peat has been examined as biobed composition for point source pesticide contaminated groundwater from farms (Coppola et al., 2007). Alfalfa and woodship has been used in a biobarrier used for the removal of selenate and selenite to elemental selenium through the reduction of these electron acceptors during the microbial oxidation of these substrates in the biobarrier (Stringer et al., 2020). Microbially mediated sulfate reduction enabled the removal of sulfate, iron and various heavy metals (Benner et al., 1999). Groundwater contaminated with chlorinated solvents like tetrachloroethene (PCE), trichloroethene (TCE) is often remediated using mulch, compost, peat and similar organic substrates as an electron donor for the biological reductive dechlorination process in biobarriers (US Air Force, 2008; Upadhyay and Sinha, 2018). The anaerobic process in the treatment zone is also capable for the transformation/degradation hexahydro-1,3,5-trinitro-1,3,5-triazine (RDX), octahydro-1,3,5,7-tetranitro-1,3,5,7-tetrazocine (HMX), 2,4,6-trinitro-toluene (TNT), perchlorate, chlorate and other chlorinated organic compounds (Ahmad et al., 2009).

Table 2. Recent studies on organic residues examined as potential substrates for permeable biobarrier systems

Barrier materials	Contaminants	Application	Process	Influent Conc.	Flow rate	Kinetic data/HRT	Reference
Lab Scale- Batch Tests							
Date, Tamarind and Moringa seeds	Nitrate	2 g seed + 25 mL solution	denitrification	22.6 mg NO_3-N/L	-	-	Dahiru et al. (2017)
Ca(OH)$_2$ treated comcob, wheat straw	Nitrate	1 g carbon material + 50 g pre-treated soil	denitrification	399 mg/kg	-	removal in 28 days	Sun et al. (2018)
Compost, sisal, Seaweed, corn stover	2,4-D, Atrazine Carbofuran Diazinon	500 cm^3 biomixture 90% water holding capacity	degradation	10,800 mg 2,4-D/L 25,000 mg Ant/L 2,290 mg /L,	-	DT_{50}= 5.5 d DT_{50}= 1.6 d DT_{50}= 5.7 d	Góngora-Echeverría et al. (2017)
Lab Scale- Continuous Flow Tests							
Cabuya fibers	Heavy metals	4.4 cm x 60 cm	adsorption	43 mg Cu/L 65 mg Zn/L	10 m/d	-/90-124 h Cu -/124-142 h Zn	Rojas et al. (2017)
Woodchip	Nitrate	200 L barrel	denitrification	14-17 mg NO_3-N/L	48 -58 mL/min	-/33-54 h	Cameron &Schipper (2010)
Crude cottonwool	Nitrate	10 cm x 120 cm	denitrification	100 mg NO_3/L	10 mL/min 0.13 cm/min	-	Aloni & Bremner (2017)
Straw, diatomite, attapulgite, calcium peroxide	Phenanthrene	4 cm x 50 cm	Aerobic degradation	0.9 mg Ph/L	0.127 mL/min	-/24.9 h	Liu et al. (2019)
Green waste							
Luffa sponge	1,1,1-TCA	45x15x15 cm^3 sand box	anaerobic degradation	14.4 mg TCA/L	0.490 L/min (0.130 m/h)	data available	Wang & Wu (2019)
Mulch compost mixture (4:3)	TCE	2.5 cm x 20 cm	anaerobic degradation	600 mg TCE/L	40 rpm => 9.1- 15.2 m/yr	-	de Guzmán et al. (2018)
Rice bran	AMD	110 cm PVC column	Anaerobic reduction	320 mg SO_4/L Heavy metals	variable	-/6-25 h	Aoyagi et al. (2017)
Cellulose, leaf compost, manure, limestone		80x6.5x30 cm	Anaerobic reduction	2600 mg SO_4/L Heavy metals	0.14 L/d	16.4 d	Torregrosa et al. (2019)
Sewage sludge, bone meal, sawdust, activator, ZVI	Uranium	8 cm x 30 cm	Anaerobic degradation.	10 mg U/L	0.006-0.15 L/h	-	Komilovych et al. (2018)
Field-Scale							
Woodship, S(0), shell	Vanadium	25 cm column	Bio-reduction	10-50 mg V(V)/L	-	0.5-1 (3 d cycle)	Li & Zhang (2020)
Sawdust	Nitrate, ammonium	horizonal placement below latrine	denitrification	≤43 mg NO_3-N/L ≤70 mg NH_4-N/L	130 L/d (0.2-0.5 m/d)	1-2 d	Suhogusoff et al. (2019)
Limestone, sewage sludge, vegetal compost ZVI	AMD (acidity, heavy metals, sulfate)	110 mx6 mx1.4 m	Reduction, precipitation	15 mg/L Zn and Al 1000 mg SO_4/L	0.6-1 m/d	1-2 d	Gibert et al. (2011)

SELECTION OF REACTIVE MATERIAL

In biobarrier systems, the most appropriate energy and carbon resources are tried to be selected to enable the conditions that support the heterotrophic or autotrophic transformation of pollutants. For a successful treatment, knowledge on the characteristics of pollutants and relevant process conditions is very important during the selection of reactive materials. Therefore, efforts are still being made to find longer-lasting and cost-effective materials that can be recycled (Malá et al., 2017) and used for a more expanded spectrum of pollutants. Information about the chemical composition and physical properties of the reactive materials (porosity, density, surface area etc.) will ease the decision on its suitability for biobarriers. The pollution swapping potential of substrates (e.g. release of greenhouse gases and dissolved pollutants) is also a serious issue for research (Healy et al., 2012). Özkaraova et al. (2019) observed with batch leaching and denitrification experiments conducted with hazelnut husk and tea factory waste, that the level of dissolved organic carbon, pH, oxidation reduction potential (ORP) and presence of other compounds in solution can inhibit the transformation process. Thus, to fully understand the treatment process, by-products and the influence of hydrochemical parameters (pH, dissolved oxygen, ORP, electrical conductivity (EC), temperature etc.) need to be identified. Biofilm and precipitate formation and gas production should be inspected as these can reduce the porosity and thus the permeability of media in the long run.

Screening of reactive materials generally starts with lab-scale batch experiments and continues with continuous flow column experiments before pilot-scale field studies (Figure 3). The residues require degradation to be able to release the dissolvable constituents in the long run and therefore can be seen as indirect substrate sources. Thus, the leaching behavior of organic residue and thus the change in water composition within time should be evaluated before pilot scale applications. For this purpose batch tests are very suitable as they can be relatively quickly performed with low amounts of substrates and water using easily available laboratory instruments. Batch experiments for biotransformation, on the other hand, help to determine degradability of pollutants with potential reactive material and the optimum conditions (size and percentage of reactive material, pH, ORP etc.) and reaction rate of transformation. Column studies enable the determination of the most appropriate reactive materials and more importantly the necessary residence time for complete transformation under continuous flow conditions. Sampling ports along the column will enable a thorough determination of reaction conditions and thus transformation ongoing within the column. Therefore, column studies are seen as representatives of the processes and flow conditions occurring in a biobarrier. Especially

with the use of real contaminated groundwater samples, the influence of groundwater geochemistry and multiple contaminants on the performance of biobarrier material under competitive environmental conditions will be observed. The samples observed from the ports will deliver reliable kinetic data that will be further used for the design of pilot-scale or field scale biobarrier. Experiments run for longer time periods will represent the long-term reactivity and permeability of material and changes in the effluent composition (end-products, by-products) that will reflect the performance and thus the life time of material.
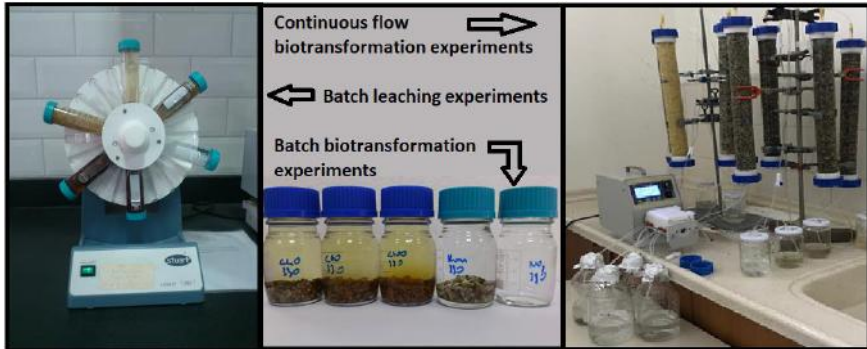

Figure 3. Batch and continuous flow experiments to test the potential use of agricultural residues as biobarrier materials.

CONFIGURATIONS

Permeable biobarriers or biowalls are generally constructed as continuous trenches, emplaced perpendicular to capture the entire contaminant plume (Figure 4). Continuous trenches are generally vertically and horizontally over extended in size considering the seasonal fluctuations in groundwater table and groundwater flow direction (Figure 5a). To enhance the flow into the reactive zone the permeability of reactive media should be equal or greater than the permeability of aquifer (USEPA, 1998). For this purpose are reactive materials blended with clean sand. By ensuring higher water velocity in the reactive zone, overflow around or underneath the trench can be avoided. The flow underneath the reactive zone is generally overcome by going deep enough to reach a low permeable layer or bedrock if possible (Figure 5b). Similarly, the funnel and gate system, which is the second alternative of PRB technology, uses cutoff walls (the funnel) that direct the groundwater and plume to flow through a gate or gates that contain the high conductivity reactive materials. The reactives in the gates are generally designed for easy exchange, which is generally accepted as an advantage of the funnel and gate system. Permeability of reactive media, groundwater velocity and hydraulic residence time are key parameters for the determination of the thickness of biobarrier.
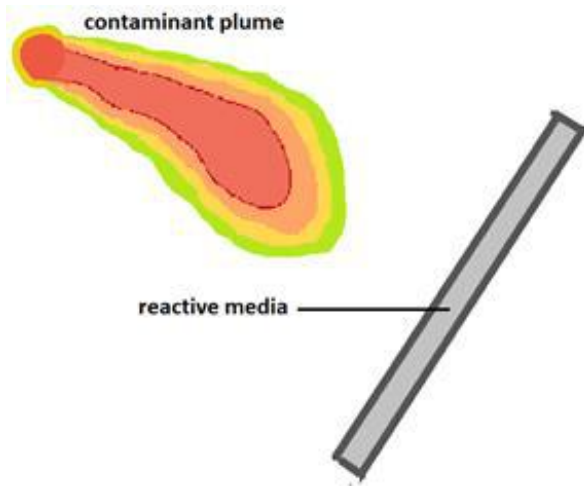
Figure 4. Conventional continuous trench permeable reactive barrier

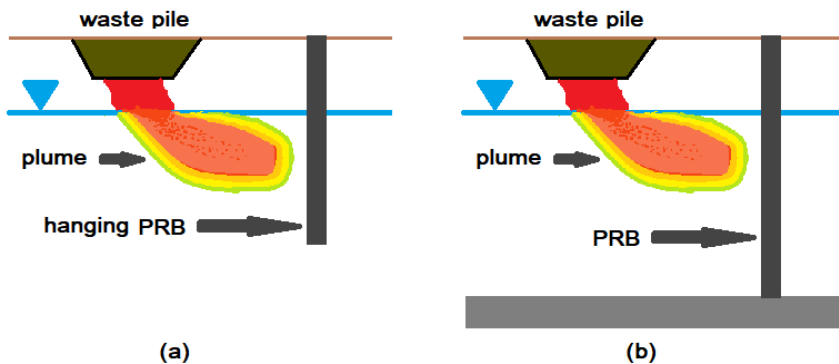(a)   (b)

Figure 5. Conventional continuous trench PRB configurations

For the success of a biobarrier, combined use of reactive materials, installed as a mixture or in sequence is possible (Upadhyay and Sinha, 2018; Chu and Eivazi, 2018). Mixtures of substrates may also be more effective in providing longevity and sustainability of microorganism in the zone (Jamil and Clarke, 2013). This might be especially needed for sites with multiple contaminants. In cases with higher pollutant concentrations wider trenches may be needed to ensure the retention time in biobarrier, the construction of additional trenches in parallel may be a solution (US Air Force, 2008). These multiple biobarrier systems may also enable the additional use of alternative reactives for providing supportive and/or stimulative conditions before removal of target contaminant (Figure 6) (Liu et al., 2006; Liu et al., 2013). These may also reduce intermediate products directly or by extending the reaction zone, especially when emplaced close to each other. Angled placement of biobarrier centered to plume path may ensure capture of contaminants, by avoiding their escape at the biobarrier ends (Figure 7).
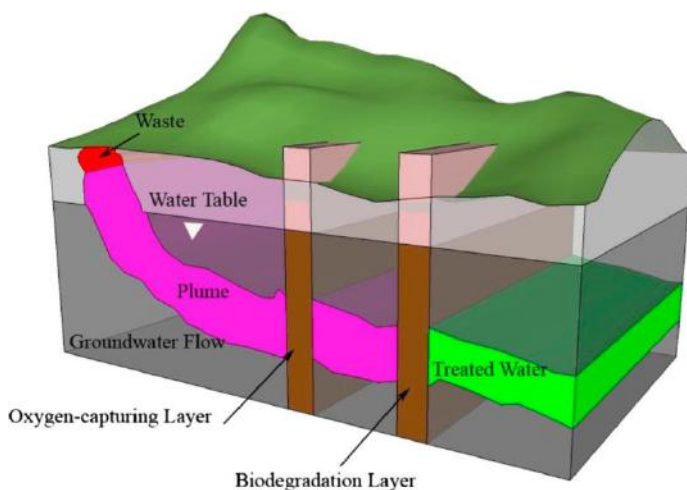
Figure 6. Schematic presentation of a multiple biobarrier system (Liu et al., 2013)
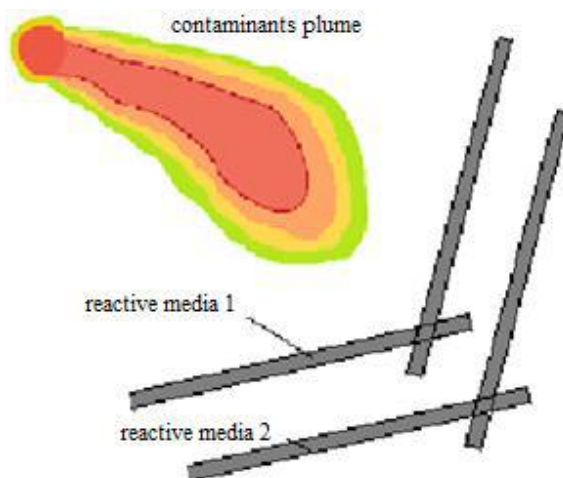

Figure 7. Schematic presentation of an angled multiple biobarrier system

Biobarriers can also be a solution for large plumes with poorly defined, widely distributed or inaccessible source areas (US Air Force, 2008). Sites with a contaminant plume with wide width may require the funnel and gate system that may contain more than one gate to gather the whole plume (Figure 8). The cut-off walls have a great influence on directing the plume towards the gates. Similarly, arrays of closely located unpumped wells function like discontinuous PRB systems (Wilson et al., 1997). Reactive unpumped wells allow an easy exchange of filter material emplaced as fully-penetrating cartridges or cassettes Figure 9.
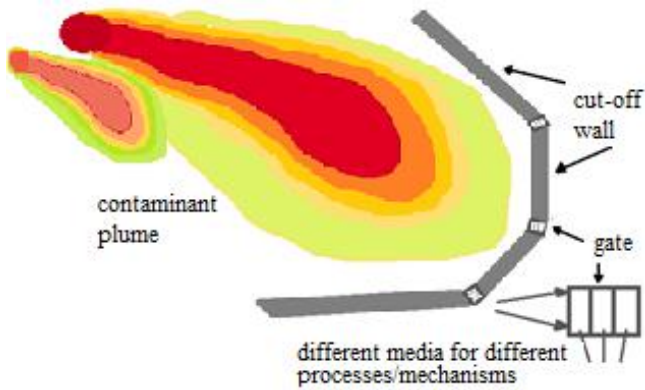
Figure 8. Schematic presentation of a funnel-gate system with multiple gates to treat plumes of bigger sizeﷲ
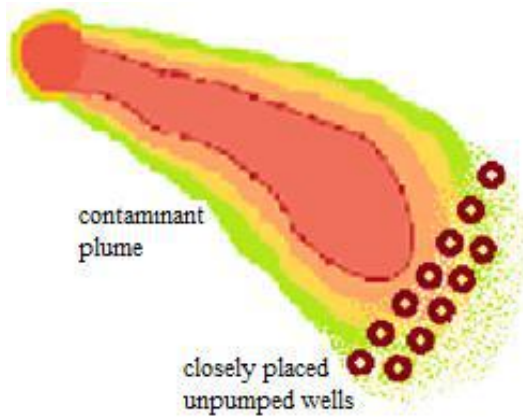

Figure 9. Closely placed unpumped wells working like a discontinuous permeable barrier

Reactive placement in serial order into separate cells in the gate may enable different environmental conditions needed for the sequential transformation of pollutants. These sequenced multi-barriers enable sequential treatments of target contaminants combining abiotic and biotic processes (e.g. granular iron for chlorinated hydrocarbon treatment followed by nutrient and carbon substrate to stimulate anaerobic biodegradation of VOC (ITRC, 2005)) and/or different (aerobic, anoxic and anaerobic) biological processes (Kong et al., 2014; Singh et al., 2020a).

As can be seen in Figure 10, injection of supporting solutions providing additional dissolved carbon, alkalinity and air using wells and/or perforated pipes enhances the biological process for complete destruction of contaminant.

Horizontal biobarriers or biowalls have been constructed to control and/or treat vertically migrating contaminated groundwater or source zones such as septic systems (ITRC, 2011; Suhogusoff et al., 2020), waste piles, etc. The reactive material is directly placed as a horizontal layer below the source zone, perpendicular to the vertical flow path. When source area treatments are required and contaminated soil removal is necessary biobarriers can be installed as a part of planned source area activity (US Air Force, 2008). As seen in Figure 11, a recirculation biobarrier placement within the excavated area may be helpful for remediation below water table. The recirculation of contaminated groundwater will rise the residence time in the treatment zone and thus the removal efficiencies of pollutants. Additionally, the fluid injection will result in hydraulic mounding within the biobarrier, increasing the flow rate and thus the transport of released constituents down gradient of the biobarrier. This actually may extend the treatment zone but may need regulatory acceptance.
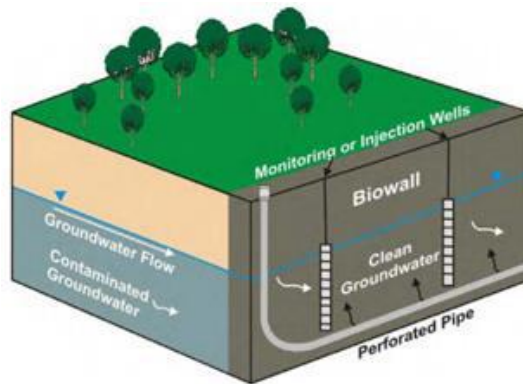

Figure 10. Schematic presentation of a permeable mulch biowall (US Air Force, 2008)
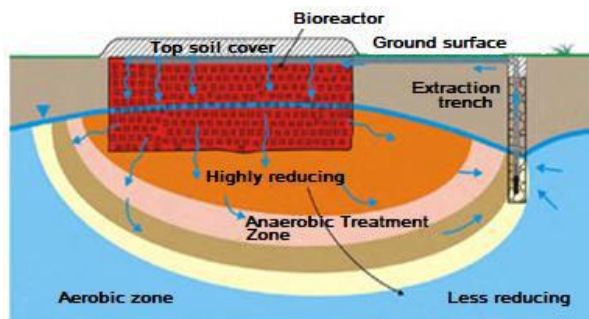

Figure 11. Schematic presentation of a recirculating biobarrier (US Air Force, 2008).

BIOBARRIER TECHNOLOGY AND APPLICATION

Novel configurations as alternatives of the conventional PRB systems are under continuous research aiming to reach lower costs, easiness of construction and greater depth below ground surface. The use of vertical and/or horizontal boreholes/wells for the remediation of plumes at different depth of the aquifer with multiple water-bearing zones is getting attention (Divine et al., 2018; Freethey et al., 2003; Nzeribe et al., 2020). Vertical boreholes and non-pumped wells generally aim to reach deeper contaminated aquifers. These systems require a right placement of the permeable portion of the boring into the specific hydrogeologic unit. Short circuiting should be avoided, thus detailed information about aquifer properties and plume characteristics is of great value. Permeable filled boreholes or non-pumped wells may rely on two different strategies. They may be designed to catch the contaminated plume (Figure 12(a)) or to deliver the necessary reactives by natural flow to the contaminated groundwater zone down gradient of the well (Figure 12(b)) (Buscheck et al., 2019; Wilson et al., 1997). In cases where hydraulic containment is applied with low-capacity wells (Hudak, 2016), permeable filled boreholes may serve as a treatment potential that can be easily combined into the system. Re-injection of the treated groundwater up-gradient of the extraction wells containing reactive materials enables additional treatment and helps to increase the hydraulic gradient and thus the groundwater transport through the reactive media in low-permeability aquifers (Bekele et al., 2019).

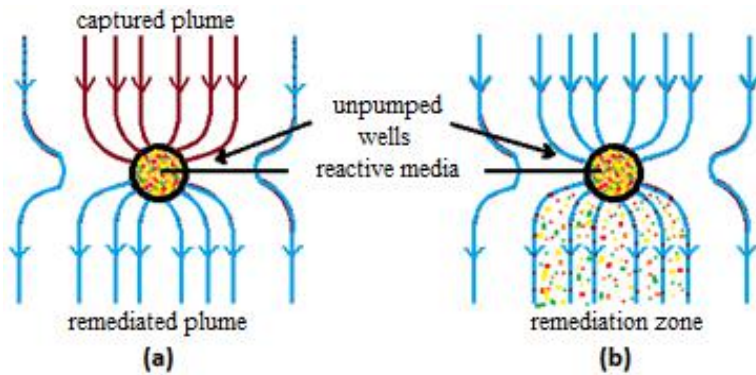Figure 12. Schematic presentation of hydraulic capture (top view) by an unpumped well and (a) treatment by the reactive zone in the well, (b) down gradient plume treatment by the reactive zone created up gradient of the plume.

Horizontal directional drilling is expected to facilitate a transition to more sustainable remediation implementations (Lubrecht, 2012). Horizontal reactive media treatment (HRX) wells have been developed as

a passive treatment technique capable for the treatment of various pollutants (Divine et al., 2018). This treatment technique involves a fully screened large-diameter horizontal well located underground roughly parallel to the main ground water flow direction. Working as an engineered preferential flow path, it captures the contaminated ground water and as passive flow continuous pollutants are cleaned-up by the reactive media in the well (Figure 13).
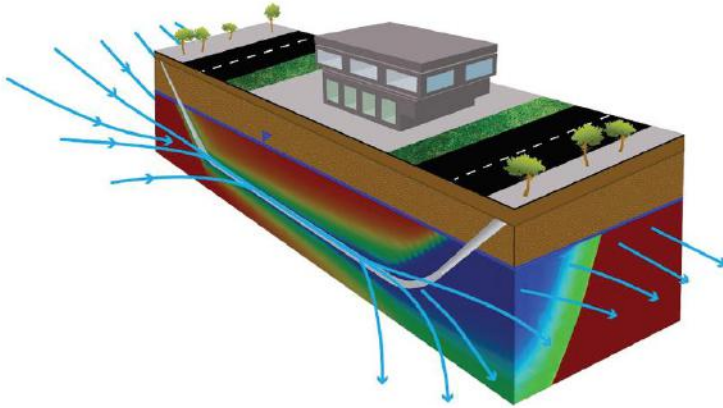

Figure 13. Conceptional presentation of a horizontal reactive media treatment well (Divine et al., 2018).

Electrokinetic (EK) soil remediation has recently been applied on-site for the treatment of contaminated less permeable (clayey) soils for which conventional remediation techniques were not found to be effective (Reddy and Cameselle, 2009). Using sustainable energy sources EK soil remediation is accepted as a green technology relying on the installation of anode and cathode electrodes. By applying electrical potential (I) ions (e.g. nutrients) are driven towards one of the electrodes (electromigration), (II) pore water is moving (electroosmosis) and (III) small colloids (e.g. microorganisms) become mobile (electrophoresis) (Lima et al., 2017). This technology has been coupled with bioremediation (Barba et al., 2018; Wick et al., 2007). EK is reported to increase the transport of contaminants, nutrients, electron acceptors and microorganisms, which are present in the soil pore fluid, consequently promoting processes like bioattenuation, biostimulation and bioaugmentation (Barba et al., 2019; Gill et al., 2014). To increase this influence, the combination of EK with permeable biobarrier systems seems very encouraging especially for low permeable soils (Mena et al., 2016). Research on the combination of electrokinetic remediation with both biotic and abiotic permeable reactive barriers (EK-PRB) systems lead to the commercialization of technology under names such as Lasagna[TM] and Electro-Klean (Andrade and dos Santos, 2020; Reddy and

Cameselle, 2009; Weng, 2009). A schematic diagram of a EK-PRB system can be seen in Figure 14. Studies on the development of permeable well systems with bioelectrochemical degradation are continuing (Liang et al., 2020). Using flushing solutions together with electro kinetic treatment in biobarrier system is found to increase removal efficiency especially in diesel contaminated clay soil without additional treatment of flushing solution (Mena et al., 2015).
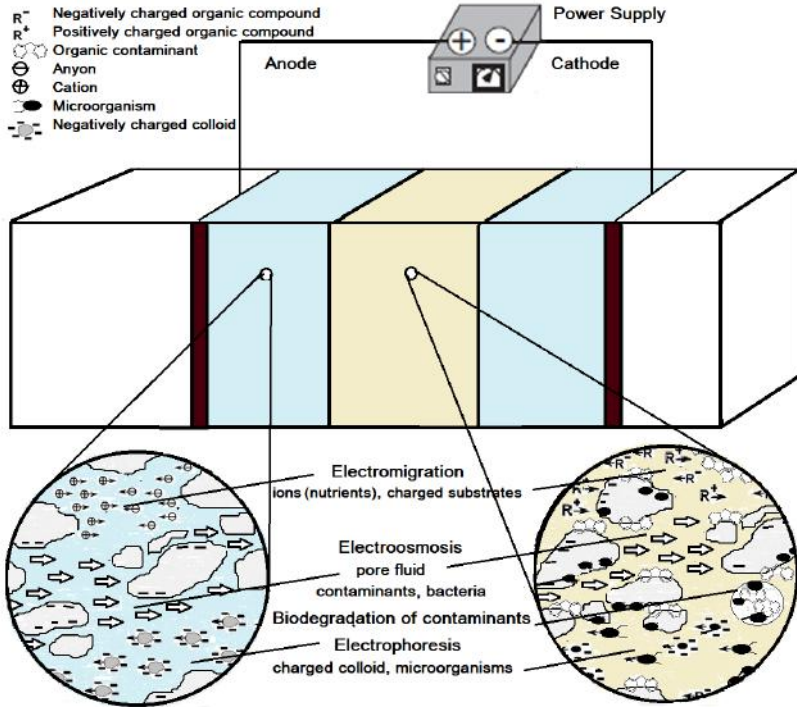
Figure 14. Schematic presentation of EK-biobarrier system

DESIGN OF PRB, BIOBARRIERS AND BIOWALLS

The selection of remedial actions is often done with respect to site specific conditions (plume size, site characteristics etc.) and regulatory compliance requirements. Site specific human health risk assessments generally support the determination of cleanup targets. Thus, bioreactor should be capable in treating the contaminants below maximum contaminant levels (MCLs), risk based target values or drinking water standards. The design of biobarrier as an individual action or a unit of a combined remedial action starts with the determination of applicability of biobarrier system at site, which relies on site characteristics and availability of reactive materials to be used for the removal of target contaminants. Vertical and horizontal distribution of the target contaminants requires detailed site investigation, but delivers reliable

site-specific contaminant data. Additionally, hydrogeological features of the site such as groundwater flow and geochemical information ensure more reliable lab-scale and pilot-scale experiments and field-scale applications. Hydrogeological characterization delivers data on groundwater flow regime which may influence the velocity and direction of plume movement and thus the design and placement of biobarrier system. Thus, site investigation with conventional or newer drilling and sampling techniques should be planned based on pre-existing data and judgment of hydrogeologist. Site specific data should enable a reliable conceptualization of subsurface hydrogeologic formations (Gavaskar et al., 2000). The steps of permeable biobarrier/ biowall design are presented in Figure 15.
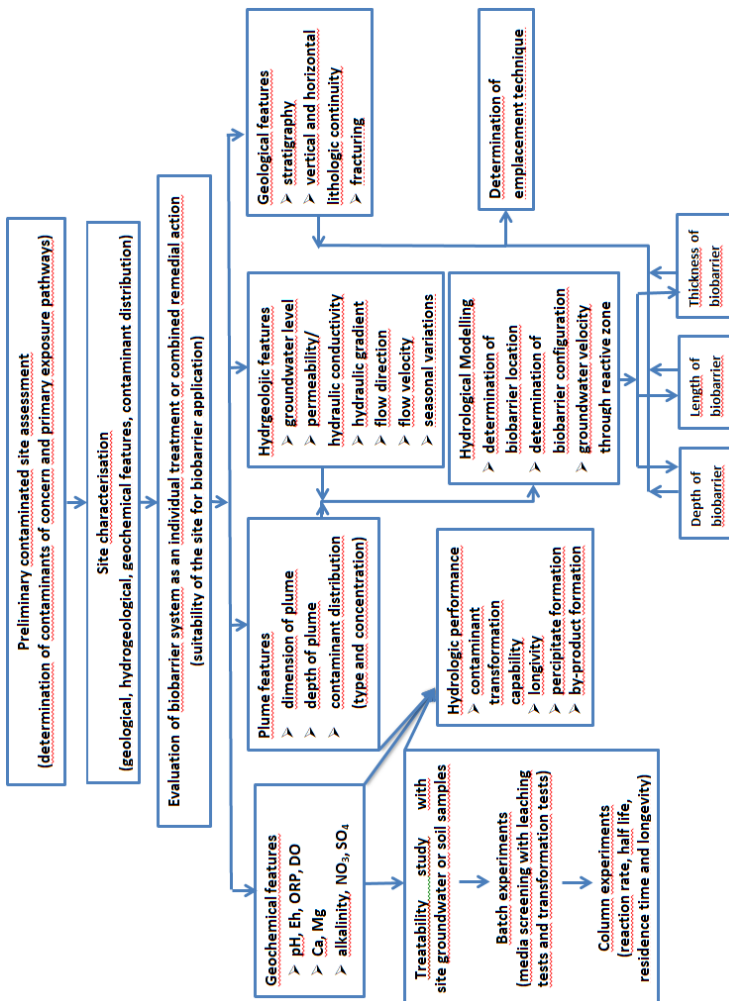

Figure 15. Schematic presentation of the steps of permeable biobarrier/biowall design

Lab-scale and pilot-scale experiments provide the relevant data for material selection and reaction rates and half-lives of the relevant transformation mechanism for contaminant removal. Longevity, cost-effectiveness and environmental compatibility of reactive materials are among the key parameters (USEPA, 1998). Longevity is not only related to the properties of reactive material (leaching potential, material structure, etc.) but also a function of contaminant distribution and concentration variation, and geochemical (pH, ORP, EC and constituents) and hydraulic characteristics (hydraulic conductivity and gradient) of the groundwater within time. The hydraulic conductivity of the filter material is always higher than the value of aquifer so that the contaminant plume can be easily captured by the biobarrier system (USEPA, 1998). Thus, the hydraulic conductivity of the site will guide the determination of the hydraulic conductivity of reactive material, which is adjusted with lab-scale experiments and so to say engineered before field-scale applications.

The groundwater velocity is one of the most important parameters. The groundwater velocity can be determined through tracer testing (single-well tracer test, multiple-well test), direct in-situ measurement with appropriate probes (e.g. colloidal borescope, University of Waterloo Drive –Point Probe etc. (ITRC, 2005)). The velocity can be calculated using the Darcy's Law and site specific data on hydraulic gradients (horizontal and vertical) and hydraulic conductivity of the aquifer (Gavaskar et al., 2000). If the biobarrier is embedded into a confining layer the determination of the vertical hydraulic gradient may not be of importance, but if a confining layer is not available at relevant working depth, the vertical hydraulic gradient needs to be investigated to enable to selection of the depth of biobarrier for avoiding shortcuits.

As the horizontal hydraulic gradient and hydraulic conductivity is influencing the residence time of contaminant and thus the determination of the thickness of biobarrier system, the highest potential groundwater velocity observed for the site should be used for system design. Groundwater velocities below 0.3 m/day are found to be suitable for biobarrier systems (US Air Force, 2008; ITRC, 2011). Velocities above this value may require multiple trenches to ensure the residence time for effective removal. Thus, at sites with high groundwater velocities, other remediation techniques instead or for integration may be evaluated as alternative options regarding the overall cost effectiveness of system. Aquifers with low groundwater velocities may require a long time to treat the contaminant plume as plume migration towards the biobarrier will take time. In order to increase the velocity, the recirculation of water will raise the hydraulic gradient and thus speed up the plume migration towards the biobarrier system (US Air Force, 2008).

As the groundwater velocity is directly related to the hydraulic conductivity a thorough investigation of aquifer system is required. Aquifer systems comprised of different soil layers with lower or higher hydraulic conductivities may induce preferential flow path of the contaminant plume. Thus, a good understanding of the geology, hydrogeology and geochemistry of the site is of primary importance during the design of biobarrier system. The groundwater flow direction is a key parameter for the placement of biobarrier and can be interpreted using groundwater contour maps, which also enable the determination of hydraulic gradient. If groundwater contour maps are not available, the flow direction can be determined using three-groundwater elevations (Kuo, 2014). Hydrogeological modeling may help to locate the biobarrier system with regard to the plume size and behavior and variation in vertical locations and thicknesses of soil layers. Generally, computer programs like MODFLOW, FEFLOW or similar programs are used for this purpose. These models and others like MODPATH also help to determine the biobarrier configuration and dimensions, and assess potential flow conditions within, below or around the barrier (Scott and Folkes, 2000; Rad and Fazlali, 2020; Grajales-Mesa et al., 2020). The so-called process-based models, on the other hand, help to evaluate the longevity of biowall/biobarrier by interpreting potential biogeochemical processes ongoing in the biobarrier (Singh et al., 2020b). On the contrary, inadequacy in the investigation of geological and hydrogeological features of the site often resulted in failure of permeable reactive barrier and biobarrier systems.

The sizing and design of biobarrier systems depends entirely on the concentration of pollutants in the groundwater and the groundwater flow (EPA, 1998). Thus, the configuration and dimension of the biobarrier system is determined according to site specific conditions (Figure 16). Continuous trench biobarrier systems, called biowalls or mulch trenches, are generally installed into shallow aquifers. The depth is between 15-21 m or less (Day and Schindler, 2020; Day et al., 1999; USEPA, 1998). Actually, the trench depth is totally depending on the stability of geological formation and the availability of equipment used for excavation. Construction techniques and appropriate trenchers or hydraulic excavators may be available, but costs are increasing respectively. Systems such as sludge injection and hydraulic fracture enable to overcome this kind of placement problem (USEPA, 1998).

Biobarrier systems should be long enough to capture the whole width of plume under different seasonal variations of groundwater behavior. Similarly, the biobarrier should be deep enough to cover the total depth of plume. The thickness of biobarrier system should ensure the necessary retention time of contaminants within the reactive zone for

complete transformation. Therefore, the reaction order and reaction rate of biological mechanism needs to be investigated.
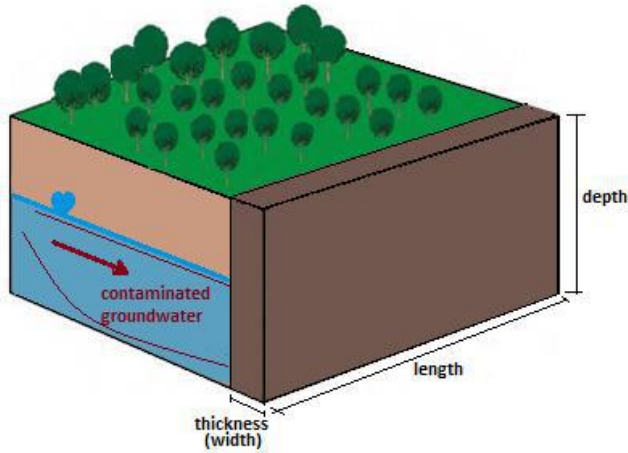

Figure 16. Schematic presentation of dimension of permeable biobarrier/biowall

Lab-scale column studies conducted under site specific conditions (hydrochemistry, contaminant concentrations, etc.) will easily deliver kinetic data for these calculations and design interpretations. Additionally, the flow rate determined for the column study should be based on contaminated site specific flow rate conditions. If rate limiting conditions obey first-order kinetic model, first-order kinetic model is used for the calculation of reaction rate, half-life and residence time. The order of reaction is generally verified with the correlation coefficient (r^2), which indicates how well the model represents the experimental data. The reaction rate (k) is calculated from the slope of linearized plots of $ln[C_t/C_0]$ versus time (t) [Eq. (1)], respectively.

$$ln[C_t] = ln[C_0] - kt \rightarrow \qquad ln\left[\frac{C_t}{C_0}\right] = -k \times t \qquad (1)$$

where C_t is the regulatory relevant target contaminant concentration down-gradient of the biobarrier; C_0 is the up-gradient concentration entering the biobarrier, and k is the reaction rate. Once the reaction rate is determined, the half-life ($t_{1/2}$) and residence time (t_{res}) of first-order reaction prevailing in the column can be calculated using Eq. (2) and Eq. (3), respectively.

$$t_{1/2} = \left[\frac{ln\,2}{k}\right] \qquad (2)$$

$$t_{res} = \left[-\frac{ln(C_t/C_0)}{k}\right] \qquad (3)$$

This kinetic data represent the time required for transformation obeying the reaction rate of case specific transformation process (e.g. denitrification, anaerobic degradation etc.). The residence time of solute in the column or permeable barrier should meet the residence time of transformation process. Regarding the residence time spent in the column during the study Eq. (4) can be used for calculation (Maamoun et al., 2020).

$$t_{res}(column) = \left[\frac{n(BV)}{Q}\right]$$ (4)

where n is the effective porosity of reactive material, BV (mL) is bed volume used in the column and Q (mL/min) is the influent flow rate.

The thickness of biobarrier (b) can be calculated from Eq. (5).

$$b = v \times t_{res} \times SF$$ (5)

where v is the velocity of contaminated groundwater through the reactive media and SF is the safety factor with regard to the uncertainties in the reactive zone (mechanisms, hydraulic conductivity, temperature etc.). Variations in temperature (e.g. environmental conditions, location or season) may influence the microbial activity and thus the reaction rate/kinetics of transformation process. The temperature of the laboratory ($25\pm2°C$) may not mimic site specific conditions ($<15°C$). To understand the level of temperature influence on the reaction rate Arrhenius equation can be interpreted for the determination of SF (Gavaskar et al., 1997). Reaction rates generally decrease at lower temperatures resulting in higher half-lives and residence times which are compensated with this slope factor. Similarly, seasonal changes may also influence the hydraulic gradient and thus the velocity of the groundwater. Additionally, differences in bulk density, due to consolidation variations in the laboratory and on site, may reflect different total surface area and consequently reaction rates resulting from variations in and porosity. Thus, safety factors for seasonal temperature and hydrogeological variations compensate uncertainties and ensure performance. Depending on the heterogeneity of aquifer system or expected uncertainties the safety factor can be chosen to be between 2 and 5 and more if necessary (Eykholt et al., 1999). A typical safety factor of 2 was reported to compensate heterogeneity and temporal variability, but for systems with higher heterogeneities a factor of 5 will ascertain that 95% of effluent will meet required water quality (Elder et al., 2002; Maamoun et al., 2020).

The velocity of the groundwater can be determined from the Darcy Law using Eq. (6).

$$v = \frac{K}{\emptyset} \times \frac{\Delta h}{\Delta l}$$ (6)

where K is the hydraulic conductivity of the reactive zone, $\Delta h / \Delta l$ is the hydraulic gradient and Ø is the porosity of reactive material. Pilot-scale studies and investigations on-site will minimize uncertainties for hydraulic conductivity, hydraulic gradient, and porosity. The hydraulic conductivity of site can be determined with field measurements, such as pump test or slup/bail test (ITRC, 2005). The hydraulic conductivity of the reactive media is ideally determined in the laboratory with falling-head or constant-head permeameter tests. Constant-head permeameter tests are conducted with conventional permeameter facilities (Fetter, 1994; Gavaskar et al., 1997). Laboratory studies with columns set up as constant head permeameters, also enables the determination of hydraulic conductivity (Figure 17). Standard procedures explaining the experimental study in detail, are available (e.g. ISO/TS 17892-11 and ISO/FDIS 17312). The hydraulic conductivity can be calculated with the help of Darcy law using Eq. (7) or Eq. (8).

$$K = \frac{Q_{out}}{A} \times \frac{\Delta l}{\Delta h} \quad\quad (7)$$

where Q_{out} is the discharge flow at the outlet of column, A is the cross-sectional area, Δh is the difference in hydraulic head and Δl is the length of reactive medium.

$$K = \frac{V}{A \times t} \times \frac{\Delta l}{\Delta h} \qu\quad (8)$$

where V is the water volume discharged during time (t). For an appropriate determination of hydraulic conductivity, the hydraulic gradient should be close to the value observed for the contaminated site. If possible multiyear variations in the hydraulic gradient should be considered during the study.
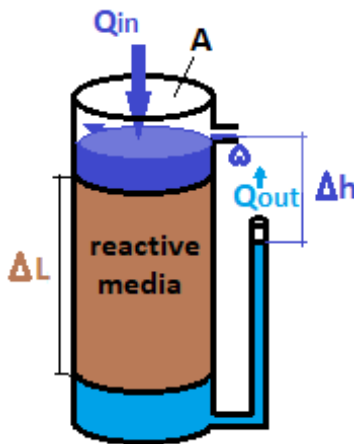

Figure 17. Schematic presentation of a column set up as a permeameter

The thickness of reactive zone; which can change from a few tens of centimeters to several meters (Day et al., 1999), should ensure the required residence time. Depending on the contaminant of concern, the residence time for total transformation of by-products or intermediate products that may have been produced in the reactive zone, needs to be considered as well before final decision. Thus, these by-products require monitoring as well, as transformations generally occur concurrently. Figure 18 represent the residence times needed for the transformation of contaminant A and its by-products I and II to their MCLs. As regulatory requirements generally ask for the reduction of the contaminants and by-products to their MCLs, the residence time selected should be the longest time.
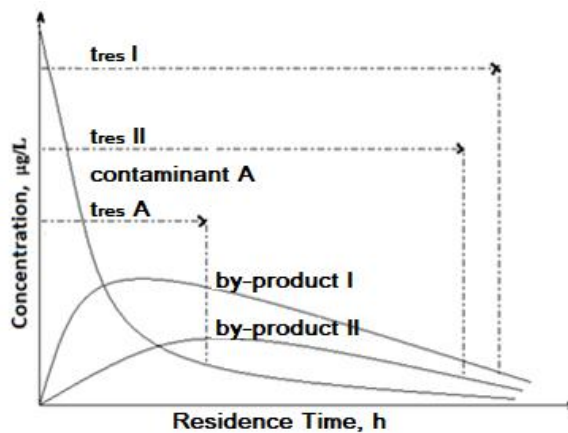
Figure 18. Residence times needed for the transformation of contaminant and its by-products.

SUMMARY

Permeable biobarrier systems have been used during the last two decades for passive in-situ treatment of contaminated groundwater. It is widely accepted as a sustainable remediation technique as it is relying on the natural flow of groundwater through a reactive zone supporting the biotransformation of various contaminants. Materials are chosen with respect to the target contaminant to be removed by aerobic, anoxic and anaerobic processes. While oxygen releasing compounds (e.g. calcium oxide, calcium peroxide) are prefered for the stimulation of aerobic conditions; organic compounds, sulfurous compounds and some other reactives like zero valent iron are used for the formation of anoxic and anaerobic conditions. This chapter focuses on biobarrier systems in which agricultural and plant processing residues can be used as the major reactive material. Aiming the re-use of organic residues research

continues on alternative materials, permeable biobarrier configurations and technology combinations. Starting with batch and continuous flow lab-scale studies, pilot scale and full-scale investigations complete the research process. Batch and continuous flow studies carried out in the laboratory deliver data for the suitability (leaching behaviour, kinetic data, HRT and longevity) of reactive material. Relying on the laboratory and site investigation data the biobarrier can be designed. Modeling studies help to understand the groundwater regime and thus supports proper selection of biobarrier location. Regarding the size and contaminant distribution in the subsurface different biobarrier configurations can be installed as a sustainable remedial action.

REFERENCES

Addy, K., Gold, A.J., Christianson, L.E., David M.B., Schipper, L.A. and Ratigan, N.A. (2016). Denitrifying bioreactors for nitrate removal: A meta-analysis. Journal of Environmental Quality, 45, 873-881. doi:10.2134/jeq2015.07.0399.

Agamuthu, P. (2009, November). Challenges and opportunities in agro-waste management: An Asian perspective. Inaugural meeting of First Regional 3R Forum in Asia, Tokyo, Japan.

Ahmad, F., Adamson, D.T. and Farhat, S.K. (2009). Treatment of an explosives plume in groundwater using an organic mulch biowall. Remediation, 20, 21-40. doi: 10.1002/rem.20227.

Aloni, A. and Brenner, A. (2017). Use of cotton as a carbon source for denitrification in biofilters for groundwater remediation. Water, 9, 714-724. doi: 10.3390/w9090714.

Andrade, D.C. and dos Santos, E.V. (2020). Combination of electrokinetic remediation with permeable reactive barriers to remove organic compounds from soils. Current Opinion in Electrochemistry, 22, 136-144. doi: 10.1016/j.coelec.2020.06.002.

Aoyagi, T., Hamai, T., Hori, T., Sato, Y., Kobayashi, M., Sato, Y., Inaba, T., Ogata, A., Habe, H. and Sakata, T. (2017). Hydraulic retention time and pH affect the performance and microbial communities of passive bioreactors for treatment of acid mine drainage. AMB Express, 7, 142. doi: 10.1186/s13568-017-040-z.

Cameron, S.G. and Schipper, L.A. (2010). Nitrate removal and hydraulic performance of organic carbon for use in denitrification beds. Water Research, Ecological Engineering, 36, 1588–1595. doi:10.1016/j.ecoleng.2010.03.010.

Barba, S., Villaseñor, J., Cañizarres, P. and Rodrigo, M.A. (2019). Strategies for electrobioremediation ofoxyfluorten polluted soils. Electrochimica Acta, 297, 137-144. doi: 10.1016/j.electacta. 2018.11.195.

Barba, S., López-Vizcaíno, R., Saez, C., Villaseñor, J., Cañizarres, P., Navarro, V. and Rodrigo, M.A. (2018). Electro-bioremediation at the prototype scale: What it should be learned for scale-up. Chemical Engineering Journal, 334, 2030-2038. doi:10.1016/j.cej.2017.11.172.

Bekele, D.N., Du, J., de Freitas, L.G., Mallavarapu, M., Chadalavada, S. and Naidu, R. (2019). Actively facilitated permeable reactive barrier for remediation of TCE from a low permeability aquifer: Field application, Journal of Hydrology, 572, 592-602. doi: 10.1016/j.jhydrol.2019.03.059.

Benner S.G., Blowes, D.W., Gould, W.D., Herbert, R.B. and Ptacek, C.J. (1999). Geochemistry of a permeable reactive barrier for metals and acid mine drainage. Environmental Science and Technology, 33, 2793-2799. doi: 10.1021/es981040u.

Buscheck, T., Mackay, D., Paradis, C., Schmidt, R. and de Sieyes, N. (2019). Enhancing microbial sulfate reduction of hydrocarbons in groundwater using permeable filled borings. Groundwater Monitoring and Remediation, 39, 48-60. doi: 10.1111/gwmr. 12346.

Cameron, S.G. and Schipper, L.A. (2010). Nitrate removal and hydraulic performance of organic carbon for use in denitrification beds. Ecological Engineering, 36, 1588-1595. doi: 10.1016/j.ecoleng. 2010.03.010.

Chu, B. and Eivazi, F. (2018). Enhanced dissipation of selected herbicides in a simulated organic matrix biobed: A system to control on-farm point source pollution. Journal of Environmental Quality, 47, 221-227. doi: 10.2134/jeq.2016.04.0124.

Coppola, L., Castillo, M.D.P., Monaci, E. and Vischetti, C. (2007). Adaptation of the biobed composition for chlorpyrifos degradation to southern europe conditions. Journal of Agricultural and Food Chemistry, 55, 396-401. doi: 10.1021/jf062744n.

Dahiru, M., Bakar, N.K.A., Yusoff, I. and Ladan, M. (2017). Carbon source screening for nitrate remediation in permeable reactive barrier: Ion chromatography technique. Malaysian Journal of Fundamental and Applied Sciences, 13, 732-736.

Day, S. and Schindler, R. (2020). *Construction methods for the installation of permeable reactive barriers using the bio-polymer slurry method*. [Adobe Acrobat Reader version] available at: https://www.geo-solutions.com/wp-content/uploads/2017/03/4_Installation_of_Permeable_ Reactive_Barriers.pdf

Day, S.R., O'Hannesin, S.F. and Marsden, L. (1999). Geotechnical techniques for the construction of reactive barriers. Journal of Hazardous Materials, B67, 285-297. doi: 10.1016/S0304-3894(99)00044-8.

De Guzmán, G.T.N., Hapeman, C.J., Millner, P.D., Torrets, A., Jackson, D. and Kjellerup, B.V. (2018). Presence of organohalide-respiring bacteria in and around a permeable reactive barrier at a trichloroethylene-contaminated Superfund site. Environmental Pollution, 243, 766-776. doi: 10.1016/j.envpol.2018.08.095.

Divine, C.E., Roth, T., Crimi, M., DiMarco, A.C., Spurlin, M., Gillow, J. and Leone, G. (2018). The Horizontal reactive media treatment well (HRX well) for passive in-situ remediation. Groundwater Monitoring and Remediation, 38, 56-65. doi: 10.1111/gwmr.12252.

El Nadi, M.H., Elazizy, I. M. and Abdalla, M.A.F. (2014). Use of agricultural wastes as biofilter media in aerobic sewage treatment. Australian Journal of Basic and Applied Sciences, 8, 181-185.

Eykholt, G.R., Elder, C. and Benson, C.H. (1999). Effects of aquifer heterogeneity and reaction mechanism uncertainty on a reactive barrier. Journal of Hazardous Materials, 68, 73-96. doi: 10.1016/S0304-3894(99)00032-1.

Fetter, C.W. (1994). *Applied hydrogeology*. 3rd Ed. Merrill Publishing Company, Columbus, Ohio, USA.

Freethey, G.W., Naftz, D.L., Rowland, R.C. and Davis, J.A. (2003). *Chapter 5-Deep aquifer remediation tools: theory, design, and performance modeling*. in: D.L. Naftz, S.J. Morrison, J.A. Davis and C.C. Fuller (Ed.) Handbook of groundwater remediation using permeable reactive barriers, application to radionuclides, trace metals, and nutrients, Elsevier Science, USA, pp. 133-161.

Gavaskar, A., Gupta, N., Sass, B., Fox, T., Janosy, R., Cantrell, K. and Olfenbuttel, R. (1997). *Design guidance for application of permeable reactive barriers to remediate dissolved chlorinated solvents*. AL/EQ-TR-1997-0014, Battelle, Columbus, Ohio, USA.

Gavaskar, A., Gupta, N., Sass, B., Janosy, R. and Hicks, J. (2000). *Design Guidance for Application of Permeable Reactive Barriers*

for Groundwater Remediation, Final Report. Battelle, Columbus, Ohio, USA.

Ghazy, M.R., Basiouny, M.A. and Badawy, M.H. (2016). Performance of agricultural wastes as a biofilter media for low-cost wastewater treatment technology, Advances in Research, 7, 1-13. doi: 10.9734/AIR/2016/27926.

Gibert, O., Rötting, T., Cortina, J.L., de Pablo, J., Ayora, C., Carrera, J. and Bolzicco, J. (2011). In-situ remediation of acid mine drainage using a permeable reactive barrier in Aznalcóllar (Sw Spain). Journal of Hazardous Materials, 191, 287-295. doi:10.1016/j. jazmat.2011.04.082

Gill, R.T., Harbottle, M.J., Smith, J.W.N. and Thornton, S.F. (2014). Electrokinetic-enhanced bioremediation of organic contaminants: A review of processes and environmental applications. Chemosphere, 107, 31-42. doi: 10.1016/j.chemosphere. 2014.03.019.

Góngora-Echeverría, V.R., Martin-Laurent, F., Quintal-Franco, C., Giácoman-Vallejos, G. and Ponce-Caballero, C. (2017). Agricultural effluent treatment in biobed systems using novel substrates from southeastern Mexico: the relationship with physicochemical parameters of biomixtures. Environmental Science Pollution Research International*,* 24 (10) 9741-9753. doi:10.1007/s11356-017-8643-z

Grajales-Mesa, S.J., Malina, G., Kret, E., Szklarczyk, T. (2020). Designing a permeable reactive barrier to treat TCE contaminated groundwater: Numerical modeling. Tecnologia y Ciencias del Aqua, 11, 78-106. doi: 10.24850/j-tyca-2020-03-03.

Healy, M., Ibrahim, T.G., Lanigan, G.J., Serrenho, A.J. and Fenton, O. (2012). Nitrate removal rate, efficiency and pollution swapping potential of different organic carbon media in laboratory denitrification bioreactors. Ecological Engineering, 40, 198-209. doi: 10.1016/j.ecoleng.2011.12.010.

Hudak, P.F. (2016). ReNon-Pumped wells in backfilled trenches versus permeable reactive barriers for containing and treating contaminated groundwater. Environmental Practice, 18, 247-252. doi: 10.1017/S1466046616000442.

Interstate Technology and Regulatory Council (ITRC), PRB: Technology Update Team. (2011). *Permeable reactive barrier: Technology update*. Technical/Regulatory Guidance SDMS DOCID#1142231, Washington DC, USA.

Interstate Technology and Regulatory Council (ITRC). Permeable Reactive Barrier Team. (2005). *Permeable reactive barriers: Lessons learned/New directions*. PRB-4 Washington DC, USA.

Jamil, I.N. and Clarke, W.P. (2013). Bioremediation for acid mine drainage: organic solid waste as carbon sources for sulfate-reducing bacteria: A review. Journal of Mechanical Engineering and Sciences, 5, 569-581. doi: 10.15282/jmes.5.2013.3.0054.

Kuo, J. (2014). *Practical design calculations for groundwater and soil remediation*. CRC Press, Boca Raton, Fl, USA, ISBN-13: 978-1-4665-8524-9.

Kong, X., Lui, F. and Huang, G. (2014). Removal of ammonium from groundwater using multi-material permeable reactive barriers. Chinese Journal of Environmental Engineering, 8, 1355-1360.

Kornilovych, B., Wireman, M., Ubaldini, S., Guglietta, D., Koshik, Y., Caruso, B. and Kovalchuk, I. (2018). Uranium removal from groundwater by permeable reactive barrier with zero-valent iron and organic carbon mixtures: laboratory and field studies. Metals, 8, 408-422. doi: 10.3390/met8060408.

Li, J. and Zhang, B. (2020). Woodship-sulfur packed biological permeable reactive barrier for mixotrophic vanadium (V) detoxification in groundwater. Science China Technological Sciences, doi.org/10.1007/s11431-020-1655-6.

Liang, S.H., Kao, C.M., Kuo, Y.C. and Chen, K.F. (2011). Application of persulfate-releasing barrier to remediate MTBE and benzene contaminated groundwater. Journal of Hazardous Materials, 185, 1162-1168. doi.org/10.1016/j.jhazmat.2010.10.027.

Liang, Y., Ji, M., Zhai, H. and Wang, R. (2020). Removal of benzo[a]pyrene from soil in a novel permeable electroactive well system: Optimal integration of filtration, adsorption and bioelectrochemical degradation. Separation and Purification Technology, 252, 117458. doi: 10.1016/j.seppur.2020.117458.

Lima, A.T., Hofmann, A., Reynolds, D., Ptacek, C.J., Van Cappelen, P., Ottosen, L.M., Pamukcu, S., Alshawabekh, A., O'Carroll, D.M., Riis, C., Cox, E., Gent, D.B., Landis, R., Wang, J., Chowdhury, A.I.A., Secord, E.L., Sanchez-Hachair, A. (2017). Environmental electrokinetics for a sustainable subsurface. Chemosphere, 181, 122-133. doi: 10.1016/j.chemosphere.2017. 03.143.

Liu, C., Chen, X., Mack, E.E., Wang, S., Du, W., Yin, Y., Banwart, S.A. and Guo, H. (2019). Evaluating a novel permeable reactive bio-barrier to remediate PAH-contaminated groundwater. Journal of

Hazardous Materials, 368, 444-451. doi: 10.1016/j.jhazmat. 2019.01.069.

Liu, S.-J., Jiang, B., Huang, G-Q. and Li, X-G. (2006). Laboratory column study for remediation of MTBE-contaminated groundwater using a biological two-layer permeable barrier. Water Research, 40, 3401-3408. doi: 10.1016/j.watres.2006.07.015.

Liu, S-J., Zhao, Z-Y., Li, J., Wang, J. and Qi, Y. (2013). An aerobic two-layer permeable reactive biobarrier for the remediation of nitrate-contaminated groundwater. Water Research, 47, 5977-5985. doi: 10.1016/j.watres.2013.06.028.

Lubrecht, M.D. (2012). Horizontal directional drilling: A green and sustainable technology for site remediation. Environmental Science and Technology, 46, 2484-2489. doi: 10.1021/es203765q.

Maitra, S. (2019). Permeable reactive barrier: A technology for groundwater remediation- A mini review, Research Journal of Life Sciences, Bioinformatics. Pharmaceutical and Chemical Science, 5, 203-217. doi: 10.26479/2019.0501.21.

Malá, J., Bílková, Z., Hrıch, K., Schrımpelová, K., Michal Krıška, M. and Šereš, M. (2017). Sustainability of denitrifying bioreactors with various fill media. Plant and Soil Environment, 63, 442–448. doi: 10.17221/372/2017-PSE.

Maamoun, I., Aljamal, O., Falyouna, O., Eljamal, R. and Sugihara, Y. (2020). Multi-objective optimization of permeable reactive barrier design for Cr(VI) removal from groundwater. Ecotoxicology and Environmental Safety, 200, 110773. doi: 10.1016/j.ecoenv. 2020.110773.

Mateo-Sagasta, J., Zadeh, S.M. and Turral H. (2017). *Water pollution from agriculture: a global review, Executive Summary*, the Food and Agriculture Organization (FAO) of the United Nations and the International Water Management Institute (IWMI). [Adobe Acrobat Reader version] available at: www.fao.org/3/a-i7754e.pdf

Mayacela Rojas, C.M., Rivera Velàsquez, M.F., Tavolaro, A., Molinari, A. and Fallico, C. (2017). Use of vegetable fibers for PRB to remove heavy metals from contaminated aquifers-Comparisons among cabuya fibers; broom fibers and ZVI. International Journal of Environmental Research and Public Health, 14, 684-701. doi: 10.3390/ijerph14070684.

Mena, E., Villaseñor, J., Rodrigo, M.A. and Cañizares, P. (2016). Electrokinetic remediation of soil polluted with insoluble organics using biological permeable reactive barriers: Effect of periodic

polarity reversal and voltage gradient. Chemical Engineering Journal, 299, 30-36. doi: 10.1016/j.cej.2016.04.049.

Mena, E., Ruiz, C., Villaseñor, J., Rodrigo, M.A. and Cañizares, P. (2015). Biological permeable reactive barriers coupled with electrokinetic soil flushing for the treatment of diesel-polluted clay soil. Journal of Hazardous Materials, 283, 131-139. doi: 10.1016/j.jhazmat.2014.08.069.

Menz, J., Schneider, M. and Kümmerer, K. (2015) Usage pattern-based exposure screening as a simple tool for the regional priority-setting in environmental risk assessment of veterinary antibiotics: A case study of north-western Germany. Chemosphere, 127, 42-48. doi: 10.1016/j.chemosphere.2014.12.091.

Naval Facilities Engineering Command (NAVFAC) and Expeditionary Warfare Center (EXWC). *Permeable Reactive Barriers*. [Adobe Acrobat Reader version] available at: https://www.navfac.navy.mil /navfac_worldwide/specialty_centers/exwc/products_and_services/ ev/go_erb/program-support/technologies.html

Newell, C. (2008). *Treatment of RDX & HMX plumes using mulch biowalls, Final Report* (ESTCP Project ER-0426). GSI Environmental, Inc., [Adobe Acrobat Reader version] available at: file:///C:/Users/Burcu/ Downloads /ER-0426-FR.pdf

Nzeribe, B.N., Li, W., Crimi, M., Yao, G., Divine, C.E., McDonough, J. and Wang, J. (2020). Hydraulic performance of the horizontal reactive media treatment well: pilot and numerical study. Groundwater Monitoring and Remediation, 40, 30-41. doi: 10.1111/gwmr.12406.

Obi, F.O., Ugwuishiwu B.O. and Nwakaire, J.N. (2016). Agricultural waste concept, generation, utilization and management. Nigerian Journal of Technology, 35, 957-964. doi: 10.4314/njt.v35i4.34.

Obiri-Nyarko, F. and Grajales-Meaa, S. (2014). An overview of permeable reactive barriers for in situ sustainable groundwater remediation. Chemosphere, 111, 243-259. doi: 10.1016/j. chemosphere.2014.03.112.

Özkaraova, E.B., Kalin, B., Gkiouzepas, S. and Knapp, C.W. (2019). Industrial and agricultural wastes as a potential biofilter media for groundwater nitrate remediation, Desalination and Water Treatment, 172, 330-343. doi:10.5004/dwt.2019.25015.

Rad, P.R. and Fazlali, A. (2020). Optimization of permeable reactive barrier dimensions and location in groundwater remediation

contaminated by landfill pollution. Journal of Water Process Engineering, 35, 101196. doi:10.1016/j.jwpe.2020.101196.

Rasmussen, G., Fremmersvik, G. and Olsen, R.A. (2002). Treatment of creosote-contaminated groundwater in a peat/sand permeable barrier-a column study. Journal of Hazardous Materials, B93, 285-306. doi: 10.1016/s0304-3894(02)00056-0.

Reddy, K.A. and Cameselle, C. (2009). *Overview of electrochemical remediation technologies*. in K.A. Reddy and C. Cameselle (Ed.), Electrochemical remediation technologies for polluted soils, sediments and groundwater, John Wiley & Sons, Inc., New Jersey, USA. doi: 10.1016/j.gsd.2019.100317.

Sabiiti, E. (2011). Utilizing agricultural waste to enhance food security and conserve the environment. African Journal of Food, Agriculture, Nutrition and Development, 11, 1-9.

Scott, K.C. and Folkes, D.J. (2000, May). Groundwater modelling of a permeable reactive barrier to enhance system performance, Proceedings of the 2000 Conference on Hazardous Waste Research, Denver Colorado, 348-355.

Singh, R., Chakma, S. and Birke, V. (2020a). Numerical modeling and performance evaluation of multi-permeable reactive barrier system for aquifer remediation susceptible to chloride contamination. Groundwater for Sustainable Development, 10, 100317. doi: 10.1016/j.gsd.2019.100317.

Singh, R., Chakma, S. and Birke, V. (2020b). *Long-term performance evaluation of permeable reactive barrier for groundwater remediation using visual Modflow*. in: R. Sing, P. Shukla and P. Singh, (Ed.), Environmental processes and management, Water Science and Technology Library, Vol. 91, Springer.

Stringer, C., Wright, M. and Leatherman, C. (2020). *Passive treatment of selenium impacted groundwater with a biowal*l. NewFields, [Adobe Acrobat Reader version] available at: https://www.mtech. edu/mwtp/2015_presentations/tuesday/cam-stringer.pdf.

Suhogusoff, A.,V., Hirta, R., Aravena, R., Robertson, W.D., Ferrari, L.C.K.M., Stimson, J., Blowes, D.W. (2019). Dynamics of nitrate degradation along an alternative latrine improved by a sawdust permeable reactive barrier (PRB) installed in an irregular settlement in the municipality of São Paolo (Brazil). Ecological Engineering, 138, 310-322. doi: 10.1016/j.ecoleng.2019.08.001.

Sun, Z., Zheng, T., Xin, J., Zheng, X., Hu, R., Subhan, F. and Shao, H. (2018). Effects of alkali-treated agricultural residues on nitrate

removal and N$_2$O reduction of denitrification in unsaturated soil. Journal of Environmental Management, 214, 276-282. doi: 10.1016/j.jenvman.2018.02.078.

Thakur, A.K. and Kumar, M., *Reappraisal of Permeable Reactive Barrier as a sustainable groundwater remediation technology*, in M. Kumar, D.D. Snow, R. Honda and S. Mukherjee (Ed.), Contaminants in drinking and wastewater sources, Challenges and reigning technologies, Springer Nature Singapure Pte Ltd., ISBN 978-981-15-4598-6, 2021. pp. 179-208.

Thiruvenkatachari, R., Vigneswaran, S. and Naidu, R. (2008). Permeable reactive barrier for groundwater remediation. Journal of Industrial and Engineering Chemistry, 14, 145-156. doi:10.1016/j.jiec. 2007.10.001.

Torregrosa, M., Schwarz, A., Nancucheo, I. and Balladares, E. (2019). Evaluation of the bio-protection mechanism in diffusive exchange permeable reactive barriers for the treatment of acid mine drainage. Science of the Total Environment, 655, 374-383. doi: 10.1016/j. scitotenv.2018.11.083.

United Nations (UN), Department of Economic and Social Affairs, Population Division (2019). *World population prospects 2019: highlights*. (ST/ESA/SER.A/423), ISBN: 978-92-1-148316-1.

Upadhyay, S. and Sinha, A. (2018). Role of microorganisms in Permeable Reactive Bio-Barriers (PRBBS) for environmental clean-up: A review. Global Nest Journal, 20, 269-280.

US Air Force. (2008). Technical protocol for enhanced anaerobic bioremediation using permeable mulch biowalls and bioreactors, Final Report, Air Force Center for Engineering and the Environment Technical Directorate Environmental Science Division Technology Transfer Outreach Office, [Adobe Acrobat Reader version] available at: https://clu-in.org/download/ techfocus/prb/Final-Biowall-Protocol-05-08.pdf.

U.S. Environmental Protection Agency (USEPA). (1998). *Permeable reactive barrier technologies for contaminant remediation*. Office of Solid Waste and Emergency Response, EPA/600/R-98/125.

U.S. Environmental Protection Agency (USEPA). (2012). *A citizen's guide to permeable reactive barriers*. Office of Solid Waste and Emergency Response, EPA 542-F-12-015.

Warneke, S., Schipper, L.A., Matiasek, M.G., Scow, K.M., Cameron, S., Bruesewitz, D.A. and Mc Donald, I.R. (2011). Nitrate removal, communities of denitrifiers and adverse effects in different carbon

substrates for use in denitrification beds. Water Research, 45, 5463-5475. doi: 10.1016/j.wtrs.2011.08.007.

Wang, W. and Wu, Y. (2017). A multi-path chain kinetic reaction model to predict the evolution of 1,1,1-trichloroethane and its daughter products contaminant-plume in permeable reactive bio-barriers. Environmental Pollution, 253, 1021-1029. doi: 10.17632/d9mgynhmc4.1.

Weng, C. (2009). *Coupled Electrokinetic-Permeable Reactive Barriers*. in K.A. Reddy and C. Cameselle (Ed)., Electrochemical Remediation Technologies for Polluted Soils, Sediments and Groundwater, John Wiley & Sons, Inc., New Jersey, USA. doi: 10.1002/9780470523650.ch23.

Wick, L.Y., Shi, L. and Harms, H. (2007). Electro-bioremediation of hydrophobic organic soil-contaminants: A review of fundamental interactions. Electrochimica Acta, 52, 3441-3448. doi: 10.1016/j.electacta.2006.03.117.

Wilson, R.D., Mackay, D.M. and Cherry, J.A. (1997). Arrays of unpumped wells for plume migration control by semi-passive in situ remediation. Groundwater Monitoring and Remediation, 17, 185-193.

Zhang, Z., Gonzalez, A.M., Davies, E.G.R. and Lui, Y. (2012a). Agricultural wastes. Water Environment Research, 84, 1386-1406. doi: 10.2175/106143012X13407275695193.

Zhang, J., Feng, C., Hong, S., Hao, H. and Yang, Y. (2012b). Behavior of solid carbon sources for biological denitrification in groundwater remediation. Water Science Technology, 65, 1696-1704. doi: 10.2166/wst.2012.070.

ACTIVE FOOD PACKAGING TECHNOLOGY AS AN APPLICATION IN THE FOOD INDUSTRY

Demet Aydınoğlu[1]

[1]*(Assoc. Prof. Dr). Yalova University, e-mail: daydinoglu@yahoo.com*

ORCID *0000-0002-6104-7668*
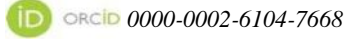
Increasing the shelf life of food products in the food industry is one of the vital issues in terms of the national economies both on a sectoral basis and in total. Various technologies are available to present food products to the consumer in the best quality, without losing their nutritional values and specific properties. These technologies, also known as food preservation techniques, start from the simplest and traditional drying and fermentation, and can be listed as much more complex pasteurization, sterilization, freezing technologies, the addition of various food preservatives, and storage in a controlled-modified atmosphere[1]. At this point, active food packaging technology emerges as a new method that can be used in food preservation, and can be an alternative to some of the above-mentioned methods. This technology can be defined as a technique that aims to change or modify the atmosphere in the package by including some active substances in the composition of packaging materials or placing various active substances inserted in sachets or pads inside the packaging. This way, the nutritional value and quality of the product is preserved for a long time and thus the shelf life is extended[2].
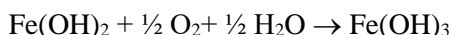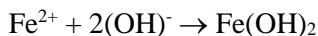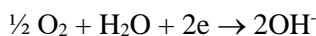
In terms of food safety, active food packaging technology has received great attention recently and increasingly replacing the food additives used during the food production processess. In fact, the degradation of food products starts on the surface of the food, and in the classical sense, the preservatives included in the food during production are used more than necessary in this sense[3]. Essentially, protecting only the surface of the food is very effective in increasing its shelf life.

The materials used in the active packaging technique for this purpose are generally divided into two main groups as absorbing/scavenging and releasing/emitting systems and the most commonly used active packaging systems are: Oxygen scavengers, moisture absorbers, ethylene scavengers, carbon dioxide releasers, antioxidant releasers, and antimicrobial releasers[2].

1) Oxygen scavenger systems: The oxygen scavengers contained in this type of packaging help to preserve the quality of the food material for a long time by reducing the oxygen ratio in the package to a certain level, preventing oxidation reactions which is especially important for fatty foods. These systems are also effective in the decrement in the growth of mold and aerobic microorganisms in an oxygenated environment[4,5]. In fact, foods are usually packaged in a modified atmosphere (MAP) or vacuum to eliminate these mentioned unwanted situations[6]. However, these methods alone are not fully sufficient. For example, in the study performed by Gibi et al.[7], the oxygen level in the headspace was achieved to decrease to only 0.5-2 vol% by applying vacuum packaging or MAP. On the other hand, Mills at al.[8] reported that it can be reduced to less than 0.1% in the case of using oxygen scavengers.

Some of the oxygen absorbers/scavengers:iron powder, ascorbic acid, various enzymes, unsaturated fatty acids[9]. Among them, the most widely used oxygen scavenger is the iron powder, which easily oxidizes and absorbs the oxygen in the environment[2]. In a study carried out with polymer films incorporated to an iron powder it was observed that the film had oxygen capacity of $33 cm^3 O_2/m^2$ film in 4 day[9].

The oxidation mechanism occurred in this type of packages is as below[10]:

$$Fe \rightarrow Fe^{2+} + 2e$$

$$\frac{1}{2} O_2 + H_2O + 2e \rightarrow 2OH^-$$

$$Fe^{2+} + 2(OH)^- \rightarrow Fe(OH)_2$$

$$Fe(OH)_2 + \frac{1}{2} O_2 + \frac{1}{2} H_2O \rightarrow Fe(OH)_3$$

Some of the commercial oxygen scavenger active packagings are Ageless® (Mitsubishi Gas Chemical), Amosorb® (ColorMatrix Group Inc), Desi Pak® (Süd-Chemie AG), Oxbar® (Constar International Inc.), FreshMax® (Multisorb Technologies), and Freshilizer® (Toppan Printing Co.) etc.[11].

2) Moisture scavenger systems: In this type of active packaging system, containing moisture-retaining substances, , moisture absorbers ensure that the humidity of the atmosphere in the food packaging is kept at a certain level.. In this way, the absorption of moisture by the food, and thus the growth of mold, yeast and bacteria on the food surface that depends on water content/ activitiy is prevented or at least reduced, and consequently the shelf life of the food is extended[12,13]. High humidity should not be considered only from a microbial point of view. For example, the high humidity percentages might cause the food to soften and reduce the quality in dry products such as biscuits. Humidity is also an important

factor in packaged fruits and vegetables. The harvested fruits and vegetables continue respiration, and this could cause formation of water vapor resulted in an increment of humidity in the packaging. This increase leads to both the fogging of the package and microbiological degradation and also enzyamtic activity after a certain period of time. In order to control the humidity in the packaging, humectants are used either by incorporating them into the packaging material or by placing them in an adsorbent pad, film coating, or pouch. Moisture scavengers can be divided into two main groups: liquid absorbers and moisture traps[14].
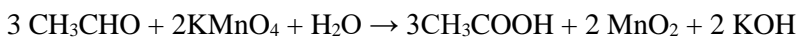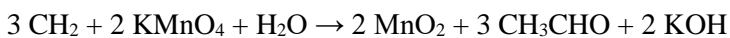
a) Liquid absorbers: These are in the form of a pad, paper, etc., and are usually placed under the food product in the package. The most common uses are for meat, fish, chicken, fruit and vegetables cuts with high water activity[5.] These pads in the package usually consist of porous materials, polymers such as polypropylene and polystyrene, foam and porous polystyrene sheets or cellulose and their combination with superabsorbent polymers/minerals/salts[16]. Essentially, adsorbent pads are generally not considered as active packaging. However, there is a difference here. According to the European Union Regulation No: 450/2009, it is stated that while adsorbent materials consisting of only a natural structure, for example 100% cellulose, are not considered as active materials, pads prepared by adding various active substances to the structure to increase absorption can be considered as active packaging[17].

b) Moisture scavengers (Desiccants): These are generally used by placing them in a permeable bladder. They can also be integrated into an absorbent pad, polymeric films, and humidity-regulating trays. The most commonly used humectants are: silica, zeolite, bentonite, activated carbon, salts (NaCl, KCl, and $CaCl_2$), etc. While they absorb moisture thanks to their highly porous structure, salts such as NaCl and KCl, in addition, create an electrostatic interaction between the charge they carry and the water molecules in the air, allowing moisture to be retained. The moisture holding capacity of desiccants depends on their water vapor retention isotherms[18]. In a study carried out by Mahajan et al.[19], the moisture absorber, prepared by combining bentonite/sorbitol/$CaCl_2$ in certain proportions, was proven to have moisture scanvenging capacity of 0.94 g water per g desiccant at 96% relative humidity.

Some moisture-retaining active food packaging materials that have taken place in the markets areHumidipak[®/©], Thermarite[®/©], Toppan[®/©], Peaksorb[®/©], MINIPAX[/©] STRIPAX[®/©], and DesiMax[®/©11].

3) Ethylene scavenger systems: This system is particularly useful for packaging of fresh or poorly processed fruits and vegetables. After the harvesting of fruits and vegetables, their respiration continues for a while causing them to become moist and soft, aside with destruction of chlorophyll, especially in leafy vegetables reducing their shelf life[20,21]. The

main factors effective on the increment in respiratory rate are ambient temperature and oxygen/carbon dioxide ratio. Ethylene is another effective factor, also known as the maturation hormone[2]. Preventing the accumulation of ethylene gas in the packaging and removing it from the packaging atmosphere is very important in terms of increasing the shelf life of vegetables and fruits. In this sense, various materials that are placed in the package and ensure the capture of ethylene gas are used. Many of these are either incorporated into the composition of the packaging material or placed in the sachets that are inserted in the package. In general, potassium permanganate is preferred by companies to obtain an ethylene scavenger system. Potassium permanganate oxidizes ethylene to acetaldehyde, and acetaldeyde to acetic acid, then acetic acid into carbon dioxide and water[22].

$$3\ CH_2 + 2\ KMnO_4 + H_2O \rightarrow 2\ MnO_2 + 3\ CH_3CHO + 2\ KOH$$

$$3\ CH_3CHO + 2KMnO_4 + H_2O \rightarrow 3CH_3COOH + 2\ MnO_2 + 2\ KOH$$

$$3\ CH_3COOH + 8\ KMnO_4 \rightarrow 6\ CO_2 + 8\ MnO_2 + 8\ KOH + 2\ H_2O$$

Because of being toxic, potassium permanganate can not be used for he packages that are directly in contact with food, but it can be applied in sachets. In most applications, potassium permanganate is used by mixing at a ratio of 4-6% with various substances such as activated carbon, silica gel, perlit, alümina, etc., and placed in a pouch[23].

Another group used to absorb ethylene gas is nanoparticles such as titanium dioxide and zinc oxide. In the study performed by Yang et al.[24], polyethylene blended with nanoparticles of Ag, TiO_2 and kaolin were tested to observe the effect of the prepared packaging material on the shelf life of fresh strawberries at 4°C. The study revealed that active packaging reduced the decay of fruit to 16.7%, while normal packaging contained no active agent decreased to 26.8%.

Ethylene scavenger systems based on the principle of dispersing minerals such as zeolite and clay in the packaging film have also been developed[11]. Minerals added to the film material absorb ethylene, and at the same time change the film's permeability properties and increase the diffusion rates of ethylene and carbondioxide.

Ethylene scavengers are successfully used in the preservation of tropical fruits such as kiwi, banana, avocado, pear, apple, grape, tomato, sliced-chopped onion, spinach, and similar products[2]. Some of the commercial ethylene scavengers are Neupalon®/© (Sekisu Jushi, Japan), Hatofresh®/©Honsu paper, Japan), Evert-Fresh®/© Evert-Fresh,USA), Peakfresh®/© (Peak fresh products, Australia), and Orega bag®/© (Cho Yang Heung San. Co. USA)[2,11].

4) Carbondioxide release/ scavenger systems: It is known from the literature that CO_2 has an antimicrobial effect and high levels of carbon dioxide are widely used in certain foods such as fish, meat, cheese, etc. to slow or prevent microbial growth. Since generally plastic films have higher permeability for CO_2 compared to O_2 gas, gradually decreasing of the rate of CO_2 in the packaging cause increment in O_2 rate, thus, promote microbial growth.[22]. At this point, a packaging system that emits CO_2 and compensates for the lost CO_2 is needed. A mixture of citric acid-sodium bicarbonate is mostly used with this purpose. The reaction of citric acid-sodium bicarbonate to capture carbon dioxide is as follows[25]:

$$NaHCO_3 + C_6H_8O_7 \rightarrow CO_2 + C_6H_7O_7Na$$
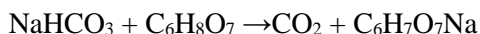
On the other hand, in some cases, carbon dioxide formed as a result of food spoilage or respiratory reactions should be removed from the packaging. For example; in packed coffees carbon dioxide scavengers are used, as, in the roasting stage of coffee beans, high amounts of CO_2 is released due to the Strecker decomposition reactions that takes place between sugars and amines, and causing the packaging to swell, and even explode. Generally, the active agent in carbondi oxide scavengers is calcium hydroxide ($Ca(OH)_2$). The reaction of calcium hydroxide to capture carbon dioxide is as follows[26]:

$$CaO + H_2O \rightarrow Ca(OH)_2$$

$$Ca(OH)_2 + CO_2 \rightarrow CaCO_3 + H_2O$$
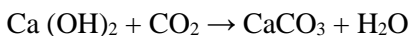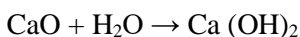
The most produced and used carbon dioxide scavenger systems have two functions (oxygen and carbon dioxide scavengers. This way, they provide both retardation of oxidative aroma changes and absorption of carbon dioxide in the packaging. For example; the commercial O_2 and CO_2 scavenger sachets of FreshLock[®/©] and Ageless[®/©] retardate aromatic changes and, at the same time, they absorb carbon dioxide in the headspace[26].

5) Antioxidant release systems: These active packaging systems consist of various antioxidant substances that prevent food from degradation occurby the effect of oxygen. As is known, in many food products, autoxidation reactions take place naturally between the food components and the oxygen in the atmosphere inside packaging and cause a decrease in the quality of the product[27]. These reactions are largely inhibited by the use of antioxidants. In general, antioxidants enable free radicals to be inactivated by either binding the free oxygen radical that causes autoxidation or by transferring the hydrogen atoms to these oxygen

radicals. This way, they keep from the formation of unwanted by-products and new free radicals, and hence, extend the shelf life by preventing or at least delaying the spoilage of foods[28]. The most known materials as antioxidant release food packaging are butylated hydroxy anisole (BHA), butylated hydroxytoluene (BHT) and various phenolic molecules such as tertiary butylated hydroxyquinone (TBHQ) and silver zeolite[29]. In these compounds, there is a mechanism that starts from the phenolic hydroxyl group in the structure, and then proceeds as the free radical is retained by the antioxidant[30].

In recent years, considering the negative effects of synthetic compounds on human health, the use of natural antioxidants rather than synthetic ones is encouraged. Especially the use of polyphenols, tocopherols, plant extracts and essential oils as natural antioxidants is of great interest[31-34], and with the use of natural antioxidants remarkable results have been achieved. For example, Graciano-Verdugo et al.[35] reported that LDPE films containing 1.9% and 3% α-tocopherol preserved the oxidative stability of corn oil for more than four weeks compared to a control bag without antioxidant. On the other hand, the antioxidant activity of C (ascorbic acid) and E vitamins are also assesable. Vitamin E inhibits free radicals with a mechanism similar to BHT, which originates from phenolic hydroxyl in its structure, while ascorbic acid inactivates free radicals by giving its hydrogen atom to the oxygen radical[36]. Especially in America, BHT and BHA are used in the packaging of breakfast cereals and some snack food products. However, the point to be considered here is that the antioxidant effect required by the food is provided by the necessary diffusion by the packaging material, and the relevant research on this subject is ongoing[37].

6) Antimicrobial release systems: In antimicrobial packaging systems, an antimicrobial substance is added to the composition of the packaging material or into a sachet placed in the package, or the inner surface of the packaging material is coated with an antimicrobial substance[38]. The basic mechanism in this type of packaging is that, the antimicrobial substance either included in the packaging composition or placed in the package with several ways, such as a sachet, is released in a controlled manner and diffuses towards the surface of the food substance. The releasing antimicrobial substance helps the food to remain intact for a long time by preventing the occurrence of microbial degradation reactions that might occur on the outer surface of the food product. Silver is often utilized as an antimicrobial agent in the antimicrobial packaging. In the study of Soysal et al.[39], it was proven that LDPE films containing silver-zeolite reduced the total aerobic mesophilic bacteria count of chicken samples 0.51 times compared to the samples in normal bags. Especially in the Japanese plastic food packaging industry, silver zeolite is frequently

used. However, since it is expensive, it is applied as a thin layer laminate. On the other hand, some antimicrobial substances that cannot withstand the temperature at which polymer films are produced, are prepared by coating them on the film surface afterwards. Nisin/methylcellulose or nisin/zein coated polyethylene films can be given as examples. Apart from these, nisin/ EDTA/citric acid adsorbed on polyethylene (PE), polypropylene (PP), polyethylene terephthalate (PET) and polyvinylchloride (PVC), and also pediosin adsorbed in cellulosic sachets are other examples that can be evaluated as antimicrobial active packaging [23,40].

Farther than this, in some applications, polymer films such as chitosan and poly-L-lysine, which have antimicrobial properties, are used. Organic acids and their salts such as sorbate, benzoate and propionate, and bacteriocins such as nisin and pediosin, and enzymes such as lysozyme are the leading substances that have antimicrobial properties, and are used in various ways. However, in recent years, natural antimicrobials such as essential oils have replaced the synthetic antimicrobials especially in order to increase food safety[21,40].

Apart from all these, both oxygen absorbers and humidifiers, as well as ethanol and carbon dioxide releases indirectly show antimicrobial properties and can be evaluated within this group. In antimicrobial packaging, there are many products under various trade names in the foreign market, especially in Japan, America, England and France. Zeomic®, Microban®, Microatmosphère™, Novaron®/™/©, MicroFree™ are some of them[11].

Conclusion

Active packaging technology has being received growing interest day by day, because with the use of this technology it is achieved to extend food shelf life that is great importance in food industry, without using food additive, most of which are harmful for human health.

However, on the one hand, researches continue with various materials to increase the effectiveness of these materials. On the other hand, researches are carried out with natural materials to replace synthetic-containing packaging materials. And it still stands before us as one of the issues open to improvement.

REFERENCES

1. Adegoke GO, Olapade AA: Preservation of Plant and Animal Foods: An Overview, in Bhat R, Alias AK, Paliyath G (Eds). Progress in Food Preservation, West Sussex, John Wiley & Sons, 2012: 603-611.

2. Yıldırım S, Röcker B, Pettersen MK, Nilsen-Nygaard J, Ayhan Z, Rutkaite R, Radusin T, Suminska P, Marcos B, and Coma V. Active packaging applications for food. Compr. Rev. Food Sci. Food Saf, 2017: 17: 165–199.

3. Majumdar A, Pradhan N, Sadasivan J, Acharya A, Ojha N, Babu S, Bose S: Food Degradation and Foodborne Diseases: A Microbial Approach, in Holban AM, and Alexandru Mihai Grumezescu AM (Eds). Microbial Contamination and Food Degradation A volume in Handbook of Food Bioengineering Book, Massachusetts, Academic Press, 2018:115-116.

4. Solovyov SE, Oxygen scavengers, in Yam KL (Ed). The Wiley encyclopedia of packaging technology. 3 ed. Hoboken, New Jersey, U.S.A.:John Wiley & Sons Ltd. 2010:841–50.

5. Arvanitoyannis IS, and Oikonomou G. Active and intelligent packaging, in Arvanitoyannis IS (Ed). Modified atmosphere and active packaging technologies. Boca Raton, Florida, U.S.A.: CRC Press. 2012: 628–54.

6. Rooney ML, Introduction to active food packaging Technologies, in Han J (Ed). Massachusetts, Academic Press, 2005:63-77.

7. Gibis D, Rieblinger K, Oxygen scavenging films for food application. Procedia Food Science, 2011; 1: 229–234.

8. Mills A, Doyle G, Peiro AM, and Durrant J, Demonstration of a novel, flexible, photocatalytic oxygen-scavenging polymer film. J. Photochem. Photobiol. A. 2006; 177: 328–331.

9. Dey A, and Neogi S, Oxygen scavengers for food packaging applications: A Review. Trends Food Sci Techno. 2019; 90: 26-34.

10. Biji KP, Application of Active Packaging for Enhancing the Shelf life of Yellowfin Tuna (Thunnus albacares Bonnaterre, 1788) During Chilled Storage, Cochin University of Science and Technology, 2016: 101-102.

11. Pereira de Abreu DA, Cruz JM, and Paseiro Losada P. Active and intelligent packaging for the food industry. Food Reviews International, 2012; 28:146–187.

12. Labuza TP, Hyman CR, Moisture migration and control in multi-domain foods. Trends Food Sci Technol 1998; 9: 47–55.

13. Day B, Active packaging of food, in: Kerry J, Butler P, (Eds)., Smart packaging technologies for fast moving consumer goods. Chichester, England: John Wiley & Sons Ltd. 2008: 1-18.

14. Brody AL, Strupinsky E, and Kline LR. Antimicrobial Packaging, Active Packaging for Food Applications, Boca Raton, Florida, U.S.A.: CRC Press. Brody and others 2001: 128-144.

15. Vermeiren L, Devlieghere F, van Beest M, de Kruijf N, and Debevere J, Developments in the active packaging of foods, Trends in Food Science&Technology, 1999; 10:77-86.

16. Scetar M, Kurek M, and Galic K, Trends in meat and meat products packaging–a review, CJFST, 2010; 2: 32-48.

17. European Commission. 2009. EU Guidance to the Commission Regulation (EC) No 450/2009 of 29 May 2009 on active and intelligent materials and articles intended to come into the contact with food (version 1.0). Available from: https://ec.europa.eu/food/safety/chemical_safety/food_contact_m aterials_en. Accessed 2017 October 24.

18. Sangerlaub S, Bohmer M, and Stramm C, Influence of stretching ratio and salt concentration on the porosity of polypropylene films containing sodium chloride particles, J. Appl. Polym. Sci, 2013; 3: 1238-1245.

19. Mahajan PV, Rodrigues FA, Motel A, Leonhard A, Development of a moisture absorber for packaging of fresh mushrooms (*Agaricus bisporous*). Postharvest Biol Tec 2008; 48: 408-414.

20. Saltveit ME. Effect of ethylene on quality of fresh fruits and vegetables, Postharvest Biol Tec 1999; 15: 279-292.

21. Ozdemir M, and Floros JD, Active food packaging technologies. Crit Rev Food Sci Nutr 2004; 44: 185-193.

22. Gaikwad KK, Singh S, Negi YS, Ethylene scavengers for active packaging of fresh food produce. Environ. Chem. Lett. 2019. doi:10.1007/s10311-019-00938-1.

23. Abe K, and Watada A, Ethylene absorbent to maintain quality of lightly processed fruits and vegetables. J. Food Sci. 1991; 56: 1589–1592.

24. Yang FM, Li HM, Li F, Xin ZH, Zhao LY, Zheng YH, Hu QH, Effect of nano-packing on preservation quality of fresh strawberry (*Fragaria ananassa* Duch. cv Fengxiang) during storage at 4 °C. J Food Sci 75(3): C236-40..

25. Sadik T, Pillon C, Carrot C, and Reglero Ruiz JA, Dsc studies on the decomposition of chemical blowing agents based on citric acid and sodium bicarbonate. Thermochimica Acta, 2018; 659: 74-81.

http://www.plastik-ambalaj.com/tr/plastik-ambalaj-makale/887-aktif-ambalajlama-teknolojisi-ve-akll-ambalajlar-Food Packaging Technology, Mustafa Üçüncü)

26. Çakmakçı S, and Gökalp HY, Briefly oxidation in foods; antioxidants and their use in the food industry. Journal of Atatürk University Faculty of Agriculture, 1992; 232: 174-192.

27. Nerin C, Oxidation in foods and beverages and antioxidant applications. Volume 2: Management in different industry sectors, in : Deck EA, Elias RJ, McClements DJ, Antioxidant active food packaging and antioxidant edible films, C. Nerin, CPS-University of Zaragoza, Spain,2010, Cambridge, Woodhead Publishing Limited 2010: 496-515

28. Karagöz Ş, and Demirdöven A, Current Applications in Food Packaging: Modified Atmosphere, Active, Intelligent and Nanotechnological Packaging Applications, Gaziosmanpasa Journal of Scientific Research, 2017; 6: 9-21.

29. Abdel-Hameed HS, Ahmed NS, Amal M, and Nassar AM, Some Ashless Detergent/Dispersant Additives for Lubricating Engine Oil, Publisher: OmniScriptum GmbH & Co. KG, Germany, 2015: 38-39.

30. Ner´ın C, Tovar L, Djenane D, Camo J, Salafranca J, Beltr´an JA, and Roncal´es P. Stabilization of beef meat by a new active packaging containing natural antioxidants. J Agr Food Chem, 2006; 54: 7840-7846.

31. Park HY, Kim SJ, Kim KM, You YS, Kim SY, and Han J, Development of antioxidant packaging material by applying corn-zein to LLDPE Film in combination with phenolic compounds. J Food Sci 2012; 77: E273-279.

32. Barbosa-Pereira L, Cruz JM, Send´on R, Rodr´ıguez Bernaldo de Quir´os A, Ares A, Castro-L´opez M, Abad MJ, Maroto J, and Paseiro-Losada P, Development of antioxidant active films containing tocopherols to extend the shelf life of fish. Food Contr 2013; 31: 236-243.

33. Marcos B, S´arraga C, Castellari M, Kappen F, Schennink G, and Arnau J, Development of biodegradable films with antioxidant properties based on polyesters containing α-tocopherol and olive leaf extract for food packaging applications. Food Pack Shelf Life 2014; 1:140-150.

34. Graciano-Verdugo AZ, Soto-Valdez H, Peralta E, Cruz-Z´arate P, Islas-Rubio AR, S´anchez-Valdes S, S´anchez-Escalante A, Gonz´alez-M´endez N, and Gonz´alez-R´ıos H, Migration of α-tocopherol from LDPE films to corn oil and its effect on the oxidative stability. Food Res Intl, 2010; 43:1073-1078.

35. Nimse SB, Pal D, Free radicals, natural antioxidants, and their reaction mechanisms, RSC Advances, 2015; 5: 27986-28006.

36. Gómez-Estaca J, López-de-Dicastillo C, Hernández-Muñoz P, Catalá R, and Gavara, R, Advances in antioxidant active food packaging. Trends in Food Science & Technology 2014; 35: 42-51.

37. Coma V, Bioactive packaging technologies for extended shelf life of meat–based products. Meat Sci. 2008; 78: 90-103.

38. Soysal C¸ Bozkurt H, Dirican E, Güçlü M, Bozhüyük ED, Uslu AE, and Kaya S. Effect of antimicrobial packaging on physicochemical and microbial quality of chicken drumsticks. Food Contr 54: 294–299.

39. Corrales M, Fernández A, and Han JH, Antimicrobial packaging systems. Innovations in Food Packaging, 2014: 133-170.